
**A search for exotic decay modes on the
proton drip-line
- *the cases of* $^{20-21}\text{Mg}$**

MORTEN VINTHER LUND

Department of Physics and Astronomy
Aarhus University, Denmark

**Dissertation for the Degree
of Doctor of Philosophy**

February 2016

Morten Vinther Lund
Department of Physics and Astronomy
Aarhus University
Ny Munkegade, Bldg. 1520
8000 Aarhus C
Denmark
E-mail: mv107@phys.au.dk

This dissertation has been submitted to the Faculty of Science and Technology at Aarhus University, Denmark, in partial fulfillment of the requirements for the PhD degree in physics. The work presented has been performed in the period from February 2012 to January 2016 under the supervision of Hans O. U. Fynbo and Karsten Riisager. The experimental work was carried out at the ISOLDE facility at CERN, Geneva, Switzerland. The analysis work was mainly carried out at the Department of Physics and Astronomy in Aarhus. The ISOLDE group at CERN, Geneva, Switzerland, is acknowledged for its hospitality in the period from August to December 2014.

Contents

| | |
|--|-----------|
| Table of Contents | iii |
| Preface | vii |
| Acknowledgements | ix |
| Summary | xi |
| Dansk resumé (Summary in Danish) | xiii |
| List of Publications | xv |
| 1 Introduction | 1 |
| 1.1 Beta-decay | 3 |
| 1.1.1 Fermi and Gamow-Teller decays | 3 |
| 1.1.2 ft -values | 4 |
| 1.1.3 Beta-decay strength distribution | 5 |
| 1.1.4 Isospin symmetry breaking | 7 |
| 1.2 Beta-delayed particle emission | 8 |
| 1.3 Gamma-ray emission | 9 |
| 1.4 Production of exotic nuclei | 10 |
| 1.4.1 Methods of production | 10 |
| 1.4.2 Production of magnesium at the ISOLDE facility | 11 |
| 1.5 Experimental strategy | 12 |
| 2 Motivation ^{21}Mg | 15 |
| 2.1 The history of the ^{21}Mg research | 15 |
| 2.2 Possible decay modes of ^{21}Mg | 18 |
| 3 Experimental methods: ^{21}Mg | 21 |
| 3.1 Detector setup | 21 |
| 3.2 Energy loss calculations | 23 |
| 3.3 Calibration of detectors | 26 |
| 3.3.1 DSSSD | 26 |
| 3.3.1.1 Geometry calibration | 26 |
| 3.3.1.2 Energy calibration | 28 |
| 3.3.2 Energy calibration of unsegmented detectors | 31 |

| | | |
|----------|---|-----------|
| 4 | ^{21}Mg: modified decay scheme and other results | 35 |
| 4.1 | Initial overview of the data | 35 |
| 4.2 | Half-life determination | 39 |
| 4.3 | Time distribution analysis | 39 |
| 4.4 | Spectroscopic properties deduced from line shape fit | 43 |
| 4.4.1 | Line shape | 43 |
| 4.4.2 | Fitting procedure | 45 |
| 4.4.3 | Energy dependence of Γ | 49 |
| 4.4.4 | Relative intensities | 50 |
| 4.5 | Decay scheme | 52 |
| 4.6 | Beta-decay strength distribution | 61 |
| 4.7 | Summary and conclusions | 63 |
| 5 | ^{21}Mg: new exotic decay modes | 67 |
| 5.1 | $\beta\alpha$ - and $\beta p\alpha$ -emission from ^{21}Mg | 67 |
| 5.1.1 | Overview of the data | 67 |
| 5.1.2 | Time distribution analysis | 69 |
| 5.1.3 | Decay scheme | 70 |
| 5.2 | Systematics of beta-delayed particle emission | 70 |
| 5.2.1 | Other cases | 72 |
| 5.2.2 | Systematics of beta-delayed decays | 73 |
| 6 | Motivation ^{20}Mg | 77 |
| 6.1 | The history of the ^{20}Mg research | 77 |
| 6.2 | Characteristics of the ^{20}Mg beta-decay | 81 |
| 6.3 | Astrophysical motivations | 82 |
| 6.3.1 | Breakout of the hot CNO cycles | 82 |
| 6.3.2 | Spin and parity of the 2.645(6) MeV resonance in ^{20}Na | 83 |
| 6.3.3 | Beta-delayed proton-alpha emission | 84 |
| 7 | Experimental methods: ^{20}Mg | 85 |
| 7.1 | Detector setup | 85 |
| 7.2 | Calibration of silicon detectors | 87 |
| 7.2.1 | Carbon foil thickness | 88 |
| 7.2.2 | Silicon Strip Detectors | 90 |
| 7.2.2.1 | Geometry | 90 |
| 7.2.2.2 | Energy | 91 |
| 7.2.3 | The U2 detector | 94 |
| 7.2.4 | Pad detectors | 98 |
| 7.3 | Calibration of HPGe-detectors | 100 |

| | | |
|----------|--|------------|
| 7.3.1 | Energy | 100 |
| 7.3.2 | Absolute efficiency | 100 |
| 8 | ^{20}Mg: beta-delayed proton spectrum | 107 |
| 8.1 | Particle spectra | 107 |
| 8.1.1 | Proton spectra | 109 |
| 8.1.2 | Alpha-particle spectra | 115 |
| 8.1.3 | Gamma-ray spectra | 118 |
| 8.2 | Half-life determination | 119 |
| 8.3 | Decay scheme | 121 |
| 8.3.1 | Proton energies | 121 |
| 8.3.2 | Classification of proton peaks | 127 |
| 8.3.3 | Reconstruction of the decay scheme | 130 |
| 8.4 | Beta-decay strength distribution | 133 |
| 8.4.1 | Relative intensities | 133 |
| 8.4.2 | Absolute normalization with the 984 keV gamma-ray | 134 |
| 8.4.3 | Absolute beta-decay branching ratios | 136 |
| 8.5 | Summary and conclusions | 142 |
| 9 | Summary and outlook | 143 |
| 9.1 | Beta-decay study of ^{21}Mg | 143 |
| 9.1.1 | Summary of results | 143 |
| 9.1.2 | Outlook | 144 |
| 9.2 | Beta-decay study of ^{20}Mg | 149 |
| 9.2.1 | Summary of results | 149 |
| 9.2.2 | Outlook | 149 |
| | Bibliography | 153 |
| | List of Figures | 161 |
| | List of Tables | 169 |

Preface

Two experiments performed at the ISOLDE facility at CERN in November 2011 and April 2015 constitutes the basis of this PhD thesis. The motivation for both experiments have been to study the beta-decay of ^{20}Mg by using advanced charged particle and gamma-ray detection setups. We have used a beam of ^{21}Mg in both experiments in order to do the calibration of the charged particle detectors. We quickly realized that a lot of new results could be extracted from the ^{21}Mg data, and as a consequence I have focused on analyzing these from the 2011 experiment. I have analyzed the ^{20}Mg data from the 2015 experiment.

The first experiment was performed by the group before I started my PhD studies, however, I was invited to take part. I spent the first three years of my PhD analyzing the ^{21}Mg data and writing the two papers published last year, [Lund 2015a, Lund 2015b]. Intermittently I spend half a year analyzing data from a beta-decay study of ^{11}Be also performed at the ISOLDE facility from which we published the results in 2014 (see paper number five on the list of publications). The results of this study is not included in the thesis.

In the fall of 2014 I stayed for four months at the ISOLDE facility working at the newly established ISOLDE Decay Station (IDS). I took part in the experiments being performed at the setup during this period, among which were fast-timing beta-decay measurements, gamma-ray spectroscopy measurements, beta-delayed charged particle spectroscopy of ^{31}Ar , and beta-decay study of ^{11}Li measuring the beta-delayed neutron spectrum.

The knowledge and experience that I acquired during these months helped me immensely in the spring of 2015 when I was one of the lead figures in the planning, setting up, and execution of our collaborations latest experiment on ^{20}Mg . Since then I have worked in high speed to get as many results out of the data as possible before I had to start writing my thesis in November. During the summer I also presented preliminary results from the April experiment at the PROCON'15 conference in Lanzhou, China.

Acknowledgements

First of all, I would like to thank my supervisors Hans O.U. Fynbo and Karsten Riisager for their help and support during the last five years. I am very grateful for their continued guidance throughout my studies and the support they have given me. To times, the PhD studies have been quite difficult and they helped me overcome these challenges. It has been a delight to always be able to discuss the day-to-day problems in the analysis with them.

During my eight years at the Department of Physics and Astronomy I have been so lucky to meet many excellent persons. Among these, I have been very pleased with my fellow students during the bachelor degree, and the continued friendship with all of you. I have been especially thankful for the coffee breaks and the lunch breaks I have had with Rune, Nikolaj, Sara, and Serdar - especially during my PhD studies. I would also like to thank all of the people from the experimental and the theoretical group in Aarhus. The canoe trips, the hockey games, the beers, and the viking festivals have all been a delight. A special thanks goes to Oleksandr for proof-reading large parts of the thesis. It is a big help for me.

I would also like to thank the people who participated in both the 2011 and the 2015 experiments on ^{20}Mg from Aarhus, Gothenburg, Madrid, and elsewhere. A special thank goes to Michael and Alan for making the data acquisition system work for the experiment we performed in April last year.

I would also like to thank Maria J.G. Borge for welcoming me at ISOLDE during the fall of 2014. It was an excellent time and I enjoyed the physics challenge very much. I would also like to thank all the people that I worked with at ISOLDE and the IDS during these months.

Finally, I would like to thank my parents for their support during all these years, without whom I could not have made it this far. And finally, should my beloved girlfriend Maja have a big thank you for always being supportive. I am looking forward to moving in with you at our new place.

*Morten Vinther Lund
Aarhus, January 2016*

Summary

The two lightest bound magnesium isotopes, ^{20}Mg and ^{21}Mg , are both positioned on the proton drip-line as they become unbound if an extra proton is added. As the available beta-decay energy increases and the particle separation energies generally decreases when moving closer to the drip-lines, the two nuclei have several energetically allowed decay modes. The two magnesium nuclei have been produced at the ISOLDE facility, and their beta-decays have been studied.

In the first half of this thesis we will present the results of a study of the ^{21}Mg beta-decay. We have measured the beta-decay with a detection setup consisting of two charged particle telescopes surrounding the decay point. Altogether 27 βp branches were measured with center-of-mass energies between 0.4-7.2 MeV. Seven new βp branches were observed. The observed beta-delayed protons were used to determine the half-life of ^{21}Mg as 118.6 ± 0.5 ms. From a line shape fit of the βp branches we extract the widths, spins, and parities of the resonances of ^{21}Na . An improved interpretation of the decay scheme in accordance with the results obtained in reaction studies, studies of the mirror decay, and comparisons with the mirror nucleus is presented.

We have also observed beta-delayed alpha-particle emissions to ^{17}F and the rare beta-delayed proton-alpha emission to ^{16}O . This is the third identified case of $\beta p \alpha$ emission. We discuss the systematic of beta-delayed particle emission decays, show that the decays observed here fit naturally into the existing pattern, and argue that the patterns to a large extent are caused by odd-even effects.

In the second half of this thesis we will present the results of a study of the ^{20}Mg beta-decay. We have measured the beta-decay with a detection setup consisting of a silicon detector array in close geometry to the decay point and surrounded by four HPGe-clover detectors. The silicon detector array consisted of four charged particle telescopes placed vertically around the decay point and a single thick segmented silicon detector placed horizontally below the decay point.

From the measured beta-delayed proton spectrum we observe two new resonances in ^{20}Na with energies 5507(10) keV and 5836(13) keV. Furthermore, we have measured 5 new beta-delayed proton peaks and we confirm the existing interpretation of the decay scheme. The beta-delayed proton spectrum have been used to determine the half-life of ^{20}Mg as 90.9 ± 1.2 ms. Due to the high degree of isobaric contamination of ^{20}Na (roughly a factor 10 more than magnesium in the detection

chamber), we are unable to observe signs of the low-intensity beta-delayed proton branch going through the astrophysical interesting level at 2645(6) keV.

Dansk resumé

(Summary in Danish)

De to letteste bundne magnesium isotoper, ^{20}Mg og ^{21}Mg , er begge placeret på proton dryplinien, da de ved tilføjelse af en ekstra proton begge bliver ustabile. Da den tilgængelige energi for beta-henfald vokser og partikel separationsenergien generelt falder, når man bevæger sig mod drypliniere, betyder det at de to kerner vil have mange åbne henfaldskanaler. De to magnesium isotoper er blevet produceret på ISOLDE faciliteten, og beta-henfaldet af de to er blevet observeret.

I første halvdel af denne afhandling vil vi præsentere resultaterne af studiet af ^{21}Mg 's beta-henfald. Vi har målt beta-henfaldet med en detektor opstilling, som består af to partikel teleskoper som omgiver henfaldspunktet. Vi har sammenlagt observeret 27 βp henfaldsgrene med en center-of-mass energi som strækker sig fra 0,4 MeV og op til 7,2 MeV. Af disse er de 7 βp henfaldsgrene aldrig observeret før. De målte beta-forsinkede protoner blev brugt til at måle halveringstiden for ^{21}Mg til at være $118,6 \pm 0,5$ ms. Fra et fit af linieformen af de observerede βp henfaldsgrene har vi bestemt bredderne, spinet og pariteten af resonanserne i ^{21}Na . En forbedret fortolkning af henfaldsskemaet som er i overensstemmelse med opnåede resultater i reaktionseksperimenter, sammenligning med spejl-henfaldet og sammenligning med spejl-kernen bliver også præsenteret.

Vi har også observeret beta-forsinket alfa partikel udsendelse til ^{17}F og det sjældne henfald beta-forsinket proton-alfa udsendelse til ^{16}O . Dette er det kun tredje observerede tilfælde af $\beta\text{p}\alpha$ henfaldet. Vi vil diskutere generelle mønstre i beta-forsinket partikel udsendelse, demonstrere at de her observerede henfald naturligt passer ind i disse mønstre, og vi vil argumentere for at disse mønstre i stor udstrækning er forårsaget af ulige-lige effekter.

I den anden halvdel af denne afhandling vil vi præsentere resultaterne af studiet af ^{20}Mg 's beta-henfald. Vi har målt dette henfald med en detektor opstilling som består af en tæt pakket silicium detektor opstilling tæt på punktet hvor kernerne henfalder og er yderligere omgivet af fire HPGe-kløver detektorer. Silicium detektor opstillingen består af fire partikel teleskoper som er placeret oprejst rundt om henfaldspunktet, og direkte under dette punkt er der en enkelt tyk og segmenteret silicium detektor.

Fra det målte spektrum af beta-forsinkede protoner, kan vi etablere eksistensen af

to hidtil usete resonanser i ^{20}Na med energierne 5507(10) keV og 5836(13) keV. Endvidere har vi målt 5 nye beta-forsinkede proton toppe og vi bekræfter den eksisterende fortolkning af henfaldsskemaet. Proton spektret er blevet brugt til at bestemme halveringstiden af ^{20}Mg til at være 90.9 ± 1.2 ms. På grund af den store isobariske forurening af det producerede beam (der er ca. 10 gange så meget natrium som magnesium) er det ikke muligt at observere tegn på lav-intensitets proton grenen som går via den astrofysisk interessante resonans med energien 2645(6) keV.

List of Publications

- I. **M.V. Lund**, M.J.G. Borge, J.A. Briz, J. Cederkäll, H.O.U. Fynbo, J.H. Jensen, B. Jonson, K. L. Laursen, T. Nilsson, A. Perea, V. Pseudo, K. Riisager, and O. Tengblad, *Beta-delayed proton emission from ^{21}Mg* , Eur. Phys. J. A **51**, 113 (2015).
- II. **M.V. Lund**, M.J.G. Borge, J.A. Briz, J. Cederkäll, H.O.U. Fynbo, J.H. Jensen, B. Jonson, K. L. Laursen, T. Nilsson, A. Perea, V. Pseudo, K. Riisager, and O. Tengblad, *Systematic trends in beta-delayed particle emitting nuclei: The case of $\beta p\alpha$ emission from ^{21}Mg* , Phys. Lett. B **750** (2015).
- III. J. Refsgaard, O. S. Kirsebom, E. A. Dijck, H. O. U. Fynbo, **M. V. Lund**, M. Nuñez Portela, R. Raabe, G. Randisi, F. Renzi, S. Sambhi, A. Sytoma, L. Willmann, and H.W. Wilschut, *Measurement of the branching ratio for β -delayed α decay of ^{16}N* , Phys. Lett. B **752** (2015).
- IV. M. Pfützner, W. Dominik, Z. Janas, C. Mazzocchi, M. Pomorski, A.A Bezbakh, M.J.G. Borge, K. Chrapkiewicz, V. Chudoba, R. Frederickx, G. Kamiński, M. Kowalska, S. Krupko, M. Kuich, J. Kurcewicz, A.A. Lis, **M.V. Lund**, K. Miernik, J. Perkowski, R. Raabe, G. Randisi, K. Riisager, S. Sambhi, O. Tengblad, and F. Wenander, *β decay of ^6He into the $\alpha + d$ continuum*, Phys. Rev. C **92**, 014316 (2015).
- V. K. Riisager, O. Forstner, M.J.G. Borge, J.A. Briz, M. Carmona-Gallardo, L.M. Fraile, H.O.U. Fynbo, T. Giles, A. Gottberg, A. Heinz, J.G. Johansen, B. Jonson, J. Kurcewicz, **M.V. Lund**, T. Nilsson, G. Nyman, E. Rapisarda, P. Steier, O. Tengblad, R. Thies, and S.R. Winkler, *$^{11}\text{Be}(\beta p)$, a quasi-free neutron decay?*, Phys. Lett. B **732** (2014).
- VI. R. Lica, H. Mach, L.M. Fraile, A. Gargano, M.J.G. Borge, N. Marginean, C.O. Sotty, V. Vedia, A.N. Andreyev, G. Benzoni, P. Bomans, R. Borcea, L. Coraggio, C. Costache, H. De Witte, F. Flavigny, H.O.U. Fynbo, L.P. Gaffney, P.T. Greenlees, L.J. Harkness-Brennan, M. Huyse, P. Ibáñez, D.S. Judson, J. Konki, A. Kor gul, T. Kröll, J. Kurcewicz, S. Lalkowski, I. Lazarus, **M.V. Lund**, M. Madurga, R. Marginean, I. Marroquín, C. Mihai, R.E. Mihai, A.I. Morales, E. Nácher, A. Negret, R.D. Page, J. Pakarinen, S. Pascu, V. Paziyy, A. Perea, M. Pérez-Liva, E. Picado, V. Pucknell, E. Rapisarda, P. Rahkila, F. Rotaru, J.A. Swartz, O. Tengblad, P. Van Duppen, M. Vidal, R. Wadsworth, W.B. Walters, and N. Warr (IDS Col-

laboration), *Fast-timing study of the l-forbidden $1/2^+ \rightarrow 3/2^+$ M1 transition in ^{129}Sn* , submitted to Phys. Rev. C (2016).

- VII. R. Garg, I.M. Alonso, C. Barton, C.Aa. Diget, S. Courtin, G. Fruet, H.O.U. Fynbo, A. Howard, A. Illana, D.G. Jenkins, O. Kirsebom, **M.V. Lund**, I. Moore, J. Refsgaard, J.E. Riley, S. Rinta-Antila, L. Sinclair, O. Tengblad, and The IGISOL Collaboration, *Rotational excitation of the Hoyle state in ^{12}C* , submitted to JPCS (October 2015).
- VIII. J.P. Ramos, A. Gottberg, T.M. Mendonca, C. Seiffert, A.M.R. Senos, H.O.U. Fynbo, O. Tengblad, J.A. Briz, **M.V. Lund**, G.T. Koldste, M. Carmona-Gallardo, V. Pseudo, and T. Stora, *Intense $^{31-35}\text{Ar}$ beams produced with a nanostructured CaO target at ISOLDE*, NIM B 320 (2014).

Introduction

Nuclear physics was born more than 100 years ago when Rutherford in 1911 published the first model describing the existence of the atomic nucleus in [Rutherford 1911]. Rutherford had been investigating the structure of the atom by aiming a beam of alpha-particles with a fixed kinetic energy at a stationary gold foil. By measuring the outcome of the scattering process - i.e. which particles emerged in which directions and with what energy - Rutherford determined that the atom consists of a centrally placed nucleus containing all mass and positive charge and with a radius smaller than at least $30 \cdot 10^{-15} \text{m}$. As the atomic radius is about 10^{-10}m , the atomic nucleus must be at least four orders of magnitude smaller. The conclusion is that the electrons of the atom are orbiting a much smaller nucleus, which has almost all the mass of the atom and a positive charge exactly equal in magnitude to that of all the electrons.

The main aim of nuclear physics is to study the structure and dynamics of the atomic nucleus. Today it is believed that the fundamental constituents of the nucleus are the quarks and gluons. These are bound in nucleons and the nucleons are bound in nuclei by the strong interaction, which is described by quantum chromodynamics (QCD). A major challenge in nuclear physics today is to bridge the gap between the few-body interactions of the quarks and the many-body interactions that govern the structure and properties of nucleons and nuclei. As QCD is a strongly coupled theory at low energy, which is evident by color-confinement, it is not possible to compute observables to very high precision, which is in contrast to the electromagnetic and weak interactions. For instance, the spectrum of bound states in QCD has only been computed for the proton and the deuteron [Dürr 2008, Beane 2012].

The way to proceed in order to make theoretical predictions of the properties of the nucleus is to model the system based on a few fundamental assumptions. This approach has led to several interesting models of the nucleus, like the liquid drop model and the independent particle model (IPM). The liquid drop model assumes that the nucleus is a uniform sphere of nuclear matter, which is equivalent to an incompressible liquid droplet. In 1935 Weizsäcker developed the Semi-Empirical Mass Formula on the basis of the liquid drop model, which describes the general trend of the binding energy quite well.

The IPM goes to the other extreme and assume that the nucleons are moving

around independently in an effective overall potential describing the interaction with all other nucleons. The effective potential could be that of a harmonic oscillator, and filling the energy levels with nucleons according to the Pauli exclusion principle leads to the spectrum of the nucleus. Including a strong spin-orbit coupling in the effective potential, the model successfully reproduces the magic numbers describing particular strongly bound nuclei, which the liquid drop model fails to predict.

The main part of the nuclear chart is described by these so-called mean field models, however, no single model can by itself describe all parts of the nuclear chart or all of the different nuclear properties. Different models are needed to describe different properties of the nucleus. The evolution of the mean field models have closely followed the results of experiments, and it is therefore essential to keep pushing the experimental boundaries in order to study more and more exotic nuclei. To date roughly 3000 different nuclei have been studied but estimates suggest that approximately 7000 bound nuclei exist with $Z \leq 120$, [Erlar 2012].

A modern development in theoretical nuclear physics is the modeling of the nuclear structure approached from a more fundamental level in *ab-initio* calculations. In such calculations the structure of the nucleus is determined directly from the first principles of quantum mechanics. Using an interaction deriving from QCD it is possible to reproduce the structure and properties of the low-mass nuclei rather well in e.g. no-core shell models as described in [Navrátil 2009]. However, the calculations requires a large number of numerical computations, which limits the precision for heavier nuclei and the possibility of using higher-order interactions like three- and four-body forces.

To continue the expansion of our knowledge about the nucleus and to further develop the theoretical understanding we need to study in principle all nuclei that potentially can be produced. By studying all of these so far unobserved nuclei the hope is to answer some of the fundamental questions that still persist in nuclear physics today: Where are the limits of nuclear stability? How heavy elements can we produce? How did the Universe come to contain exactly the composition of nuclei observed today? And many others.

One way of studying nuclear structure in exotic nuclei close to the drip-lines is by using beta-decay to probe certain states in the beta-decay daughter nucleus. As beta-decay is subject to certain selection rules it is an efficient way of probing only a subset of the excited states in the daughter nucleus. Especially at high excitation energies the level density is large and the beta-decay selection rules make sure that we only study a few of the resonances here.

This thesis will cover two studies of the beta-decay of the proton drip-line nuclei $^{20-21}\text{Mg}$. After this general introduction the thesis is split into two parts - the first half describes an experiment performed in November 2011 and the results obtained

from the study of the beta-decay of ^{21}Mg . The second half of the thesis describes an experiment performed in April 2015 and the results obtained from the study of the beta-decay of ^{20}Mg .

In the following section, Sect. 1.1, we will describe various aspects of beta-decays. In Sect. 1.2 we will give a quick introduction to the subject of beta-delayed particle emission. In Sect. 1.3 we will give a short description of gamma-ray emission from excited nuclear states. In Sect. 1.4 we will describe two methods for the production of exotic nuclei and we will present the ISOLDE facility. Finally, in Sect. 1.5 we will explain the experimental strategy that we have applied for the two experiments.

1.1 Beta-decay

The nuclei on both sides of the valley of stability are unstable and decay by beta-decay and other processes towards the stability line. The beta-decay will change a neutron into a proton or vice versa, which is the equivalent of changing the isospin of the nucleon. On the neutron rich side of stability the nuclei decay by β^- -decay,

$$n \rightarrow p + e^- + \bar{\nu}_e \quad (1.1)$$

On the proton rich side of stability the nuclei decay by β^+ -decay or electron capture (EC),

$$p \rightarrow n + e^+ + \nu_e \quad (1.2)$$

$$p + e^- \rightarrow n + \nu_e \quad (1.3)$$

The energy released in these decays, the Q -value, is given as

$$Q_{\beta^-} = M(Z)c^2 - M(Z+1)c^2 \quad (1.4)$$

$$Q_{\beta^+} = M(Z)c^2 - M(Z-1)c^2 - 2m_e c^2 \quad (1.5)$$

$$Q_{\text{EC}} = M(Z)c^2 - M(Z-1)c^2 \quad (1.6)$$

where $M(Z)$ and $M(Z \pm 1)$ are the atomic mass of the parent and daughter nucleus, respectively, and m_e is the mass of the electron. As the Q -value has to be positive for the beta-decay to occur, electron-capture often occurs close to the line of stability as the isobaric mass difference generally is smaller here.

1.1.1 Fermi and Gamow-Teller decays

The weak interaction is responsible for the beta-decay of the atomic nucleus. The Lagrangian of the weak interaction is in the Standard Model of particle physics described mathematically by a V-A structure, i.e. a vector minus an axial-vector part.

Because of this structure it is possible to split the weak interaction into two parts. According to [Jensen 1987] can the two parts of the interaction for allowed β^+ -decay be expressed as

$$\hat{O}_F^+ = -\frac{G_F}{\sqrt{2}}\delta(\vec{r}-\vec{r}')T_- \quad (1.7)$$

$$\hat{O}_{GT}^+ = -\frac{G_F}{\sqrt{2}}\frac{g_A}{g_V}\frac{2\vec{s}}{\hbar c}\delta(\vec{r}-\vec{r}')T_- \quad (1.8)$$

where g_V and g_A are the free vector and axial vector coupling constants, T_- is the isospin lowering operator, G_F is the Fermi constant, and \vec{s} is the spin operator. The vector part is called the Fermi interaction (F) and the axial vector part is called the Gamow-Teller interaction (GT). The isospin lowering operator T_- changes the proton, $T_3 = +\frac{1}{2}$, into a neutron, $T_3 = -\frac{1}{2}$. For the β^- -decay the isospin lowering operator T_- is exchanged with the isospin raising operator T_+ as a neutron is changed into a proton. The two operators both include a δ -function in terms of the space coordinates. It means that the beta-decay of a proton (neutron) into a neutron (proton) occurs at a certain point in space, i.e. the interaction can be considered as a point interaction.

The spin operator \vec{s} , which is only present in the GT operator, will change the spin of the nucleon. The total leptonic spin in a GT beta-decay will be 1 and it means that the spin of the nucleus may change by one unit ($\Delta J = 0, \pm 1$ ($0 \rightarrow 0$ not allowed) and $\Delta T = 0, \pm 1$). For a Fermi beta-decay the total leptonic spin is 0 and the spin of the nucleus is therefore conserved ($\Delta J = \Delta T = 0$). In both allowed Fermi and Gamow-Teller decays are the nuclear parity conserved.

1.1.2 ft -values

The intensity of a beta-decay transition can be expressed in terms of its reduced transition probability, which is defined as the product of the partial half-life t of the beta-decay transition and the phase space factor f . It is also called the ft -value. The partial half-life t is equal to $T_{1/2}/I_\beta$, where $T_{1/2}$ is the total half-life of the beta-decaying nucleus and I_β is the intensity of the beta-decay transition considered. The phase space factor is a dimensionless integral over the beta-decay energy spectrum and it is proportional to the decay rate. It depends on the charge Z of the daughter nucleus and the maximum kinetic energy of the beta-particle emitted. It can be approximated by

$$f \approx \frac{E_\beta^5}{30(m_e c^2)^5}, \quad (1.9)$$

where $E_\beta = Q - E^*$ is the maximum kinetic energy of the beta-particle, Q is the available beta-decay energy, and E^* is the excitation energy of the final state, [Blank 2008]. The approximation works best for large values of E_β and low Z . A more complete

parametrization of the phase space factor is given in [Wilkinson 1974], which we will use in later chapters for the determination of f . This parametrization determines f with an accuracy better than 0.1%.

The beta-decay branching ratio expressed in terms of the ft -value is directly related to the nuclear matrix elements [Blank 2008] by

$$ft = \frac{C}{B_F + \frac{g_A^2}{g_V^2} B_{GT}}, \quad (1.10)$$

where $B_F = |M_F|^2$ and $B_{GT} = |M_{GT}|^2$ are the reduced matrix elements squared for the Fermi and Gamow-Teller parts of the interaction, respectively, and C is a constant. g_V and g_A are the free vector and axial vector coupling constants, respectively. The present values of the parameters are $C = 6144.2(16)$ and $\frac{g_A}{g_V} = -1.2694(28)$ according to [Towner 2010].

As the phase space factor f has a very strong energy dependence, see Equation (1.9), the conversion from beta-decay branching ratio to the corresponding matrix element will also be strongly energy dependent. This poses an experimental challenge when searching for the total beta-decay strength, as low-intensity beta-decay branches to levels at high excitation energy will contribute with a large part of the strength in terms of the reduced matrix elements.

1.1.3 Beta-decay strength distribution

As the Fermi interaction for allowed beta-decay has to obey the selection rules $\Delta J = \Delta T = 0$, the beta-decay strength attributed to the Fermi interaction will only populate a single final state, which belongs to the same isospin multiplet as the initial state. This state is referred to as the Isobaric Analogue State (IAS) and it will have a similar nuclear structure as the initial state. The members of an isospin multiplet will have slightly different masses, as a consequence of the difference in Coulomb energy and because of the mass difference of the proton and the neutron. This mass difference can be given by

$$M_{GS}(Z) - M_{IAS}(Z-1) = \frac{\Delta E_C}{c^2} + M(^1\text{H}) - m_n, \quad (1.11)$$

where $M_{GS}(Z)$ is the atomic mass of the ground state of the nuclei with Z protons, $M_{IAS}(Z-1)$ is the atomic mass of the IAS in the beta-decay daughter, ΔE_C is the Coulomb displacement energy, m_n is the mass of the neutron, and $M(^1\text{H})$ is the mass of the hydrogen atom. The atomic mass of hydrogen is used instead of the proton mass in order to account for the missing electron when using atomic masses.

The Coulomb displacement energy, ΔE_C , is introduced when exchanging a neutron with a proton in equivalent nuclear orbits. In this case, the extra proton will interact through the Coulomb interaction with the original Z protons in the nucleus

and this causes an energy gain. If a proton is replaced by a neutron it will have the opposite effect of course, i.e. a lowering of the energy. As a consequence, the Fermi decay is only energetically allowed for β^+ -decay and EC where the IAS is moved down in energy compared to the ground state of the decaying nucleus.

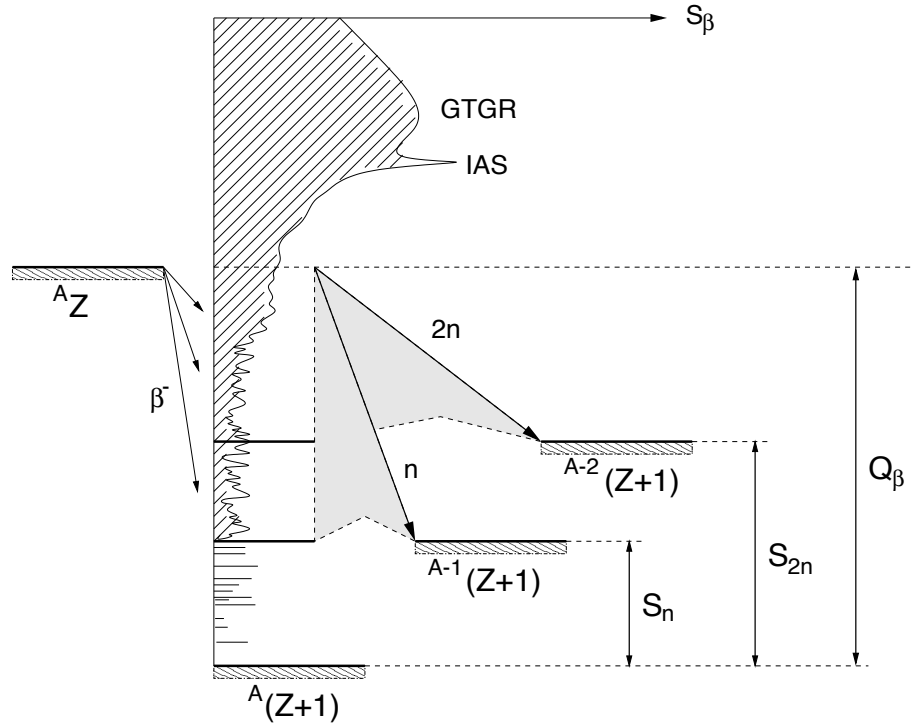


Figure 1.1: A schematic overview of the beta-decay strength distribution, S_{β} , for a neutron rich nucleus. As discussed in the text B_F will mainly be collected in the IAS, while B_{GT} has a broader distribution over the final states in the beta-decay daughter nucleus. However, the B_{GT} strength is collected in the Gamow-Teller Giant Resonance (GTGR). For proton rich nuclei the IAS and the GTGR will be situated inside the available beta-decay energy window. Figure taken from [Fynbo 1999].

As a consequence of the spin dependence of the Gamow-Teller interaction there does not exist a state similar to the IAS for Gamow-Teller decays. However, the main part of the Gamow-Teller strength will be gathered in a group of states in the beta-decay daughter nucleus, and the center of this distribution, which is called the Gamow-Teller Giant Resonance (GTGR), will roughly be given by the Coulomb displacement energy. Hence, the main part of the Gamow-Teller strength will be inaccessible for $Z < N$ nuclei, as is also the case for the Fermi strength. A schematic overview of the beta-decay strength distribution for a $Z < N$ nucleus is shown on

Figure 1.1.

From the operators that govern Fermi and Gamow-Teller beta-decays, Equation (1.7-1.8), and using that $T_3 = \frac{Z-N}{2}$, it is possible to calculate the sum rules for the total strength to be [Pfützner 2012]

$$\sum B_F^+ - \sum B_F^- = Z - N \quad (1.12)$$

$$\sum B_{GT}^+ - \sum B_{GT}^- = 3(Z - N) \quad (1.13)$$

where B_{GT}^\pm and B_F^\pm are the β^\pm -decay reduced matrix element squared for the Gamow-Teller and Fermi part of the interaction, respectively. When comparing the theoretical and the experimental Gamow-Teller strength, it is normal to have a discrepancy between the two numbers. This is caused by the need to limit the number of final states included in the model space when calculating the Gamow-Teller strength as described in [Caurier 1995]. This effect is referred to as quenching of the Gamow-Teller strength.

1.1.4 Isospin symmetry breaking

As isospin symmetry is only an approximate symmetry for the nucleus, the Fermi decay will not only feed the IAS, but a small part of the Fermi strength ($\approx 1-2\%$) will also go to other states close in energy to the IAS. Two effects are believed to be the cause of this effect: an incomplete overlap of the initial and final state nuclear wave functions and isospin mixing. Together, the two effects are called isospin symmetry breaking. The Coulomb force is responsible for the isospin mixing, and it means that the IAS is not a pure isospin state. In fact, it consists of two contributions which may be described by

$$|IAS\rangle = \sqrt{1-a}|T\rangle + \sqrt{a}|T-1\rangle, \quad (1.14)$$

where T is the isospin of the parent nucleus. The mixing amplitude a is typically small, at most 0.1%, and it is inversely proportional to the energy difference between the IAS ($|T\rangle$) and the state it mixes with ($|T-1\rangle$). The state $|T-1\rangle$ must lie close in energy to the IAS, due to the energy dependence of the mixing amplitude.

Considering the fact that the theoretical description of the nuclear beta-decay is identical whether the decaying nucleon is a proton or a neutron, and assuming for a moment that isospin symmetry is not broken, then the β^+ -decay of a nucleus with (N, Z) neutrons and protons ($Z > N$) will be identical to the β^- -decay of the mirror nucleus with (Z, N) neutrons and protons ($Z < N$). In particular, should the reduced transition probability (the ft -value) for two mirror beta-decay transitions be identical. However, as isospin symmetry is not a perfect symmetry, it is natural to measure

the degree of the isospin symmetry breaking in terms of the mirror asymmetry parameter, which is given by

$$\delta = \frac{\log(ft)^+}{\log(ft)^-} - 1, \quad (1.15)$$

where $\log(ft)^\pm$ is the $\log(ft)$ value of the β^\pm -decay, respectively. Under the hypothesis of complete charge independence of the nuclear interactions, this parameter has to vanish. Therefore, if any deviation from zero is observed for the mirror asymmetry parameter, it reflects the fact that one of the two beta-decays are dominant over the other. In other words, it is a sign of isospin symmetry breaking.

1.2 Beta-delayed particle emission

When moving away from the line of stability, the isobaric mass difference increases parabolically and in turn gives an increase in the available beta-decay energy, i.e. the Q -value. The closer we get to the drip-lines, the point where an extra nucleon drips off the nucleus when added, the binding energy of the least bound nucleon will approach zero. As a consequence of the Q -value getting larger at the same time as the particle separation energy of the beta-decay daughter is getting smaller, more and more decay channels becomes energetically allowed. At the drip-lines we will encounter the most exotic decay modes.

The large number of open decay channels at the drip-line will complicate the reconstruction of the beta-decay strength distribution. It can be reconstructed, however, by carefully measuring all emitted gamma-rays and particles in the beta-decay with a high efficiency and high energy resolution detector setup. Such a measurement will give detailed information about the energy spectrum of the emitted particles and gamma-rays from which the decay branches can be placed with high confidence in the decay scheme. From a detection point-of-view it is easiest to make such a measurement for proton rich nuclei, as the emitted particles will be charged. Looking to the physics, the position of the IAS in neutron and proton rich nuclei, respectively, means that the majority of the strength is accessible in the beta-decay of a proton rich nucleus while it will not be accessible for a neutron rich nuclei, see Figure 1.1.

As beta-decay has to follow certain selection rules, it results in a high degree of selectivity when populating levels in the daughter nucleus. Generally, the level density will be large when approaching high excitation energies and beta-decay can, therefore, be a good way to study specific resonances in the daughter nucleus. Reaction experiments can be used to obtain similar information but with less selectivity. Besides studying the beta-decay daughter nucleus itself, it is also possible to study the beta-delayed particle daughter nuclei involved. From such beta-decay studies we can obtain information about the energy spectra of the daughter nuclei. We can also

study the intermediate resonances that are populated and for each of them measure the branching ratios of the different decay modes and determine the total width of the resonance. We can furthermore put constraints on the spin and parity of the resonances populated in the beta-decay on the basis of the selection rules for allowed and forbidden decays. More information on beta-delayed particle emission can be found in [Blank 2008, Pfützner 2012].

1.3 Gamma-ray emission

If a nucleus is excited to a state below the lowest particle separation energy it will decay by gamma-ray emission to a lower lying state. Gamma-rays are electromagnetic radiation while particle emission is governed by the strong force. Hence, if the nucleus is excited to states above the particle separation energy, it will most likely decay by particle emission because of the strength of the two interactions. Under special circumstances the particle emission can be heavily suppressed and the gamma-ray emission can then contribute significantly to the width of the state. Particle emission could e.g. be suppressed by the Coulomb or angular momentum barriers.

According to [Jackson 1998] one can expand the electromagnetic field in multipoles with each term being classified on the basis of the total angular momentum l and the parity. To determine which terms, i.e. multipolarities, that contribute to a given transition one has to consider conservation of the total angular momentum and parity. The parity is normally split into two types where the electric type has parity $(-1)^l$ and the magnetic type has parity $(-1)^{l+1}$. The standard naming convention is El and Ml for electric and magnetic multipoles, respectively. As the electric charge is conserved, the monopole term ($l = 0$) of the expansion is zero, which means that $0^+ \rightarrow 0^+$ gamma-ray transitions are not allowed. In semi-classical theory the transition rate is given by [Jensen 1987]

$$\lambda_{EM}(l) = \frac{8\pi(l+1)}{\hbar \cdot l \cdot [(2l+1)!!]^2} \left(\frac{E_\gamma}{\hbar c} \right)^{2l+1} B_{EM}(l), \quad (1.16)$$

where $(2l+1)!!$ is the double factorial of $2l+1$, which is defined as the product of all odd integers from 1 to $2l+1$. E_γ is the photon energy and $B_{EM}(l)$ is the reduced transition strength that contains all the nuclear information. In its essence it is the squared matrix element of the operator responsible for the transition and the production of a photon. $B_{EM}(l)$ is generally smallest for the magnetic multipoles. The transition rate depends strongly on l and it decreases rapidly when l is increased. As a consequence of these considerations, if El and $Ml+1$ are the lowest possible transitions, then the magnetic multipole can be safely neglected. However, if $El+1$ and Ml are the lowest possible transitions, then both terms may contribute significantly.

1.4 Production of exotic nuclei

We will now change our focus from the theoretical aspects of beta-decay and instead look closer at the production of exotic nuclei. We will first outline the two main methods for producing exotic short-lived nuclei. Then we will describe the production of exotic magnesium isotopes at the ISOLDE facility. As mentioned earlier, the aim of this thesis is to present the analysis and results of two experiments performed at the ISOLDE facility.

1.4.1 Methods of production

In present day nuclear physics there exist two main methods for the production of exotic nuclei: the in-flight method and the ISOL method (Isotope Separation On Line). The in-flight method uses a heavy ion accelerator to produce high energy (100 MeV to GeV) and high intensity beams of heavy ions. Such a beam is then used to bombard a thin production target, which is chosen to be so thin that the produced exotic nuclei will escape it and continue onwards together with the heavy ion driver beam as a fast exotic ion beam. The production of the exotic ion beam mainly occurs through fragmentation, fission, and fusion, which results in the produced beam being close in mass to the driver beam. Having produced the fast exotic ion beam, the next step is to do magnetic separation of the beam components, in order to only have the desired exotic ions implanted in the detector setup. The first advantage of using the in-flight method for production, is the fact that you know exactly how many ions and of what species that you implant in your setup. The second advantage is the opportunity to produce and study very short-lived nuclei with half-lives down to the μs scale.

The second method for production of exotic nuclei is the ISOL method. For this method it is normal to use a beam of light ions, e.g. protons, to bombard a thick high-temperature target. The target can be made of both light and heavy materials. The exotic nuclei are produced through spallation, fission, fusion, and fragmentation. After production they are transported through a transfer line to an ion source by diffusion and effusion processes. In the ion source the exotic nuclei are turned into singly-ionized ions through e.g. laser or surface ionization at a high-voltage platform of 30-60 kV. After ionization they are extracted, accelerated, and then mass separated with a magnetic mass separator. The main advantages of the ISOL method are the, in some cases, higher intensity of the produced exotic beams, the better separation of the produced exotic ions, and a wider range of reaction processes that can be employed to maximize the production.

In the past, short-lived magnesium ions have been difficult to study at ISOL facilities due to low extraction and ionization efficiencies. However, recent improvements with regards to these problems have made it possible to produce and study the light-

est magnesium isotopes at the ISOLDE facility. Therefore, we have tried to exploit these new production capabilities to study the beta-decay of $^{20-21}\text{Mg}$ at ISOLDE.

1.4.2 Production of magnesium at the ISOLDE facility

The ISOLDE facility at CERN, see Figure 1.2 and [Kugler 2000], can produce many different exotic nuclei by bombarding a production target with a 1.4 GeV pulsed beam of protons from the Proton-Synchrotron Booster (PSB). When the protons bombard the production target spallation, fragmentation, fusion, and fission are induced. All of these processes will produce lighter nuclei than the target material. In the case of magnesium a SiC target was used to produce the desired isotopes. However, other elements are also produced with one of the main concerns being the production of sodium.

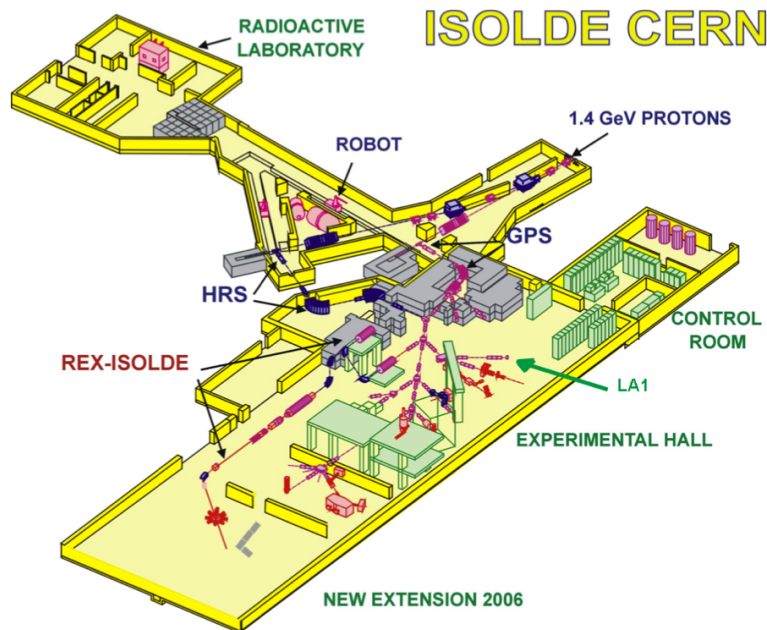


Figure 1.2: Sketch of the ISOLDE facility at CERN showing the target area behind the concrete blocks (grey colors), the High Resolution Separator (HRS), and the LA1 beam line in the experimental hall among other things.

The fragments produced in the bombardment are extracted from the production target and moved into an ion source. The ionization of magnesium is done with the Resonant Ionization Laser Ion Source (RILIS), [Fedoseyev 2000]. The technique of RILIS takes advantage of the interaction between the nucleus and the surrounding electrons, which results in the hyperfine structure of the atomic energy spectrum. It is

well known that the hyperfine structure splitting depends on the isotope in question, and hence can be used to select a specific isotope for ionization. As ionization may also happen through surface ionization, other elements produced in the target will also be ionized - in particular sodium is ionized through this process.

After production and ionization the beam is accelerated to 30-60 keV and guided through the High Resolution Separator (HRS) to separate the magnesium ions from the isobaric background of sodium. However, a significant sodium contamination remained in the beam due to the very similar masses, $\Delta M = 0.014061(17)$ u for ^{21}Mg and $\Delta M = 0.011496(29)$ u for ^{20}Mg , and because of a three orders of magnitude larger production of sodium over magnesium. The resolution of the HRS is $M/\Delta M = 5000$. We observed no magnesium when the RILIS ionization was turned off, however, the contamination of sodium remained under these conditions as expected.

In order to further suppress the amount of sodium, we took advantage of the properties of the PSB time structure where protons can be delivered every 1.2 s. Knowing that it will take the magnesium ions approximately 100 ms to diffuse out of the target, be ionized, and transported to the setup and the half-lives of magnesium and sodium are quite different (see below), we let the beam into the detection chamber only during the first 300 ms after proton impact on the ISOLDE target. This will effectively reduce the contamination of sodium. For ^{21}Mg $T_{1/2}=122(2)$ ms [Audi 2012], which is to be compared with $T_{1/2}=22.49(4)$ s for ^{21}Na [Audi 2012]. For ^{20}Mg $T_{1/2}=90(6)$ ms [Audi 2012], which is to be compared with $T_{1/2}=447.9(23)$ ms for ^{20}Na [Audi 2012]. To further suppress the sodium contamination we take advantage of a slit system installed in the beam line immediately after the HRS magnets. We use the slit on the low-mass side of the ion beam to cut part of the sodium away.

In the November 2011 experiment on average 390 ^{21}Mg ions per μC of proton beam on the ISOLDE production target were delivered to the detection chamber during a total measurement time of ≈ 3.5 hours. The average proton current delivered to the ISOLDE production target was $\approx 1.9 \mu\text{A}$ which results in $\approx 9 \cdot 10^6$ ^{21}Mg ions delivered to the detection setup in total.

The experiment in April 2015 collected ^{20}Mg ions for 68.0167 hours in total, with an average implantation rate in the detection chamber of ≈ 60 ^{20}Mg ions per second and ≈ 500 ^{20}Na per second.

1.5 Experimental strategy

The overall motivation for the two experiments that will be described in this thesis, is to study the beta-decay of ^{20}Mg in order to obtain information on three different points. We will sketch the three points briefly here and for a more extensive discussion we refer to Chapter 6. More information can also be found in [Borge 2010]. First

of all, we want to determine the spin and parity of a resonance located at 2645(6) keV in ^{20}Na , which is approximately 450 keV above the proton separation energy. The resonance is placed in the Gamow-window of the $^{19}\text{Ne}(p,\gamma)^{20}\text{Na}$ reaction, which is part of the breakout sequence from the hot CNO cycle (HCNO). Second, we want to study the mirror asymmetry of the beta-decay by comparing with the beta-decay of ^{20}O . Third, we want to measure the beta-decay strength distribution in order to make comparisons with modern shell model calculations.

The main experimental challenge when measuring the beta-decay of ^{20}Mg is the $\approx 70\%$ decay branch going to bound states in ^{20}Na . This branch will produce ^{20}Na in the ground state after a gamma deexcitation of the first excited state, and it will further beta-decay to ^{20}Ne . The problem with ^{20}Na is further enhanced as the mass difference between ^{20}Mg and ^{20}Na is so small that the magnetic separator HRS, which is used to produce a clean beam, will not be able to completely disentangle the two components from each other. The beta-decay of ^{20}Na has a roughly 20% branching ratio for beta-delayed alpha-particle emission, which will result in low energy ^{16}O recoils (down to ≈ 200 keV) and an intense alpha-particle distribution down to roughly 2 MeV. As a consequence it is very important to be able to do particle identification in order to study the beta-delayed proton spectrum from ^{20}Mg .

To fulfill the goals of the motivation we planned initially to study the beta-decay of ^{20}Mg with two different experimental setups, [Borge 2010]. For the first experiment performed in November 2011 we used a setup focused on searching for the population of the 2645(6) keV state. We employed a gas-silicon-silicon telescope with a segmented silicon-silicon telescope placed directly across in the chamber. The beam of ^{20}Mg was implanted in the window of the gas detector (more details can be found in Chapter 3 and [Jeppesen 2002]). By using a gas telescope we hoped to be able to better separate the protons from the alpha-particles and the ^{16}O recoils.

For the second experiment performed in April 2015 we used a setup with a highly segmented silicon detector array positioned as a cube with detectors covering five out of six sides. Around the collection point, at a distance of roughly 20 cm, we placed four HPGe-detectors, each of them in a clover configuration, i.e. they each contain 4 HPGe-crystals giving us 16 crystals in total. This setup allowed to collect a high statistics sample of ^{20}Mg and with many possibilities for applying advanced analysis techniques like coincidence gates. For instance, using a similar setup for studying the beta-decay of ^{20}Na we have been able to measure very weakly populated decay branches (much below the 0.1% level) at low-energy by studying coincidences between alpha-particles and ^{16}O recoils as described in [Laursen 2013]. More details on the setup can be found in Chapter 7.

For both experimental setups we have used a beam of ^{21}Mg , which is produced in the same way as ^{20}Mg , as a calibration source for the charged particle detectors.

^{21}Mg is much more abundantly produced as it is less exotic and it has strong and well-known beta-delayed proton branches. From both experiments we, therefore, have data on two different nuclei: ^{20}Mg and ^{21}Mg . As an extra bonus we also have data on ^{20}Na because it is part of the decay of ^{20}Mg but also because of the isobaric background contamination in the produced beam.

In the first part of the thesis we present the results of the analysis of the ^{21}Mg beta-decay data from the experiment performed in November 2011 with the gas-silicon-silicon telescope. We will present several new results from the study of the beta-decay of ^{21}Mg and an interesting new discussion of the systematics of beta-delayed particle emission in the low-mass region. In the second part of the thesis we present the results of the beta-decay study of ^{20}Mg and an analysis of the beta-delayed proton spectrum as measured in the experiment performed in April 2015. The data taken with the more sophisticated detection setup will give better information on the beta-decay of ^{20}Mg in general.

Motivation ^{21}Mg

The general motivation to study the beta-decay of ^{21}Mg , is to measure the beta-decay strength distribution, in order to compare it with theoretical predictions. However, as we discussed in Chapter 1 it is also rewarding to use the beta-delayed particles emitted to study the properties of the resonances populated in the daughter nucleus. Such a study can give information on the partial decay width, the total width, the spin and parity, and the position of the resonance studied in the excitation energy window. Another reason is to compare the beta-decay strength distribution and the properties of the resonances in the daughter nucleus with the mirror decay and the mirror nucleus. All of this follows naturally as a consequence of the desire to better understand the physics behind beta-decays, which were described in Chapter 1.

We will now present the history of the ^{21}Mg beta-decay research up to now in order to understand the prior knowledge about this decay and the beta-decay daughter nucleus ^{21}Na . We will finish the chapter with an outline of the decay modes that are energetically allowed but have not been observed before.

2.1 The history of the ^{21}Mg research

The proton drip line nucleus ^{21}Mg was observed for the first time in 1963 at the McGill Synchrocyclotron, [Barton 1963]. Bombarding a natural magnesium target with an extracted beam of 97 MeV protons from the McGill Synchrocyclotron resulted in the detection of two beta-delayed proton branches with a laboratory energy of 4.71(10) MeV and 4.02(10) MeV from what was inferred to be ^{21}Mg . The two proton branches were observed with poor energy resolution but they fit naturally into the known level scheme. The charged particle detector used was a silicon-junction detector. It was facing the production target of natural magnesium and with thin aluminium foils placed flat on the detector end to protect it from possible alpha-particles. The thickness of the aluminium were varied during the experiment resulting in a changing energy loss for the charged particles reaching the detector. This measurement of the charged particle energy loss was used in the particle identification. Due to the use of the aluminium foils the experiment had a lower energy limit for detection of protons of 2.5 MeV.

In 1965 two measurements of the beta-decay of ^{21}Mg extended the knowledge of the proton spectrum considerable, [McPherson 1965, Hardy 1965]. Both experiments were performed with the McGill Synchrocyclotron internal proton beam with the possibility of varying the proton energy between 30 and 98 MeV. Thin targets of sodium and magnesium were placed inside the proton beam, which resulted in the production of ^{21}Mg . The decay of the produced exotic nuclei were measured with a silicon surface barrier detector of 200 mm^2 area enclosed in a protective aluminium shield. The detector was positioned 6 cm from the point where the proton beam passed through the thin targets. The detector thickness of $300\text{ }\mu\text{m}$ allowed measurement of up to 6 MeV protons. In front of the detector they placed aluminium foils to shield it from unwanted heavier contaminants.

From the experimental results described in [McPherson 1965] much information about ^{21}Mg and its beta-decay is extracted. First of all, 9 beta-delayed proton branches are observed with center-of-mass energies ranging between 3.5 and 7.3 MeV. Second, it is established that the ground state of ^{21}Mg has the property $I^\pi = \frac{5}{2}^+$ and that its half-life is $T_{1/2}=118(4)$ ms. Third, they measure $Q_{\text{EC}} = 13.1(2)$ MeV. Finally, they also determine the 8.90(4) MeV resonance of ^{21}Na to be the IAS based on the measured $\log(ft)$ -values.

The results presented in [Hardy 1965] is based on a larger data sample than the results of [McPherson 1965], however, the experimental setup is identical. The observed beta-delayed proton spectrum from the 2.3 mg/cm^2 natural magnesium target is identical to what was observed in [McPherson 1965]. However, the main result of this higher statistics measurement is the realization of a considerable contamination of ^{17}Ne through the reaction $^{24}\text{Mg}(p, \alpha d n)^{17}\text{Ne}$ as compared to the reaction $^{24}\text{Mg}(p, d n)^{21}\text{Mg}$. As a result the half-life value is updated to be 121(5) ms. The decay scheme is also updated as two of the previously suggested resonances in ^{21}Na is no longer believed to be real.

In 1973 the beta-decay of ^{21}Mg was studied again by [Sextro 1973]. The activity of ^{21}Mg was produced with the Berkeley 88 inch cyclotron through the $^{20}\text{Ne}(^3\text{He}, 2n)$ reaction. At the beam energy used to produce ^{21}Mg , ^{20}Na was also produced. As ^{20}Na is a strong alpha-particle emitter it is a potentially dangerous contaminant. The produced beam was transported from the reaction point into the detector setup with a helium-jet transport system. For detection and particle identification they used non-segmented silicon detectors with various thicknesses in different ΔE - E telescope configurations (the ΔE detector ranged in thickness from 4 to $50\text{ }\mu\text{m}$ and the E detector were 50, 265, or $500\text{ }\mu\text{m}$ thick). This ensured that they covered the entire energy range of the Q_{EC} -window. The energy resolution obtained ranged between 25 and 45 keV in FWHM. The ΔE - E telescope covered a solid angle of 1.9% out of the total 4π sr.

With the setup described they reported 25 different beta-delayed proton branches

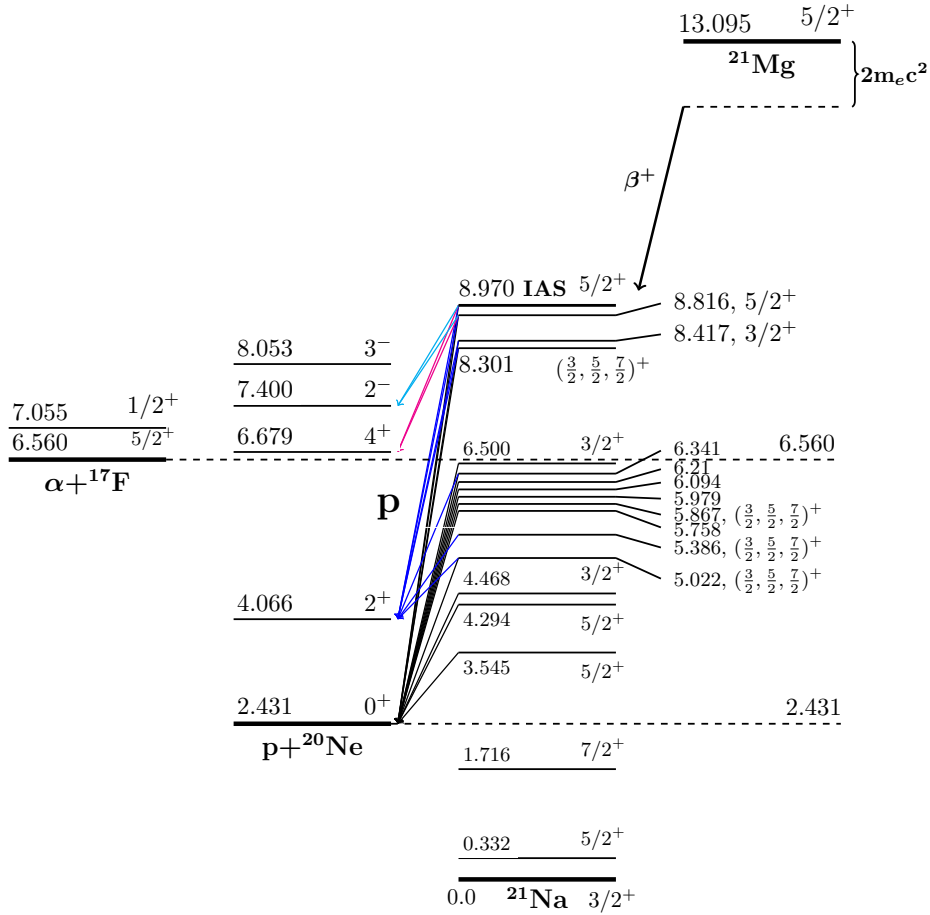


Figure 2.1: Decay scheme for the beta-decay of ^{21}Mg based on the measured proton decay branches and the resonance energies in [Sextro 1973]. We also show the energetically allowed resonances of the $\alpha + ^{17}\text{F}$ system even though the decay mode have not been observed. The lines that highlight the proton branches are color coded according to the final state (black: ground state, blue: first excited state, magenta: second excited state, cyan: third excited state).

and placed upper limits on the intensity of the energetically allowed beta-delayed alpha-particle emission through the IAS in ^{21}Na . The decay scheme of ^{21}Mg have for many years now mainly been based on the results of this experiment and it is presented in Figure 2.1. It shows a complex pattern of beta-delayed proton emissions.

The latest results on the beta-decay of ^{21}Mg is described in [Thomas 2003] and is from an experiment performed at GANIL with the in-flight production method using the LISE3 separator to remove contaminants down to a level lower than 1%. The ^{21}Mg nuclei were implanted in a stack of five silicon detectors in order to study the charged particles emitted in the beta-decay. A HPGe-detector was placed close to the collection point in order to measure any gamma-rays emitted. A 1634 keV gamma-ray was observed to be in coincidence with four beta-delayed proton branches, which fits with being the gamma-ray emitted when the first excited state of ^{20}Ne deexcites. This observation is valuable as input for a precise determination of the decay scheme.

To summarize the status of the ^{21}Mg beta-decay research the half-life and the Q -value are well-known and the IAS in ^{21}Na is identified. The two main decay modes, $^{21}\text{Mg}(\beta)$ and $^{21}\text{Mg}(\beta p)$, have been studied and the beta-decay strength distribution has largely been determined. The main part of the B_{GT} strength distribution has been accounted for according to a comparison with a shell-model calculation except at energies higher than ≈ 7.5 MeV, [Thomas 2003]. Beta-delayed alpha-particle emission is energetically allowed but it has not been observed yet. In the next section we will give a more detailed overview of the expected decay modes to be observed from ^{21}Mg - a few have not been observed yet.

The experiments performed up to know have all used the in-flight production method, see Sect. 1.4.1. However, the use of an ISOL facility to produce ^{21}Mg should help us to obtain a substantially higher number of ^{21}Mg ions implanted in our setup. This should hopefully help us with the identification and observation of the energetically allowed low-intensity decay branches.

2.2 Possible decay modes of ^{21}Mg

The focus in the previous studies of the beta-decay of ^{21}Mg have been to characterize and measure the beta-decay strength distribution to as high precision as possible. This have been done by measurements of the main decay modes, which are beta-decay to bound states in ^{21}Na ($B_\beta = 67(7)\%$ [Sextro 1973]) and beta-delayed proton emission ($B_{\beta p} = 29.6(7)\%$ [Sextro 1973]). It is not surprising that the beta-delayed proton emission is one of the main decay modes, as it is well known that $T_z = -\frac{3}{2}$ nuclei with even Z in general has a high probability for beta-delayed proton emission, [Blank 2008]. As ^{21}Mg is located on the proton drip-line it has a short half-life ($T_{1/2} = 122(2)$ ms [Audi 2012]) and a large available beta-decay energy, $Q_{EC} = 13.098(16)$ MeV

[Wang 2012]. Drip-line nuclei are in general also known to have the smallest proton and neutron separation energies. The large available energy opens the possibility for more exotic decay modes than the ones already studied, however, they will naturally also be much less intense. Therefore, the main challenge in order to study these decay modes is to produce a large enough sample of ^{21}Mg ions to have a chance of observing such decay modes.

The most likely resonance in ^{21}Na to be the parent resonance of these more exotic decay modes is the IAS, as it is the strongest fed resonance in the beta-decay of ^{21}Mg at the high excitation energies needed. The reason for this strong beta-decay feeding is the very similar nuclear structure of the $T = \frac{3}{2}$ IAS in ^{21}Na and the $T = \frac{3}{2}$ ground state of ^{21}Mg . The excitation energy of the IAS is 8975(4) keV. This energy is to be compared with the various particle separation energies of the beta-decay daughter nucleus ^{21}Na , which are $S_p = 2431.68(28)$ keV, $S_\alpha = 6561.3(4)$ keV, and $S_{ap} = S_{p\alpha} = 7161.5(3)$ keV according to [Wang 2012]. All three decay modes can therefore proceed via the IAS, making this the natural place to start a search for these decay modes. In the decay scheme for ^{21}Mg shown on Figure 2.1, we have included the energetically allowed states in ^{17}F relevant for beta-delayed alpha-particle emission.

The main reason for the non-observation of these decay modes are the expected low intensity. In the specific case of beta-delayed alpha-particle emission from the IAS to the ground state of ^{17}F , the absolute intensity have been determined to be <1.60% by [Sextro 1973]. Another problem with regards to the detection of such an alpha-particle is the expected center-of-mass energy of $E_{\text{cm}} = 2.410$ MeV. This places it in the energy range of the most intense beta-delayed protons, which makes it very difficult to observe the alpha-particle. Using a ΔE - E telescope configuration that will allow you to distinguish alpha-particles of such an energy from protons, i.e. using a very thin ΔE detector, could work. In [Sextro 1973] they use a 4 μm thin silicon detector as the thinnest ΔE detector. To punch through 4 μm of silicon a proton needs to have a laboratory energy of 375 keV and an alpha-particle needs to have a laboratory energy of 1.2 MeV. With such a thin ΔE detector it should have been possible for [Sextro 1973] to distinguish between protons and alpha-particles in the energy range of the IAS alpha-particle branch, however, the experiment must have been limited by the produced number of ^{21}Mg ions for each configuration of detectors. Remember that the experiment was performed with many different ΔE - E configurations and not all of them will allow good separation of the alpha-particle and the protons.

With regards to the more exotic beta-delayed multi-particle emission $\beta p\alpha$ and $\beta\alpha p$, it have previously only been observed from ^9C and ^{17}Ne . However, the decay mode is also known to be present in ^{13}O but it has not been observed yet. In ^{17}Ne and ^{13}O the absolute intensity is known to be $\approx 1\text{-}2 \cdot 10^{-2}\%$. The case of ^9C is special in the sense that all states populated in the beta-decay daughter will break up into two

alpha-particles and one proton. A more detailed discussion of the $\beta p \alpha$ and $\beta \alpha p$ decay modes and general systematics of beta-delayed particle decays are presented in Sect. 5.2.

Experimental methods: ^{21}Mg

As we have discussed in Chapter 2 it is important to be able to do particle identification down to low energies in order to distinguish low-intensity alpha-particle branches from the high-intensity proton branches. One way of doing this is to use a very thin ΔE detector in a ΔE - E charged particle telescope as the alpha-particle branches will stand out clearly from the proton branches. To also study the beta-delayed protons and to measure the beta-decay strength distribution reliably, it is important to have a highly segmented detector array, in order to avoid beta-summing, [Schardt 1993], with a high solid angle coverage. The detector setup for the November 2011 experiment have been chosen with these points in mind. We present the detector setup in detail in Sect. 3.1. Furthermore, good energy calibrations of the detectors are important in order to have a good energy resolution. To be able to perform a proper energy calibration, we need to understand the mechanism behind the energy loss of charged particles in matter. We present this in Sect. 3.2 and based on these methods, we perform the energy and geometry calibrations in Sect. 3.3.

3.1 Detector setup

The detector setup for the experimental study of the ^{21}Mg β -decay can be seen on Figure 3.1 (all silicon detectors are from Micron Semiconductors Ltd.). It consists of a compact geometry detector setup designed to identify different low-energy charged particles. It contains two charged particle telescopes; a gas telescope with a gas detector in the front backed by two circular silicon detectors (number 1-3 on Figure 3.1, see also [Jeppesen 2002]). Opposing the gas telescope is a thin Double Sided Silicon Strip Detector (DSSSD - a schematic picture can be seen on Figure 3.2) backed by a thick silicon pad detector (number 5-6 on Figure 3.1). The gas detector was filled with CF_4 gas at a pressure of 20 mbar and had a thickness of 7.9 mm with a dead layer thickness of 8.5 mm (also CF_4 gas). It was closed off in one end by a 1 μm thick polypropylene window (number 4 on Figure 3.1) into which the ^{21}Mg beam was implanted. The beta-particle response of the gas detector is very small and allowed for effective discrimination between beta-particles, protons, and alpha-particles which is an essential property of the detector setup. The gas detector was backed by a 300 μm thick circular

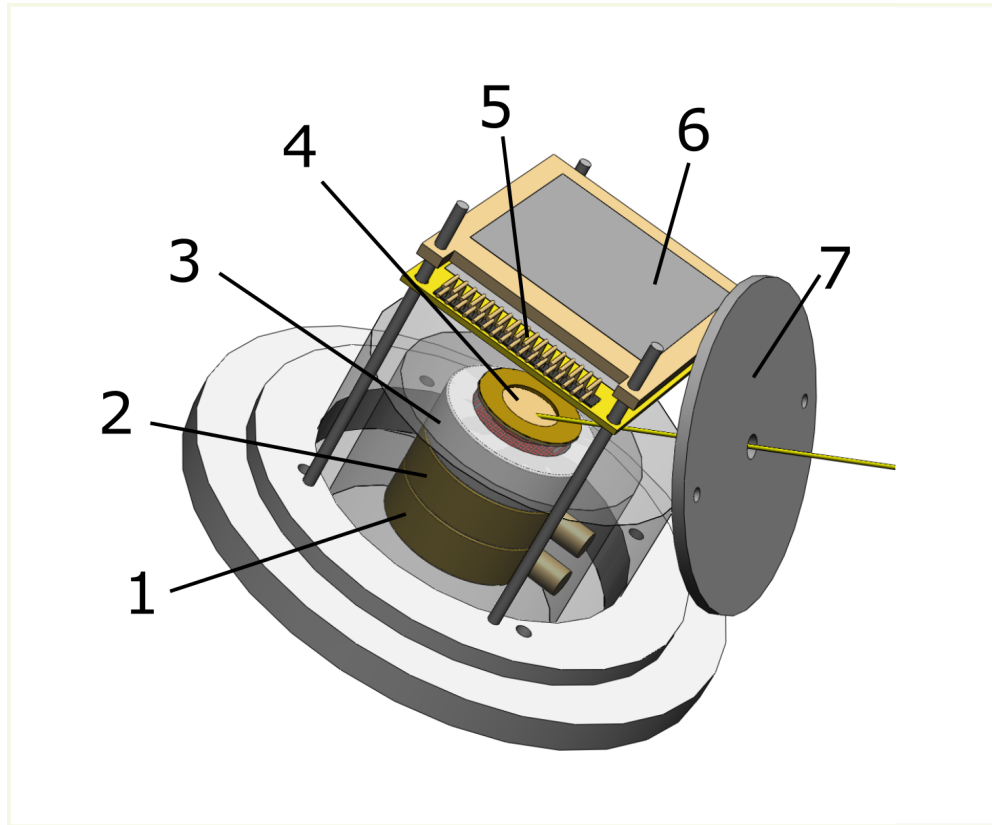


Figure 3.1: Sketch of the experimental setup for the beta-decay study of ^{21}Mg . The beam is transported from the right, passing through the collimator (no. 7) and is implanted in the polypropylene window (no. 4). The window contains the CF_4 gas in the gas detector (no. 3) which is backed by two non-segmented silicon detectors (no. 1-2). Directly opposite is a thin DSSSD detector (no. 5), backed by a thick silicon pad detector (no. 6). From [Lund 2015a].

silicon detector with a frontside and backside dead layer thickness of $0.08\ \mu\text{m}$ each. It covered a solid angle of $7.1(9)\%$. An additional circular $500\ \mu\text{m}$ thick silicon detector was located behind the first silicon detector with a dead layer thickness of $0.08\ \mu\text{m}$. It covered a solid angle of $3.6(1)\%$. Both silicon detectors were located inside the gas volume and all three detectors were circular with an area of $300\ \text{mm}^2$.

The DSSSD telescope opposite to the gas telescope consisted of a $61\ \mu\text{m}$ thick, $5 \times 5\ \text{cm}^2$ DSSSD front detector. It covered a solid angle of $7.7(3)\%$. The dead layer thickness on the frontside is $0.1\ \mu\text{m}$ and $0.8\ \mu\text{m}$ on the backside. It was backed by a $1.5\ \text{mm}$ thick silicon pad detector of the same surface area. It had a frontside dead layer of $0.8\ \mu\text{m}$ and covered a solid angle of $6.6(4)\%$. The DSSSD detector is



Figure 3.2: A schematic drawing of the DSSSD detector type. The detector has 16 vertical strips on the frontside, each of them separated by a so-called interstrip region. On the backside the detector has 16 horizontal strips also separated by interstrip regions. If a particle deposits energy in the interstrip region, it will not be detected by the detector. A strip is rectangular in shape and characterized by the fact that if a particle deposits energy in it, only this specific strip observes the signal. This is due to the fact that an electrical conductor is running along the strip. The combination of vertical and horizontal strips gives a position sensitive detector with 256 pixels in the case of a 16×16 strip detector.

a 16×16 strip detector which results in 256 pixels. Each individual pixel covers a solid angle of 0.030(1)%. This makes the DSSSD telescope ideal for measuring the intensities of the beta-delayed charged particles as beta-summing, which is discussed in [Scharadt 1993], is not an issue. Finally, the combination of the two charged particle telescopes will allow us to set coincidence or anti-coincidence gates on the data which is a powerful tool for identification of low-energy and low intensity decay branches.

A summary of the detector properties can be found in Table 3.1.

3.2 Energy loss calculations

As particles travel through matter they lose energy. In order to make proper calibrations of the detectors and to reconstruct the energy of the detected particles cor-

Table 3.1: Dead layer and detector thicknesses with the detector names referring to Figure 3.1.

| Detector no. | Thickness (μm) | Dead layer (μm) ^a |
|--------------|-----------------------------|---|
| 1 | 500 | 0.08 |
| 2 | 300 | 0.08 + 0.08 |
| 3 | 7900 | 7000 + 1500 |
| 5 | 61 | 0.1 + 0.8 |
| 6 | 1498 | 0.760 |

^axx + yy meaning xx μm on frontside and yy μm on backside. If only xx it is just the frontside dead layer.

rectly we need to take these energy losses into account. To understand how particles lose energy in matter we can start out by dividing them into three groups: particles with no charge (e.g. gamma-rays), light charged particles (beta-particles), and heavier charged particles (e.g. protons and alpha-particles). As we do not employ any gamma-ray detectors in the present experiment we will skip the discussion of gamma-ray energy loss in matter.

Charged particles traveling through matter will interact with the electrons and the nuclei of the material. As the charged particles have a large cross section for interacting with the material they will experience many successive collisions with the medium and therefore a gradual loss of the energy of the charged particle. This process are the same for both light and heavy charged particles. However, the many interactions with the material will give rise to a spread of the traveling particles to other directions than their original. Due to their small mass beta-particles will experience a large spread, which results in energy deposition in several of the pixels on the DSSSD. On the other hand will the heavier protons and alpha-particles generally only deposit energy in a single pixel unless they hit the detector close to the edge of a pixel. In this case the particle may deposit some energy in a neighboring pixel but also in the region between the strips where the signals are read out, which is called the interstrip region.

It is important to be aware that the measured energy of the charged particle is not the same as the original emitted energy of the particle, as the charged particle will need to travel out of the polypropylene window of the gas detector and through the dead layer of the detector. It means that the particle will already have lost some energy when it reaches the detector. We need to be able to reconstruct the original emitted energy of the charged particles. To do this we use the stopping power tables of SRIM (Stopping and Range of Ions in Matter, [Ziegler 2008]). The stopping power tables in SRIM is calculated in a Monte Carlo simulation that uses the binary collision

approximation, which assumes that the ion traveling through the material undergoes several independent binary collisions with the nuclei of the material. In between these collisions the ion is assumed to travel on a straight line gradually losing energy due to the interaction with the electrons of the medium. As an input to the calculation SRIM takes two parameters. First, it needs the type of incoming ion, e.g. ^1H or ^4He for protons and alpha-particles respectively. Second, it needs to know the composition of the target material. From these inputs SRIM generates a table containing the projected range, the electronic and nuclear stopping powers, and the longitudinal and lateral straggling. All of these are given as a function of the energy of the incoming ion.

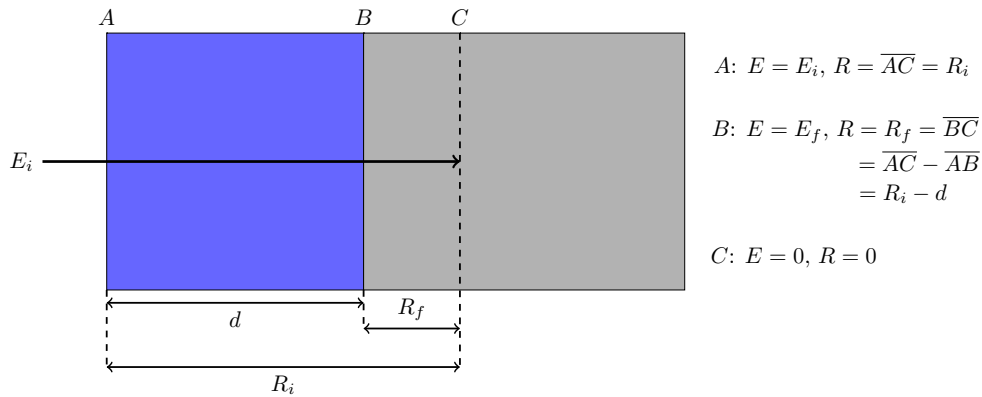


Figure 3.3: Illustration of the energy loss calculation. The ion enters the material at point A with energy E_i . The material has the thickness d (blue rectangle) and the ion will leave the material at point B with energy E_f after having lost the energy $E_i - E_f$. The grey rectangle is a hypothetical extension of the physical material (blue rectangle). The equations shown in the right part of the figure specifies the energy E and the range R of the ion at the three different points (A, B, C).

Assuming that we have an ion with initial energy E_i traveling through a specified material with thickness d , we can use the SRIM projected range as a function of energy for the given material to find the energy of the ion E_f after it has passed through the slab of material. An illustration of the calculation can be seen in Figure 3.3. The ion travels on a straight line and it enters the material at point A with the energy E_i . It leaves the material at point B with energy E_f . Assuming hypothetically that the ion had continued in the material beyond point B , it would have stopped at point C . The distance between point A and point C are equivalent to the projected range R_i of the ion with initial energy E_i which we find in the SRIM tables. The projected range is only given at a certain grid of energies in the SRIM tables. To get the projected range at any energy we make an interpolation. To find the energy E_f at point

B we use the projected range table to find out what energy corresponds to the range $R_f = R_i - d$ which is the projected range of the ion with energy E_f in point B . The energy deposited in the material is then $E_i - E_f$.

By following this recipe it is possible to calculate the energy loss of any ion in any material. We use this procedure for the energy calibrations in order to calculate the energy deposited in the detectors. By doing the reverse process, i.e. starting out with the measured energy in the detector, we can determine the emitted energy of the ion.

3.3 Calibration of detectors

To obtain a good energy resolution in all detectors it is crucial that the energy and geometry calibration is made with great care. This is no simple task and it will often take a long time and much work to get a good calibration. In this section we will go through the calibration procedure for the different detectors.

3.3.1 DSSSD

As charged particles lose energy when traveling through a material (see Sect. 3.2) it is necessary to know the geometry of the experimental setup to energy calibrate the detectors and to correctly reconstruct the emitted energy of the measured charged particles. It means that the exact position of the implanted beam with respect to the detectors must be reconstructed from measurements of emitted particles from an implanted source. One could argue that the geometry could be measured in a simpler manner by using a standard ruler, however, the detectors are very fragile so it is in general not a desirable thing to move any long objects around close to the silicon detectors. The method of using an implanted beam to reconstruct the geometry will also give more precise and accurate knowledge of the detector setup. When the geometry is known, it is possible to determine the effective thickness of the various dead layers the particles traverse.

The first step in the energy calibration will be to determine the position of the implanted beam in the polypropylene window. This can be done with the ^{21}Mg beam itself, as it is a high intensity beam and the beta-delayed proton emission includes several intense decay branches.

3.3.1.1 Geometry calibration

The position of the implanted beam with respect to the DSSSD is determined from the hit pattern of the DSSSD using the ^{21}Mg data, which is shown on Figure 3.4, assuming the beam spot is a point source. As the decay of ^{21}Mg has no preferred direction the

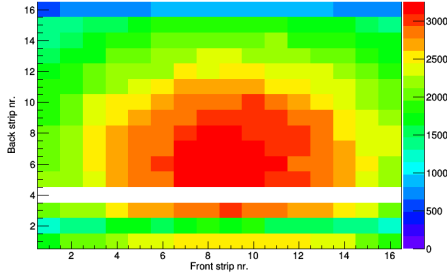


Figure 3.4: Hit pattern of DSSSD from ^{21}Mg data. Back strip 2, 4, and 16 did not work properly as is clearly seen (horizontal lines). The color gives the number of counts in each pixel.

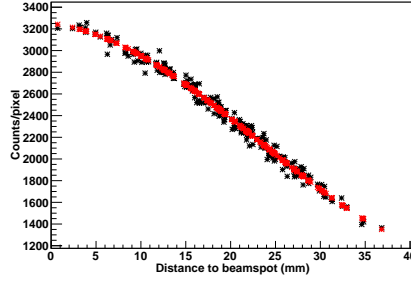


Figure 3.5: Result of the fitting procedure. Red dots are the values of the fitting polynomial, black dots are the pixels. The x-axis shows the distance from the center of each pixel to (x_0, y_0) in millimeters.

emitted protons are expected to be uniformly distributed over 4π and the intensity distribution will directly give the beam spot position.

Defining a coordinate system with $(0, 0)$ in the center of the DSSSD and the beam spot having the coordinates (x_0, y_0) , geometrical considerations give the distance from the beam spot to the center of any pixel, $|\vec{d}|$, by

$$\vec{d} = \vec{p} - \vec{r} = \begin{pmatrix} i \cdot (a + b) - c - x_0 \\ j \cdot (a + b) - c - y_0 \end{pmatrix} \quad (3.1)$$

where $c = \frac{49.5\text{mm}}{2} + \frac{a}{2} + b^1$, \vec{p} is the vector from $(0, 0)$ to the center of the pixel, \vec{r} is the vector from $(0, 0)$ to the beam spot, i is the front strip number, and j is the back strip number. $a = 3.0$ mm and $b = 0.1$ mm are respectively the strip width and the interstrip width.

The beam spot coordinates, (x_0, y_0) , are found by fitting a 4th order polynomial to the number of hits in a pixel as a function of the distance, $|\vec{d}|$, from the beam spot to the center of the pixel. The 4th order polynomial is given as a linear combination of orthogonal polynomials, which are defined in [Barlow 2000].²

Using a standard χ^2 -minimization procedure and fitting to the intensity distribution shown on Figure 3.4, while excluding back strip 2, 4, and 16, produces the result shown on Figure 3.5 with the following parameter values

$$x_0 = 1.62 \text{ mm} , y_0 = -7.03 \text{ mm} \quad (3.2)$$

¹The 49.5mm is the detector width given by 16 strip widths and 15 interstrip widths.

²The coefficients in the linear combination are independent of each other, making the fit more robust, as there will be no correlation terms.

The error on the position are negligible as it is of the order 10^{-5} mm.

The assumption of a point source is not true as the beam will have a certain width when produced. However, the consequences of this assumption is not severe. For the x - and y -directions the centroid of the beam spot is found correctly. However, if the z -distance had been included in the fit the point source assumption produces a systematically larger value. But, as the z -distance is already known to a sufficient accuracy from measurements of the chamber, it is not a problem.

3.3.1.2 Energy calibration

As the position of the beam spot is determined, it is now possible to do the energy calibration with protons emitted from the beta-decay of ^{21}Mg . The beta-decay are well-known and can be used for a reliable proton energy calibration of the DSSSD. Assuming that the daughter nucleus $^{21}\text{Na}^*$ is at rest when emitting the protons, the proton energy can be determined from the center-of-mass energies of the proton emission, E_{cm} , and the mass of the daughter ^{20}Ne , by

$$E_p = E_{cm} \cdot \frac{M(^{20}\text{Ne})}{M(^{20}\text{Ne}) + M_p} \quad (3.3)$$

The three most intense proton emissions are used, giving the proton energies 1252.0 keV (7.47%), 1773.7 keV (16.48%), and 1939.0 keV (32.09%). The proton intensities are quoted as measured in [Sextro 1973].

For the calculation of the energy loss of the protons the solid angle with respect to the source for each pixel must be known. It is given by

$$\Omega = \int \int_S \frac{\vec{R} \cdot \hat{n}}{R^3} dS = \int \int_S \frac{|\vec{R}| \cos \theta}{R^3} dS = \int \int_S \frac{\cos \theta}{R^2} dS \quad (3.4)$$

$$\approx \frac{\cos \theta}{R^2} \int \int_S dS = \frac{\cos \theta}{R^2} A(S) \quad (3.5)$$

where S is the smooth surface for which the solid angle is calculated, \vec{R} is the vector from the source to the infinitesimal surface area dS , \hat{n} is the normal vector of the infinitesimal surface dS , $A(S)$ is the area of the surface S , and θ is the angle between \vec{R} and \hat{n} . Equation (3.5) is true if it is assumed that S , i.e. the pixel, is sufficiently far away from the source so that \vec{R} does not change significantly when integrating over S .

Now the literature energies, given by Equation (3.3), have to be corrected for energy loss in the gas window ($0.0161 \mu\text{m}$ polypropylene and $0.04 \mu\text{m}$ Al for the shortest distance) and in the frontside dead layer of the DSSSD. The average energy loss of the

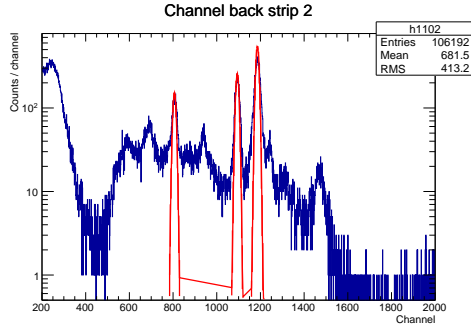


Figure 3.6: Example of a fit with a Gaussian response function and a linear background. Strip number 2 on the backside is shown with channel number on the axis. The data are from the beta-decay of ^{21}Mg .

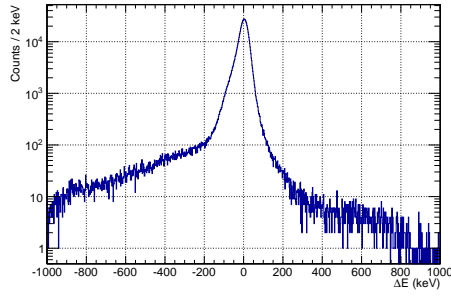


Figure 3.7: The DSSSD energy calibration applied to the ^{21}Mg data. The figure shows the energy difference between front- and backside strips for the individual events measured.

protons in each strip of the DSSSD is calculated as the weighted average of the energy loss in all pixels covered by the strip. The weights are the solid angle of each pixel given by Equation (3.5). The energy loss in each pixel is calculated assuming a constant dead layer thickness across the pixel, which is equal to the thickness in the center of the pixel. The SRIM stopping power tables are used, [Ziegler 2008].

The calibration is performed in two steps. First, a simple peak finding routine, which searches for the channel with the most counts, is used to find the centroid channel of the most intense peaks. The centroids are used in a preliminary linear calibration. Correcting the literature energy for the average energy loss in a strip, the preliminary calibration is used to convert this energy into a channel number. The channel numbers are used as a starting point in a more advanced fitting routine, taking into account the detector response function.

The advanced fitting function calculates the number of counts between ch_- and ch_+ (the difference $ch_+ - ch_-$ equals the bin width in the fitted histogram) from a normalized Gaussian response function on top of a linear background. The resulting function is

$$f(ch) = p_0 \cdot ch + p_1 + \frac{p_2}{2} \left[\text{Erf} \left(\frac{ch_+ - p_3}{p_4 \cdot \sqrt{2}} \right) - \text{Erf} \left(\frac{ch_- - p_3}{p_4 \cdot \sqrt{2}} \right) \right] \quad (3.6)$$

where p_0 is the slope of the linear background, p_1 is the offset of the linear background, p_2 is the peak area, p_3 is the centroid value, and p_4 is the standard width σ of the Gaussian distribution. The function $\text{Erf}(x)$ is defined by

$$\text{Erf}(x) = \frac{1}{\sqrt{2\pi}} \int_{-\infty}^x e^{-t^2/2} dt, \quad (3.7)$$

where $x = \frac{E-\mu}{\sigma}$. Figure 3.6 shows an example of the fit from strip number 2 on the backside of the DSSSD.

From the more advanced Gaussian fit, the parameter p_3 for the peak centroid and the uncertainty on p_3 , is used in a final linear calibration that uses a standard χ^2 -minimization procedure. This produces the desired final energy calibration of all 32 strips in the DSSSD.

As a check of the calibration it is helpful to look at the energy difference between the front- and backside of the DSSSD for all physics events. This should be zero if the calibration is perfect and no noise is present in the detector, as it is the same signal that is read out on front- and backside. On Figure 3.7 the energy difference between front- and backside events is presented. The data represents the full ^{21}Mg data set. The energy difference shows a sharp peak with a centroid value of +2 keV. It is slightly asymmetric but it levels off very nicely. The calibration is successful.

For the analysis of the data it is important to look at real particle events and to avoid noise events. To fulfill this goal a matching of the energy measured in the frontside of the detector with the energy measured in the backside is performed. The routine that performs the matching of the energies uses the two parameters E_{\min} and ΔE to check which signals is to be matched with each other. The parameter E_{\min} specifies a minimum energy necessary to start the matching of the energies. The main reason for this is the presence of noise signals from the detector or the data acquisition system that shows up as low-energy signals in the data. To remove most of these unwanted events we set E_{\min} at an appropriate level depending on the noise level of the detector. The second parameter, ΔE , describes the maximum allowed energy difference between a signal in the front- and backside in order to match them as a single-particle event. For the analysis of the ^{21}Mg data we use $E_{\min} = 200$ keV and $\Delta E = 50$ keV.

The matching of the energies are somewhat complicated by the fact that for a single trigger in the DSSSD it is possible to have 16 energy signals in the frontside and 16 energy signals in the backside, as there can be one signal from each of the 32 strips. To match the energies in the case with several energy signals in both the front- and the backside, we use the criterium that for a given energy signal in say the frontside, it must be matched with the energy signal in the backside closest in energy. If more than one energy signal in the backside is less than ΔE from the energy signal in the frontside, the remaining energy signal(s) will have to be matched with a different energy signal in the frontside.

When a frontside energy signal is matched with a backside energy signal we take the average energy of the two signals as the energy of the event. We also count the number of matched events for each trigger and we will refer to this as the particle multiplicity.

3.3.2 Energy calibration of unsegmented detectors

For the gas detector it was not possible to make an energy calibration. The problem is that the punch through energy, i.e. the energy above which the charged particles will pass through the detector, for protons is only 24 keV and for alpha particles is only 46 keV. It means that the decay spectrum will not exhibit any peaks making it very difficult to calibrate the detector.

For the first silicon detector in the gas telescope (no. 2 on Figure 3.1) a calibration has been made using the ^{21}Mg proton source implanted in the gas detector window. The proton energies need to be corrected for energy lose in the gas window ($1\ \mu\text{m}$), in the gas (16.4 mm), and in the frontside dead layer of the silicon detector ($0.08\ \mu\text{m}$). The distances quoted are the shortest possible distances from source to detector. As the detector is unsegmented an expression for the energy lose averaged over all angles covering the detector has to be made to get a more accurate calibration. The average weighted energy lose is given by

$$\langle E_{\text{lose}} \rangle = \frac{\int_0^{2\pi} \int_0^{\theta_{\text{max}}} E_{\text{lose}}(\theta) \frac{d\Omega}{\Omega_{\text{det}}} = \frac{\int_0^{\theta_{\text{max}}} E_{\text{lose}}(\theta) \sin \theta d\theta}{\int_0^{\theta_{\text{max}}} \sin \theta d\theta} \quad (3.8)$$

where $d\Omega = \sin \theta d\theta d\phi$ is an infinitesimal solid angle, Ω_{det} is the total solid angle of the detector, and $d\Omega/\Omega_{\text{det}}$ is the weights of each circular disc.

For small angles, θ , it may be assumed that $E_{\text{lose}}(\theta) \approx \frac{E_{\text{lose}}(\theta=0)}{\cos \theta}$, which is the same as assuming that the energy loss is proportional to the length travelled. The final result for the averaged energy loss becomes

$$\langle E_{\text{lose}} \rangle \approx E_{\text{lose}}(\theta=0) \frac{\int_0^{\theta_{\text{max}}} \tan \theta d\theta}{\int_0^{\theta_{\text{max}}} \sin \theta d\theta} = E_{\text{lose}}(\theta=0) \frac{-\ln(|\cos \theta_{\text{max}}|)}{1 - \cos \theta_{\text{max}}} \quad (3.9)$$

Using the ^{21}Mg proton energies 1773.7 keV (16.48%), 1939.0 keV (32.09%), and 4675 keV (4.78%) and correcting for the average weighted energy lose given by Equation (3.9), the following calibration of the silicon detector is obtained,

$$E(ch) = 1.421(6) \cdot ch - 35.6(1.3) \quad (3.10)$$

The calibration of the second silicon detector of the gas telescope (no. 1 on Figure 3.1) is made with events from the proton branch connecting the IAS of ^{21}Na and the ground state of ^{20}Ne . It is the only intense proton branch with enough energy to punch-through the two detectors sitting in the front of the gas telescope. No alpha-source measurements were made for this detector. Hence, the proton branch from the decay of ^{21}Mg is the only possible calibration point for this detector. Therefore, the calibration have been performed on an event-by-event basis. For every event in

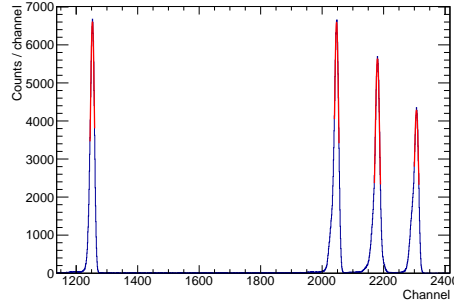


Figure 3.8: Gaussian function fitted to the four individual alpha peaks from the quadruple alpha-source (^{148}Gd , ^{239}Pu , ^{241}Am , ^{244}Cm) as seen in the thick pad detector behind the DSSSD.

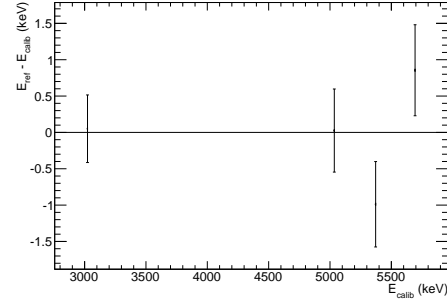


Figure 3.9: Residuals from a linear energy calibration using the quadruple alpha-source (^{148}Gd , ^{239}Pu , ^{241}Am , ^{244}Cm) for the pad detector behind the DSSSD. The assumption of linearity appears to be good.

the proton peak the channel number measured in the detector has been compared with the reconstructed measured energy of the proton. The reconstruction of the measured proton energy is done by correcting the known emitted energy, E_p , for the angular-averaged energy lose, $\langle E_{\text{lose}} \rangle$, given by Equation 3.9 in the corresponding dead layers. The energy lost in the silicon detector in the center of the gas telescope is known from measurement, $E_{\text{Det. 2}}^{\text{measured}}$, and this energy is subtracted from E_p as well. In summary, the reference energies used for the energy calibration is given by

$$E_{\text{Det. 1}} = E_p - \langle E_{\text{lose}} \rangle - E_{\text{Det. 2}}^{\text{measured}} \quad (3.11)$$

This procedure is not very robust as we have no angular information of the protons due to the use of unsegmented detectors only. As expected the linear fit to the measured channel number versus the reconstructed measured energies gives coefficients with large uncertainties.

The calibration of the thick pad detector positioned behind the DSSSD (no. 6 in Figure 3.1) was made with a dedicated quadruple alpha-source (^{148}Gd , ^{239}Pu , ^{241}Am , ^{244}Cm) measurement where the DSSSD was removed. The alpha-source covers a wide range of energies from 3 MeV up to 5.7 MeV and is thus a good source to use. The measured energy spectrum is shown on Figure 3.8 with Gaussian line shape fits to the four intense peaks. Assuming a linear translation from channel number to energy gives a good calibration. The residuals seen on Figure 3.9 compares the reference energies with the calibrated energies and they agree very well to within 1 keV.

However, alpha-particles and protons have different stopping powers in silicon. Hence, the energy calibration will not properly reproduce the proton energies mea-

sured and this is really what we want. Therefore, we want to transform the calibration coefficients to better describe proton energies. The transformation can be made according to the description in [Lennard 1986]. First, we need to divide the stopping power into an ionizing and a non-ionizing part owing to interactions with the electrons of the atom and the nucleus, respectively. Both parts of the stopping power behave differently for protons and alpha-particles. Second, we correct the alpha calibration energy for the difference in the non-ionizing energy lost for the two types of particles. As an average over energy this is given by $(\Delta E_{ni})_{4\text{He}} - (\Delta E_{ni})_{1\text{H}} = 9\text{ keV} - 1\text{ keV} = 8\text{ keV}$. Third, we correct for the difference in the ionizing energy loss. The correction for an alpha-particle can be made with the factor $C(^1\text{H})/C(^4\text{He}) = 0.986(2)$. Here C is the slope of a linear fit to the pulse height versus the deposited energy.

The obtained energy calibrations give a Full Width at Half Maximum (FWHM) energy resolution of 39.3(2) keV for the DSSSD, 53.9(3) keV for the sum spectrum of the DSSSD and the pad detector behind it, and 49.0(3) keV for the first silicon detector in the gas telescope. These FWHM values have been obtained from a line shape fit of the ^{21}Mg beta-delayed proton spectrum. The line shape used is described in detail in Sect. 4.4.1.

The energy calibrations suffer from systematic uncertainties. The magnitude of the systematic uncertainty have been estimated from the ^{21}Mg beta-delayed proton branches which are emitted from resonances in ^{21}Na that also will decay by gamma-ray emission. As the energy of these ^{21}Na resonances are accurately known this is a good way of understanding the systematic uncertainties. The systematic uncertainty of the energy calibrations are estimated to be 10 keV.

^{21}Mg : modified decay scheme and other results

As described in Chapter 2 the main focus in the previous measurements of the beta-decay of ^{21}Mg have been to study the beta-delayed proton spectrum. In this chapter we will keep our focus on the measurement of the many different beta-delayed proton branches in order to extract structure information about the nuclear states involved and to determine the decay scheme and the beta-decay strength distribution. In Chapter 3 we presented the experimental setup that we use for this purpose. In this chapter will we give an overview of the data in Sect. 4.1 and we will continue by determining the half-life of ^{21}Mg in Sect. 4.2. In Sect. 4.3 and 4.4 we will discuss the analysis of the time distribution of the low-intensity decay branches and we will describe the line shape fitting of the proton branches from, which we extract information about the energy, the total width, and the intensities. We finish the chapter with a reconstruction of the decay scheme (Sect. 4.5) and the determination of the $\log(ft)$ -values (Sect. 4.6). This chapter is to a large extent based on the work published in [Lund 2015a].

4.1 Initial overview of the data

The measured decay products from the beta-decay of ^{21}Mg with the charged particle detection setup described in Sect. 3.1 is presented in Figure 4.1 in the form of a ΔE - E spectrum with the data from the gas telescope. Rescaled stopping power curves from SRIM [Ziegler 2008] for alpha-particles and protons in silicon have been drawn on top of the data. The rescaled stopping power curves represent the combined energy lose in the collection foil, the gas detector, and the silicon detector dead layer. We clearly observe correlations between the data and the stopping power curves which divides the data into two major parts: one part is alpha-particles, the other part is protons. It is evidence for the presence of at least two different decay modes: βp and $\beta\alpha$ emission. The beta-delayed alpha-particle emission is discussed in more detail in Sect. 5.1. In Sect. 5.2 the first observation of the rare $\beta p\alpha$ decay mode is discussed

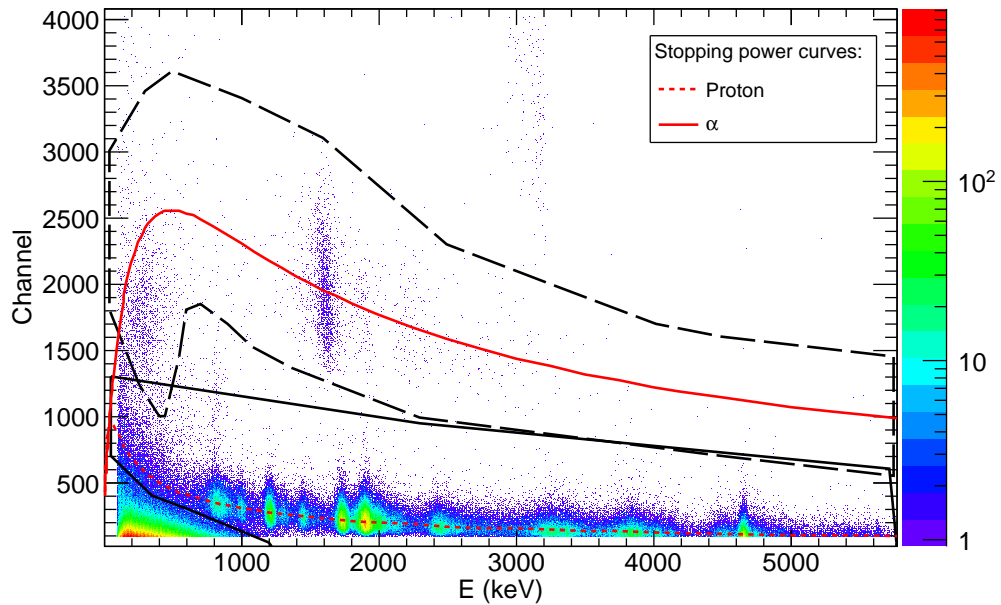


Figure 4.1: ΔE - E figure from the gas telescope with the gas channel number on the y-axis and the deposited energy in the first silicon detector on the x-axis. Scaled stopping power curves from SRIM [Ziegler 2008] for alpha-particles and protons in silicon is drawn on top of the data in solid and dashed red respectively. The graphical cuts to produce the alpha-particle spectrum and the proton spectrum are also drawn as long-dashed black and solid black respectively. The events located at 3.18 MeV in the silicon detector and above channel number 2300 in the gas detector is a contamination source of ^{148}Gd located inside of the silicon detector. Figure from [Lund 2015b].

in detail. In the rest of this chapter we will focus on the analysis of the beta-delayed proton spectrum.

The production of a clean proton spectrum from the first silicon detector in the gas telescope relies on two gates. First, a gate to remove the high energy protons that punch through the first silicon detector is applied. This gate is determined on the basis of a ΔE - E spectrum not shown here with the energy of the first silicon detector on the vertical axis and the energy of the second silicon detector on the horizontal axis. The second gate which we apply to the data is the graphical gate shown on Figure 4.1 as the solid black line. This gate is produced such that it follows the stopping power curve for a proton in silicon in order to most efficiently cut away alpha-particles, beta-particles, and nuclear recoils. The proton spectrum produced by applying these two gates can be seen on Figure 4.2. The proton spectrum has a minimal contamination of

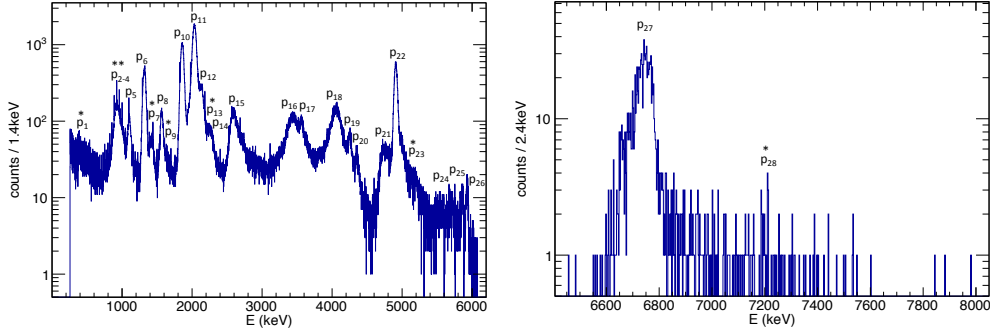


Figure 4.2: Proton singles spectrum from the gas telescope with the center-of-mass energy shown. New proton branches are marked with a \star . A $\star\star$ indicates two new proton branches in the same peak. *Left:* events from the first silicon detector of the gas telescope. *Right:* events from the second silicon detector of the gas telescope. Figure from [Lund 2015a].

other components above approximately 1150 keV. Below this energy, however, does especially beta-particles and nuclear recoils start to be an issue but also the alpha-particles can contribute at the very lowest energies as the stopping powers start to overlap.

Comparing the present data with the two main beta-decay studies performed earlier, [Sextro 1973, Thomas 2003] (see Sect. 2.1 for more detail), we can conclude that a slightly worse energy resolution is achieved in the present experiment, however, more statistics is collected. We should therefore be able to observe less intense decay branches. Comparing the overall beta-delayed proton spectrum with the earlier measurements many similarities are immediately observed as expected, which confirms that the overall setup is working as it should. A closer look at the data on Figure 4.2 also reveals several new beta-delayed proton branches with low intensity. Their center-of-mass energies are determined to be $E_{\text{cm}}(p_1) = 396(10)$ keV, $E_{\text{cm}}(p_7) = 1427(10)$ keV, $E_{\text{cm}}(p_9) = 1630(10)$ keV, $E_{\text{cm}}(p_{23}) = 5171(12)$ keV, and $E_{\text{cm}}(p_{28}) = 7.2(3)$ MeV.

Due to a different interpretation of the line shape of the proton peak p_{2-4} as compared with the work in [Sextro 1973] three individual proton branches instead of a single proton branch is now assumed to contribute to this peak. The center-of-mass energies of these three proton branches are $E_{\text{cm}}(p_2) = 906(10)$ keV, $E_{\text{cm}}(p_3) = 919(21)$ keV, and $E_{\text{cm}}(p_4) = 937(10)$ keV. More details can be found in Sect. 4.5 and 5.2.

To produce a clean proton spectrum in the DSSSD detector we demand that the energy measured in the frontside can be matched with the energy measured in the backside of the detector as described in Sect. 3.3.1.2. We use the average energy of the front- and backside as the particle energy. The second condition used to produce a clean spectrum in the DSSSD is a demand that no events must be measured in the

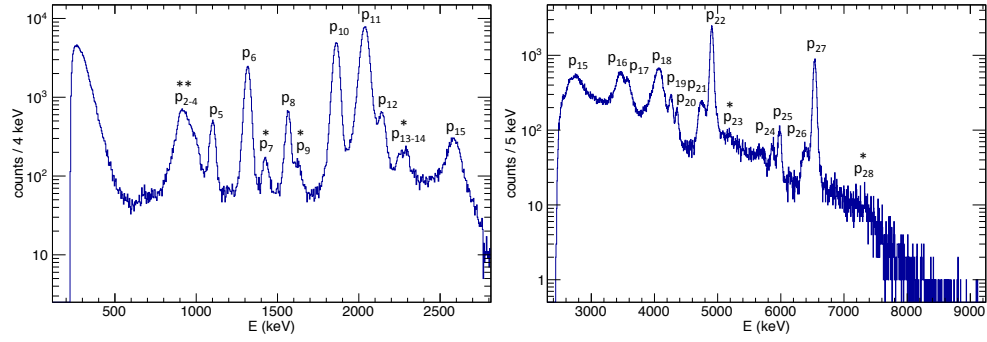


Figure 4.3: Proton singles spectrum in the DSSSD telescope with the center-of-mass energy shown. New proton branches are marked with a \star . A $\star\star$ indicates two new proton branches in the same peak. Note that proton branch p_{15} punch-through the central part of the DSSSD but is stopped in the outer parts of the detector. The proton branch p_{28} is placed tentatively at the expected energy. The small peak just below p_{24} is not identified as a proton branch and a further discussion can be found in Sect. 4.5 as part of the discussion on the 8135(15) keV resonance. *Left:* events from the DSSSD. *Right:* events from the pad detector. Figure from [Lund 2015a].

pad detector at the same time.

The conditions applied to produce a clean spectrum in the pad detector is first of all that we need to have a real particle event in the DSSSD which means that we have a front-back matched event. The energy from the DSSSD is together with the energy measured in the pad detector, used to reconstruct the center-of-mass energy by use of the SRIM stopping power tables [Ziegler 2008]. A second gate applied to produce the pad energy spectrum is a gate to only look at the particles that punch through the DSSSD but at the same time to remove beta-particles as they in many cases will reach the pad detector. This is done through a gate applied to the ΔE - E spectrum.

Applying the described gates to the DSSSD telescope data results in the proton spectra for the DSSSD and the pad detector as shown on Figure 4.3. The spectrum exhibits the same features as we observe in the gas telescope which is an important cross check of the consistency of the data. In the case of proton branch p_1 the two telescopes diverge as it is not visible in the DSSSD due to the more pronounced beta-particle response. But this discrepancy were expected. On the other hand does the better energy resolution obtained in the DSSSD help us to realize that the proton peak located just above p_{12} actually consists of two proton branches. They have center-of-mass energies $E_{\text{cm}}(p_{13}) = 2263(11)$ keV and $E_{\text{cm}}(p_{14}) = 2302(10)$ keV. Finally, the proton branch p_{23} stand out from the background more clearly in the DSSSD telescope than in the gas telescope.

4.2 Half-life determination

We determine the half-life of ^{21}Mg from the time distribution of the two most intense beta-delayed proton branches, i.e. p_{10} and p_{11} on Figure 4.3. Using all data from these two proton branches measured in the DSSSD detector we obtain the time distribution shown on Figure 4.4. The time distribution is fitted with a function describing the standard radioactive decay law

$$A(t) = \lambda \cdot N_0 \cdot e^{-\lambda \cdot t} \quad (4.1)$$

and the fitting parameters are minimized by the use of the MINOS error estimation technique in the MINUIT2 minimization package [James 2004]. As we collect the ^{21}Mg ions in the detection chamber only during the first 300 ms after proton impact on the ISOLDE production target, we limit the fitting interval to be between 300 ms and 2400 ms. The upper limit is chosen such that it coincide with two times the proton beam pulse spacing of 1.2 s. At this upper limit there is no activity left.

We used a standard Poisson log-likelihood method for the fitting in order to include bins with zero counts. This method will generally also give a more reliable fit when one is dealing with small count number (≈ 10 counts per bin or less). The resulting half-life determined from the fit is

$$T_{1/2} = 118.6(5) \text{ ms} \quad (4.2)$$

with a $\chi^2/\text{ndf} = 1234/2099 = 0.59$. Based on the results of [Bergmann 2002] this value of χ^2/ndf is in good agreement with the expected value for a good fit when the number of counts in each bin on average is low.

The latest evaluation of the half-life for ^{21}Mg gives a value of $T_{1/2} = 122(2) \text{ ms}$, [Audi 2012], which within two standard deviations is in agreement with the value determined here. The uncertainty of our new determination is a factor of four lower than the evaluation. Therefore we use the new value in the calculation of the $\log(ft)$ -values in Sect. 4.6.

4.3 Time distribution analysis

The beta-delayed proton spectrum of ^{21}Mg includes several weak branches. As we know the produced ion beam is contaminated with at least ^{21}Na and perhaps other less intense contaminants, an extra cross-check of the assignment is desirable. One way of doing this is by comparing the time distributions of the weak decay branches with that of a known source of ^{21}Mg . This can be done efficiently by using a goodness-of-fit test based on the empirical distribution function (EDF) statistics.

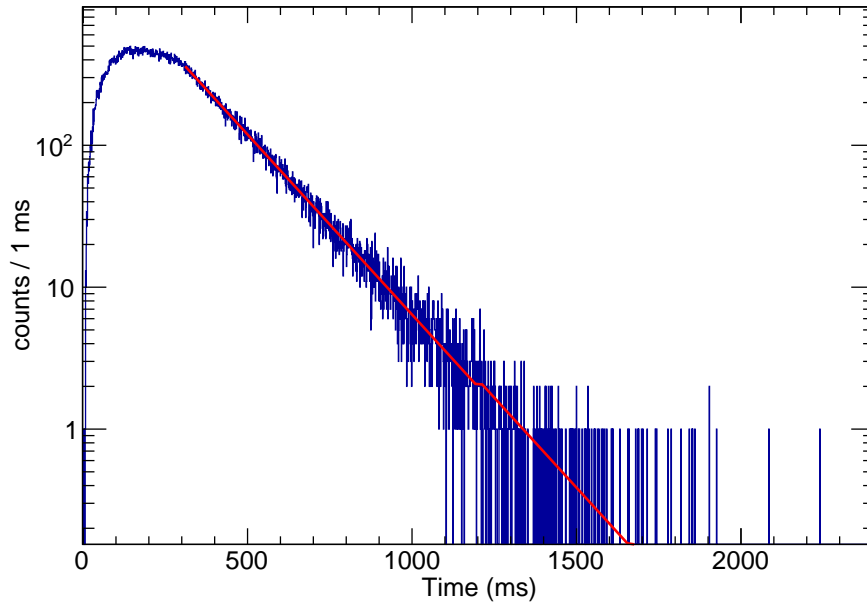


Figure 4.4: Half-life fit for the ^{21}Mg decay. The time distribution is from the two most intense proton branches, p_{10} and p_{11} , measured in the DSSSD. Figure from [Lund 2015a].

The EDF statistics [Stephens 1986] are known to produce more powerful goodness-of-fit tests than e.g. the often employed χ^2 -test. The EDF statistics compare the shape of the distribution in question (also called the experimental distribution) with a reference distribution by measuring the distance between the two cumulated time distributions. In the case of binned data the experimental and reference distributions have the values EDF_i and F_i in bin i . The three most frequently used EDF statistics [Choulakian 1994] are the Kolmogorov-Smirnov

$$D = \sqrt{N} \max_i |EDF_i - F_i|, \quad (4.3)$$

the Cramer-Von Mises

$$W^2 = N \sum_i (EDF_i - F_i)^2 p_i, \quad (4.4)$$

and the Anderson-Darling

$$A^2 = N \sum_i \frac{(EDF_i - F_i)^2 p_i}{F_i(1 - F_i)}, \quad (4.5)$$

where N is the total number of counts and p_i is the probability to be in bin i in the reference distribution. To establish the value of each of these statistics which corre-

Table 4.1: Established confidence levels for the three different EDF statistics based on Monte Carlo simulations. The confidence levels are calculated for the hypotheses that the time distribution in question belong to the decay of ^{21}Mg . Hence a good fit will have a confidence level less than 95 %.

| c.l.: | 75 % | 85 % | 90 % | 95 % | 97.5 % | 99 % |
|-------|------|------|------|------|--------|------|
| D | 0.98 | 1.10 | 1.18 | 1.31 | 1.43 | 1.57 |
| W^2 | 0.21 | 0.29 | 0.35 | 0.46 | 0.57 | 0.72 |
| A^2 | 1.24 | 1.63 | 1.94 | 2.49 | 3.09 | 3.85 |

Table 4.2: Results of the three different goodness-of-fit tests of the time distribution to settle if the events in question do belong to the ^{21}Mg decay. The values are to be compared with the confidence levels in Table 4.1.

| | p_3 | p_7 | p_9 | p_{28} |
|-------|-------|-------|-------|----------|
| D | 1.22 | 0.95 | 1.03 | 0.78 |
| W^2 | 0.33 | 0.15 | 0.21 | 0.13 |
| A^2 | 1.46 | 1.01 | 1.01 | 0.86 |

sponds to a certain confidence level we have to perform simulations. In the present case the reference distribution is taken to be the time distribution for the events inside the proton gate on Figure 4.1 and which have an energy above 1150 keV. This subset of the data is expected to only contain protons from the decay of ^{21}Mg . We have performed Monte Carlo simulations with 40000 randomly generated spectra each with 400 counts in order to determine the confidence levels. The number of counts in the spectra have been varied, however, this does not change the results much. The resulting confidence levels can be seen in Table 4.1.

We have applied the described EDF statistics to all the new beta-delayed proton branches observed; p_1 , p_3 , p_7 , p_9 , p_{28} . The results of these goodness-of-fit tests can be seen in Table 4.2. However, in the case of p_1 the result is not quoted in the table as we will return to this below. The goodness-of-fit tests for p_7 , p_9 , and p_{28} gives results which are less than the 85% confidence level. It means that these proton branches are consistent with being emitted in the decay of ^{21}Mg . For the proton branch p_3 the goodness-of-fit test returns a somewhat unclear picture. However, as two out of the three tests shows confidence levels less than 90% and as the Kolmogorov-Smirnov test is marginally consistent with p_3 being part of the ^{21}Mg decay, we conclude that it do belong to the ^{21}Mg decay.

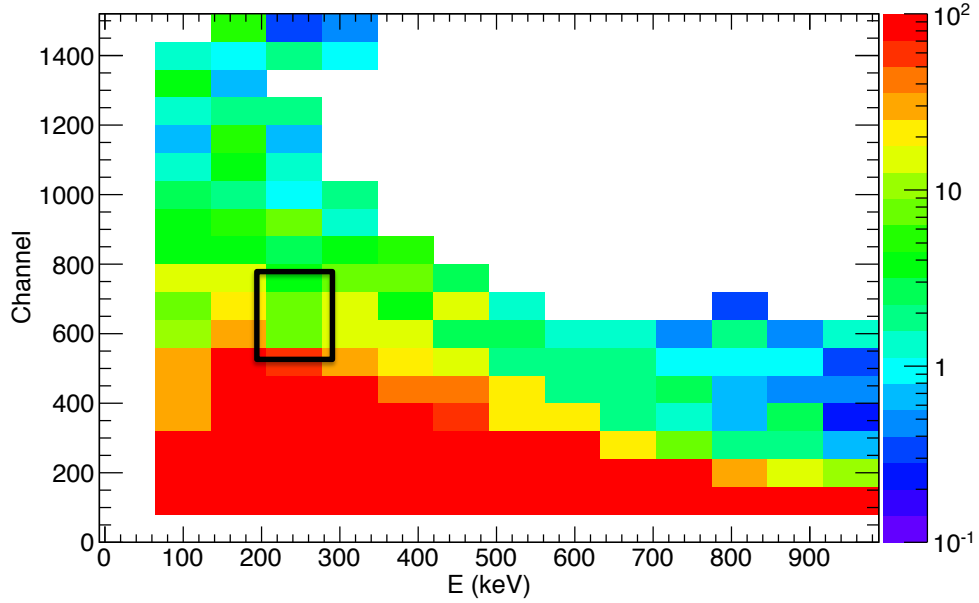


Figure 4.5: Result of the Anderson-Darling goodness-of-fit test, A^2 , of the β -particle region in the ΔE - E plot with the $^{21}\text{Mg}(\beta p)$ time distribution as the reference distribution. The vertical axis shows the channel number of the gas detector and the horizontal axis shows the energy of the first silicon detector in the gas telescope. The proton branch p_1 is marked with a black rectangle. Figure from [Lund 2015a].

We now return to the results for the proton branch p_1 . It is located in a part of the ΔE - E spectrum on Figure 4.1 which contains a mixture of beta-particles from ^{21}Mg as well as from ^{21}Na but also nuclear recoils. As a consequence, we do not expect the goodness-of-fit tests to confirm that p_1 belongs to the decay of ^{21}Mg . In fact the three tests do agree that the time distribution of p_1 is not consistent with the ^{21}Mg time distribution. We have therefore confirmed the reliability of the method. However, as a support of the assignment of p_1 as part of the ^{21}Mg decay we perform a detailed study of the low energy region of the ΔE - E spectrum close to p_1 . We divide the events in the ΔE - E spectrum into small rectangles with respect to their energy in both the front and the back detector, see Figure 4.5. To each of these rectangles we apply the Anderson-Darling goodness-of-fit test in order to understand the contents of the specific energy region. As a reference distribution we use the ^{21}Mg time distribution as we did earlier. For the events to be mainly from ^{21}Mg the goodness-of-fit test needs to return a value less than the 95% confidence level of $A^2 = 2.49$ according to Table 4.1.

On Figure 4.5 the position of p_1 is marked by the black rectangle. It is evident

from the figure that the events here stands out from the surroundings, as events at lower and larger energy in the silicon detector shows a considerably higher value of A^2 . From this we can conclude that the events inside the black rectangle, i.e. belonging to p_1 , belong to a different time distribution than the general background. Also, the position of p_1 in the ΔE - E spectrum coincides with the rescaled proton stopping power in silicon as shown on Figure 4.1. Based on these two observations we conclude that it is very likely that p_1 is a low-energy beta-delayed proton branch from ^{21}Mg with a large background of beta-particles from ^{21}Na .

4.4 Spectroscopic properties deduced from line shape fit

The measured line shape of the beta-delayed protons as seen on Figure 4.2 and 4.3 contains information about the resonances involved in the proton emission. By modeling the line shape it is therefore possible to extract spectroscopic information on the resonances like the widths, the resonance energy, and the spin and parity. In this section we will describe the line shape that we use to fit the proton peaks and what information we obtain about the resonances.

4.4.1 Line shape

To describe the observed charged particle line shape as measured with the silicon detectors, it is necessary to account for three effects. The first effect is the recoil broadening due to the beta-decay kinematics which for a decay to a given excited state in the beta-daughter nuclei gives rise to a symmetric broadening of the energy. The second effect is the response and pulse formation in the silicon detector when the charged particle interacts with the silicon and produces electron-hole pairs. The third effect is the resonance behavior of the decay probability for beta-delayed emission of charged particles. This includes the available phase space for the beta-decay, the beta-decay strength to the relevant resonance, an account of all available decay channels and resonances, decay widths, the resonance energy, possible quantum interference effects, and the effect of the penetrability. The overall line shape will then be a convolution of these three effects and can be expressed by

$$\psi_{\text{tot}} = \psi_{\text{physics}} \times \psi_{\text{detector}} \times \psi_{\text{recoil}} \quad (4.6)$$

An exact modeling of this line shape would be very complex and time consuming. As a consequence, we use an approximate line shape which we will argue is sufficient in the present case.

We have tried two different approximations of the line shape. As a first-order approximation of the line shape we tried a normalized Gaussian distribution with a

constant background multiplied by a parameter describing the number of events in the peak. Local fits of the proton peaks, i.e. fitting in a limited energy range close to the relevant proton peak, will determine the number of events measured in the proton peak. The same analysis method was used by [Sextro 1973]. However, comparing the relative intensities obtained in the two charged particle telescopes clearly demonstrates an inconsistency in our results. Hence, a more physically correct approximation of the line shape was developed.

As an approximation on ψ_{physics} we assume non-interfering and narrow resonances, which gives a simple modeling as a Breit-Wigner distribution. A proper treatment of the resonant behavior of the decay probability for beta-delayed charged particle emission involves R-matrix theory [Lane 1958] as it is a very complex quantum mechanical problem. In some cases the approximations will not be valid as both interference and broad resonances most likely will be present. Hence, it is important to know when to take these effects into consideration. The signature of interference and of broad resonances are an asymmetric line shape of the charged particle. Interference happens if two charged particles of the same kind, say protons, is emitted from resonances close in energy and with the same spin and parity. Both decay branches need to end in the same final state.

The detector response, ψ_{detector} , is approximated by a normalized and integrated Gaussian distribution, which describes the number of events per channel in the detector from a monoenergetic beam. In this case it is a sufficient approximation.

The kinematic recoil broadening ψ_{recoil} is negligible in this experiment. As the detector energy resolution is larger than the recoil broadening we may safely neglect the latter as it will only give rise to a small perturbation on the widths. From [Bhattacharya 2002] we have calculated the maximum recoil shift T_{max} to be between 20 and 26 keV depending on which resonance is populated in ^{21}Na . The FWHM of the recoil broadening will be less than $2 \cdot T_{\text{max}}$ and it is therefore smaller than the best energy resolution obtained in this experiment and it is safe to neglect. The detector energy resolutions were discussed at the end of Sect. 3.3.

In conclusion, the line shape used for extracting the number of events in each peak, assuming a background of zero, is

$$\psi(E) = \frac{A}{2} \left[\text{Erf} \left(\frac{E + \Delta - E_0}{\sqrt{2}\sigma} \right) - \text{Erf} \left(\frac{E - \Delta - E_0}{\sqrt{2}\sigma} \right) \right] \times \frac{\Gamma}{2\pi} \frac{1}{(E - E_0)^2 + (\Gamma/2)^2}, \quad (4.7)$$

where $\text{Erf}(x) = \frac{2}{\sqrt{\pi}} \int_0^x e^{-u^2} du$. The parameter A is the number of events in the peak, E_0 is the peak centroid energy, σ is the Gaussian width of the response function which gives the detector resolution. The parameter Δ is half the bin-width of the spectrum and it is a fixed property of the individual spectra. Finally, Γ is the Breit-Wigner width of the resonance emitting the corresponding charged particle. The convolution is performed numerically.

4.4.2 Fitting procedure

The first step is to determine the detector energy resolution σ by fitting a narrow proton branch with the line shape function in Equation (4.7) and the Breit-Wigner width Γ fixed to the literature value. The known widths Γ_{tot} can be found in Table 4.3. For the DSSSD energy spectrum we use the proton branch p_{10} which is emitted from the 4294.3(6) keV resonance in ^{21}Na . The width of this resonance is known to be $\Gamma_{\text{tot}} = 3.93(10)$ keV. The Breit-Wigner width Γ is fixed to this value and the fit gives a value of $\sigma_{\text{DSSSD}} = 16.74(7)$ keV. For the silicon pad detector placed behind the DSSSD we fit to the proton branch p_{22} which is emitted from the IAS in ^{21}Na . The total width of the IAS is known from the literature to be $\Gamma_{\text{tot}} = 0.65(5)$ keV. Using this value for Γ we obtain a value of $\sigma_{\text{pad}} = 22.95(14)$ keV. Finally, we also determine the energy resolution of the first silicon detector in the gas telescope by fitting the proton branches p_{10} and p_{22} . A weighted average of the parameter σ gives the value $\sigma_{\text{Si1}} = 20.84(14)$ keV.

The next step is to use the detector energy resolution that we have determined as the parameter σ in the fitting of the line shape of the proton peaks. We keep σ as a fixed parameter as we do not observe any significant energy dependence of the detector energy resolution. The consequence of this procedure is that we will overestimate the detector energy resolution, because we neglect the recoil broadening of the line shape caused by the beta-decay kinematics. However, the width of the recoil broadening in terms of the FWHM will change as a function of the excitation energy in ^{21}Na . For instance, assuming a pure Fermi beta-decay we can determine the FWHM on the basis of [Bhattacharya 2002] to be 25 keV at an excitation energy of 4.0 MeV, to be 28 keV at an excitation energy of 6.0 MeV, and to be 22 keV at the position of the IAS in ^{21}Na (≈ 9.0 MeV). As we assumed an energy independent detector energy resolution only part of the recoil broadening will be accounted for in the parameter σ . Therefore, the recoil broadening will give rise to a minor systematic uncertainty of the order of 3 keV on the measured resonance widths Γ . This systematic uncertainty is added in quadrature to the statistical uncertainty from the fit.

The fit of the proton line shape were not performed to the entire spectrum at the same time. Instead we divided the energy spectrum into several intervals, each containing a single proton peak or, if the proton peaks were overlapping the interval included all of the overlapping peaks. In each interval we assumed a background of zero events. As an example the combined fit of p_{10} , p_{11} , p_{12} , p_{13} , and p_{14} can be seen on Figure 4.6. Based on the χ^2/ndf value obtained the quality of the fit is poor. This is the case in general and not only for this example. We believe the large χ^2/ndf value can be explained by a too simple approximation of the detector response function, ψ_{detector} . A more accurate detector response function is expected to include exponential tails on the low-energy side of the peak [Bhattacharya 2006]. Visually the

Table 4.3: Comparison of the fitted Breit-Wigner widths Γ with the known literature values (Γ_{tot}). For references to the literature values see Table 4.5. An upper limit on Γ is set when the obtained value from the line shape fit is less than the Gaussian detector resolution. Such cases are assigned an upper limit $\Gamma \leq \sigma_{\text{det}}$.

| Peak | Γ_{Gas} (keV) | Γ_{DSSSD} (keV) | Γ_{tot} (keV) |
|-----------------|-----------------------------|-------------------------------|-----------------------------|
| p ₁ | 65(25) ^a | - ^b | 21(3) |
| p ₂ | 23(13) | ≤ 17 | - |
| p ₃ | 0.65 ^c | 0.65 ^c | 0.65(5) |
| p ₄ | 132(7) | 104(4) | 112(20) |
| p ₅ | 0.01550 ^c | 0.01550 ^c | 0.01550(14) |
| p ₆ | ≤ 21 | ≤ 17 | - |
| p ₇ | 53(5) | 44(5) | 32(9) |
| p ₈ | 0.65 ^c | 0.65 ^c | 0.65(5) |
| p ₉ | 56 ^d | 56(7) | - |
| p ₁₀ | 3.93 ^c | 3.93 ^c | 3.93(10) |
| p ₁₁ | 23(3) | 18(3) | 21(3) |
| p ₁₂ | 26(4) | ≤ 17 | - |
| p ₁₃ | 64 ^d | 64(12) | - |
| p ₁₄ | 0.65 ^c | 0.65 ^c | 0.65(5) |
| p ₁₅ | 136(4) | - ^b | - |
| p ₁₆ | 235 ^d | 235(10) | - |
| p ₁₇ | 133 ^d | 133(16) | 112(20) |
| p ₁₈ | 173(5) | 163(4) | 145(15) |
| p ₁₉ | ≤ 21 | ≤ 23 | - |
| p ₂₀ | ≤ 21 | 23(6) | 30(13) |
| p ₂₁ | 145(8) | 145(6) | 138(16) |
| p ₂₂ | 0.65 ^c | 0.65 ^c | 0.65(5) |
| p ₂₃ | - ^b | 204(30) | 112(20) |
| p ₂₄ | - ^b | 71(12) | - |
| p ₂₅ | - ^b | 19(5) | 30(13) |
| p ₂₆ | - ^b | 173(19) | 138(16) |
| p ₂₇ | 0.65 ^c | 0.65 ^c | 0.65(5) |
| p ₂₈ | - ^b | - ^b | 256(20) |

^aNote that the fit of p₁ suffers from large uncertainties due to the background and the width presented here is the best estimate.

^bNot possible to perform the line shape fit either because of low statistics, the proton line is partly punching through the detector, or it is hidden in background.

^cFixed to the literature value Γ_{tot} as it is known to be less than the detector resolution.

^dThe DSSSD value is adopted.

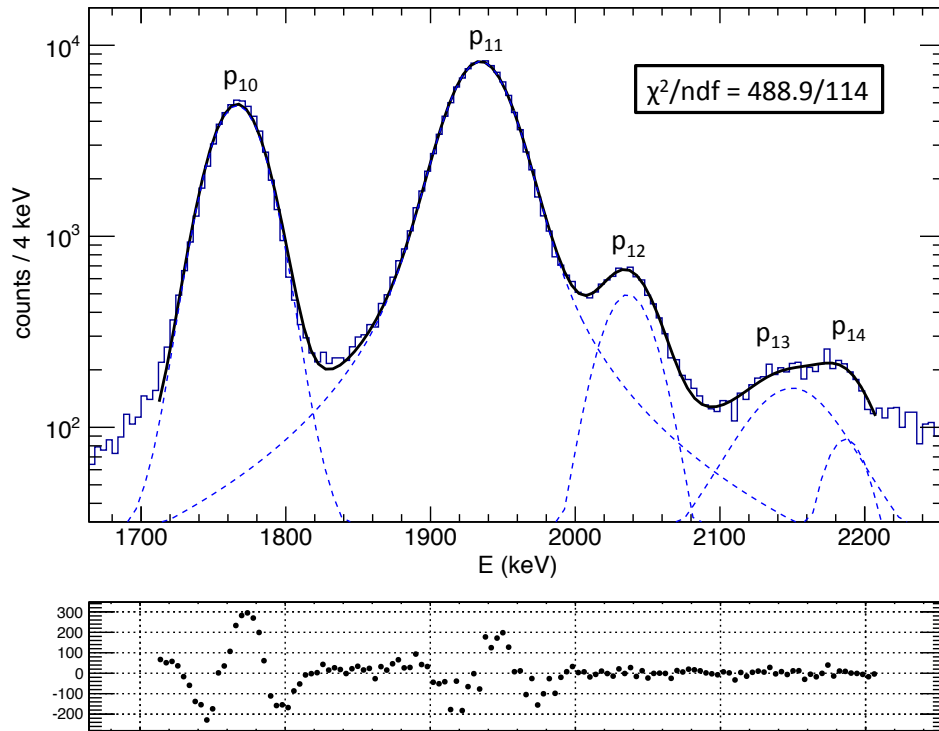


Figure 4.6: The result of a simultaneous fit of p_{10} , p_{11} , p_{12} , p_{13} , and p_{14} as measured in the DSSSD. The solid black line is combined line shape of all five proton branches. The line shape of the individual proton branches is shown with dashed blue. The residuals from the fit are drawn without indicating the uncertainty. Note that only the combined line shape is limited to the fitting interval. Figure from [Lund 2015a].

fitted line shape appears to describe the data well. In a few cases an asymmetric line shape of the proton peak cannot be reproduced with the chosen line shape function and it will therefore also lead to a large value of χ^2/ndf .

With regards to the Breit-Wigner width Γ of the line shape function in Equation (4.7) a few comments are necessary. First, in case the total width of the resonance from which the proton is emitted is known to be smaller than the detector energy resolution, then Γ is fixed to the known value of the total resonance width. Second, in case the total width of the resonance is smaller than the detector energy resolution but the width is unknown, the obtained value of Γ may suffer from a systematic uncertainty. If the total width of the resonance is much smaller than σ we expect the value of Γ to be unreliable. The procedure to quantify the magnitude of this systematic uncertainty would be to compare the determined values of Γ for resonances with

known total widths smaller than σ with the known literature value. However, none of the resonances in ^{21}Na with known total widths have values between 5 and 20 keV. Such a study is, therefore, not possible in this case. To be safe we will assign the upper limit $\Gamma \leq \sigma$ in case the fitted value of Γ is less than σ . Third, when fitting the gas telescope spectra it was in a few cases necessary to fix Γ to the value determined in the DSSSD telescope.

In Table 4.3 a summary of the measured Breit-Wigner resonance widths is presented and it is also specified if the value of the gas telescope, Γ_{Gas} , is fixed to the value of the DSSSD telescope, Γ_{DSSSD} .

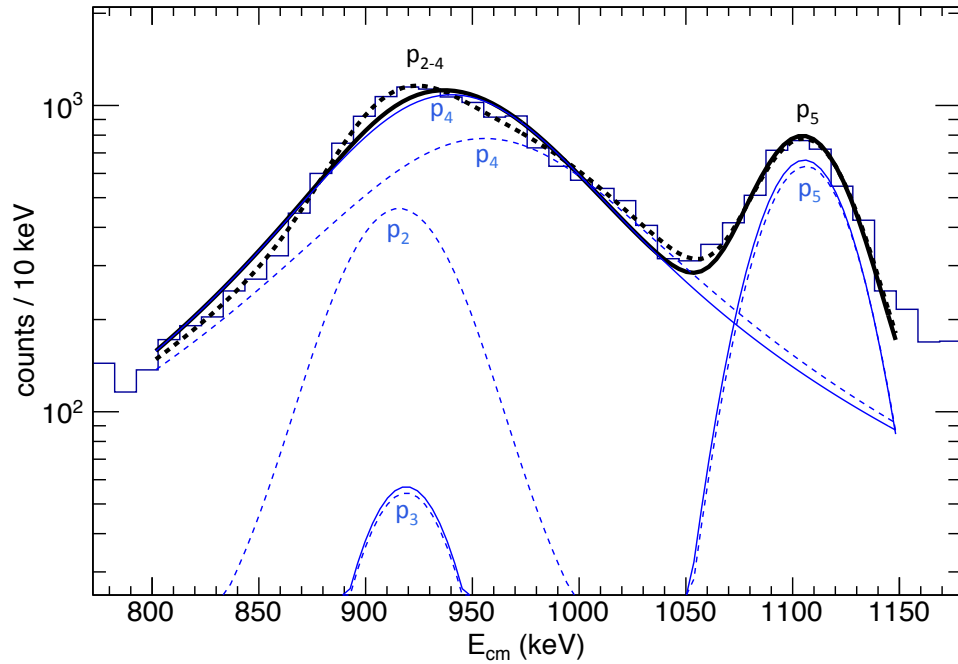


Figure 4.7: Two different line shape fits are shown here. The energy region contains two peaks that overlap and the two line shape fits are based on different assumptions about the proton branches contributing to the low energy peak. The thick full drawn line shape (black) assumes a broad proton branch with an energy dependent width Γ as described in the text ($L = 0$ and $r_0 = 1.4$ fm). This line shape also includes p_5 and the low intensity branch p_3 . The second interpretation of the low energy peak is shown by the thick dashed line shape (black) which assumes two proton branches, both with a constant width Γ , instead of the broad proton branch. The low intensity branch p_3 and the proton branch p_5 is also included. The thin blue curves in solid and dashed shows the individual components of the two line shape fits. Figure from [Lund 2015a].

4.4.3 Energy dependence of Γ

In the energy region between 0.8 and 1.2 MeV we observe two peaks in the proton spectrum. Out of the two peaks, the one at lowest energy has an asymmetric line shape - see Figure 4.7. The asymmetry is such that the number of events is enhanced on the high energy side as compared to the low energy side. To explain the asymmetry several scenarios can be used. First, it could be that the low energy peak contains more than one proton branch. The second scenario is if the peak only contains one proton branch, which is so wide that the penetrability will change significantly when moving across the emitting resonance. Finally, it could also be a quantum interference effect. In the earlier experiment described in [Sextro 1973] the peak is assumed to consist of a single proton branch.

By studying the beta-delayed alpha-particle spectrum we have discovered the presence of a low intensity proton branch p_3 placed in the asymmetric proton peak - for more detail on p_3 see Chapter 5. However, the intensity of p_3 is not sufficient to account for the observed asymmetry. We include p_3 in the two different fits shown on Figure 4.7 with the intensity fixed relative to the intensity of proton branch p_5 .

To continue further with the possibility of having several proton branches in the asymmetric peak we have tried to assume that two branches with high intensity and the additional known low intensity branch p_3 is present in the peak. The fit of such a line shape to the data is shown on Figure 4.7 as the thick dashed black curve. It reproduce the data very well as it gives a $\chi^2/\text{ndf} = 41.0/26 = 1.6$.

The second possible explanation for the asymmetric line shape is that a resonance in ^{21}Na is so wide that the penetrability of an emitted proton through the Coulomb barrier varies significantly across the width of the resonance. It would give rise to an asymmetric line shape like the one observed, i.e. with an enhancement on the high energy side. In order to model such a dependence we make the following change to the parameter Γ :

$$\Gamma \rightarrow \Gamma(E_0) \frac{P(E, L)}{P(E_0, L)} \quad (4.8)$$

where $P(E, L)$ is the penetrability, L is the angular momentum, and E_0 is the centroid energy. The penetrability is calculated on the basis of the algorithm presented in [Michel 2007] and with the nuclear radius parameter set to $r_0 = 1.4$ fm. A line shape based on this second interpretation of the asymmetric peak will include the low intensity p_3 , one additional and broad proton branch in the low energy peak, and the proton branch p_5 . On Figure 4.7 this line shape fit can be seen as the thick solid black curve. The fit results in $\chi^2/\text{ndf} = 147.5/29 = 5.1$. It is a significantly worse fit than the assumption of an additional narrow proton branch.

Besides the proton peak shown on Figure 4.7 another peak is having an asymmetric line shape with an enhancement on the high energy side. This is proton branch

p_{15} and also in this case does an energy dependent width Γ caused by the penetrability not describe the observed line shape well. In Sect. 4.5 we will discuss the other possible explanations for the asymmetric line shapes observed for these two proton peaks.

4.4.4 Relative intensities

The relative proton intensities can be extracted from the line shape fit of the individual proton branches. From the parameter A in Equation (4.7) we directly get the number of events in each proton branch and the relative intensities will then be given as the ratio of A for proton branch p_i with respect to A for p_{11} . As p_{11} is the most intense of the beta-delayed proton branches this is the obvious choice as a reference point. However, to get consistent relative intensities we need to correct for the difference in the solid angle coverage when comparing the individual detectors within a telescope. To reconcile this inconsistency a scaling factor is applied to the relative intensities. For the DSSSD telescope the scaling factor is $\frac{\Omega_{\text{DSSSD}}}{\Omega_{\text{pad}}} = 1.17(8)$ and for the gas telescope it is $\frac{\Omega_{\text{Si front}}}{\Omega_{\text{Si back}}} = 1.97(25)$.

In Table 4.4 the measured relative proton intensities of the identified proton branches are presented and compared with earlier measurements by [Sextro 1973, Thomas 2003]. We have mainly adopted the values from the DSSSD telescope as the use of a highly segmented DSSSD detector reduces the beta-summing probability considerably because it scales with the solid angle. On average the solid angle of each of the 256 pixels on the DSSSD detector is $\Omega = 0.030(1)\%$. Another reason for using the DSSSD intensities is the better energy resolution obtained here. Finally, the data acquisition threshold on the gas detector is cutting part of the high energy proton events which can be seen on Figure 4.1. However, for the proton branches p_1 , p_{15} , and p_{28} we have adopted the gas telescope value as p_1 is not observed in the DSSSD, p_{15} is punching through the central part of the DSSSD but is stopped in the outer parts, and for p_{28} we simply have more reliable data in the gas telescope - see Figure 4.2 and 4.3.

Comparing the measured relative proton intensities with the results of the previous works by [Sextro 1973, Thomas 2003], see Table 4.4, it becomes clear that we disagree with one or both of the previous measurements on several points. However, the overall trend in the present data agrees with the earlier measurement of [Thomas 2003]. It is also clear that the results from our experiment and from [Thomas 2003] systematically disagrees with the results of [Sextro 1973]. For the proton branches p_1 to p_{14} the relative proton intensities from our experiment are systematically lower than [Sextro 1973], while for the proton branches p_{15} to p_{28} the relative intensities are systematically larger than [Sextro 1973].

An investigation of the analysis methods used in the previous experiments makes it clear that the relative intensities we measure are more reliable. First of all, both

Table 4.4: E_{cm} in keV and relative proton intensities with respect to p_{11} compared to earlier results [Sextro 1973, Thomas 2003]. #: p_{13} – p_{14} and p_2 – p_4 were observed as a single proton line in [Sextro 1973, Thomas 2003].

| | E_{cm} (keV) | | Relative intensity (%) | |
|----------|------------------------|-------------|------------------------|---------------|
| | This work | This work | [Sextro 1973] | [Thomas 2003] |
| p_1 | 396(10) | 3.91(45) | - | - |
| p_2 | 906(10) | 2.0(5) | #16.6(6) | #8.3(35) |
| p_3 | 919(21) | 0.28(3) | #16.6(6) | #8.3(35) |
| p_4 | 937(10) | 19.4(5) | #16.6(6) | #8.3(35) |
| p_5 | 1102(10) | 3.34(6) | 4.3(6) | 8.6(23) |
| p_6 | 1316(10) ^a | 20.01(15) | 23.3(17) | 18.1(33) |
| p_7 | 1427(10) | 2.84(11) | - | - |
| p_8 | 1564(10) | 4.66(9) | 6.3(6) | - |
| p_9 | 1630(10) | 2.95(17) | - | - |
| p_{10} | 1861(10) ^{ab} | 44.05(24) | 51.4(21) | 46.1(73) |
| p_{11} | 2037(10) ^{ab} | 100.0(4) | 100.0(15) | 100(15) |
| p_{12} | 2144(10) | 4.58(14) | 8.3(10) | - |
| p_{13} | 2263(11) | 3.79(55) | #4.6(4) | - |
| p_{14} | 2302(10) | 0.73(20) | #4.6(4) | - |
| p_{15} | 2587(10) | 20.89(24) | 7.6(20) | 7.0(21) |
| p_{16} | 3443(10) | 34.6(31) | 5.9(3) | <21.5(35) |
| p_{17} | 3585(11) | 8.0(15) | 4.5(5) | <11.8(22) |
| p_{18} | 4055(10) | 33.58(2.45) | 10.3(4) | 9.3(19) |
| p_{19} | 4257(10) | 1.99(20) | 2.5(2) | 4.4(13) |
| p_{20} | 4356(10) | 1.94(19) | 1.0(2) | - |
| p_{21} | 4769(10) | 10.9(8) | 2.5(5) | - |
| p_{22} | 4913(10) ^b | 24.29(176) | 14.9(7) | 24.7(43) |
| p_{23} | 5171(12) | 5.63(75) | - | - |
| p_{24} | 5868(10) | 1.56(18) | 0.5(6) | - |
| p_{25} | 5983(10) | 1.37(13) | 0.7(6) | - |
| p_{26} | 6388(11) | 2.86(29) | 0.6(9) | - |
| p_{27} | 6537(10) | 8.85(65) | 5.5(4) | 9.7(18) |
| p_{28} | 7200(300) | 0.05(2) | - | - |

^aUsed for energy calibration of the DSSSD, see Sect. 3.3.

^bUsed for energy calibration of the first silicon detector in the gas telescope, see Sect. 3.3.

[Sextro 1973] and [Thomas 2003] use unsegmented detectors which gives rise to a much higher beta-summing probability as the solid angle coverage is higher. Beta-summing can potentially give a systematic uncertainty in the determination of the relative intensities if it is not properly accounted for. Second, the line shape used in our analysis of the proton spectrum is physically more correct than the normalized Gaussian functions used in both [Sextro 1973] and [Thomas 2003]. Third, as a consistency check of our results we have compared the measured relative proton intensities between the two charged particle telescopes and we obtain consistent results. We therefore conclude that the result of [Sextro 1973] is suffering from an unknown systematic error.

4.5 Decay scheme

A detailed interpretation of the beta-decay of ^{21}Mg has been performed based on the resonance properties determined from the line shape fit of the proton peaks. The conclusions of this work is presented in Table 4.6 and on Figure 4.8. The proposed reinterpretation is supported by a previous study of mirror symmetries [Hoffmann 1989].

The interpretation is based on a few simple steps which take advantage of all the knowledge available about the resonances in the daughter nuclei. First, we assume that no new resonances in the particle daughters are observed. Based on this assumption we match the energy of the observed charged particle with the known resonances in ^{21}Na , which can be populated in allowed beta-decay, i.e. $I^\pi = (\frac{3}{2}, \frac{5}{2}, \frac{7}{2})^+$. Second, we investigate for a given resonance in ^{21}Na if the assigned ground state and excited state decay branches have the correct intensity ratio when comparing with the known $\Gamma_{p,el}/\Gamma_{tot}$. Several examples are given in the text below. Third, we compare the measured total widths, Γ from the line shape fit, with the known total width Γ_{tot} from the literature.

Since the last major reinterpretation of the decay scheme of ^{21}Mg in [Sextro 1973], several experiments have been performed in order to characterize the properties of the resonances involved in the decay. Most resonances in ^{21}Na above 6.4 MeV have been studied and characterized in terms of Γ_{tot} , $\Gamma_{p,el}$, and I^π through $^{20}\text{Ne}(p, p)$ scattering experiments as described in [Fernández 1981, Wilkerson 1992] - see Table 4.5. The beta-decay of ^{21}Mg have also been studied in more detail by measuring the most intense γp -coincidences as described in [Thomas 2003]. The knowledge obtained in these three experiments have been used in the interpretation of the decay of ^{21}Mg . Due to the much better knowledge about the resonances in ^{21}Na , together with the knowledge extracted from our data, we have been able to produce a more solid interpretation than what was done by [Sextro 1973].

Based on this procedure we have discarded 5 out of the 25 previously reported

beta-delayed proton branches. We also eliminate the 5979(15) keV resonance in ^{21}Na which has only been suggested in [Sextro 1973]. The 5380(9) keV resonance was also suggested in [Sextro 1973] and it is confirmed in this work. We have identified 27 different beta-delayed proton branches including seven new low intensity proton branches. We have also identified four $\beta\alpha$ decay branches and the very rare $\beta p\alpha$ decay branch. Both of these will be discussed in more detail in Chapter 5.

Asymmetry of p_{2-4} and p_{15} : As discussed in Sect. 4.4.3 the combined line shape of the proton peak p_{2-4} is asymmetric as shown on Figure 4.7. We tried to model the line shape by assuming that it was caused by a single proton branch emitted from a broad resonance. If the resonance is sufficiently broad then the penetrability of the proton will vary across the resonance width and as a consequence the line shape will become asymmetric. However, it turned out that we could not reproduce the observed line shape by this hypothesis. Much better agreement was seen when trying to fit the observed peak with a theoretical line shape consisting of two intense and narrow proton branches.

As mentioned earlier it is also possible that quantum interference effects are responsible for the line shape of p_{2-4} . Interference happens when two close-lying resonances with the same I^π both emits a proton to the same final state. It is possible to have interference between p_{2-4} and p_5 assuming that p_{2-4} consists of the low intensity proton branch p_3 and one other proton branch. However, to fulfill the requirements of interference we need to assign the single proton branch in p_{2-4} and p_5 as proton emission from the 8303(13) keV and the 8464(15) keV resonances respectively. However, this position of the two proton branches in the decay scheme are unlikely as the final state would have to be the 2^- resonance of ^{20}Ne . Also, if the asymmetric line shape of p_{2-4} really is caused by interference with p_5 it would mean that p_5 would be asymmetric on the low-energy side towards p_{2-4} . However, it is unclear if p_5 really is asymmetric or if the line shape is just distorted by a partial overlap with p_{2-4} .

A less problematic interpretation of p_{2-4} is to assume three proton branches in the peak as was already demonstrated on Figure 4.7. With this interpretation we can place p_5 independently of p_{2-4} which gives a much more convincing position as the ground state transition from the narrow 3544.3(4) keV resonance. Another strength of the three component interpretation is that the relatively broad proton branch p_4 solves a problem of missing strength to the 7609(15) keV resonance. The ground and first excited state transitions from this resonance are assigned to p_{23} and p_{17} respectively. If we only assign these two proton branches to the resonance we find that the ratio of the known widths, Γ_{tot} and $\Gamma_{p,\text{gs}}$, does not match the intensities measured for the two proton branches. We have that $\left(\frac{\Gamma_{p,\text{gs}}}{\Gamma_{\text{tot}}}\right)^{\text{exp}} = 0.11(3)$ while the measured intensities from p_{23} and p_{17} gives us $\left(\frac{\Gamma_{p,\text{gs}}}{\Gamma_{\text{tot}}}\right)^{\text{exp}} \approx \left(\frac{I_{p,\text{gs}}}{I_{p,\text{tot}}}\right) = 0.41(7)$. The discrepancy means that

we are missing strength to the higher excited states in ^{20}Ne . However, if we include p_4 as a transition to the second excited state of ^{20}Ne we get a much better agreement: $\left(\frac{\Gamma_{p,gs}}{\Gamma_{\text{tot}}}\right)^{\text{exp}} \approx \left(\frac{I_{p,gs}}{I_{p,\text{tot}}}\right) = 0.17(2)$. Now the only problem remaining is the position of the narrow proton branch p_2 . It cannot be placed convincingly in the decay scheme but is tentatively assigned to the 8303(13) keV resonance.

In Sect. 4.4.3 we also shortly discussed the asymmetric line shape of the proton branch p_{15} . In this case can an energy dependent width also not reproduce the observed line shape. Trying to explain the line shape by adding a second component to the peak is successful in terms of having a nice fit of the data. However, the second proton branch does not fit in the known decay scheme. The same problem was encountered in [Sextro 1973] where they just did not assign the proton branch to any level. This is a clear sign that another explanation should be sought.

Invoking quantum interference as an explanation for the asymmetry of p_{15} is successfully done. The most intense βp decay branch is p_{11} and both p_{11} and p_{15} has the ground state of ^{20}Ne as the final state. As a consequence we can explain the line shape of p_{15} by having interference between these two proton branches only if we assign $I^\pi = \frac{3}{2}^+$ to the 5020(9) keV resonance as it is the parent of p_{15} . This assignment is supported by comparison with the mirror nucleus ^{21}Ne as described in [Hoffmann 1989].

4467.9(7) keV resonance: With a center-of-mass energy of 396(10) keV the new proton branch p_1 is only observed in the gas telescope due to the fact that the beta-particle response extends to higher energies in the DSSSD. Based on the energy of p_1 and the known resonances in ^{20}Ne and ^{21}Na , it can only be placed as a proton emission from the 4467.9(7) keV resonance. As is evident from Figure 4.2 the peak is suffering from a large background. It makes the uncertainty of the parameters in the line shape fit large. Therefore, we estimate the width of p_1 to be $\Gamma_{\text{Gas}} = 65(25)$ keV, which is in part based on the value obtained in the line shape fit.

5380(9) keV resonance: The energy region of the 5380(9) keV resonance has not yet been studied in $^{20}\text{Ne}(p, p)$ scattering experiments. The resonance has only been observed in the beta-decay of ^{21}Mg [Sextro 1973, Thomas 2003]. The proton branch p_6 is placed here by [Sextro 1973] and our data support such an assignment. Based on the center-of-mass energy of p_6 , it can only be placed here or with the 8715(15) keV resonance with $I^\pi = 3/2^+$, $\Gamma_{\text{tot}} = 360(25)$ keV, and $\Gamma_{p,\text{el}} = 160(13)$ keV.

Assuming that p_6 were emitted from the 8715(15) keV resonance there would have to be an intense proton branch to the ground state of ^{20}Ne with $E_{\text{cm}} = 6283$ keV. This is based on the known widths Γ_{tot} and $\Gamma_{p,\text{el}}$. However, no proton peak with this energy and appropriate intensity is observed in the data (it would be 100 keV below p_{26}). Also, as the total width of this resonance is known to be 360(25) keV and as the

measured width of p_6 is below 17 keV, we can rule out the 8715(15) keV resonance as the parent.

The final conclusion about p_6 is confirmed by the observation of this proton branch in coincidence with a 1634 keV gamma-ray in [Thomas 2003].

6165(30) keV resonance: The energy region of the 6165(30) keV resonance has not yet been studied in $^{20}\text{Ne}(p, p)$ scattering experiments. The total and partial widths of this resonance are therefore unknown. We have assigned p_{12} to this resonance on the basis of the measured energy, $E_{\text{cm}} = 2144(10)$ keV. The proton branch could also be assigned to the 8827(15) keV resonance, however, the total width of the resonance, $\Gamma_{\text{tot}} = 138(16)$ keV, does not match with the measured width of the proton branch, $\Gamma_{\text{DSSSD}} \leq 17$ keV.

7609(15) keV resonance: The total width of this resonance is according to Table 4.5 known to be $\Gamma_{\text{tot}} = 112(20)$ keV and the elastic proton scattering width to be $\Gamma_{\text{p,el}} = 12(3)$ keV. As a ground state transition from this resonance we place the new proton branch p_{23} . It is measured to have $E_{\text{cm}} = 5171(12)$ keV and $\Gamma_{\text{DSSSD}} = 204(30)$ keV. Both values are in support of the assignment.

The proton branch p_{17} is measured to have $E_{\text{cm}} = 3585(11)$ keV and $\Gamma_{\text{DSSSD}} = 133(16)$ keV. Both values are consistent with p_{17} being the decay branch from the 7609(15) keV resonance to the first excited state.

As the proton branch to the second excited state of ^{20}Ne we have assigned p_4 , which we have measured to have $E_{\text{cm}} = 937(10)$ keV and $\Gamma_{\text{DSSSD}} = 104(4)$ keV. Both values are consistent with the assignment.

Finally, it is important to check that the intensities measured for the three decay branches agree with the ratio of the known total and partial decay widths. Neglecting the low intensity gamma-ray decay branches we obtain the following approximate result $\left(\frac{\Gamma_{\text{p,gs}}}{\Gamma_{\text{tot}}}\right)^{\text{exp}} \approx \left(\frac{I_{\text{p,gs}}}{I_{\text{p,tot}}}\right) = 0.17(2)$. This value should be compared with the value $\left(\frac{\Gamma_{\text{p,gs}}}{\Gamma_{\text{tot}}}\right)^{\text{exp}} = 0.11(3)$. The two values are consistent, however, the result allows for a low intensity proton branch to the third excited state yet to be found.

In [Sextro 1973] the proton branch p_{17} was assigned to a new resonance at 5979(15) keV. However, as a result of the reinterpretation of p_{17} no evidence now exist for the presence of such a resonance. This conclusion is supported in [Hoffmann 1989] where a careful comparison between the mirror nuclei ^{21}Ne and ^{21}Na is performed.

8135(15) keV resonance: The proton branch p_7 is measured to have an energy of $E_{\text{cm}} = 1427(10)$ keV and the width is measured to be $\Gamma_{\text{DSSSD}} = 44(5)$ keV. Based on the energy it can be assigned to the 8135(15) keV resonance or to the 8827(15) keV resonance, however, the measured width agrees best with first case, $\Gamma_{\text{tot}} = 32(9)$ keV. It is

Table 4.5: A comparison of the measured weighted averages of the ^{21}Na resonances ($\bar{E}_{\text{meas.}}^*$) with the literature energies (E^*) is shown in the first two columns. The column marked I^π is the spin and parity according to the literature, Γ_{tot} is the total width of the resonance according to the literature, and $\Gamma_{\text{p,el}}$ is the elastic proton scattering width of the resonance according to the literature. In the following column is the reference for this information given. Note that if $I^\pi = \left(\frac{3}{2}, \frac{5}{2}, \frac{7}{2}\right)^+$ it is marked by a #. The quoted uncertainties on $\bar{E}_{\text{meas.}}^*$ do not take the systematic uncertainty of around 10 keV (see Sect. 3.3) into account - only the statistical uncertainty from the line shape fit is included.

| $E^*(^{21}\text{Na})$ | $\bar{E}_{\text{meas.}}^*$ (keV) | I^π | Γ_{tot} (keV) | $\Gamma_{\text{p,el}}$ (keV) | Reference |
|---------------------------|----------------------------------|------------------|-----------------------------|------------------------------|------------------|
| 0.0, T= $\frac{1}{2}$ | | 3/2 ⁺ | - | - | |
| 331.90(10) | | 5/2 ⁺ | - | - | |
| 1716.1(3) | | 7/2 ⁺ | - | - | |
| 3544.3(4) | 3533.5(4) | 5/2 ⁺ | 0.01550(14) | - | [Bloch 1969] |
| 4294.3(6) | 4292.3(3) | 5/2 ⁺ | 3.93(10) | - | [Bloch 1969] |
| 4467.9(7) | 4468.4(3) | 3/2 ⁺ | 21(3) | Observed | [der Leun 1964] |
| 5020(9) | 5018.9(14) | # | - | - | |
| 5380(9) | 5381.1(3) | # | - | - | |
| 5770(20) | - | # | ~20 | - | [Firestone 2004] |
| 5884(20) | 5874.8(24) | # | - | - | |
| 5979(15) | - | # | - | - | |
| 6165(30) | 6209.1(5) | # | - | - | |
| 6341(20) | 6328(4) | # | - | - | |
| 6468(20) | 6486.2(10) | 3/2 ⁺ | 145(15) | 130(12) | [Fernández 1981] |
| 7609(15) | 7620(2) | 3/2 ⁺ | 112(20) | 12(3) | [Fernández 1981] |
| 8135(15) | 8106.5(13) | 5/2 ⁺ | 32(9) | 7(3) | [Fernández 1981] |
| 8303(13) | 8312.8(8) | # | - | - | |
| 8397(15) | 8417.5(10) | 3/2 ⁺ | 30(13) | 5(2) | [Fernández 1981] |
| 8464(15) | - | 3/2 ⁺ | 25(9) | 5(1) | [Fernández 1981] |
| 8562(15) | - | 3/2 ⁺ | < 20 | 1.0(5) | [Fernández 1981] |
| 8595(15) | - | 5/2 ⁺ | 138(15) | 25(5) | [Fernández 1981] |
| 8715(15) | - | 3/2 ⁺ | 360(25) | 160(13) | [Fernández 1981] |
| 8827(15) | 8833(2) | 5/2 ⁺ | 138(16) | 38(5) | [Fernández 1981] |
| 8975(4), T= $\frac{3}{2}$ | 8971.1(2) | 5/2 ⁺ | 0.65(5) | 0.117(10) | [Wilkerson 1992] |
| 8981(15) | - | 5/2 ⁺ | 23(16) | 2.5(1.0) | [Fernández 1981] |
| 9155(15) | - | 3/2 ⁺ | 34(13) | 8(2) | [Fernández 1981] |
| 9280(30) | - | # | - | - | |
| 9725(25) | 9632(300) | 3/2 ⁺ | 256(20) | 136(15) | [Fernández 1981] |

problematic that the ground state and first excited state transitions are not observed but hints of the ground state transition is observed below p_{24} . However, other explanations are possible and better data with proton-gamma-ray coincidences is needed.

8303(13) keV resonance: The 8303(13) keV resonance is only observed in the $^{23}\text{Na}(p, t)$ experiment described in [Butler 1968] and in the beta-decay studies of ^{21}Mg described in [Sextro 1973, Thomas 2003]. Based on the beta-decay experiments the resonance has been assigned $I^\pi = \left(\frac{3}{2}, \frac{5}{2}, \frac{7}{2}\right)^+$. The $^{20}\text{Ne}(p, p)$ scattering experiment described in [Fernández 1981] covers the excitation energy region of the resonance, however, no evidence for it is observed. The absence from the scattering data could mean it does not exist. However, the proton branch p_{19} is known from proton-gamma-ray coincidences in the beta-decay study of ^{21}Mg by [Thomas 2003] to belong with the 8303(13) keV resonance. The measured width of p_{19} is determined to be $\Gamma_{\text{DSSSD}} \leq 23$ keV. It constrains the width of the resonance.

Based on the center-of-mass energy of the proton branches p_2 , p_9 , and p_{24} we can assign them to the 8303(13) keV resonance. However, when comparing the measured widths of the four proton branches ($\Gamma_{\text{DSSSD}, p_2} \leq 17$ keV, $\Gamma_{\text{DSSSD}, p_9} = 56(7)$ keV, $\Gamma_{\text{DSSSD}, p_{19}} \leq 23$ keV, $\Gamma_{\text{DSSSD}, p_{24}} = 71(12)$ keV), it becomes clear that an assignment of p_2 , p_9 , and p_{24} to this resonance can only be tentative. New data with gamma-ray detection and an improved energy resolution are needed to make a conclusive assignment.

8397(15) keV resonance: As transitions to the first excited state and the ground state we place p_{20} and p_{25} . The measured widths, $\Gamma_{\text{DSSSD}, p_{20}} = 23(6)$ keV and $\Gamma_{\text{DSSSD}, p_{25}} = 19(5)$ keV, both has a smaller uncertainty than the literature value of $\Gamma_{\text{tot}} = 30(13)$ keV and both is smaller than the literature value. We can conclude that the total width of the 8397(15) keV resonance is smaller than the literature value.

8827(15) keV resonance: Based on the measured center-of-mass energy and the measured widths, we assign p_{21} and p_{26} as transitions to the first excited state and the ground state from the 8827(15) keV resonance in ^{21}Na . The total width and the elastic proton scattering width is both known and the ratio of these two gives $\left(\frac{\Gamma_{p,gs}}{\Gamma_{\text{tot}}}\right)^{\text{ref}} = 0.28(5)$. This number is to be compared with the corresponding measured quantity $\left(\frac{\Gamma_{p,gs}}{\Gamma_{\text{tot}}}\right)^{\text{exp}} \approx \left(\frac{I_{p,gs}}{I_{p,\text{tot}}}\right) = 0.21(2)$, where the known alpha-particle decay branch α_2 (see Chapter 5) and possible gamma-ray emission has been neglected due to their low intensity. The measured intensities agree with the known total and partial widths within one standard deviation. We can conclude that the assignment of p_{21} and p_{26} to this resonance is consistent.

Table 4.6: The first two columns show the measured weighted averages of the ^{21}Na resonances ($\bar{E}_{\text{meas.}}^*$) and the literature energies (E^*). The right part of the table shows the new interpretation of the decay scheme. If the proton line is in italic, p_i , the assignment is not conclusive. An x marks an unobserved but energetically allowed proton emission. The particle emission thresholds are $S_p(^{21}\text{Na})= 2431.68(28)$ keV and $S_\alpha(^{21}\text{Na})= 6561.3(4)$ keV, [Wang 2012]. The quoted uncertainties on $\bar{E}_{\text{meas.}}^*$ do not take the systematic uncertainty of around 10 keV (see Sect. 3.3) into account - only the statistical uncertainty from the line shape fit is included.

| $E^*(^{21}\text{Na})$ | $\bar{E}_{\text{meas.}}^*$ (keV) | ^{20}Ne resonances (MeV, I^π) | | | | |
|---------------------------|----------------------------------|---|-----------------|-----------------|----------------|----------------|
| | | 0.0, 0^+ | 1.63, 2^+ | 4.25, 4^+ | 4.97, 2^- | 5.62, 3^- |
| 0.0, $T= \frac{1}{2}$ | | | | | | |
| 331.90(10) | | | | | | |
| 1716.1(3) | | | | | | |
| 3544.3(4) | 3533.5(4) | p ₅ | | | | |
| 4294.3(6) | 4292.3(3) | p ₁₀ | x | | | |
| 4467.9(7) | 4468.4(3) | p ₁₁ | p ₁ | | | |
| 5020(9) | 5018.9(14) | p ₁₅ | x | | | |
| 5380(9) | 5381.1(3) | x | p ₆ | | | |
| 5770(20) | - | x | x | | | |
| 5884(20) | 5874.8(24) | p ₁₆ | x | | | |
| 5979(15) | - | x | x | | | |
| 6165(30) | 6209.1(5) | x | p ₁₂ | | | |
| 6341(20) | 6328(4) | x | p ₁₃ | | | |
| 6468(20) | 6486.2(10) | p ₁₈ | x | | | |
| 7609(15) | 7620(2) | p ₂₃ | p ₁₇ | p ₄ | x | |
| 8135(15) | 8106.5(13) | x | x | p ₇ | x | x |
| 8303(13) | 8312.8(8) | p ₂₄ | p ₁₉ | p ₉ | p ₂ | x |
| 8397(15) | 8417.5(10) | p ₂₅ | p ₂₀ | x | x | x |
| 8464(15) | - | x | x | x | x | x |
| 8562(15) | - | x | x | x | x | x |
| 8595(15) | - | x | x | x | x | x |
| 8715(15) | - | x | x | x | x | x |
| 8827(15) | 8833(2) | p ₂₆ | p ₂₁ | x | x | x |
| 8975(4), $T= \frac{3}{2}$ | 8971.1(2) | p ₂₇ | p ₂₂ | p ₁₄ | p ₈ | p ₃ |
| 8981(15) | - | x | x | x | x | x |
| 9155(15) | - | x | x | x | x | x |
| 9280(30) | - | x | x | x | x | x |
| 9725(25) | 9632(300) | p ₂₈ | x | x | x | x |

A further check of the assigned strength to the IAS can be made by checking that the sum rule is obeyed: $\sum B_F = Z - N$ (see Sect. 1.1.3). We have measured $\log(ft) = 3.45(17)$ for the IAS, which translates into $B_F = 2.18^{+1.04}_{-0.71}$. Within one standard deviation the total assigned strength agrees with the sum rule. Hence, the assignments are also supported by the sum rule.

Finally, it should be noted that the proton branch p_{22} has been measured in coincidence with a gamma-ray in [Thomas 2003]. This measurement confirms the assignment of p_{22} as the proton branch from the IAS to the first excited state of ^{20}Ne .

9725(25) keV resonance: The last proton branch to assign to a resonance is p_{28} , however, this is not straightforward as the energy calibration of the second silicon detector in the gas telescope suffers from large uncertainties - see Sect. 3.3. The center-of-mass energy for p_{28} is measured to be 7.2(3) MeV. As the energy suggest it must be emitted from a resonance above the IAS. This is also confirmed by the fact that the proton branch p_{27} is the ground state transition from the IAS. Based on the $^{20}\text{Ne}(p, p)$ scattering experiment described in [Fernández 1981] three resonances are open for feeding in allowed beta-decay of ^{21}Mg . The possible candidates are the 8981(15) keV, the 9155(15) keV, and the 9725(25) keV resonances. Based on the energy of p_{28} we favor the 9725(25) keV resonance as the parent. Another argument in favor of this resonance, is the fact that it is also the parent of the alpha-particle branch α_5 and most likely also α_4 - see chapter 5. However, even though the 9725(25) keV resonance emits alpha-particles a calculation of the reduced widths, γ_c^2/γ_{sp}^2 , shows no signs of alpha-particle clustering.

In the energy region between p_{22} and p_{24} in the proton spectrum of the DSSSD telescope on Figure 4.3 we observe a structure similar to the one seen above p_{27} in the energy region of p_{28} . A more careful investigation of this energy region reveals hints of a weak and broad proton peak with a center-of-mass energy of 5600-5750 keV. An estimation of the intensity of this possible proton branch together with the rough center-of-mass energy allows for an assignment as the proton emission from the 9725(25) keV resonance to the first excited state of ^{20}Ne . As the 9725(25) keV resonance is broad, $\Gamma_{\text{tot}} = 256(20)$ keV, the energy dependence of the beta-decay phase space factor may be responsible for the structure above p_{27} and also for the structure between p_{22} and p_{24} . This interpretation cannot finally be confirmed with the present data. An alternative interpretation of the broad peak at 5600-5750 keV is as the ground state transition from the 8135(15) keV resonance which is the resonance where p_7 has been tentatively assigned as the only proton branch.

The final interpretation of the beta-decay of ^{21}Mg is presented on Figure 4.8 and in Table 4.6. The decay scheme is to a large extent constructed by comparing the ear-

lier measurements of the total and partial widths as presented in Table 4.5 with the measured total widths, energies, and relative intensities which are presented in Table 4.3 and in Table 4.4. In order to resolve the ambiguities described here a dedicated measurement of the beta-decay with both gamma-ray and charged particle detection is needed, as an observation of charged particles and gamma-rays in coincidence will give valuable information on the populated final states. Such information is already available for the most intense beta-delayed proton transitions [Thomas 2003] and we have also used this information when possible. However, to observe coincidences with gamma-rays for the less intense transitions much more statistics is required.

4.6 Beta-decay strength distribution

With the knowledge of the reconstructed decay scheme it is possible to determine the absolute branching ratios and the beta-decay $\log(ft)$ -values. As we did not measure the total number of ^{21}Mg implanted in the collection foil and we did not measure the gamma-ray emission, we must seek a different way to perform an absolute normalization of the measured relative intensities. In Sect. 4.4.4 we realized that the results of [Sextro 1973] suffers from a systematic error. Hence, we can not convincingly use these results for the normalization. We turn to the work of [Thomas 2003] to find a proper and accurate normalization factor. The normalization factor is constructed from the ratio of the absolute and relative intensities for proton branch p_{22} and p_{27} after discussion with the authors of [Thomas 2003] about which proton branches are most reliably known. The weighted average of this ratio from the two proton branches is $R = 0.057(9)$. This normalization factor can now be used to convert the relative intensities with respect to p_{11} into absolute intensities. The proton branch p_{11} is also used as the reference point of the relative intensities in [Thomas 2003].

As both the proton and alpha-particle relative intensities are determined with respect to p_{11} , the normalization factor R can be applied to both set of relative intensities to get the absolute intensities (see Table 5.2 in chapter 5 for more detail on the alpha-particle intensities). Then it is straightforward to determine the beta-decay branching ratios as the gamma-decay widths are of the order 10^2 to 10^3 times smaller than the charged particle decay widths (see [Bloch 1969]) which means that the gamma-decays can be safely neglected in this calculation. The resulting beta-decay branching ratios can be seen in Table 4.7.

The $\log(ft)$ -values are calculated according to the parametrization of the phase space factor for allowed beta-decay in [Wilkinson 1974] and with $Q_{\beta^+} = 12.076(16)$ MeV. The resulting values can be found in Table 4.8. The uncertainty quoted for the $\log(ft)$ -values only takes into account the uncertainty of the absolute beta-decay branching ratios presented in Table 4.7. The relative uncertainty on the absolute beta-

Table 4.7: Absolute β branching ratios compared to earlier results by [Sextro 1973, Thomas 2003].

| $E^*(^{21}\text{Na})$ (keV) | B.R. from ^{21}Mg (%) | | |
|-----------------------------|--------------------------------|---------------|---------------|
| | This work | [Sextro 1973] | [Thomas 2003] |
| 3544.3(4) | 0.19(3) | 0.45(7) | 0.7(2) |
| 4294.3(6) | 2.5(4) | 5.36(31) | 3.7(6) |
| 4467.9(7) | 5.89(96) | 10.45(46) | 8.00(13) |
| 5020(9) | 1.18(19) | 2.53(25) | 1.2(3) |
| 5380(9) | 1.13(18) | 2.43(21) | 1.5(3) |
| 5770(20) | 0.0 | 0.34(3) | 0.0 |
| 5884(20) | 1.96(36) | 0.62(4) | <1.7(3) |
| 5979(15) | 0.0 | 0.47(6) | <0.9(2) |
| 6094(35) | 0.0 | 0.14(1) | 0.0 |
| 6165(30) | 0.26(4) | 0.0 | 0.0 |
| 6210(50) | 0.0 | 0.14(2) | 0.0 |
| 6341(20) | 0.21(5) | 0.86(7) | 0.0 |
| 6468(20) | 1.90(34) | 1.07(6) | 0.8(2) |
| 7609(15) | 1.88(36) | 0.0 | 0.0 |
| 8135(15) | 0.16(3) | 0.0 | 0.0 |
| 8303(13) | 0.5(1) | 0.31(3) | 0.4(1) |
| 8397(15) | 0.19(4) | 0.0 | 0.0 |
| 8464(15) | 0.0 | 0.18(2) | 0.0 |
| 8827(15) | 0.79(14) | 1.19(13) | 0.0 |
| 8975(4) | 2.3(4) | 2.79(16) | 2.8(4) |
| 9725(25) | 0.010(2) | 0.0 | 0.0 |

decay branching ratios are an order of magnitude larger than the relative uncertainty on the half-life and the excitation energy in ^{21}Na . We can therefore safely neglect the uncertainty from the half-life and the excitation energy.

The $\log(ft)$ -values measured for the 5884(20) keV and the 8303(13) keV resonances are so low that the beta-decay to these resonances has to be allowed. As a consequence we can conclude that $I^\pi = (\frac{3}{2}, \frac{5}{2}, \frac{7}{2})^+$ for both resonances. This assignment is supported by the mirror level in ^{21}Ne for the 5884(20) keV resonance - see [Hoffmann 1989]. No mirror level is identified for the 8303(13) keV resonance.

It is desirable to compare the beta-decay strength distribution of ^{21}Mg with the mirror beta-decay of ^{21}F as described in Chapter 1. Such a comparison can be done through the mirror asymmetry parameter

$$\delta = \frac{\log(ft)^+}{\log(ft)^-} - 1, \quad (4.9)$$

where $\log(ft)^\pm$ is the values from the ^{21}Mg and ^{21}F beta-decays, respectively. The mirror state of the 3.54 MeV resonance in ^{21}Na is the 3.74 MeV resonance in ^{21}Ne in which case $\delta = -0.09(8)$. The mirror state of the 4.29 MeV resonance in ^{21}Na is the 4.53 MeV resonance in ^{21}Ne in which case $\delta = 0.02(3)$. Finally, the mirror state of the 4.47 MeV resonance is the 4.68 MeV resonance in ^{21}Ne in which case $\delta = 0.05(4)$. The $\log(ft)$ -values from the β -decay of ^{21}F have in all three cases been adopted from [Thomas 2003]. In all three cases is the value of δ consistent with zero.

4.7 Summary and conclusions

The study of the beta-decay of ^{21}Mg presented in this chapter have given several results worth mentioning. A summary of the main results are gathered in the following list:

- Seven new beta-delayed proton branches were observed. A total of 27 beta-delayed proton branches were measured with energies ranging between 0.39 MeV and 7.2 MeV.
- An improved interpretation of the ^{21}Mg beta-decay is proposed, which is based on the extracted spectroscopic information from the delayed protons. The proposed decay scheme is consistent with the results of various reaction studies.
- The line shape of p_{15} is interpreted as being due to interference with the high-intensity proton branch p_{11} . As a consequence we assign $I^\pi = \frac{3}{2}^+$ to the 5020(9) keV resonance in ^{21}Na in agreement with a study of the mirror nucleus ^{21}Ne in [Hoffmann 1989].

Table 4.8: $\log(ft)$ -values compared to earlier results by [Sextro 1973, Thomas 2003].

| $E^*(^{21}\text{Na})$ (keV) | $\log(ft)$ | | |
|-----------------------------|------------|---------------|---------------|
| | This work | [Sextro 1973] | [Thomas 2003] |
| 3544.3(4) | 6.45(16) | 6.09(6) | 5.90(17) |
| 4294.3(6) | 5.14(16) | 4.82(2) | 4.99(8) |
| 4467.9(7) | 4.73(16) | 4.48(2) | 4.61(8) |
| 5020(9) | 5.27(16) | 4.95(4) | 5.26(16) |
| 5380(9) | 5.18(16) | 4.85(3) | 5.08(10) |
| 5770(20) | - | 5.59(3) | - |
| 5884(20) | 4.90(18) | 5.30(3) | >4.87(10) |
| 5979(15) | - | 5.38(5) | >5.07(10) |
| 6094(35) | - | 5.86(3) | - |
| 6165(30) | 5.68(15) | - | - |
| 6210(50) | - | 5.84(6) | - |
| 6341(20) | 5.71(24) | 4.99(3) | - |
| 6468(20) | 4.71(18) | 4.84(2) | 5.00(11) |
| 7609(15) | 4.26(19) | - | - |
| 8135(15) | 5.08(19) | - | - |
| 8303(13) | 4.5(2) | 4.60(3) | 4.56(20) |
| 8397(15) | 4.87(21) | - | - |
| 8464(15) | - | 4.77(5) | - |
| 8827(15) | 4.01(18) | 3.73(4) | - |
| 8975(4) | 3.45(17) | 3.26 | 3.27(8) |
| 9725(25) | 5.3(2) | - | - |

- The 5979(15) keV resonance proposed by [Sextro 1973] is no longer needed, as the proton branch p_{17} now is assigned as having the first excited state in ^{20}Ne as final state. This new assignment is supported by the study of the mirror nucleus ^{21}Ne presented in [Hoffmann 1989].
- For the first time has the total width Γ_{tot} of the 5020(9) keV, 5380(9) keV, 5884(20) keV, 6165(30) keV, 6341(20) keV, 8135(15) keV, and the 8303(13) keV resonances been measured. The values can be found by looking in Table 4.3 and 4.6.
- We constrain the total width Γ_{tot} of the 6468(20) keV resonance to be close to the upper uncertainty limit of the literature value $\Gamma_{\text{tot}} = 145(15)$ keV.
- We constrain the total width Γ_{tot} of the 8397(15) keV resonance to be close to the lower uncertainty limit of the literature value $\Gamma_{\text{tot}} = 30(13)$ keV.
- The half-life of ^{21}Mg is determined to be $T_{1/2} = 118.6(5)$ ms, which is a factor of four improvement on the uncertainty.

The modified interpretation of the decay scheme resulting from the study of the beta-decay of ^{21}Mg , calls for a dedicated measurement of the beta-decay with both charged particle and gamma-ray detectors to verify the results. In particular coincidences between beta-delayed charged particles and gamma-rays could prove valuable in the reconstruction of the decay scheme. We will discuss this further in Sect. 9.1.2.

^{21}Mg : new exotic decay modes

As discussed in Sect. 2.2 a few different and previously unobserved decay channels are energetically open in the beta-decay of ^{21}Mg due to the large Q -value available and the position of the IAS in ^{21}Na . We have already mentioned in Sect. 4.1 that we observe new decay channels for the first time from ^{21}Mg . In this chapter we will go through both the $\beta\alpha$ decay mode and the rare $\beta p\alpha$ decay mode in much more detail than has previously been done. In Sect. 5.2 we will present a study of the systematics of beta-delayed particle emission, and show that the cases observed from ^{21}Mg fits naturally into the developed picture. The results presented are to a large extent based on the work published in [Lund 2015b].

5.1 $\beta\alpha$ - and $\beta p\alpha$ -emission from ^{21}Mg

In this section we will discuss the first observation of beta-delayed alpha-particle emission and beta-delayed proton-alpha emission from ^{21}Mg . First, we will give a short overview of the data. Second, we will use the time distribution goodness-of-fit tests developed in Sect. 4.3 to establish the observed alpha-particle peaks as part of the ^{21}Mg beta-decay. Finally, we will place the decay branches in the decay scheme.

5.1.1 Overview of the data

In Sect. 4.1 we presented the ΔE - E spectrum measured in the gas telescope, see Figure 4.1. On top of the data we have drawn the rescaled SRIM [Ziegler 2008] stopping power curves for protons and alpha-particles in silicon. They are rescaled in such a way that they represent the combined energy loss in the collection foil, the gas detector, and the silicon detector dead layer. As is evident from Figure 4.1 the stopping power curve for alpha-particles clearly identifies a region of the ΔE - E spectrum which is well separated from the beta-delayed protons. This suggests the presence of beta-delayed alpha-particle decays from ^{21}Mg in addition to the well known beta-delayed proton emission as described in Chapter 4. The alpha-particles are clearly separated from the beta-particles and the protons above a silicon detector energy of approximately 700 keV. Below this energy a clear identification can be difficult due to the presence of several other components.

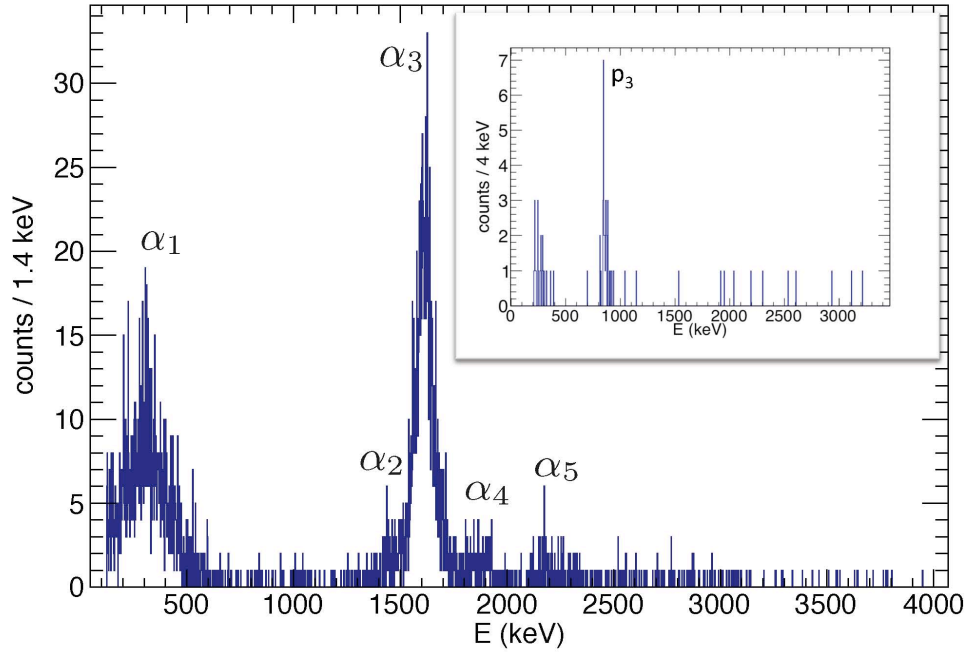


Figure 5.1: Alpha-particle spectrum as measured in the first silicon detector of the gas telescope. The inset in the top right corner shows the DSSSD proton spectrum in coincidence with the alpha-particle branch α_1 . Figure from [Lund 2015b].

The alpha-particles are only observed in the gas telescope as they are stopped in the $60\ \mu\text{m}$ thick DSSSD together with the protons. As a consequence, it is not possible to separate the low-intensity alpha-particle decay branches from the high-intensity proton decay branches in the DSSSD telescope. In order to produce an alpha-particle spectrum we apply the graphical gate drawn on Figure 4.1 with the long-dashed black line. The resulting spectrum as observed in the silicon detector is shown on Figure 5.1. As already discussed, we have a background component present at energies below $700\ \text{keV}$. However, we can clearly identify five alpha-particle branches in the spectrum with the α_2 , α_3 , α_4 , and α_5 decay branches fitting naturally into the known decay scheme of ^{21}Mg as shown on Figure 5.2. As already discussed in Sect. 2.2, the alpha-particle separation energy for ^{21}Na is $S_\alpha = 6561.3(4)\ \text{keV}$ and the ^{21}Mg Q -value is $Q_{EC} = 13.098(16)\ \text{MeV}$ [Wang 2012], which means that beta-delayed alpha-particle emission is energetically allowed.

The peak marked as α_1 on Figure 5.1 has a measured laboratory energy of $714(12)\ \text{keV}$. It does not fit in the decay scheme as an alpha-particle transition between any known resonances in ^{21}Na and ^{17}F . However, it does agree with a known alpha-particle decay

branch from the 3^- resonance at 5.621 MeV in ^{20}Ne to the ground state of ^{16}O , which is measured to have a laboratory energy of 714(4) keV in the beta-decay of ^{20}Na . For more detail on the ^{20}Na beta-decay see [Laursen 2013].

As the events in the peak α_1 is suffering from background contamination, a conclusive particle identification is not possible from the ΔE - E spectrum. However, in coincidence with α_1 we observe a low-intensity proton peak, p_3 , in the DSSSD detector, which is placed opposite to the gas telescope. The coincidence spectrum with p_3 is shown as the inset on Figure 5.1. When gating on the more intense alpha-particle peak α_3 we do not observe a structure similar to p_3 , which tells us that p_3 is no random coincidence. We measure the center-of-mass energy of p_3 to be 919(18) keV, which fits naturally with a proton transition from the $5/2^+$ IAS at 8.975 MeV in ^{21}Na to the 5.621 MeV 3^- resonance in ^{20}Ne , which is the resonance believed to emit α_1 . Hence, we have strong evidence for the first observation of the very rare $\beta p\alpha$ decay mode in the beta-decay of ^{21}Mg . However, before we can make any firm conclusions we need to test if the time distribution of the events are consistent with the known time distribution of the beta-delayed proton emission from ^{21}Mg . We will do this in Sect. 5.1.2.

It should be noted that alpha-particle emission from excited states in ^{21}Na have only been observed in one earlier experiment described in [Gruhle 1977].

5.1.2 Time distribution analysis

As mentioned in Sect. 1.4 the data are contaminated with ^{21}Na due to the closeness in mass with ^{21}Mg . However, other small contaminants could be present as well. A comparison of the time distributions of the five observed low intensity alpha-particle peaks with the time distribution of the known beta-delayed protons will make for a valuable cross-check of the assignments. To compare the time distributions we use the methods developed and described in detail in Sect. 4.3. As the time distributions are influenced by several factors (see Sect. 1.4) we will use the measured time distribution of the beta-delayed protons with energy above 1150 keV as the reference time distribution. We used the same reference time distribution in Sect. 4.3. It is important to remember that the half-lives of ^{21}Na and ^{21}Mg , 22.49(4) s and 122(2) ms [Audi 2012], differs significantly. If other contaminants are present we also expect them to differ in half-life from ^{21}Mg .

The results of the goodness-of-fit tests can be seen in Table 5.1. A 95% confidence level is quoted in the table. Other confidence levels can be found in Table 4.1. From the results it is clear that the decay branches α_2 , α_3 , α_4 , and α_5 all agree with the reference time distribution of ^{21}Mg . Hence, we can safely conclude that α_2 , α_3 , α_4 , and α_5 belongs to the beta-decay of ^{21}Mg .

The result of the goodness-of-fit test for α_1 does, however, not agree with the refer-

Table 5.1: EDF goodness-of-fit test results of the time distribution of the individual observed alpha-particle peaks and of the proton branch p_3 . The first column specifies which test is used, the second column gives the 95% confidence level (obtained through Monte Carlo simulations) for having the ^{21}Mg time distribution. For other confidence levels see Table 4.1.

| | 95% c.l. | p_3 | α_1 | α_2, α_3 | α_4 | α_5 |
|-------|----------|-------|------------|----------------------|------------|------------|
| D | 1.31 | 1.22 | 1.64 | 0.64 | 1.08 | 0.81 |
| W^2 | 0.46 | 0.33 | 0.41 | 0.05 | 0.33 | 0.12 |
| A^2 | 2.49 | 1.46 | 3.61 | 0.64 | 1.73 | 0.80 |

ence time distribution. As we expect the peak to be contaminated with beta-particles from both ^{21}Na and ^{21}Mg , we expect the time distribution to be that of ^{21}Mg with a small component of ^{21}Na . The goodness-of-fit tests applied are sufficiently sensitive to observe the small component of ^{21}Na . However, performing the goodness-of-fit test only for the upper part (in terms of the gas detector channel) of the α_1 time distribution, we observe a lower contamination level as expected. The goodness-of-fit test of the time distribution for the coincident proton branch p_3 are consistent with being part of the ^{21}Mg decay. This implies that we can safely assign the observed $\beta p \alpha$ transition to the decay of ^{21}Mg .

5.1.3 Decay scheme

As discussed α_2 , α_3 , α_4 , and α_5 fits naturally in the decay scheme of ^{21}Mg and has been proven to belong here by a goodness-of-fit test of the time distributions. We have also presented evidence for α_1 and p_3 to be emitted in coincidence as a $\beta p \alpha$ decay. The resulting decay scheme can be seen on Figure 5.2.

The measured relative intensities with respect to p_{11} and the corresponding absolute intensities can be seen in Table 5.2. The determination of the absolute intensities are made according to the described procedure for the beta-delayed proton decays in Sect. 4.6.

5.2 Systematics of beta-delayed particle emission

As discussed in the previous section we observe for the first time the $\beta p \alpha$ decay mode from ^{21}Mg . This is a very rare decay mode as discussed in [Blank 2008] and it is only observed in two other cases: ^9C and ^{17}Ne . ^{13}O is known to decay by $\beta p \alpha$ emission but it has not been observed yet. In this section we will discuss the other $\beta p \alpha$ cases and we will discuss the systematics of beta-delayed charged particle emission.

Table 5.2: E_{cm} in keV, relative intensities with respect to the proton branch p_{11} , and absolute intensities.

| | E_{cm} (keV) | Relative intensity (%) | Absolute intensity (%) |
|------------|-----------------------|------------------------|------------------------|
| α_1 | 882(18) | 0.28(3) | 0.016(3) |
| α_2 | 2201(27) | 0.11(1) | 0.0064(13) |
| α_3 | 2397(10) | 1.79(5) | 0.10(2) |
| α_4 | 2700(43) | 0.10(1) | 0.0054(11) |
| α_5 | 3060(81) | 0.04(1) | 0.0024(8) |

5.2.1 Other cases

As mentioned previously only two nuclei are known to decay by the $\beta p \alpha$ decay mode: ^9C and ^{17}Ne . In the case of ^9C we are dealing with a special case as all states populated in the beta-daughter ^9B will break-up into two alpha-particles and a proton, [Gete 2000]. In principle this could be interpreted as a 100% branching ratio for beta-delayed proton-alpha and alpha-proton emission to ^4He . However, as all the $A = 8$ nuclei are unstable it makes the decay of the $A = 9$ nuclei special in many respects. See [Blank 2008, Pfützner 2012] for more details on the decay of the $A = 9$ nuclei.

The proton rich nucleus ^{13}O must have beta-delayed proton-alpha decay branches even though it has not been observed so far. ^{13}O is known to decay to the IAS of the beta-daughter ^{13}N as is reported in [Knudsen 2005]. From reaction experiments [Ajzenberg-Selove 1991] it is known that approximately half of the ^{13}N IAS decays go via proton emission to alpha-particle unbound resonances in ^{12}C or by alpha-particle emission to proton unbound resonances in ^9B . In both cases will the final state be a proton and three alpha-particles which makes it challenging to detect the decay mode. Based on the present knowledge of decay of the IAS in ^{13}N , the total branching ratio for the $\beta p \alpha$ and $\beta \alpha p$ decay mode can be estimated to be $0.9(3) \cdot 10^{-2} \%$.

In the second observed case of ^{17}Ne both the $\beta p \alpha$ and the $\beta \alpha p$ decay ordering have been seen according to [Chow 2002]. The total branching ratio for the decay mode have been measured to be $1.6(4) \cdot 10^{-2} \%$ with all the observed decays passing via the IAS in ^{17}F and with the final nucleus being ^{12}C .

With the new observation of beta-delayed proton-alpha emission from ^{21}Mg with the final nucleus being ^{16}O it is now clear that in all cases the decay go through an intermediate alpha-conjugate nucleus, namely ^8Be , ^{12}C , ^{16}O , and ^{20}Ne respectively. In the final section we will take a broader look on the systematics of beta-delayed particle emission in $Z > N$ nuclei and present the relevant structure conclusions to be

systematics of the Q_{EC} -values for $Z > N$ nuclei as shown on Figure 5.4. Many effects will contribute to the masses in this region of the nuclear chart so no simple estimate is expected to reproduce the masses. However, a liquid drop estimate for the odd A nuclei with $T_3 = -1/2$ (dashed line) with only the Coulomb term included and an estimate for the odd A nuclei with $T_3 = -3/2$ (dotted line) where the asymmetry term also contributes reproduces the overall trend of the Q_{EC} -values well.

From the experimental data on Figure 5.4 it is evident that the Q_{EC} -values are approximately the same for each of the so-called quartets. These quartets consists of four nuclei as illustrated in the left part of Figure 5.5 and they have proton and neutron numbers (Z, N) , $(Z, N - 1)$, $(Z - 1, N)$, and $(Z - 1, N - 1)$ where both Z and N are even numbers. The similarity of the Q_{EC} -values within the quartet holds very well when the even-even nucleus has $T = 1$. For the $T = 2$ even-even nucleus the similarity is less pronounced but it seems to hold at least for $A < 40$.

The similar Q_{EC} -values can be explained with odd-even effects. In each quartet the two nuclei with odd A are at the same distance to the beta-stability line resulting in similar Q_{EC} -values. This is also evident from the liquid drop estimates. If we do not include the pairing term in the liquid drop estimates the Q_{EC} -value for the even-even nuclei would be larger and the odd-odd nuclei smaller. However, the odd-even effects works against this trend and in many cases does the odd-odd nuclei have a larger Q_{EC} -value than the even-even nuclei which is evident from Figure 5.4. The quartets for which the even-even nucleus has $T = 1$ and $T_3 = -1$ (green symbols on Figure 5.4) the odd-odd nucleus will have the same number of protons and neutrons making it extra bound. As a consequence the Q_{EC} -values are almost the same for all four nuclei.

In the right part of Figure 5.5 we present the dominating decay modes based on the conclusions drawn for the Q_{EC} -values from the odd-even effects. The beta-delayed alpha-particle emission is expected to happen in the odd-odd nucleus of the quartet, as it has the highest Q_{EC} -value and the alpha-particle separation energy in the beta-daughter nucleus tends to be smallest here. For the beta-delayed proton emission it is important to have a low proton separation energy in the beta-daughter nucleus. This decay mode are therefore most prominent from the even Z nuclei. Continuing by this line of arguments the $\beta p \alpha$ decay mode should happen predominantly from the even-odd nuclei, and the $\beta 2p$ and $\beta 3p$ decays should happen in the odd-odd and the even-odd nuclei, respectively.

Comparing these predictions with the experimental evidence, which are summarized on Figure 5.3, it is immediately clear that we to a large extent can explain the observed systematics of beta-delayed particle emissions as a consequence of odd-even effects. It is therefore not necessary to include structure effects such as alpha-particle clustering in order to explain the observed systematics even though alpha-conjugate

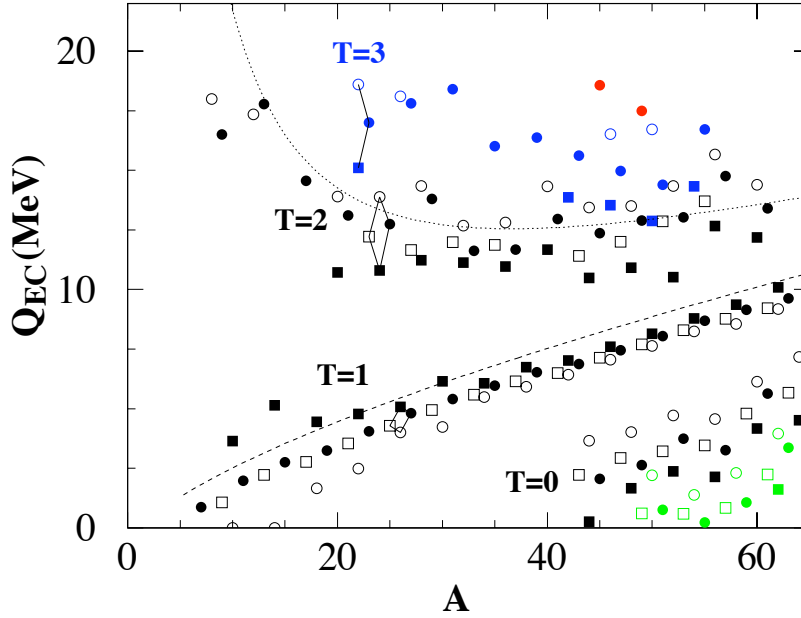


Figure 5.4: Q_{EC} -values for nuclei up to Ge. Filled symbols marks nuclei with even Z and open symbols odd Z nuclei. The squares marks nuclei with even N and the circles marks odd N nuclei. The isospin values shown are for the even-even nuclei. The green symbols correspond to $T = 1$ ($T_3 = 1$) and the red symbols correspond to $T = 4$. The dashed and dotted lines are a liquid drop estimate of Q_{EC} for nuclei with $T_3 = -1/2$ and $T_3 = -3/2$ respectively. The full lines marks a quartet of Al-Si nuclei. Figure from [Lund 2015b].

nuclei often occur as intermediate and final state nuclei. With future observation of new instances of these decay modes are made the present interpretation can be put to the test. The model can be used for prediction of where to search for exotic decay modes like $\beta p \alpha$. This decay mode may not happen in heavier $T_3 = -3/2$ nuclei than ^{21}Mg due to the evolution of the separation energies and the Q_{EC} -values, however, it may be found in the $T_3 = -5/2$ nuclei ^{23}Si , ^{27}S , ^{31}Ar , etc.

If the $\beta p \alpha$ decay mode is found in ^{20}Mg it may help to quantify the $^{15}\text{O}(\alpha, \gamma)^{19}\text{Ne}$ reaction rate, which is relevant for the astrophysically break-out sequence of the hot

| | | |
|------------|---------------------|---------------------|
| | N | N+1 |
| Z | e-e T | e-o T-1/2 |
| Z-1 | o-e T-1/2 | o-o T-1 |

| | | |
|------------|-----------|------------------------------|
| | | |
| $\beta 3p$ | βp | βp $\beta p\alpha$ |
| $\beta 2p$ | | $\beta\alpha$ |

Figure 5.5: *Left:* The quartet of nuclei with similar Q_{EC} -value. *Right:* The favored beta-delayed particle decay modes. Figures from [Lund 2015b].

CNO cycle. For more detail see Chapter 6 and [Wrede 2014].

Motivation ^{20}Mg

We will now change our focus to the beta-decay study of ^{20}Mg . The general motivations for studying the beta-decay of ^{20}Mg are the same as for studying ^{21}Mg , i.e. to measure the beta-decay strength distribution, characterize and measure the properties of the populated resonances, and to make comparisons with theoretical calculations and with the mirror decay and the mirror nucleus. We made a brief overview of all these aspects in Chapter 1. In the present chapter we will start out by presenting some of the main highlights of the ^{20}Mg research in Sect. 6.1. Then we will discuss a few aspects and characteristics of the beta-decay of ^{20}Mg in Sect. 6.2. Finally, in Sect. 6.3 we will discuss the astrophysical motivation for studying ^{20}Mg .

6.1 The history of the ^{20}Mg research

The history of the ^{20}Mg research is rich with publications. In this section we will present selected highlights, so the reader should not expect to find an exhaustive list of all publications. The most recently compiled decay scheme of ^{20}Mg from [TUN 2014] is shown on Figure 6.1.

One of the very first publications on ^{20}Mg is the 1979 study of the beta-decay of ^{20}Mg , [Moltz 1979]. The experiment used the Lawrence Berkeley Laboratory 88-in. cyclotron to produce 70 MeV beams of ^3He ions, which subsequently were used to produce ^{20}Mg through the reaction $^{20}\text{Ne}(^3\text{He}, 3n)$. The produced activity was transported by a helium-jet system to a magnetic mass separator into which the beam was injected as singly-charged ions accelerated to 18 keV. The mass separated beam was implanted in foils of aluminized polyethylene, which was placed in front of the two ΔE - E telescopes employed for detection of charged particles. The main result of the experiment is the observation of two beta-delayed proton branches believed to originate from the $T = 2$ and $I^\pi = 0^+$ IAS in ^{20}Na , which establish the position of the IAS to be at an excitation energy of 6.57(5) MeV. They also measured for the first time the half-life of ^{20}Mg , $T_{1/2} = 95_{-50}^{+80}$ ms, which is in good agreement with the theoretical prediction of $T_{1/2} = 0.1$ s by [Lanford 1973]. However, the experiment was seriously contaminated by directly produced ^{20}Na through the reaction $^{20}\text{Ne}(^3\text{He}, p2n)$, which resulted in $\approx 10^5$ ^{20}Na 2.16 MeV alpha-particles per beta-delayed proton from ^{20}Mg .

A later study of the beta-decay of ^{20}Mg was published in 1992 [Kubono 1992]. The experiment was performed at RIKEN with a 100 MeV per nucleon primary beam of ^{24}Mg , which was used to produce $^{20-21}\text{Mg}$ with a target of beryllium and subsequently mass separated with the RIKEN projectile fragment separator [Kubo 1989]. The beam of ^{21}Mg was used as a cross-check of the experimental setup. The detector setup consisted of a stack of five silicon detectors ($4 \times 100 \mu\text{m} + 1 \times 500 \mu\text{m}$) with the produced beam of $^{20-21}\text{Mg}$ being implanted in the center of the third of these five silicon detectors. The array of silicon detectors were surrounded by a beta-ray spectrometer consisting of three sets of ΔE - E telescopes made up of plastic scintillators. The primary beam was turned off for 200 ms every time a ^{20}Mg ion was identified with the energy loss and time of flight method. The resulting beta-delayed particle spectrum observed show clear signs of both $^{20}\text{Mg}(\beta p)$ and $^{20}\text{Na}(\beta \alpha)$, which is only natural as a large fraction of the ^{20}Mg decays are expected to populate bound states in ^{20}Na . From the beta-delayed protons is the half-life measured to be $T_{1/2} = 114(17)$ ms. They put an upper limit of 1% on the beta-decay feeding to the first excited 1^+ state above the proton threshold ($E_x = 2645$ keV), which is located in the Gamow-window of the $^{19}\text{Ne}(p, \gamma)$ break-out reaction from the Hot CNO (HCNO) cycle - more details can be found in Sect. 6.3.

The next study of the ^{20}Mg beta-decay was also published in 1992 and is described in [Görres 1992]. This study addressed the question of the value of I^π for the 2645 keV resonance in ^{20}Na located just above the proton threshold. The production of ^{20}Mg was achieved with the in-flight method discussed in Sect. 1.4.1 at the National Superconducting Cyclotron Laboratory at Michigan State University with a primary beam of ^{36}Ar . The produced beam of ^{20}Mg ions was mass separated and implanted in a stack of four silicon detectors. The implanted nuclei were identified by energy loss and time of flight measurements. On the basis of this identification it is concluded that 65% of the implanted beam was ^{20}Mg with the remaining part being ^{18}Ne . Even though the experiment only had a production rate of 0.7 ^{20}Mg ions per second, they put an improved upper limit on the beta-decay branching ratio to the 2645 keV resonance of $B_\beta \leq 0.2\%$.

One of the most extensive beta-decay studies of ^{20}Mg to date was published in [Piechaczek 1995]. As for the other experiments the beam was produced by the in-flight method - this time at GANIL. A primary beam of 95 MeV per nucleon ^{24}Mg was put on a target of natural nickel and the resulting secondary beam of ^{20}Mg was mass separated with the LISE3 spectrometer. The produced secondary beam consisted of 97.6% ^{20}Mg ions and of 2.4% contaminating isotopes with a total of $4.5 \cdot 10^6$ ^{20}Mg ions. The beam of ^{20}Mg was implanted in a 300 μm thick DSSSD with a 45° rotation with respect to the beam axis. The implantation detector was squeezed in between two segmented large area silicon detectors with a thickness of 500 μm each, which

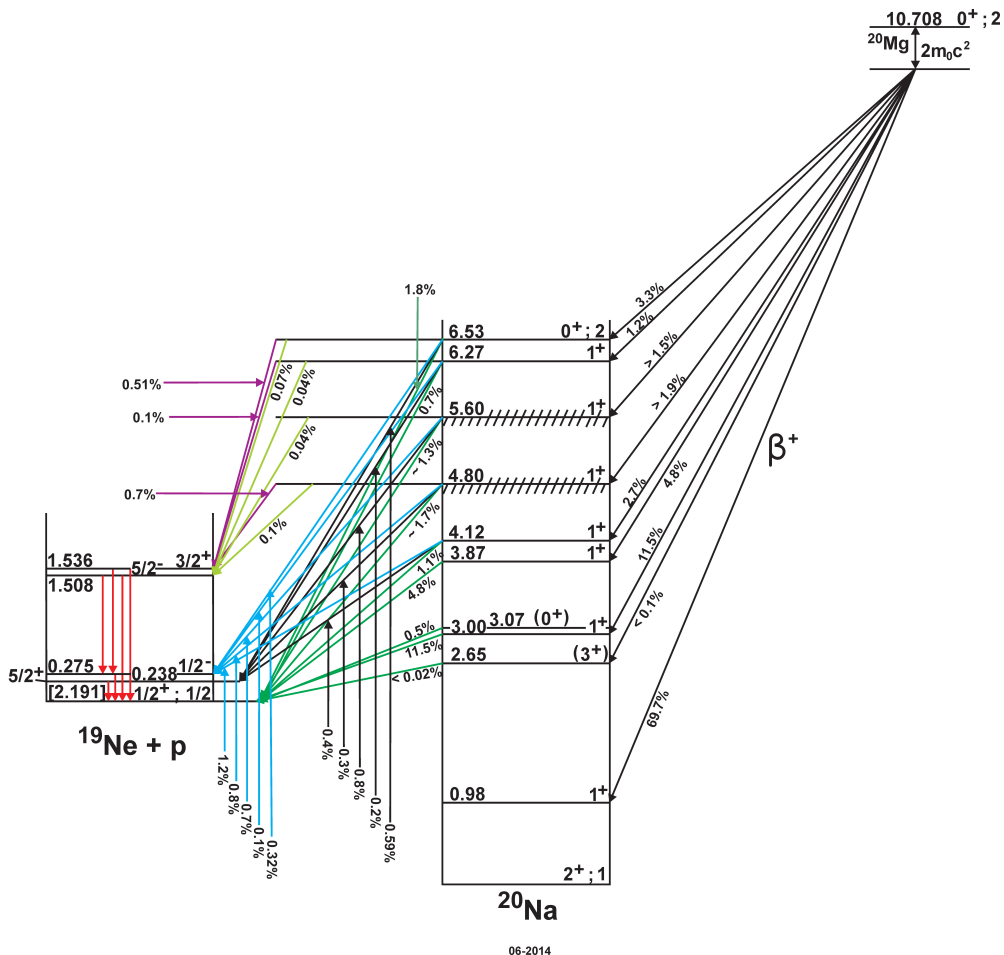


Figure 6.1: Decay scheme for allowed beta-decay of ^{20}Mg populating 1^+ states in ^{20}Na . Figure from the TUNL evaluation in [TUN 2014].

was used for the detection of beta-particles. In front of these three silicon detectors was a smaller and circular silicon detector positioned with the purpose of performing the isotope identification. This silicon detector setup was surrounded by three large-volume HPGe-detectors for measuring any gamma-rays. The measured proton and gamma-ray spectra are used to construct an improved decay scheme for ^{20}Mg , which to a large extent is the same as what we presented on Figure 6.1. They also put an upper limit of the beta-decay branching ratio to the 2645 keV resonance of 0.1% by considering both the beta-delayed proton branch and the gamma-ray deexcitations from this resonance.

In [Wrede 2010] the mass of the ground state of ^{20}Na was measured to very high precision, which leads to a new and improved value for the proton separation energy $S_p(^{20}\text{Na}) = 2190.1(11)$ keV. From this updated value they also update the excitation energy of the IAS to be 6525(12) keV. This is based on the previously measured proton energies from the IAS. They used a quadrupole-dipole-dipole-dipole magnetic spectrograph to perform a momentum analysis of the ion of interest. The light ions was produced in $(^3\text{He},t)$ reactions between an incoming ^3He beam and a range of thin ion-implanted target foils. In the case of ^{20}Mg the target was made of carbon with ^{20}Ne implanted in it.

In a paper from 2012, [Wallace 2012b], a detailed study of the ^{20}Mg beta-decay is presented. The experiment was performed at the Cyclotron Institute at Texas A&M University. The production of ^{20}Mg was achieved by the in-flight method with a primary beam of ^{20}Ne ions at an energy of 25 MeV per nucleon. The primary beam was used to bombard a target of ^3He , which produced ^{20}Mg through the fusion-evaporation reaction $^{20}\text{Ne}(^3\text{He},3n)^{20}\text{Mg}$. The produced secondary beam of ^{20}Mg was mass separated from the other components of the beam with the Momentum Achromat Recoil Spectrometer [Tribble 1989]. The typical production rate was ≈ 30 ^{20}Mg ions per second, which resulted in a total of $3 \cdot 10^6$ ^{20}Mg ions. The mass separated beam was implanted in the center of a 45 μm thick DSSSD (24 x 24 pixels), which was placed in between two thicker silicon detectors (140 μm and 1 mm). The contaminants of ^{10}C and ^{17}Ne was stopped in the last of the three detectors. By using this kind of detector setup they manage to get a clean low-energy spectrum and they put the to date best upper limit on the beta-delayed proton intensity from the 2645 keV resonance to be $\leq 0.02\%$ with a 90% confidence level. However, they are missing gamma-ray detection capabilities and, as the resonance is expected to also deexcite by gamma-ray emission, the proton intensity should not be directly translated to a beta-decay feeding in terms of an ft -value without taking an estimate of the gamma-ray branching ratio into account. The upper limit put on the beta-decay feeding in [Piechaczek 1995] includes the possible gamma-ray deexcitation.

The latest published study of the ^{20}Mg beta-decay is presented in [Glassman 2015].

Table 6.1: The energy and intensity of the observed gamma-ray decays of the four lowest excited states in ^{19}Ne according to [Tilley 1995].

| $E(^{19}\text{Ne})$ (keV) | E_γ (keV) | I_γ (%) |
|---------------------------|------------------|----------------|
| 238.27 | 238.3 | 100 |
| 275.09 | 275.1 | 100 |
| 1507.56 | 1232.5 | 88 |
| | 1269.3 | 12 |
| 1536.0 | 1260.9 | 5 |
| | 1297.7 | 95 |

The described experiment uses the National Superconducting Cyclotron Laboratory at Michigan State University to produce a fast secondary beam of ^{20}Mg by projectile fragmentation of a 170 MeV per nucleon primary beam of ^{24}Mg incident upon a ^9Be transmission target. The ^{20}Mg ions were magnetically separated from the remaining beam by use of the A1900 fragment separator. This production method resulted in up to 4000 ^{20}Mg ions per second delivered to the experimental setup, which consisted of a 25 mm thick plastic scintillator into which the beam was implanted and it was surrounded by two segmented germanium arrays each containing eight germanium crystals. The experiment measured the gamma-ray deexcitation of the IAS in ^{20}Na , which was populated via the beta-decay of ^{20}Mg . From this measurement they determine the excitation energy of the IAS to be $6498.4(2)_{\text{stat}}(4)_{\text{sys}}$ keV, which is a significant improvement over the older value of 6525(12) keV from [Wrede 2010].

6.2 Characteristics of the ^{20}Mg beta-decay

^{20}Mg has a half-life of 90(6) ms according to [Audi 2012]. The most recent decay scheme of ^{20}Mg is presented on Figure 6.1. The beta-decay has a 26.9(32)% branching ratio for populating proton unbound resonances (number is based on Table 2 in [Piechaczek 1995]). The beta-delayed proton decay branches populate states in ^{19}Ne and feeding has been observed to the ground state and the four lowest excited states: 238.27(11) keV, 275.09(13) keV, 1507.56(30) keV, and 1536.0(4) keV [Tilley 1995]. The possible gamma-ray deexcitations of these four excited states are presented in Table 6.1. It is important to note the small energy difference between the four excited states, as it means that the beta-delayed protons to the first-second excited state and to the third-fourth excited state will only be separated by roughly 30 keV (assuming the protons are emitted from the same resonance). It will therefore be a serious chal-

lenge to reconstruct the decay scheme and to assign the proton peaks to the right decay branches. For this work we will need the gamma-rays.

Another complication when studying the beta-decay of ^{20}Mg is the 69.7% branching ratio to bound states in ^{20}Na . The ground state of ^{20}Na will decay by beta-delayed alpha-particle emission and the alpha-particles and the ^{16}O nuclear recoils will contaminate the low-energy part of the proton spectrum from ^{20}Mg . As we have already described in Sect. 1.4, the beam of ^{20}Mg produced for this study at the ISOLDE facility is dominated by a ^{20}Na isobaric contamination. This will prove to be a major challenge for the analysis of especially the low-energy part of the beta-delayed proton spectrum. A more detailed discussion of the contamination of ^{20}Na will be presented in Sect. 8.1.2.

6.3 Astrophysical motivations

The general nuclear physics motivation for measuring the beta-decay of ^{20}Mg is to determine the beta-decay strength distribution, characterize and measure the properties of the populated resonances, and to make comparisons with theoretical calculations. We would also like to compare with the mirror decay and the mirror nucleus. We made a brief overview of all these aspects in Chapter 1. Therefore, we will focus on the astrophysical motivation for studying ^{20}Mg in the present section.

The astrophysical motivation has to do with energy production in stars, more precisely in explosive environments, which is governed by fusion of light nuclei, generally starting with the reaction with the lowest Coulomb barrier. The stellar evolution is quite sensitive to the exact reaction rates, making it important to measure the relevant nuclear physics properties. In the following section we will give a more elaborate discussion of these aspects.

6.3.1 Breakout of the hot CNO cycles

A typical place for explosive hydrogen burning is a type-I X-ray burst, which is fueled by accretion of hydrogen- and helium-rich matter onto the surface of a neutron star with a strong magnetic field in a close binary system with a population I star with $M \geq 5M_{\odot}$. The type-I X-ray bursts are the most frequent type of thermonuclear stellar explosion in the galaxy.

In this case will the hot CNO (HCNO) cycles dominate the energy production by turning hydrogen into helium when the temperature of the accreted matter reaches $T = 0.1 - 0.4$ GK. The HCNO cycles are essentially closed and happens in the $A = 12 - 18$ region, [Iliadis 2007]. For type-I X-ray bursts the temperature rises to $T > 0.4$ GK and new reactions start to compete with some of the reactions in the HCNO cycles.

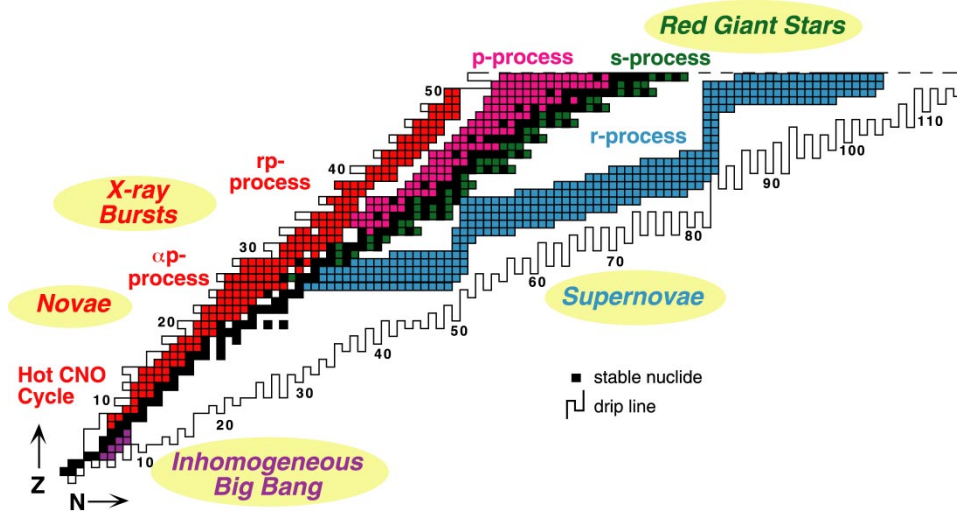
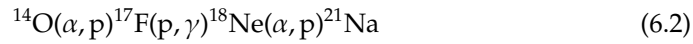


Figure 6.2: The stellar nucleosynthesis path under various different conditions. The HCNO cycle and the breakout from the HCNO cycle is running close to or at the proton drip-line in explosive environments. Figure from [Smith 2001]

This opens the possibility for transferring material from the $A = 12 - 18$ region and into the $A = 20 - 21$ region and beyond. The nuclei that are converted in this breakout are essentially lost for the HCNO cycles. Three breakout sequences exist from the HCNO cycles and they are given by



After the breakout reaction will the energy production continue by alpha-particle and proton capture on the heavier and heavier nuclei produced by the αp - ($A \leq 30$) and rp -processes ($A \geq 33$) as shown on Figure 6.2. The end point for the nucleosynthesis in type-I X-ray bursts are at $A \approx 100$ by the rp -process. The reactions runs along the proton drip-line and are very sensitive to both the exact position of the proton drip-line but also to photo disintegration.

6.3.2 Spin and parity of the 2.645(6) MeV resonance in ^{20}Na

As is evident from Equation (6.1) the first of the three breakout sequences goes through ^{20}Na by proton capture on ^{19}Ne . The level at 2.645(6) MeV in ^{20}Na , see Figure 6.1, is

located in the Gamow-window of the $^{19}\text{Ne}(p, \gamma)^{20}\text{Na}$ reaction and is therefore decisive for the reaction rate. The spin and parity of this level is not yet fully determined, but the most likely values are 1^+ or 3^+ as seen by comparison with the mirror nucleus. A 3^+ assignment is predicted to give a significantly higher reaction rate under X-ray burst conditions than a 1^+ assignment would, [Wallace 2012b, Fortune 2000]. If the resonance has $I^\pi = 1^+$, it can be populated in allowed beta-decay of ^{20}Mg . A 3^+ assignment makes it a second-forbidden transition, which greatly suppresses the beta-decay feeding to this resonance.

As already mentioned, a recent measurement of the beta-decay of ^{20}Mg put an upper limit on the beta-decay branch to this level of 0.02%, [Wallace 2012b]. This low beta-decay branching ratio favors the 3^+ assignment but does not completely rule out the 1^+ possibility.

6.3.3 Beta-delayed proton-alpha emission

As is evident from Equation (6.1) the first reaction in this breakout sequence is the $^{15}\text{O}(\alpha, \gamma)^{19}\text{Ne}$ reaction. This reaction is dominated by the 4.03 MeV resonance in ^{19}Ne at the conditions of breakout from the HCNO cycle in type I x-ray bursts according to [Davids 2011]. The resonance energy is well-known, however, the resonance strength is only known with an upper limit. The problem is the suppression of the width of the alpha-particle entrance channel by the Coulomb barrier. The resonance strength can be determined by measuring the branching ratio for alpha-particle emission from this resonance as the half-life is already known from other measurements, [Tan 2005, Kanungo 2006].

It has recently been proposed in [Wrede 2014] to study this resonance via beta-delayed proton emission from ^{20}Mg . It is energetically possible to populate this resonance in ^{19}Ne as it has an energy of 6223.0(26) keV with respect to the ground state of ^{20}Na . Beta-delayed proton emission has not yet been observed to feed such a highly excited resonance in ^{19}Ne , however, according to the results presented in [Piechaczek 1995] more than 0.05% of the ^{20}Mg beta-decays will populate $T = 1$ resonances above the 4.03 MeV resonance in ^{19}Ne . The expected branching ratio for alpha-particle emission from this resonance is $\approx 10^{-4}$ according to [Wrede 2014], which is to be compared with the intensities of the three other observed cases of $\beta p \alpha$ decays: ^9C , ^{17}Ne , and ^{21}Mg . According to the systematics of beta-delayed particle emitting nuclei developed in Chapter 5, it is expected that the $^{20}\text{Mg}(\beta p \alpha)$ decay branch is less intense than the observed $^{21}\text{Mg}(\beta p \alpha)$ decay branch. A first step towards a direct measurement of the $\beta p \alpha$ decay mode from ^{20}Mg is to search for the more likely gamma-ray deexcitation of the 4.03 MeV resonance to the ground state of ^{19}Ne .

Experimental methods: ^{20}Mg

The main aim of the experiment is to measure the beta-delayed proton spectrum from ^{20}Mg in great detail in order to both search for feeding to the 2645(6) keV astrophysical interesting resonance and to determine the beta-decay strength distribution precisely. To do this we need to make a clever design of the detector setup as the beam of magnesium is highly contaminated with sodium. As described in Sect. 1.4, the experiment was performed in April 2015 and collected ^{20}Mg ions for 68.0167 hours in total, with an average implantation rate in the detection chamber of ≈ 60 ^{20}Mg ions per second and ≈ 500 ^{20}Na per second. In Sect. 7.1 we will present the detector setup, then we will comment on the geometry and energy calibrations of the silicon detectors in Sect. 7.2, and finally we will go through the calibration of the HPGe-detectors in Sect. 7.3.

7.1 Detector setup

For the ^{20}Mg beta-decay study performed at ISOLDE we have used the ISOLDE Decay Station (IDS) taking advantage of the array of HPGe-detectors. The complete IDS setup with the four HPGe clover detectors, each consisting of four HPGe crystals, surrounding the collection chamber can be seen on Figure 7.1.

The four HPGe clover detectors surround a smaller chamber inside which we have a silicon detector array. In the center of this array we collect the beam of ^{20}Mg

Table 7.1: Punch through laboratory energies for protons and alpha-particles in the front detectors of the four charged particle telescopes. It is calculated for the thickness specified in the second column of the table with the SRIM stopping power tables [Ziegler 2008].

| Detector no. | Thickness (μm) | E_p (MeV) | E_α (MeV) |
|--------------|-----------------------------|-------------|------------------|
| U2 (SSD) | 20 | 1.15 | 4.36 |
| U4 (DSSSD) | 40 | 1.79 | 6.98 |
| U3 (DSSSD) | 60 | 2.31 | 9.09 |
| U6 (DSSSD) | 300 | 6.07 | 24.21 |



Figure 7.1: HPGe clover detector setup at the IDS. Collection chamber is at the central position where the four detectors meet.

ions in a thin carbon foil. A picture of the silicon array can be seen on Figure 7.2. A schematic drawing of the silicon detectors including detector thicknesses can be seen on Figure 7.3. We use four silicon telescope detectors each containing one DSSSD. Three of the telescopes have a non-segmented silicon pad detector as backing detector while the last telescope has a single sided Silicon Strip Detector (SSD) as a front detector and a DSSSD as back detector. On the bottom of the array we have placed a 1000 μm thick DSSSD detector with no backing detector.

Three of the four telescopes consists of thin front detectors and thick back detectors. In one telescope we placed the detector U2 in the front which is a 20 μm thin SSD with 16 vertical strips on the front side and it is backed by a 500 μm thick DSSSD (U1) with 16x16 strips. This telescope is optimal for removing the alpha particles from the ^{20}Na beta-decay as alpha-particles with an energy up to 4.36 MeV will be stopped in the front detector. At the same time will protons with energy higher than 1.15 MeV punch-through the 20 μm thin front detector which means we will have a clean proton spectrum covering a large energy range in U1. A summary of punch through energies in the front detectors is found in Table 7.1.

In the second telescope we have a 40 μm thin DSSSD with 16x16 strips as the front detector (U4) and a 500 μm thick pad detector in the back (P1). In the 40 μm thin front detector we will stop up to 6.98 MeV alpha particles while protons with energy higher than 1.79 MeV will reach the back detector. Again, we have an effectively clean proton spectrum in the back detector, however, the energy ranged covered will be smaller than for U1.

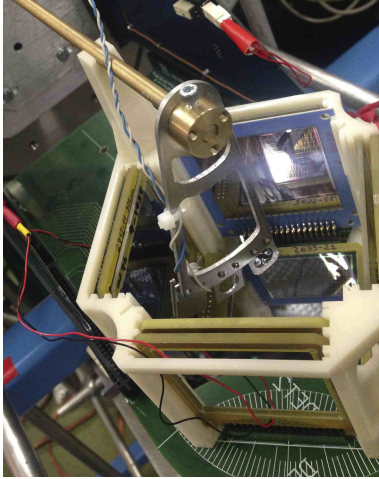


Figure 7.2: Silicon detector array surrounding the carbon collection foil in the center. In the top left corner the final collimator before the beam enters the chamber is visible.

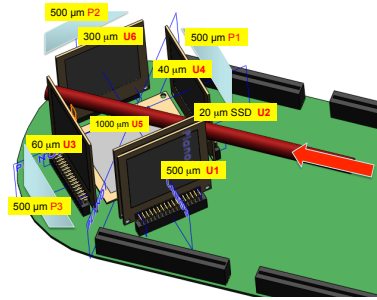


Figure 7.3: Schematic drawing of the silicon array with naming conventions and detector thicknesses.

The third telescope consists of a 60 μm thin DSSSD with 16 x 16 strips in the front (U3) which is backed by a 500 μm thick pad detector (P3). The 60 μm thick front detector will stop alpha-particles with an energy below 9.09 MeV and allow protons with an energy above 2.31 MeV to pass through.

In the fourth telescope we apply a different tactic. The idea here was to use a thicker front detector as they generally give better energy resolution and less noise than the thin DSSSD detectors. The front detector is a 300 μm thick DSSSD with 16 x 16 strips (U6) and it is backed by a 500 μm pad detector (P2). Only the very highest energy protons will punch-through the front detector as it stops up to 6.07 MeV protons.

A summary of the detector properties including the solid angle coverage can be found in Table 7.2. All the strip detectors used in the experiment have a strip width of 3.0 mm and an interstrip width of 0.1 mm.

7.2 Calibration of silicon detectors

To obtain a good energy resolution in all silicon detectors it is crucial that the energy and geometry calibration is performed with great care. It easily takes a long time to make a good calibration with a good energy resolution. In this section we will go through the calibration procedure for the different silicon detectors. First, we

Table 7.2: Dead layer and detector thicknesses with the detector names referring to Figure 7.3. The solid angle of each detector is calculated with equation (A4) in [Mathar 2015] and the uncertainty is coming from a ± 1 mm change in the distance between the carbon foil and the detector center. The determination of the detector energy resolution σ_{det} is described in more detail in Sect. 7.2.2 and in Sect. 8.3.1.

| Detector no. | Thickness (μm) | Dead layer (μm) ^a | Ω_{det} (%) | σ_{det} (keV) |
|--------------|-----------------------------|---|---------------------------|-----------------------------|
| U1 (DSSSD) | 500 | 0.1 + 0.6 | 4.69(10) | 47.0(5) |
| U2 (SSD) | 20 | 0.5 + 0.6 | 5.21(12) | 44(4) |
| U3 (DSSSD) | 60 | 0.1 + 0.6 | 5.19(12) | 19.2(2) |
| U4 (DSSSD) | 40 | 0.1 + 0.6 | 5.33(12) | 19.9(5) |
| U5 (DSSSD) | 1000 | 0.1 + 0.6 | 6.31(15) | 13.9(2) |
| U6 (DSSSD) | 300 | 0.1 + 0.6 | 5.63(14) | |
| P1 (pad) | 500 | 0.6 | 4.69(10) | 27.36(12) |
| P2 (pad) | 500 | 0.6 | 4.71(11) | |
| P3 (pad) | 500 | 0.6 | 4.57(10) | 51.1(5) |

^axx + yy meaning xx μm on frontside and yy μm on backside. If only xx it is just the frontside dead layer.

determine the thickness of the carbon foil into which we implant the beam of ^{21}Mg . Second, we perform the geometry and energy calibrations of the detectors.

7.2.1 Carbon foil thickness

To get an accurate energy calibration with good energy resolution it is important to understand the thickness of the carbon foil in which we stop the beam of magnesium ions. Therefore we measured the thickness of the carbon foil before the experiment with an alpha source in our vacuum chamber at Aarhus University. The foil was mounted on a target ladder with a hole in the ladder. Then we placed the alpha source (^{148}Gd , ^{239}Pu , ^{244}Cm) in front of the target ladder with a DSSSD detector positioned on the other side of the target ladder. Two measurements was done: one with the carbon foil between source and detector, and a second without the carbon foil, i.e. a blank target. Because of the small hole in the target ladder we do not need to consider the detector dead layer as we also select the central pixels within the target ladder hole. It gives us effectively that the dead layer is the same for the two detectors and therefore it is not important here as we look for the energy difference between the two measurements.

We make Gaussian line shape fits of four alpha particle peaks in both the blank

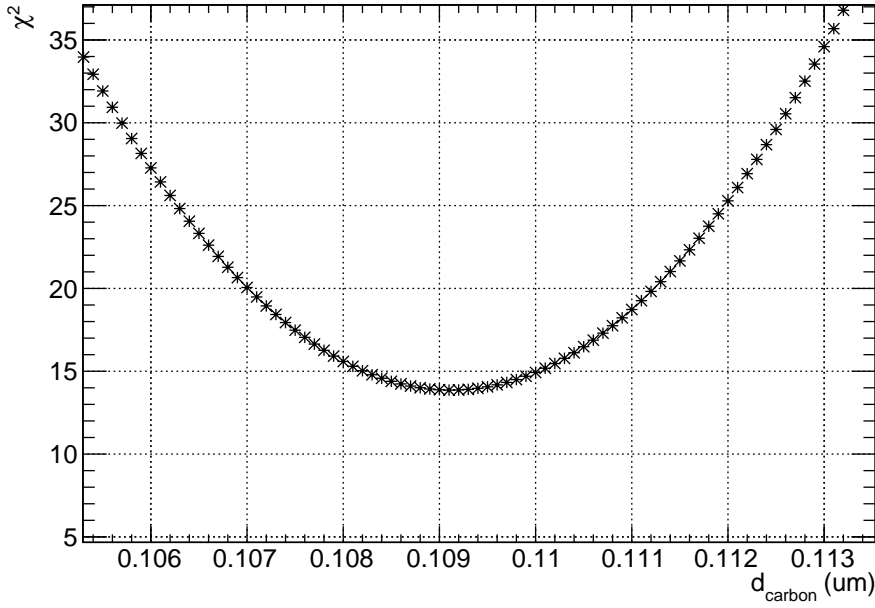


Figure 7.4: The χ^2 estimator for the carbon foil thickness. We have four data points and one parameter so the number of degrees of freedom is 3.

and the carbon foil measurement. The energy of the four peaks are 3182.690(24) keV, 5156.59(14) keV, 5762.64(3) keV, and 5804.77(5) keV. We then take the energy difference between the two measurements for all four alpha particle energies, $\Delta E_{\text{measured}}^{(i)}$ and compare it with the calculated energy loss based on the stopping power tables in [Ziegler 2008] for 200 different carbon foil thicknesses. We construct a chi-square value for each thickness in order to determine the correct thickness and the uncertainty:

$$\chi^2 = \sum_{i=1}^4 \left(\frac{\Delta E_{\text{measured}}^{(i)} - \Delta E_{\text{SRIM}}^{(i)}}{\sqrt{\sigma^2(\Delta E_{\text{measured}}^{(i)}) + \sigma^2(\Delta E_{\text{SRIM}}^{(i)})}} \right)^2 \quad (7.1)$$

where the sum is over the four different alpha-particle energies. The resulting χ^2 values can be seen on Figure 7.4. From this figure we determine the thickness to be

$$d_{\text{carbon}} = 109(2) \text{ nm} = 24.5(5) \mu\text{g}/\text{cm}^2 \quad (7.2)$$

where the uncertainty has been determined by going from $\chi_{\text{min}}^2 \rightarrow \chi_{\text{min}}^2 \pm \frac{\chi_{\text{min}}^2}{\text{ndf}}$, where ndf is the number of degrees of freedom, which is 3 in this case.

As the beam of magnesium is implanted in the carbon foil we would like to know at exactly what depth it is stopped. In order to determine this we use the SRIM projected range [Ziegler 2008] as described in Sect. 3.2. The projected range for a 30 keV ^{21}Mg ion beam is determined to be 448 Å. For a 30 keV ion beam of ^{20}Mg the projected range is 450 Å.

7.2.2 Silicon Strip Detectors

The methods used to energy and geometry calibrate the silicon strip detectors are the same as described in Sect. 3.3 and this section will be more of an overview of the obtained results. To understand the theoretical considerations behind we refer to the earlier section. The data used for the calibrations is mainly the collected sample of ^{21}Mg as we every day during the experiment measured a few hours with this nucleus. Only in the case of U2 (20 μm) and U4 (40 μm) did we use a different source for the calibrations as the beta-delayed protons mostly will punch through these two thin detectors as is evident from Table 7.1. Instead we used the beta-delayed alpha-particles from the decay of ^{20}Na as a calibration source.

7.2.2.1 Geometry

The geometry of the DSSSD detectors are determined in the same manner as described in Sect. 3.3 for the ^{21}Mg experiment. The hit patterns of the five DSSSD detectors and the SSD detector can be seen on Figure 7.5. For U1, U3, U5, and U6 the hit pattern is measured with ^{21}Mg but for U2 and U4 it is measured with ^{20}Na . To determine the position of the beam from any given detector it is essential that the particles measured actually stops in the detector. For this reason we used alpha-particles from the decay of ^{20}Na for the thinnest detectors, i.e. U2 and U4.

In all cases it is evident that the beam is well centered on the carbon foil, however, in the case of U5 (bottom left figure) the picture is somewhat blurred due to the carbon foil frame shielding along the diagonal of the detector. This is to be expected as U5 is the horizontal detector which is placed underneath the carbon foil.

The position of the beam spot as determined from the fit of the hit patterns are summarized in Table 7.3. An example of one such fit can be seen on Figure 7.6. We have assumed that the beam spot position for U2 is identical to the beam spot position determined for U1 as the frame that supports the detectors, see Figure 7.2, is constructed in such a way that the two detectors are aligned. The hit patterns of U1 and U2 does, however, not agree on the position of the beam spot.

For the pad detectors we adopt the beam spot position determined in the DSSSD in the front of the telescope. We can safely do this as the detectors in a given telescope are aligned with respect to each other and the position of the carbon foil.

Table 7.3: Summary of the geometry fits for (x_0, y_0) . All but U4 is based on ^{21}Mg data while U4 is based on ^{20}Na data. The distance z_0 from the carbon foil to the detector center is based on measurements of the support structure used for the detectors which is 3D-printed to high precision.

| Detector no. | x_0 (mm) | y_0 (mm) | z_0 (mm) |
|--------------|------------|------------|------------|
| U1 | -0.796 | -0.676 | 46.74 |
| U3 | -0.600 | 0.502 | 41.27 |
| U4 | 0.949 | -1.182 | 41.40 |
| U5 | -1.513 | -0.015 | 34.00 |
| U6 | 2.200 | 1.094 | 39.24 |

7.2.2.2 Energy

The energy calibration of the strip detectors are mostly performed as outlined in Sect. 3.3 for the ^{21}Mg experiment. However, the fitting routine of the calibration peaks have been modified to make the calibration somehow simpler. The main simplification is to fit the calibration peaks individually with a non-normalized Gaussian distribution instead of making one total fit to all the peaks at the same time as described by Equation (3.6). In this way the fitting procedure of the peaks is less sensitive to the initial guesses. For the total fit it became often very tedious to find the exact initial guess that would produce a decent fit of all the calibration peaks.

For this experiment we used several strip detectors with different thicknesses ranging between 20 μm and 1000 μm . The sources used for the calibration are for this reason varying among the detectors in order to cover most of the energy range in each detector. For the two thinnest detectors (the 20 μm SSD called U2 and the 40 μm DSSSD called U4) we used the beta-delayed alpha-particles from the decay of ^{20}Na to do the energy calibration. For the U2 detector we used the alpha-particle branches with laboratory energies 2150.4 keV, 2483.5(25) keV, and 3803.0(25) keV. For the U4 detector we used the alpha-particle branches with laboratory energies 2150.4 keV, 2483.5(25) keV, 3803.0(25) keV, 4432.2 keV, and 4884.4(25) keV. These are the most intense alpha-particle branches that are stopped in the two detectors according to [Laursen 2013]. It is also from this reference that we have taken the energies, however, no uncertainty is quoted for the 2150.4 keV and the 4432.2 keV alpha-particles as these were used for calibration. As we want to measure proton energies and not alpha-particle energies, we use the prescription given in Sect. 3.3.2 to translate the alpha-particle calibration into a proton calibration.

For the thicker strip detectors we used the collected sample of ^{21}Mg to perform the energy calibration as we really are interested in knowing the proton energies

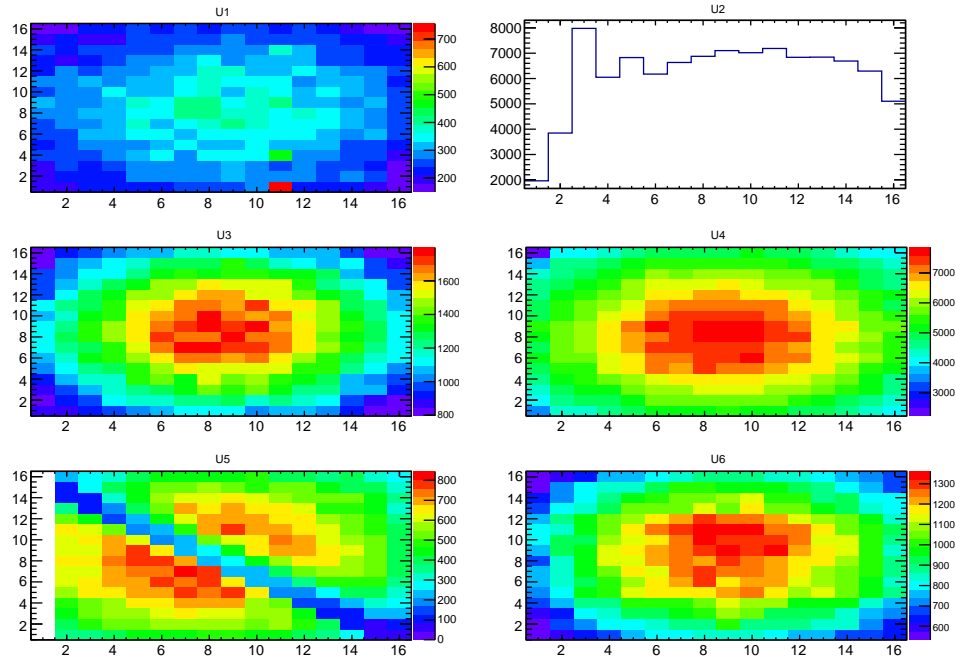


Figure 7.5: Hit patterns in the 6 strip detectors from ^{21}Mg data except in the case of U2 and U4 where ^{20}Na data is used. The 20 μm detector U2 is a single-sided strip detector with only the 16 vertical strips.

measured in the detectors. For the 60 μm thin DSSSD called U3 we use the beta-delayed proton branches with the laboratory energies 1257(10) keV, 1773(2) keV, and 1938(5) keV, i.e. p_6 , p_{10} , and p_{11} . An example of a Gaussian fit to the ^{21}Mg calibration peaks are shown on Figure 7.7. For the 300 μm thick DSSSD called U5 we use the proton branches with laboratory energies 1773(2) keV, 1938(5) keV, 4669(4) keV, and 6224(4) keV, i.e. p_{10} , p_{11} , p_{22} , and p_{27} . For the 500 μm thick DSSSD called U1 we use the proton branches with laboratory energies 1938(5) keV, 4669(4) keV, and 6224(4) keV which is p_{11} , p_{22} , and p_{27} . For the last strip detector, the 1000 μm thick DSSSD called U6, we use the proton branches with laboratory energies 1773(2) keV, 1938(5) keV, and 4669(4) keV. All the energies are based on the values measured by [Sextro 1973]. The proton branches used for the calibration are chosen such that we have several high-intensity peaks covering the as much of the desired energy range as possible.

A helpful check of the calibration of the DSSSD's is to plot the energy difference between the front- and the backside signal for the individual events after the calibration has been applied to the data. The energy difference should be zero for an ideal

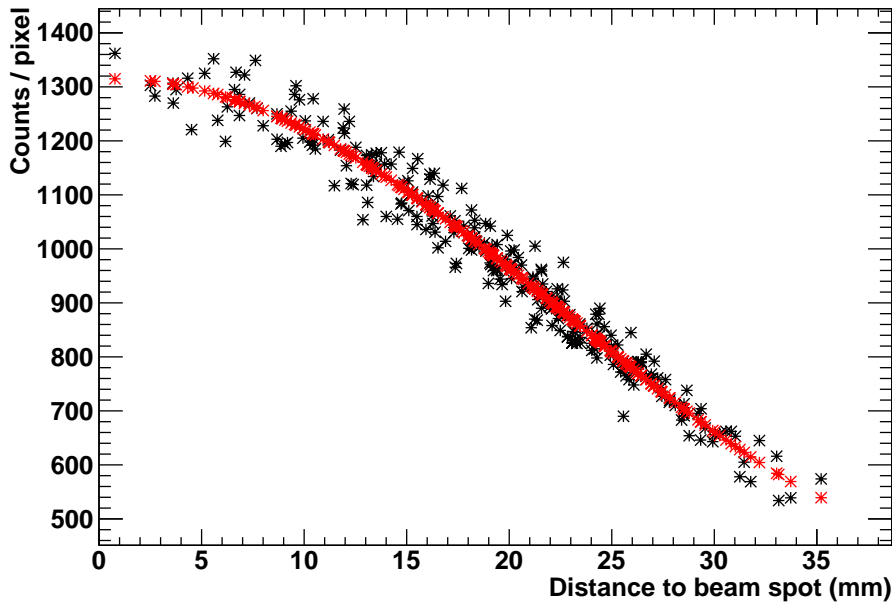


Figure 7.6: Example of a fit for the geometry from ^{21}Mg data measured with the detector U6. The black points are data points and the red points are the value of the polynomial used to describe the data.

detector with a perfect calibration, due to the fact that for a single particle stopped in the detector, the generated electronic signal is extracted through an electrode on both the front- and backside, i.e. the front and back strips. Ideally the signal will be the same. On Figure 7.8 we show the energy difference between the front- and the backside of U3 with the collected sample of ^{21}Mg . As the distribution is centered around zero and with a relatively small width it looks like a good calibration.

In Sect. 3.3.1.2 the procedure of matching the correct energies in the front- and the backside of the DSSSD with each other was described. The matching parameters E_{\min} and ΔE used in the analysis of the data can be seen in Table 7.4. ΔE was chosen based on a fit with a Gaussian distribution to the energy difference shown on Figure 7.8 such that at least 95.45% of the events in the peak has an energy difference less than ΔE . The second parameter, E_{\min} , was chosen on the basis of a background measurement with no charged particle activity in the detection chamber such that the noise is reduced as much as possible. An example background measurement with U2 is shown on Figure 7.10.

The obtained energy calibrations of the individual detectors have finally been

Table 7.4: The parameters used in the front-back matching routine for constructing the particle energies in the DSSSD detectors.

| Detector no. | E_{\min} (keV) | ΔE (keV) |
|--------------|------------------|------------------|
| U1 | 170 | 50 |
| U3 | 90 | 40 |
| U4 | 130 | 60 |
| U5 | 120 | 35 |
| U6 | 400 | 60 |

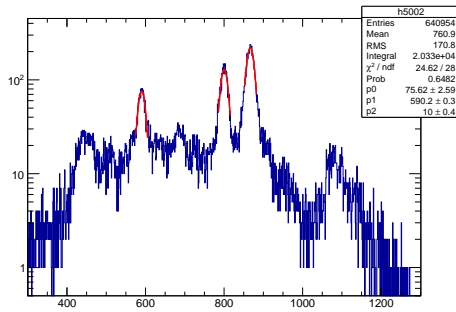


Figure 7.7: Example of a fit with a Gaussian response function to the individual calibration peaks. Strip number 2 on the frontside of detector U3 is shown. It is uncalibrated ^{21}Mg data.

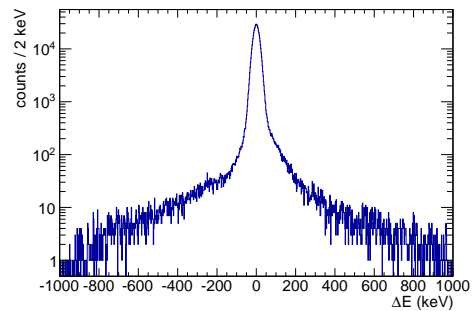


Figure 7.8: The U3 DSSSD energy calibration applied to the ^{21}Mg data. It shows the energy difference between the front- and backside strips for the individual events observed.

used to determine the detector energy resolutions which are presented in Table 7.2. They have been determined from a line shape fit of the collected data with the line shape function in Equation (4.7). More detail of the fitting procedure can be found in Sect. 8.3.1.

7.2.3 The U2 detector

Thickness: When investigating the energy loss in the U2 detector for beta-delayed protons from ^{21}Mg that punch through to the back detector, we have observed a significant change when moving across the detector from left to right (as seen from the carbon foil) with a small energy loss on the left side of the detector (strip 1) and a large energy loss on the right side (strip 16). This variation is not to be expected if the

source of ^{21}Mg is located in the carbon foil in the center of the silicon array. Instead one would expect the largest energy loss to happen in the outer edges of the detector and the smallest energy loss in the center. This is exactly what we observe when we look at the energy loss of the punch through protons from the bottom to the top of the detector as seen from the carbon foil.

In order to explain this behavior it is possible to think of several causes. First, it could be explained if the ^{21}Mg source is not positioned as the geometry calibration showed us. However, when looking at the hit pattern from U1 and U2 it seems pretty clear that the source is well centered with respect to the detectors. Second, we could have made a poor mapping of the data acquisition system electronic channel number to the strip number on the detector. However, the mapping is verified by demanding to only look at the events in U2 which are at the same time observed in a certain front strip in the backing detector U1. In this way we scan across the U2 detector from left to right and demonstrate that e.g. events observed in front strip number 8 in the backing detector U1 as expected corresponds to events in front strip 8 in U2. So assuming that the mapping of U1 is good as is demonstrated on Figure 7.5, we can also state that the mapping of U2 is good.

Finally, it could be that thickness of the detector is varying along the direction from left to right on the detector. The most direct way to see this is to determine the energy at which alpha-particles punch through U2. On Figure 7.9 we show the spectrum from the total collected ^{20}Mg data sample as observed in front strip 1 in U2 (top figure) and in front strip 16 in U2 (bottom figure). As U2 is only $20\ \mu\text{m}$ thick we mainly observe the beta-delayed alpha-particles from the decay of ^{20}Na . In front strip 1, i.e. the left edge of the detector as seen from the carbon foil, we clearly see that α_5 and α_6 are stopped (the full alpha-particle spectrum from ^{20}Na can be seen on Figure 8.6). Above 3 MeV we observe a broad structureless distribution of events which will be a mixture of fully stopped alpha-particles and alpha-particles that punch through the detector with the main contribution coming from the punch through events. When moving towards higher strip numbers on U2, i.e. from left to right, we gradually observe how less and less particles make punch through, turning the broad structureless distribution of events into a structure that exhibits several clear peaks. On top of this we also observe that the punch through energy for alpha-particles gradually increases from $\approx 4.6\ \text{MeV}$ in strip 1 to $\approx 5.4\ \text{MeV}$ in strip 16 (illustrated by the red line in the figures). Without taking the angle of incidence into account we find that alpha-particles with these two energies can penetrate $21.5\ \mu\text{m}$ and $27.2\ \mu\text{m}$ of silicon, respectively. Hence we can conclude that the thickness of U2 is approximately $21.5\ \mu\text{m}$ in strip 1 with a gradually increasing thickness when going towards higher strip numbers ending up with a thickness of approximately $27.2\ \mu\text{m}$ in strip 16. It means that it appears to be in a wedge shape with a thickness variation

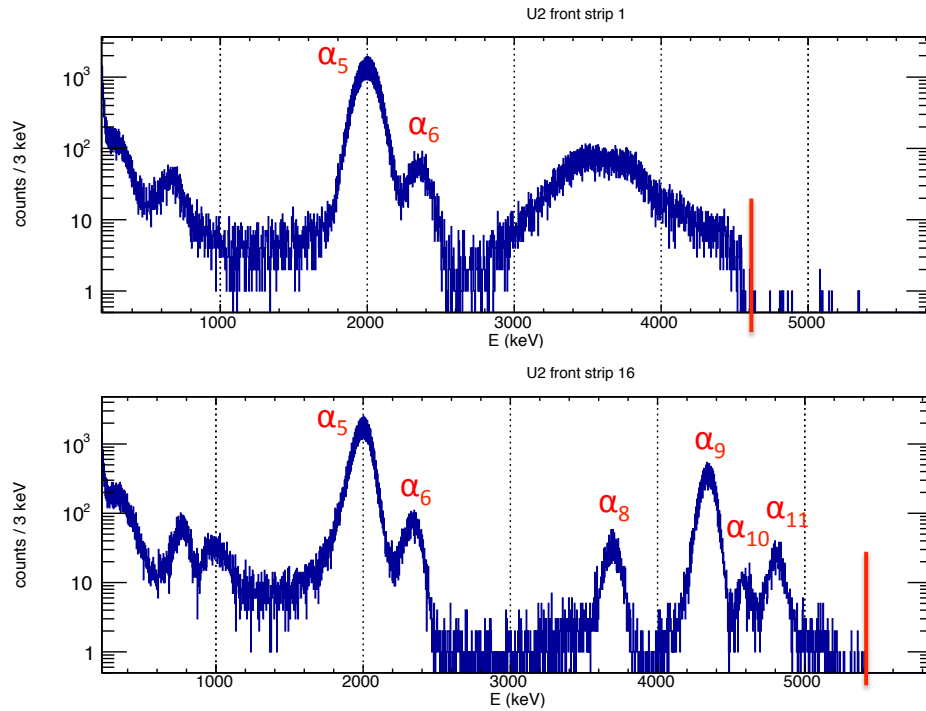


Figure 7.9: The two spectra shown here are the total data sample collected on the mass of ^{20}Mg in two different strips of the $20\ \mu\text{m}$ thin detector U2. The spectrum is dominated by the alpha-particles from ^{20}Na . The top figure is the spectrum as observed in strip 1. The bottom figure is the spectrum observed in strip 16. No cuts have been applied to the data.

of $\approx 20\%$.

Noise: Another important observation made from the data measured with the detector U2 is that it produces a lot of noise at energies below 300 keV. The noise are clearly identified when looking at data from a background measurement, i.e. for approximately 3 hours we closed the ISOLDE beam gate and took no beam into the detection chamber. During such a background measurement only very long-lived contaminants will survive and one would certainly not expect any charged particle activity to remain for that long in the chamber considering that we select the beam of ^{20}Mg . Even the known and large contamination of ^{20}Na does not live for this long. The total energy spectrum measured in U2 during this background measurement is shown on Figure 7.10. It clearly shows a distribution of noise events below approximately 300 keV.

The noise events are so excessive that for many triggers in U2, the data acquisi-

tion system records signals in most of the 16 strips of the detector. This complicates the reconstruction of the center-of-mass proton energies as this is done by adding the measured energy loss in the front detector (U2) to the measured energy deposited in the back detector (U1). The large amount of noise gives often rise to the addition of the energy of the noise-event in the front detector with the real proton energy deposited in the back detector. As a consequence we miss these proton events when constructing a graphical gate from the ΔE - E spectrum as the events does not appear along with the other protons that punch through the front detector, i.e. the reconstructed energy is wrong.

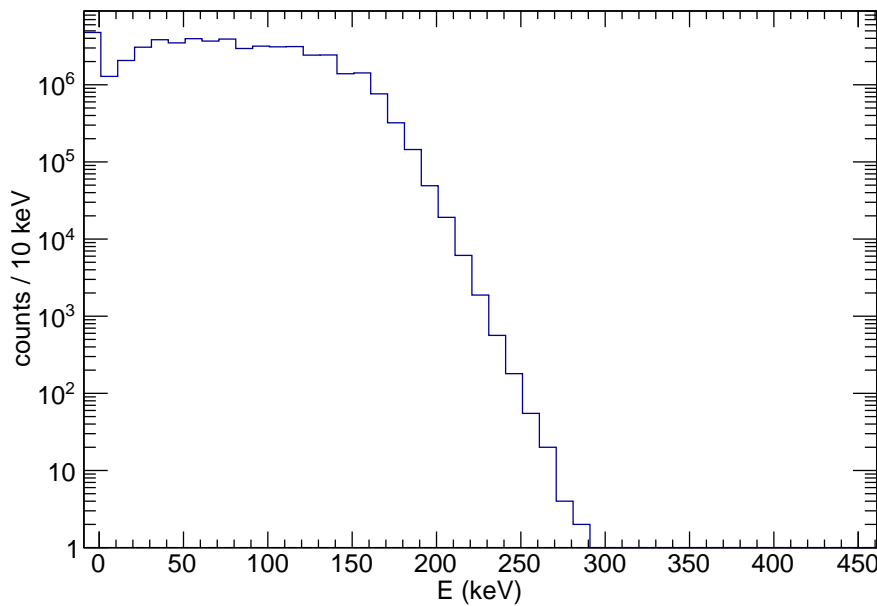


Figure 7.10: Total energy calibrated spectrum in U2 from a 3 hour background measurement with the ISOLDE beam gate closed such that no beam was allowed into the detection chamber. What is observed is electronic noise.

To solve this problem we construct a routine to match the real proton event in U2 with the proton event in U1. To simplify the matching we assumed that the particle multiplicity of U1 is one, as triggers with particle multiplicity larger than one only contributes $\approx 1\%$ of all particle events in this detector. We also put restrictions on the energy observed in U2 so that we only look at events between 170 keV and 1500 keV. This energy region is where we expect to observe the protons as we will show on Figure 8.2. We use the simple condition that for a given trigger, the event in U2 with

the highest energy inside the limited energy interval, is matched with the energy of the particle event in U1. The result of this matching is that we produce relative intensities for the proton branches observed in U1 which is consistent with what is observed in the other telescopes. In numbers we have gone from 35,000 proton events to 56,000 proton events.

7.2.4 Pad detectors

For the experiment we have used three pad detectors which all were placed as back detectors in a telescope configuration with a DSSSD in front. They were all $500\ \mu\text{m}$ thick and with a dead layer on the front side which were $0.6\ \mu\text{m}$ thick. From Figure 7.3 and Table 7.1 it is clear that the thickness of the DSSSD detectors means that we can only use the collected ^{21}Mg data sample as a calibration source of P1 and P3. For P2 we do the energy calibration with a quadruple alpha-particle source (^{148}Gd , ^{239}Pu , ^{241}Am , ^{244}Cm) where the DSSSD in front is removed.

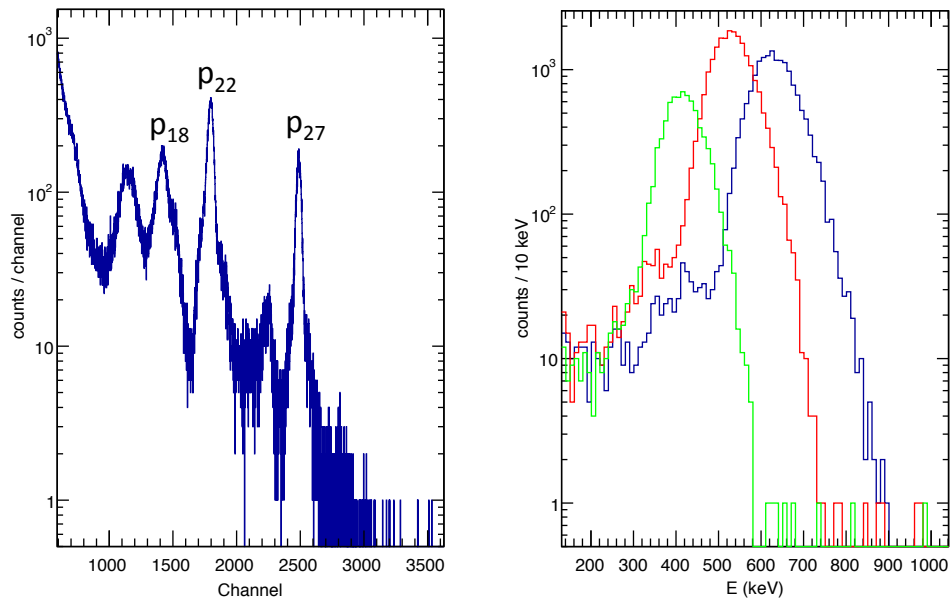


Figure 7.11: *Left:* The proton spectrum from ^{21}Mg as observed in P1. *Right:* The measured energy loss in the front detector (U4) for the three proton branches p₁₈ (blue), p₂₂ (red), and p₂₇ (green).

We will first discuss the calibration of P1 and P3. To do this we need to take care of a few complications. First, the beta-delayed protons from ^{21}Mg will punch through the DSSSD in the front of the telescope and the protons will therefore deposit

energy in the front detector. The exact amount of energy lost by the protons in the active part of the DSSSD's is naturally measured by the detectors and we use this measurement to determine an accurate number of the energy lost here. Second, we need to determine the energy lost by the protons in the carbon foil and in the detector dead layers by using the SRIM stopping power tables [Ziegler 2008] as described in Sect. 3.2. As the pad detectors are unsegmented we use the expression in Equation (3.9) to determine the average energy loss in the dead layers, however, we do not take into account that the beam spot is not perfectly centered on the detectors.

As the beta-delayed proton branches p_{18} , p_{22} , and p_{27} are the most intense branches with enough energy to punch through the DSSSD detectors we will use them for the energy calibration. The center-of-mass energies of these proton branches can be found in Table 4.4. On Figure 7.11 the non-calibrated proton spectrum from P1 is shown in the left figure. The figure on the right shows the energy lost in the front detector (U4) for the three proton branches. To determine the energy loss of the protons in the front detector we fit the peaks with Gaussian functions. In P3 we observe a larger width of the proton peaks which probably is due to the thicker front detector. Even though the energy resolution is relatively poor in the two pad detectors and it results in overlapping proton branches we do not make a weighted average of the energies of the overlapping peaks. Instead we have used the energy of the most intense of the proton branches contained in the calibration peaks as the other components are relatively weak.

The energy calibrations of P1 and P3 results in an energy resolution of

$$\sigma(\text{P1}) = 27.36(12) \text{ keV}$$

$$\sigma(\text{P3}) = 51.1(5) \text{ keV}$$

It is based on a fit of the proton branches p_{11} , p_{22} , and p_{27} from the decay of ^{21}Mg for P1 and a fit of the proton branches p_{22} and p_{27} from the decay of ^{21}Mg for P3. All the fits are made with the line shape function in Equation (4.7) and with the parameter Γ fixed to the known total width of the resonance as quoted in Table 4.3. More details on the fitting procedure can be found in Sect. 8.3.1.

The calibration of P2 is performed on a very rough basis as we neglect energy loss completely. We only expect to observe beta-particles from the decay of ^{20}Mg in this detector. We use a quadruple alpha-particle source containing ^{148}Gd , ^{239}Pu , ^{241}Am , and ^{244}Cm . As mentioned the DSSSD in front of P2 is removed for the calibration measurement.

7.3 Calibration of HPGe-detectors

As the aim of the experiment is to measure the beta-decay strength distribution, i.e. the beta-decay branching ratios, it is important to understand the absolute efficiency of the HPGe-detectors to high precision. As we also want to reconstruct the decay scheme by measuring coincidences between the silicon detectors and the HPGe-detectors we will also need to have a reliable energy calibration.

7.3.1 Energy

The HPGe-detectors we use are in the special clover configuration meaning that each of the four detectors consist of four germanium crystals, i.e. the detectors are segmented. Each of the 16 germanium crystals needs to be calibrated. However, as we are interested in measuring coincidences between the silicon and the HPGe-detectors we use the same data acquisition system, which unfortunately limits the energy resolution of the HPGe-detectors and results in relatively wide gamma-ray peaks (1085 keV gamma-ray from ^{152}Eu have a Gaussian width of 4.7 keV). This is caused by the much shorter shaping time normally used for silicon detectors while germanium detectors normally have a much longer shaping time as they are somewhat slower in transporting the signals.

All 16 crystals are energy calibrated using a ^{152}Eu source which have several intense gamma rays distributed over the region of energies that we are interested in. The energies used are taken from [Eu1 2015] and are as follows: 344.2785(12) keV, 778.9040(18) keV, 964.079(18) keV, 1085.869(24) keV, 1112.074(4) keV, and 1408.006(3) keV. An example spectrum can be seen on Figure 7.12 with the gamma-ray peaks used in the calibration marked by the Gaussian line shape fits. On Figure 7.13 is the residuals of the gamma-ray energy calibration shown for the same crystal.

7.3.2 Absolute efficiency

The absolute efficiency of a HPGe-detector is defined as the number of gamma-rays detected by the detector at a given energy relative to the total number of gamma-rays emitted by the source with the same energy. The absolute efficiency is different from the intrinsic efficiency of the detector as it is sensitive to the position of the detector with respect to the source as well as to the surroundings. In the surroundings of the detector there could be material which the gamma-rays will scatter on or attenuate in. This will of course influence the number of detected gamma-rays and therefore the absolute efficiency.

To do a proper absolute efficiency calibration we need a high statistics measurement with a source that covers the range of energies which are relevant for the present

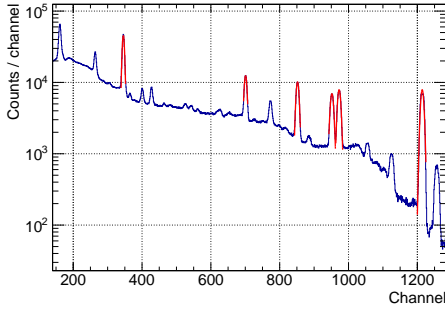


Figure 7.12: Example of a ^{152}Eu gamma-ray spectrum from crystal 1 in clover 1. The spectrum is not energy calibrated but all six calibration peaks are visible and the Gaussian fits to the peaks are also present.

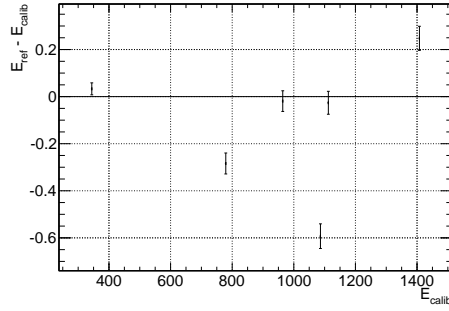


Figure 7.13: Example of residuals from the gamma-ray energy calibration of crystal 1 in clover 1. The calibration is made with a ^{152}Eu source.

experiment. For the beta-decay of ^{20}Mg we will be looking at gamma-rays with energies of 238 keV, 275 keV, 984 keV, 1232 keV, and 1298 keV. In order to cover the entire energy range we use a ^{152}Eu source. A list of the gamma-ray energies and the corresponding intensities used for the efficiency calibration is presented in Table 7.5. Due to the poor energy resolution of the HPGe-detectors we use the summed intensities of the 1085.869 keV and the 1089.737 keV gamma-rays which is $I_\gamma = 11.934(22)\%$. We also use the summed intensities of the 1109.174 keV and the 1112.074 keV gamma-rays which is $I_\gamma = 13.830(22)\%$.

For the calculation of the absolute efficiency at the measured gamma-ray energies it is necessary to know the total number of decays from the source during the measurement. This is given by the standard exponential decay law as

$$(\text{total number of decays}) = N(t=0) - N(t) = N_0 \cdot (1 - e^{-\lambda \cdot \Delta t}) \quad (7.3)$$

where λ is the decay constant and $\Delta t = 54660(120)$ s is the measurement time. The number of nuclei at the beginning of the measurement, N_0 , is determined from the activity of the source at the time of the measurement. From measurements made by the CERN Radioactivity Protection group we know the activity of the source at the 27th of March 2015 to be 16.40(33) kBq. This value for the activity can be extrapolated to the time of the measurement by using the standard exponential decay law. We get the following number for the activity

$$A = 16.31(33) \text{ kBq} \quad (7.4)$$

The line shape function used to describe the number of measured gamma-rays in

Table 7.5: ^{152}Eu gamma-ray energies and intensities according to [Eu1 2015] used for the efficiency calibration of the HPGe-detectors. Due to the poor energy resolution of the HPGe-detectors we use the summed intensities of the 1085.869 keV and the 1089.737 keV gamma-rays, $I_\gamma = 11.934(22)\%$, and for the 1109.174 keV and the 1112.074 keV gamma-rays, $I_\gamma = 13.830(22)\%$.

| E_γ (keV) | I_γ (%) |
|------------------|----------------|
| 244.6975 | 7.583(19) |
| 344.2785 | 26.5(4) |
| 778.904 | 12.942(19) |
| 867.378 | 4.245(19) |
| 964.079 | 14.605(21) |
| 1085.869 | 10.207(21) |
| 1089.737 | 1.727(6) |
| 1109.174 | 0.186(8) |
| 1112.074 | 13.644(21) |
| 1408.006 | 21.005(24) |

a given photo peak is given as

$$f(E) = p_0 + p_1 \cdot E + \int_{E_-}^{E_+} p_2 \cdot \frac{1}{\sqrt{2\pi} \cdot p_4} e^{-\left(\frac{E' - p_3}{p_4}\right)^2 / 2} \cdot dE' \quad (7.5)$$

$$= p_0 + p_1 \cdot E + p_2 \left[\text{Erf} \left(\frac{\left(E + \frac{p_5}{2}\right) - p_3}{p_4} \right) - \text{Erf} \left(\frac{\left(E - \frac{p_5}{2}\right) - p_3}{p_4} \right) \right] \quad (7.6)$$

where

$$\text{Erf}(x) = \frac{1}{\sqrt{2\pi}} \int_{-\infty}^x e^{-t^2/2} dt, \quad x = \frac{E - \mu}{\sigma} \quad (7.7)$$

The background is estimated as a linear function with parameters p_0 and p_1 . The peak is described with the HPGe-detector response function given as a normalized Gaussian distribution. The detector response function is integrated between E_- and E_+ , where $E_+ - E_- = p_5$, for the number of counts in a certain bin of the histogram. The parameter p_2 is the area of the peak, p_3 is the centroid of the Gaussian distribution, p_4 is the standard deviation of the Gaussian distribution, and p_5 is the bin width of the histogram. This is a simplified parameterization of the line shape, however, as long as the same function is used for the efficiency calibration and the estimation of the number of atoms collected, the result should be consistent.

In conclusion the absolute efficiency at the gamma-ray energy E_i is given as

$$\varepsilon(E_i) = \frac{\text{(number of counts in detector)}}{\text{(total number of decays)}} \left(\frac{I_{\gamma_i}}{100} \right)^{-1} \quad (7.8)$$

where the number of counts in the detector is given by the parameter p_2 in the fitting function in Equation (7.6), the total number of decays is given by Equation (7.3), and I_{γ_i} is the gamma intensity in per cent given in Table 7.5. Using (7.8) the efficiency is given as a dimensionless fraction.

Having determined the actual measured efficiencies of the 16 combined HPGe crystals at the eight different gamma-ray energies, see an example fit of the individual gamma-ray photo peaks on Figure 7.14, we can now make a combined fit of these measurements to an approximate efficiency function. We use a function of the following form to describe the absolute efficiency:

$$\varepsilon(E) = e^{p_0 + p_1 \cdot \ln(E)} \quad (7.9)$$

A fit with this function to the measured efficiencies is shown on Figure 7.15. The parameter values obtained from the fit is

$$p_0 = 0.869(81) \quad (7.10)$$

$$p_1 = -0.717(12) \quad (7.11)$$

$$\text{cov}(p_0, p_1) = -0.000988 \quad (7.12)$$

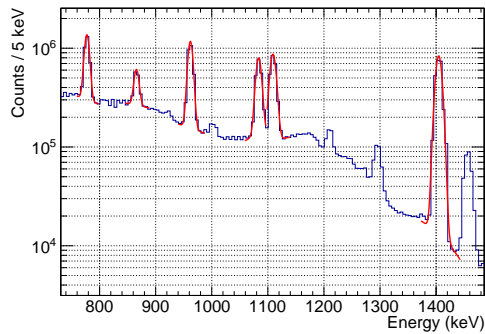


Figure 7.14: ^{152}Eu gamma-ray spectrum from the measurement for the absolute efficiency calibration. Several fits to the relevant peaks is shown.

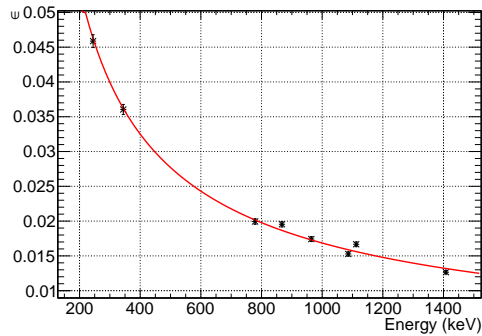


Figure 7.15: The measured absolute efficiencies at the energies summarized in Table 7.5. The best fit to the data points is shown with the analytic form presented in Equation (7.9).

The accuracy of the absolute efficiency function in Equation (7.9) is discussed on page 220-221 in [Debertin 1988]. By comparing the measured absolute efficiencies

with the values obtained from a function like Equation (7.9), it is established that deviations in the efficiency of up to 10% for gamma-ray energies above 200 keV are present. However, they also note that the deviations from the measured efficiencies will decrease in magnitude when the crystal size of the detector is increased. The deviations between the measured absolute efficiencies and the values obtained with Equation (7.9) can be explained with incomplete absorption of the gamma-ray in the crystal and with scattering of gamma-rays in the surroundings.

In order to take the deviations into account we will use the absolute efficiency function to determine a scaling factor R_{E_γ} , which we will use to transform the measured absolute efficiency at the gamma-ray energy $E_{\gamma,\text{meas.}}$ into an absolute efficiency at the interesting gamma-ray energy E_γ . As the analytical form in Equation (7.9) represents the overall behavior of the absolute efficiency this procedure should minimize the deviations in the absolute efficiency as long as the measured absolute efficiency closest in energy is used as reference point for the scaling factor. Figure 4.9 in [Debertin 1988] shows the measured deviations of the absolute efficiency from an efficiency function of the analytical form presented in Equation (7.9). The change in the deviation of the absolute efficiency between the two gamma-ray energies used for the scaling factor R_{E_γ} according to this figure will be used as an additional relative uncertainty when calculating the absolute efficiency at E_γ .

The above described procedure can be summarized in equations as

$$R_{E_\gamma} = \frac{\varepsilon(E_\gamma)}{\varepsilon(E_{\gamma,\text{meas.}})} \quad (7.13)$$

$$\varepsilon_{\text{corr.}}(E_\gamma) = R_{E_\gamma} \cdot \varepsilon_{\text{meas.}}(E_{\gamma,\text{meas.}}) \quad (7.14)$$

where $\varepsilon_{\text{meas.}}(E_{\gamma,\text{meas.}})$ is the measured efficiency at the energy $E_{\gamma,\text{meas.}}$, while $\varepsilon(E_\gamma)$ and $\varepsilon(E_{\gamma,\text{meas.}})$ are the absolute efficiencies as calculated with Equation (7.9) and the parameter values as obtained in the fit of the measured absolute efficiencies. The results of the rescaling of the absolute efficiency and the addition of the extra uncertainty due to the observed deviations between measured and calculated efficiencies can be found in Table 7.6.

Table 7.6: Calculation of the total absolute gamma-ray efficiency for the HPGe-detector array. R_{E_γ} is the scaling factor for the efficiencies. For the 238.27 keV and 275.09 keV gamma-rays we scale from the 244.6975 keV gamma-ray. For the 983.70 keV gamma-ray we scale from the 964.079 keV gamma-ray. For the 1232.47 keV gamma-ray we scale from the 1112.074 keV gamma-ray. For the 1297.73 keV gamma-ray we scale from the 1408.006 keV gamma-ray. The table includes two columns with $\varepsilon_{\text{corr.}}(E_\gamma)$ which is the corrected absolute efficiency. However, only the last column of $\varepsilon_{\text{corr.}}(E_\gamma)$ has the uncertainty corrected for the change in the deviation of the absolute efficiency as determined in Figure 4.9 in [Debertin 1988].

| E_γ (keV) | R_{E_γ} | $\varepsilon_{\text{corr.}}(E_\gamma)$ (%) | $\varepsilon_{\text{corr.}}(E_\gamma)$ (%) |
|------------------|----------------|--|--|
| 238.27 | 1.020(22) | 4.68(14) | 4.68(16) |
| 275.09 | 0.920(19) | 4.22(12) | 4.22(14) |
| 983.70 | 0.986(11) | 1.72(4) | 1.72(4) |
| 1232.47 | 0.929(12) | 1.55(4) | 1.55(4) |
| 1297.73 | 1.060(15) | 1.34(3) | 1.34(3) |

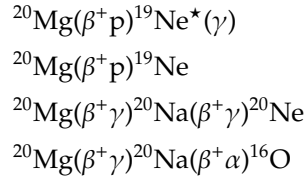
^{20}Mg : beta-delayed proton spectrum

As discussed in Chapter 6 one of the main reasons to measure the beta-decay of ^{20}Mg is to measure the beta-strength distribution with better precision and accuracy than done previously. For this purpose it is important to measure the beta-delayed protons with no significant kind of background signal. The first step towards obtaining accurate information on the beta-decay is to understand the data measured with the various detectors. In Sect. 8.1 we will describe how we take advantage of the silicon detector setup to do particle identification and how we produce clean particle spectra in general. As part of this work we will present proton and gamma-ray spectra from the beta-decay of ^{20}Mg as well as the alpha-particle spectrum from the beta-decay of ^{20}Na . In Sect. 8.2 we present how we use the clean proton spectra, that we produce in the first section, to determine the half-life of ^{20}Mg . The next step is to determine the center-of-mass energy of the beta-delayed protons in order to reconstruct the decay scheme - see Sect. 8.3. As the final states in ^{19}Ne are pairwise separated with ≈ 30 keV several beta-delayed proton branches will be contained in the observed proton peaks and knowledge of the components contained in one peak is needed for the reconstruction of the decay scheme. Hence, we will also present a classification of the proton peaks in Sect. 8.3 before we go on and present the reconstructed decay scheme of ^{20}Mg . In Sect. 8.4 we will present the relative intensity of the proton peaks. We will also determine a normalization factor from the known beta-delayed gamma-ray of 984 keV which we will use to calculate the absolute branching ratios of the individual proton branches. Finally, we will combine the knowledge of the reconstructed decay scheme with the absolute proton intensities in order to determine the beta-decay strength distribution.

8.1 Particle spectra

As discussed earlier the beam of ^{20}Mg produced at the ISOLDE facility at CERN is highly contaminated with ^{20}Na (average rate of ≈ 60 ^{20}Mg ions per second and ≈ 500 ^{20}Na ions per second implanted in the carbon foil), which also is produced in the

beta-decay of ^{20}Mg . It is therefore very important to be able to do proper particle identification in order to disentangle the two decays. The dominating decay modes for ^{20}Mg can be summarized as:



Other less intense decay modes are also energetically allowed like $\beta^+ \alpha$ and $\beta^+ \text{p} \alpha$, however, neither of these have been observed.

The main challenge of the experiment is therefore to do particle identification in order to disentangle the various decay modes from each other and to suppress the contamination. We are mainly interested in the ^{20}Mg beta-delayed proton emission which has a total branching ratio of 26.9(32)% (number is based on Table 2 in [Piechaczek 1995]). One simple way to disentangle the different components from each other are by making a clever choice for the detector setup. It has been designed in order to study the beta-delayed proton spectrum of ^{20}Mg by using mainly thin detectors in the front of the four charged particle telescopes as we discussed in Sect. 7.1. The silicon detector setup is shown on Figure 7.3.

The choice of thin front detectors will naturally give clean proton spectra in the back detectors due to the energy loss of charged particles in matter, see Sect. 3.2. The alpha-particles emitted in the beta-decay of ^{20}Na have laboratory energies ranging up to 5.7 MeV according to [Laursen 2013]. In Table 7.1 we presented an overview of the punch through laboratory energies for protons and alpha-particles in the front detectors of the four telescopes. From this property of the individual front detectors we know that all alpha-particles and nuclear recoils will stop in three out of the four front detectors. Looking at the data from the telescope with U4 and P1, see Figure 8.1, it is evident that only the protons punch through. This will also be the case for the telescope consisting of U3 and P3. Only for the front detector U2 will we expect to observe the very high energy alpha-particles to punch through and hence reach the back detector. This is clearly observed on Figure 8.2 where the alpha-particles that punch through are observed with energies above 2.8 MeV in U2 (along the vertical axis). However, by using the ΔE - E spectrum it is easy to disentangle protons and alpha-particles here (see the graphical gate drawn on Figure 8.2). Only in the case of the fourth front detector, U6, will all the beta-delayed protons be stopped due to its thickness. In conclusion, we have three back detectors with clean proton spectra (P1, P3, and U1) and several front detectors with a mixture of components which is much harder to deal with.

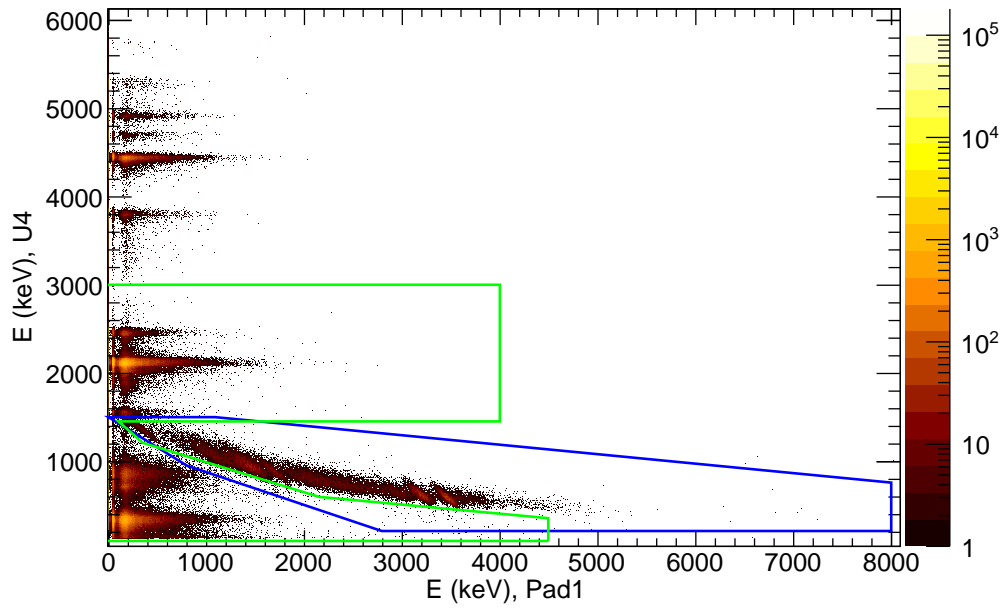


Figure 8.1: The ΔE - E spectrum from the U4-P1 telescope with no conditions applied to the data. The energies quoted are the measured proton energy in the detector. The closed blue line marks the applied graphical gate to produce a clean proton spectrum in pad 1. The closed green line marks the applied graphical gate to produce a clean proton spectrum in the U4 with no contribution from the particles that are not stopped here.

8.1.1 Proton spectra

To produce clean proton spectra in the back detectors we apply the graphical gates drawn on Figure 8.1 and 8.2. On Figure 8.3 we show the proton spectrum measured in the U1 detector which is constructed from the coincidence events between the detectors U1 and U2. These events have been matched in order to clear out the noise signals and only have real physics signals - see Sect. 7.2.3 for more details. In conclusion it means that the gates applied to produce this spectrum is the graphical gate in Figure 8.2 and a demand of particle multiplicity one in U1 which cuts away $\approx 1\%$ of the total number of events. With these cuts applied the proton spectrum will be very clean with no alpha-particle contribution and possibly a small contamination from beta-particles.

The proton spectrum measured in U1 is the one with the largest energy range from any of the back detectors simply due to the thickness of the front detector. It exhibits the same main features as the proton spectrum measured in [Piechaczek 1995] but we

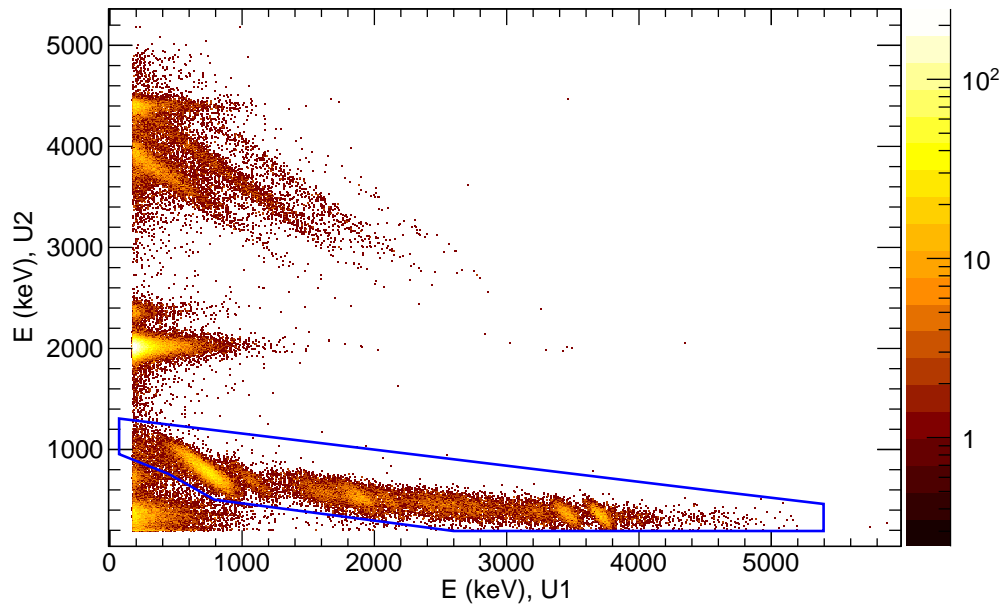


Figure 8.2: The ΔE - E spectrum from the U1-U2 telescope with the condition that the energy in U2 must be greater than 200 keV. The energies quoted are the measured proton energy in the detector. The closed blue line shows the applied graphical gate to produce a clean proton spectrum in U1. The alpha-particles that punch through U2 is visible below 3 MeV in U1 and above 2.8 MeV in U2. The data shown here have not been subjected to the matching routine of the U1 and U2 events as described in Sect. 7.2.3.

also observe structures that were not observed in the earlier measurement due to the larger statistics collected in this experiment. At energies above the proton peak p_{11} in Figure 8.3 we observe clear signs of a structure that was not observed in the previous measurement. This has to be decays going through resonances above the IAS in ^{20}Na as p_{11} is the ground state transition from the IAS. We assign the structure as being two distinct but broad proton branches and we name them p_I and p_{II} . Another region to highlight are the events located between p_8 and p_9 . This energy region appears to be structureless with no narrow peaks and only a contribution from some kind of broad resonances. However, due to the poor energy resolution of U1, $\sigma(\text{U1}) = 47.0(5)$ keV, it is not possible to give any firm conclusions. Finally, in between p_5 and p_6 we observe hints of another new proton branch which we name p_V .

The proton spectrum measured in P1 is shown on Figure 8.4. It is produced by applying the graphical gate shown on Figure 8.1 which picks out the protons that punch through the 40 μm thick front detector U4. This proton spectrum exhibits the

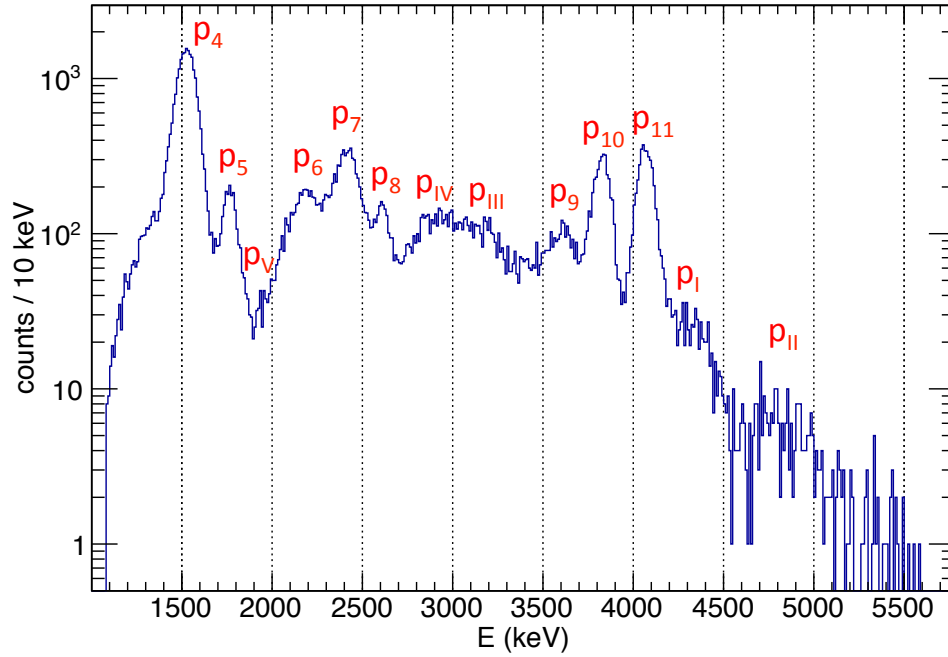


Figure 8.3: Proton spectrum measured in U1. The graphical gate shown in Figure 8.2 is applied to the data along with the condition of particle multiplicity one in U1. The signals in the U1 have been matched with the signal in U2, as to avoid the noise signals from U2. It is the measured sum energy of U1 and U2 that is shown, i.e. no corrections for dead layers have been made.

same features as observed in U1, however, the energy range is more limited due to the thicker front detector, that stops more of the low-energy protons ($40\ \mu\text{m}$ versus $20\ \mu\text{m}$). The energy resolution obtained in P1, $\sigma(\text{P1}) = 27.36(12)\ \text{keV}$, is better than what was achieved for U1 (see Table 7.2) and the proton peaks are visibly more narrow here. It is also important to note that the energy on Figure 8.4 is the center-of-mass energy while the energy on Figure 8.3 is the sum of the deposited energy in U2 and U1 with no energy loss corrections. This is evident as a offset between the two energy axes.

The proton spectrum measured in P1 have the same new features as observed in U1 when comparing with [Piechaczek 1995]. The region above p_{11} have evidence for what is believed to be two broad proton branches being emitted from resonances above the IAS in ^{20}Na (p_{I} and p_{II}). In the region between p_8 and p_9 we observe the same kind of broad structure as in U1. However, due to the better energy resolution of P1 the structure now appears to consist of two broad proton branches, which we will

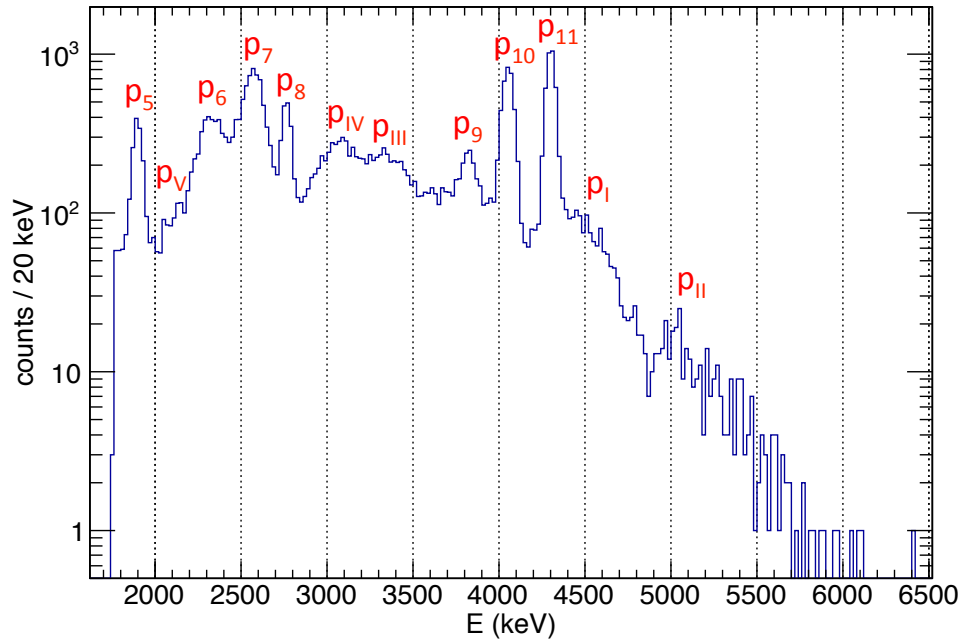


Figure 8.4: Proton spectrum measured in P1. The graphical gate shown on Figure 8.1 has been applied to the data in order to produce this spectrum. It shows the proton center-of-mass energy.

name p_{III} and p_{IV} . See Sect. 8.3 for a more detailed discussion of the interpretation. Finally, we also observe hints of p_{V} here.

On Figure 8.5 we present the data measured in detector U4 in terms of the proton center-of-mass energy. Three different spectra is shown according to three different gates applied to the data which we will use to do particle identification of the events. The spectrum with the highest number of counts (blue) is the data in Figure 8.1 submitted to the graphical gate drawn in the figure as a closed green curve. The gate removes particles that punch through U4 as they only deposit part of their energy here. It also cuts away the high energy alpha-particles as we are not interested in these anyway.

The second gate (the red spectrum on Figure 8.5) consists of the graphical punch through gate and an additional demand of $t < 100$ ms. As discussed in Sect. 1.4 the proton beam on the ISOLDE production target is pulsed with the pulse distance being a multiple of 1.2 s. We let the produced beam into the detection setup for the first 300 ms after proton impact on the ISOLDE production target in order to suppress the amount of sodium that comes into the detection chamber. As the half-lives for ^{20}Mg

and ^{20}Na are quite different, $T_{1/2}(^{20}\text{Mg}) = 90(6)$ ms and $T_{1/2}(^{20}\text{Na}) = 447.9(23)$ ms [Audi 2012], most of the produced ^{20}Mg will anyway have decayed by this time. The additional demand of $t < 100$ ms that is applied to the data will cut away a large fraction of the ^{20}Na beta-delayed alpha-particles. It will also cut away part of the ^{20}Mg events, however, due to the shorter half-life of ^{20}Mg a larger fraction of the produced ^{20}Mg as compared to ^{20}Na will survive the gate.

The effect of this extra time gate is particularly clear for the two overlapping peaks located between 600 and 1200 keV. With no time gate applied to the data we observe that the high-energy peak is the most dominant. However, when applying the time gate to the data we observe that the low-energy peak is the most intense. This behavior can only be explained if the low-energy peak belongs to the decay with the shorter half-life which is ^{20}Mg . Also the peak at ≈ 1.6 MeV appears to belong to the beta-decay of ^{20}Mg while the rest of the peaks most likely belong to the slower decay of ^{20}Na .

To further support this assignment we apply a third gate to the data in the U4-P1 telescope which consists of the graphical punch through gate, the time gate that we just discussed, and an additional demand of no observed particle events in the front detector of the opposing telescope, i.e. U3 (see Figure 7.3). The result of applying this combined gate to the data is shown as the green spectrum in Figure 8.5. It is very clear that the peaks in the spectrum we suspect to be from the decay of ^{20}Mg barely get affected by this additional gate while the peaks expected to be from the decay of ^{20}Na are heavily reduced.

The effectiveness of this multiplicity gate with respect to remove the ^{20}Na beta-decay products can be explained in terms of the energies available for the charged particle and the respective nuclear recoil emitted in the decay. In Table 8.1 and 8.2 we present the expected energies of the charged particle and the nuclear recoil as well as the range in the detector setup for the nuclear recoil from the ^{20}Na and ^{20}Mg beta-decays (see Sect. 8.1.2 for details). All the DSSSDs have a dead layer thickness of 0.1 μm on the frontside and the SSD have a dead layer thickness of 0.6 μm on the frontside according to Table 7.2. As a consequence, all of the ^{16}O nuclear recoils from the beta-decay of ^{20}Na will reach into the DSSSD's and deposit energy, whereas only the higher energy beta-delayed proton branches from ^{20}Mg will generate nuclear recoils that are capable of penetrating the dead layer of the DSSSDs. It means that a gate which demands no particle events to be observed in the opposing front detector almost exclusively will cut away ^{20}Na related events at the proton energies observed in U4.

Another effect to take into account when considering the effectiveness of this gate, is the fact that it is not enough for the recoils to just deposit some energy in the DSSSDs to be affected by the gate. As we demand that no particle events is to be

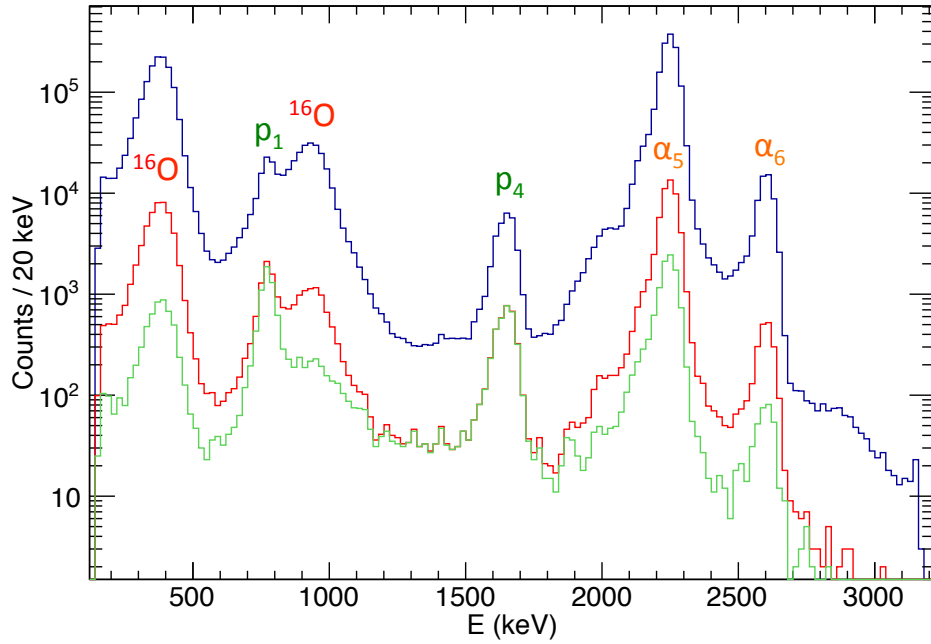


Figure 8.5: Three different proton spectra with the proton center-of-mass energy as measured in U4. *Blue:* Data from the U4-P1 telescope submitted to the graphical gate that cuts away events that punch through U4 (see green curve in Figure 8.1). *Red:* On top of the punch through gate for the blue spectrum we have also applied a time cut ($t < 100$ ms). *Green:* On top of the punch through gate and the time gate we have also applied the condition that the opposing front detector (U3) measures no particle events.

observed it means that the recoils need to be recognized as a particle event by the front-back matching routine described in Sect. 3.3.1.2. For the front-back matching routine to characterize an event as a particle, the front- and backside energies must fulfill the requirements imposed by the parameters quoted in Table 7.4 for the individual DSSSDs. As a consequence of $E_{\min}(\text{U3}) = 90$ keV, all the different ^{16}O nuclear recoils will potentially be accepted as particle events whereas only the ^{19}Ne nuclear recoils belonging to p_{10} and p_{11} will be recognized as particle events.

In conclusion, we can state with confidence that we have identified two of the peaks in the spectrum from U4 as being beta-delayed proton branches from the decay of ^{20}Mg . Based on their energy and intensity it has to be p_1 and p_4 . However, the much less intense beta-delayed proton branches p_2 and p_3 can not be clearly identified from the presented spectra. More sophisticated analysis methods are needed like e.g. the goodness-of-fit test of the time distributions described in Sect. 4.3. Unfortu-

Table 8.1: The laboratory alpha-particle energies, E_{α} , are taken from [Laursen 2013]. The ^{16}O laboratory energy, $E_{^{16}\text{O}}$, is calculated with Equation (8.3). Range of ^{16}O recoil in silicon after passing through $0.0545\ \mu\text{m}$ of carbon, i.e. the implantation depth of the Mg ion beam in the carbon foil, is calculated as described in Sect. 3.2. The last column, E_{det} , shows the remaining energy of the recoil after having passed the carbon and $0.1\ \mu\text{m}$ of silicon which is equivalent to the dead layer thickness on the DSSSD's.

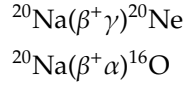
| Line | E_{α} (keV) | $E_{^{16}\text{O}}$ (keV) | Range (μm) | E_{det} (keV) |
|---------------|--------------------|---------------------------|-------------------------|------------------------|
| α_1 | 714(4) | 178.5(10) | 0.32 | 94.4 |
| α_2 | 847(5) | 211.8(13) | 0.39 | 125.2 |
| α_3 | 1220(30) | 305(8) | 0.56 | 209.7 |
| α_4 | 1589(5) | 397.3(13) | 0.71 | 291.8 |
| α_5 | 2153.2(10) | 538.3(3) | 0.91 | 415.7 |
| α_6 | 2483.5(25) | 620.9(7) | 1.01 | 488.3 |
| α_A | 2659(7) | 665(2) | 1.07 | 529.4 |
| α_7 | 3570(25) | 893(6) | 1.31 | 737.2 |
| α_8 | 3803.0(25) | 950.8(6) | 1.36 | 780.8 |
| α_9 | 4433.8(15) | 1108.5(4) | 1.50 | 919.9 |
| α_{10} | 4674.6(21) | 1168.7(5) | 1.55 | 979.9 |
| α_{11} | 4884.4(25) | 1221.1(6) | 1.60 | 1028.5 |
| α_B | 4930(6) | 1233(2) | 1.61 | 1039.1 |
| α_C | 5106(7) | 1277(2) | 1.64 | 1077.1 |
| α_{12} | 5253.5(23) | 1313.4(6) | 1.67 | 1107.5 |
| α_{13} | 5691(4) | 1422.8(10) | 1.75 | 1206.4 |

nately such work is for the future due to time constraints - see also chapter 9.

8.1.2 Alpha-particle spectra

As already discussed the beam implanted in the carbon foil inside the detection chamber is contaminated with ^{20}Na . The problem with ^{20}Na is the beta-delayed alpha-particle emission which has a total branching ratio of 20.48(23)% [Tilley 1998]. The alpha-particle spectrum have been studied by several experiments as for example described in [Laursen 2013]. To demonstrate that we really do observe the ^{20}Na beta-delayed alpha-particles we will produce as clean an alpha-particle energy spectrum as possible.

The beta-decay of ^{20}Na goes mainly by the two following decay paths



When the beta-delayed alpha-particles is emitted we will also have emission of the ^{16}O nuclear recoil from the break-up of the ^{20}Ne excited state due to the kinematics of the decay. Neglecting the small beta-decay recoil energy of the ^{20}Ne nucleus we can estimate the energy of the emitted alpha-particle and ^{16}O nuclear recoil from energy and momentum conservation to be:

$$E_\alpha = E_{\text{cm}} \cdot \frac{M(^{16}\text{O})}{M(^{16}\text{O}) + M(\alpha)} \quad (8.1)$$

$$E_{^{16}\text{O}} = E_{\text{cm}} \cdot \frac{M(\alpha)}{M(^{16}\text{O}) + M(\alpha)} \quad (8.2)$$

From these two expressions we get that:

$$E_{^{16}\text{O}} = E_\alpha \cdot \frac{M(\alpha)}{M(^{16}\text{O})} \approx 0.25 \cdot E_\alpha \quad (8.3)$$

The energy of the ^{16}O nuclear recoils can be found in Table 8.1. Based on these energies we have also calculated the range of the nuclear recoils in silicon after having passed through $0.0545 \mu\text{m}$ of carbon, i.e. the approximate implantation depth of the Mg ion beam in the carbon foil. We have also determined the energy of the nuclear recoils after having passed the carbon and $0.1 \mu\text{m}$ of silicon which is equivalent to the DSSSD frontside dead layer thickness. All of this can be found in Table 8.1. The equivalent relation for the energies of the ^{19}Ne nuclear recoils and the emitted protons are given as:

$$E_{^{19}\text{Ne}} = E_p \cdot \frac{M(p)}{M(^{19}\text{Ne})} \approx 0.053 \cdot E_p \quad (8.4)$$

A summary of the nuclear recoil energies can be found in Table 8.2.

As discussed earlier the ^{16}O recoils will have enough energy to be detected as particle events in all of the DSSSDs except in the case of α_1 and α_2 . Due to the front-back matching parameter E_{min} , see Table 7.4, they will only be identified as particles in some of the detectors. However, the main intensity of alpha-particles and the corresponding nuclear recoils will be observed as particle events in the front-back matching routine. At the same time it is only a subset of the beta-delayed proton branches that will have their corresponding nuclear recoil identified as a particle event. Therefore, we can take advantage of this difference to clearly identify the alpha-particle events in the total data set from ^{20}Mg .

On Figure 8.6 we show in the right part of the figure a spectrum of the particle energies in U4 (vertical axis) against the particle energies in U3 (horizontal axis), i.e.

Table 8.2: The center-of-mass proton energies, E_{cm} , are adopted from [Piechaczek 1995]. The laboratory energy of the ^{19}Ne nuclear recoils are calculated according to Equation (8.4). Range of ^{19}Ne recoil in silicon after passing through $0.0545\ \mu\text{m}$ of carbon, i.e. the implantation depth of the Mg ion beam in the carbon foil, is determined as described in Sect. 3.2. The last column, E_{det} , shows the remaining energy of the recoil after having passed the carbon and $0.1\ \mu\text{m}$ of silicon equivalent to the dead layer thickness on the DSSSD's. E_{det} is only assigned a value if the recoil actually have enough energy to pass through the carbon foil and the thin silicon layer.

| Line | E_{cm} (keV) | $E_{^{19}\text{Ne}}$ (keV) | Range (μm) | E_{det} (keV) |
|----------|----------------|----------------------------|-------------------------|------------------------|
| p_1 | 806(2) | 40.3(1) | 0.02 | |
| p_2 | 1056(30) | 52.8(15) | 0.04 | |
| p_3 | 1441(30) | 72.1(15) | 0.08 | |
| p_4 | 1679(15) | 84.0(8) | 0.10 | 1.3 |
| p_5 | 1928(16) | 96.4(8) | 0.13 | 11.4 |
| p_6 | 2344(25) | 117.2(13) | 0.17 | 30.1 |
| p_7 | 2559(45) | 128.0(23) | 0.19 | 39.6 |
| p_8 | 2884(45) | 144.2(23) | 0.22 | 55.2 |
| p_9 | 3837(35) | 191.9(18) | 0.31 | 102.5 |
| p_{10} | 4071(30) | 203.6(15) | 0.33 | 113.7 |
| p_{11} | 4326(30) | 216.3(15) | 0.36 | 125.7 |

two opposing front detectors. We have applied a gate to the data that demands a particle multiplicity of one in both detectors at the same time and that no events are observed in either of the two backing detectors. The events in the spectrum generally falls nicely along two lines with a slope that fits with the energy relation between ^{16}O recoils and alpha-particles, see Equation (8.3). It points to the conclusion that the events are real coincidences between the emitted alpha-particle and the ^{16}O nuclear recoil as the two are emitted approximately back-to-back due to momentum conservation. We observe similar distributions of events along the two axes. Both distributions are alpha-particles in coincidence with ^{16}O nuclear recoils, however, the distribution along the horizontal axis (no gate drawn around it) corresponds to the nuclear recoil being observed in U4, while the distribution along the vertical axis (a solid blue curve drawn around the data) corresponds to the nuclear recoil being observed in U3.

Applying the graphical gate drawn as the solid blue closed curve on the figure to the coincidence data produces the alpha-particle spectrum in the U4 detector as is shown on the left figure on Figure 8.6. This gate clearly reproduces the beta-

delayed alpha-particle spectrum from ^{20}Na with almost no background which is evident when comparing with the measurement presented in [Laursen 2013]. Only at energies below 1.4 MeV do we have contamination which most likely are the ^{16}O nuclear recoils as the two distributions start to overlap in this low-energy region, which is evident from the coincidence spectrum.

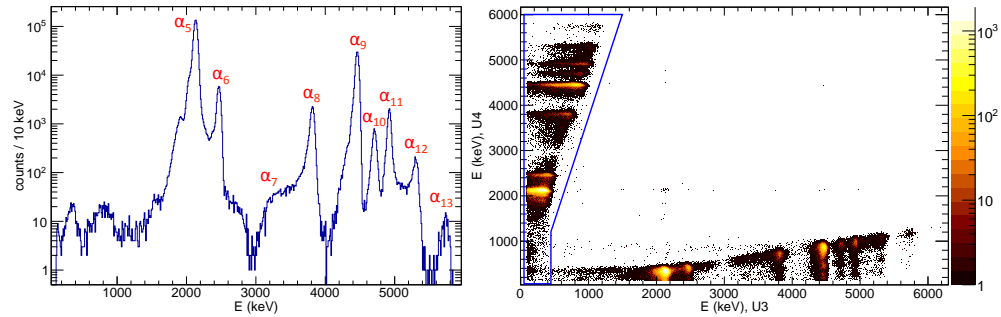


Figure 8.6: *Left:* Beta-delayed alpha-particle spectrum from the decay of ^{20}Na as measured in U4 with the deposited proton energy on the axis. It is produced by applying the gate shown on the figure to the right and by demanding particle multiplicity one in both detectors and demanding that no events are observed in the two backing detectors. *Right:* Coincidence spectrum between U4 and U3 with a demand of a particle multiplicity of one in both detectors and demanding that no events are observed in the two backing detectors. The closed blue line shows the graphical gate applied to remove the main part of the nuclear recoils.

8.1.3 Gamma-ray spectra

The setup for measuring the gamma-ray emission consisted of four HPGe-detectors with each of them being in a clover configuration, i.e. four germanium crystals in one clover detector giving a total of 16 germanium crystals. The total summed HPGe-clover spectra consists mainly of gamma-rays from the ^{20}Na beta-decay but also gamma-rays from the ^{20}Mg beta-decay is observed, see Chapter 6 for an overview of the gamma-rays emitted in the decays. On Figure 8.7 we present two different gamma-ray spectra which both are a subset of the total gamma-ray data.

The figure on the left is the total gamma-ray spectrum of all four HPGe-clover detectors but with the demand $t < 300$ ms. I.e. we only look at gamma-rays emitted during the first 300 ms after proton impact on the ISOLDE production target. The first of the three photopeaks marked (A) is the 511 keV gamma-ray from electron-positron annihilation which is expected to be observed. The second photopeak (B) is the 984 keV gamma-ray from the beta-decay of ^{20}Mg which has an intensity of $I_\gamma = 69.7(12)\%$ according to [Piechaczek 1995]. The third photopeak is the 1634 keV

gamma-ray (C) from the beta-decay of ^{20}Na which has an intensity of $I_\gamma = 79.44(27)\%$ according to [Tilley 1998]. From these gamma-ray data we observe ≈ 10 times more ^{20}Na than ^{20}Mg decays.

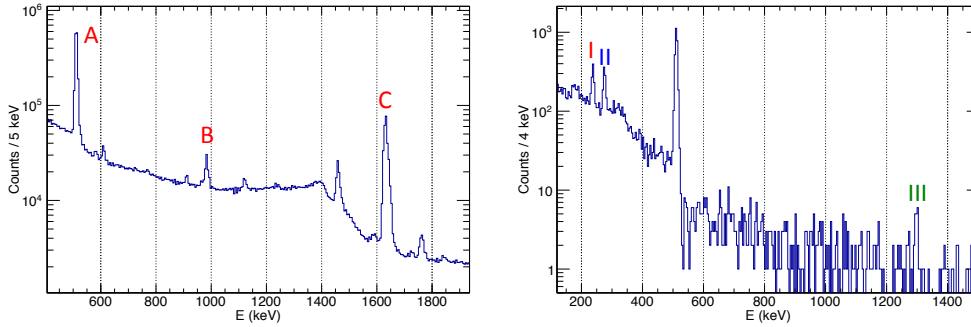


Figure 8.7: *Left:* Total gamma-ray spectrum from all crystals under the condition $t < 300$ ms. *Right:* Total data set from all crystals in coincidence with the protons measured in U1 as shown in Figure 8.3.

The figure on the right is the total gamma-ray spectrum of all four HPGe-clover detectors in coincidence with the protons in the detector U1. The proton spectrum as observed in U1 can be found on Figure 8.3. As expected the dominating gamma-ray is the 511 keV from electron-positron annihilation. More interestingly is it that we observe the 238 keV (I), the 275 keV (II), and the 1298 keV (III) gamma-rays which are emitted as transitions internally in ^{19}Ne from the excited states populated in the beta-delayed proton emission. For details see Chapter 6.

8.2 Half-life determination

We determine the half-life of ^{20}Mg from the time distribution of the proton spectrum observed in detector U1 which is shown on Figure 8.3. As discussed the events observed here will only be protons and beta-particles as the front detector with a thickness of 20 μm stops most of the alpha-particles and all of the nuclear recoils being emitted in the decay. The remaining alpha-particles have been removed with a graphical gate. The resulting time distribution is shown on Figure 8.8. It is fitted with a function describing the standard radioactive decay law

$$A(t) = \lambda \cdot N_0 \cdot e^{-\lambda \cdot t} \quad (8.5)$$

and the fitting parameters are minimized by the use of the MINOS error estimation technique in the MINUIT2 minimization package [James 2004]. We collect the ^{20}Mg

ions in the detection chamber only during the first 300 ms after proton impact on the ISOLDE target. Hence we limit the fitting interval to be between 300 ms and 1200 ms. The upper limit is chosen such that it coincide with one time the ISOLDE target proton beam pulse spacing of 1.2 s. At this upper limit there is no activity left.

We used a standard Poisson log-likelihood method for the fitting in order to include bins with zero counts. This method will generally give a more reliable fit when one is dealing with small count number (≈ 10 counts per bin or less). The resulting half-life determined from the fit is

$$T_{1/2} = 90.9(12) \text{ ms} \quad (8.6)$$

with a $\chi^2/\text{ndf} = 376/443 = 0.85$ which means that it is a good fit.

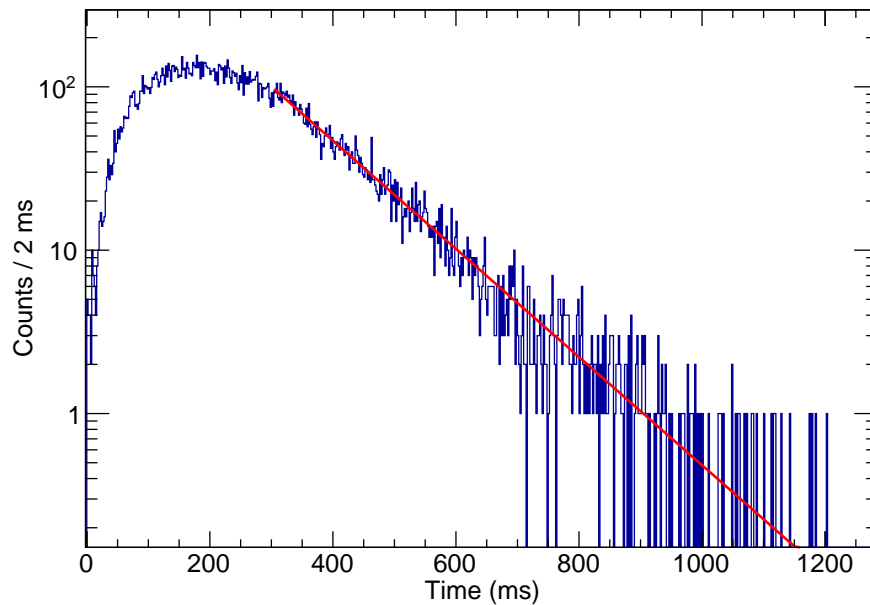


Figure 8.8: Half-life fit for the ^{20}Mg decay. The time distribution is from the U1 detector which is placed behind a $20\ \mu\text{m}$ thick silicon detector.

The latest evaluation of the half-life for ^{20}Mg quotes a value of $T_{1/2} = 90(6) \text{ ms}$, [Audi 2012], which is in agreement with the value determined here.

8.3 Decay scheme

In order to reconstruct the decay scheme of ^{20}Mg we need to investigate several aspects of the data presented in Sect. 8.1. First of all we need to know the center-of-mass energies of each of the proton branches. Second, as the detector energy resolution in terms of the Gaussian width σ of the proton spectra is large compared to the energy distance between the excited states in ^{19}Ne , the proton peaks will possibly contain several decay branches. To understand the contributions to all of the proton peaks we will perform a classification based on the gamma-rays measured in coincidence with the individual proton peaks. From this classification we will know whether the proton peak only has a decay branch going to the ground state of ^{19}Ne , only has decay branches going to excited states of ^{19}Ne , or if the proton peak has decay branches populating both the ground state and the excited states. Finally, we can reconstruct the decay scheme based on this knowledge and by using the complete picture of the low-energy ^{19}Ne resonances that is available from [Tilley 1995] together with the value $S_p(^{20}\text{Na}) = 2190.1(11)$ keV from [Wrede 2010].

8.3.1 Proton energies

Reconstruction of the proton energy: It is important to know the precise center-of-mass energies of the individual proton branches in order to reliably reconstruct the decay scheme. The center-of-mass energy spectra presented in Sect. 8.1 are all based on an event-by-event energy reconstruction routine which takes the deposited energy in the respective detector as starting point. From here we use the stopping power tables from [Ziegler 2008] together with the obtained knowledge of the detector setup from the geometry calibration to calculate the original laboratory energy of the protons. The laboratory energy can then easily be translated into a center-of-mass energy. This procedure is only applicable if the proton does not pass through any other detector first.

If the proton is stopped in one of the backing detectors, the first step is to add the energy lost in the dead layer on the frontside of the backing detector and the energy lost in dead layer on the backside of the front detector to the measured energy in the back detector, $E_1 = E_{\text{meas,Back}} + E_{\text{loss,1}}$. The second step is to add the energy measured in the front detector to the energy determined in the first step, $E_2 = E_1 + E_{\text{meas,Front}}$. The third step is to add the energy lost in the dead layer on the frontside of the front detector and the energy lost in the carbon foil to the energy from the second step, $E_3 = E_2 + E_{\text{loss,2}}$. The energy E_3 is the laboratory energy which then easily can be translated into the center-of-mass energy of the decay.

The energy loss in the dead layers are generally determined as described in Sect. 3.2. We take the rotation of the carbon foil with respect to the detector planes into

Table 8.3: Center-of-mass proton energies as measured in the various silicon detectors. The energy quoted is the centroid energy of the line shape function presented in Equation (4.7).

| Line | E_{cm} (keV), U1 | E_{cm} (keV), U3 | E_{cm} (keV), U4 | E_{cm} (keV), U5 | E_{cm} (keV), P1 | E_{cm} (keV), P3 | $\overline{E_{cm}}$ (keV) |
|-----------|--------------------|--------------------|--------------------|--------------------|--------------------|--------------------|---------------------------|
| p_1 | | 784.4(4) | 773.2(4) | 789.6(8) | | | 780(8) |
| p_4 | 1664.4(8) | 1657.8(6) | 1645.4(8) | | | | 1656(10) |
| p_5 | 1910.4(24) | 1904(2) | | | 1907.8(10) | | 1907(3) |
| p_V | | | | | 2138(6) | | 2138(6) |
| p_6 | 2344(10) | | | | 2334(3) | | 2335(3) |
| p_7 | 2574(3) | | | | 2566.0(12) | | 2567(4) |
| p_8 | 2776(4) | | | 2772.0(12) | 2764.0(12) | | 2768(6) |
| p_{IV} | | | | | 3084(6) | 3068(12) | 3081(12) |
| p_{III} | | | | | 3320(12) | 3320(6) | 3320(6) |
| p_9 | 3814(10) | | | | 3818(3) | 3804(11) | 3817(3) |
| p_{10} | 4048(2) | | | | 4052.0(8) | 4048(2) | 4051(2) |
| p_{11} | 4308.0(14) | | | 4308.0(8) | 4300.0(6) | 4304(2) | 4303(4) |
| p_I | 4572(20) | | | | 4510(22) | | 4544(25) |
| p_{II} | 5010(90) | | | | 4992(16) | | 4993(16) |

account when calculating the energy loss in the carbon foil. We use the position sensitivity of the DSSSDs to determine the angle of incidence of the protons with respect to the detectors and from this knowledge we gain more accurate information about the energy loss in the detector dead layers. To do this properly we need to use the position of the individual detectors with respect to the source position that was found in the geometry calibration. When reconstructing the center-of-mass energy we have assumed that all events are protons.

Line shape fit: With the proton center-of-mass energy spectra from the various detectors we can proceed to determine the energy of the individual peaks. To do this we use the line shape function in Equation (4.7) and we use the same fitting procedure as described in Sect. 4.4 for the ^{21}Mg data.

The first step is to determine the detector energy resolution by fitting a well-known and narrow proton peak with the Breit-Wigner width parameter Γ fixed to the total width of the resonance emitting the proton. As the beta-decay of ^{21}Mg is much better understood than the beta-decay of ^{20}Mg we use the ^{21}Mg data to determine σ except in the case of the thin detectors U2 and U4. For these two detectors we use the ^{20}Mg beta-delayed proton branch p_1 as it is a high intensity transition at relatively low energy emitted from the 2987(2) keV 1^+ resonance in ^{20}Na with a total width $\Gamma_{\text{tot}} = 20(2)$ keV.

For the remaining detectors we use a combination of the beta-delayed proton branches p_{10} , p_{11} , p_{22} , and p_{27} from the decay of ^{21}Mg with the Breit-Wigner width parameter Γ fixed to the total width Γ_{tot} as presented in Table 4.3. For the detector P1 we use the proton branches p_{11} , p_{22} , and p_{27} to make a weighted average of the energy resolution. For the detector P3 we use the proton branches p_{22} and p_{27} . For the detector U1 we use the proton branches p_{11} , p_{22} , and p_{27} . For the detector U3 we use the proton branches p_{10} and p_{11} . For the detector U5 we use the proton branches p_{11} , p_{22} , and p_{27} . Finally, for the detector U6 we use the proton branches p_{11} , p_{22} , and p_{27} but it turns out that the energy resolution varies too much with the energy to make an average. For all the detectors we use the weighted average of the determined values for σ as the real energy resolution. We do not measure the energy resolution of P2 as only beta-particles reach this detector. The resulting values can be found in Table 7.2.

The second step of the fitting procedure is to fix the parameter σ and keep the rest of the parameters free so they can be determined by the minimization routine. The energy resolution could change as a function of the energy but we do not take this effect into account. This fitting procedure should give accurate and precise proton energies of the peaks, however, in many cases the peaks contain several proton branches and we therefore only gain information about the weighted average center-of-mass energy.

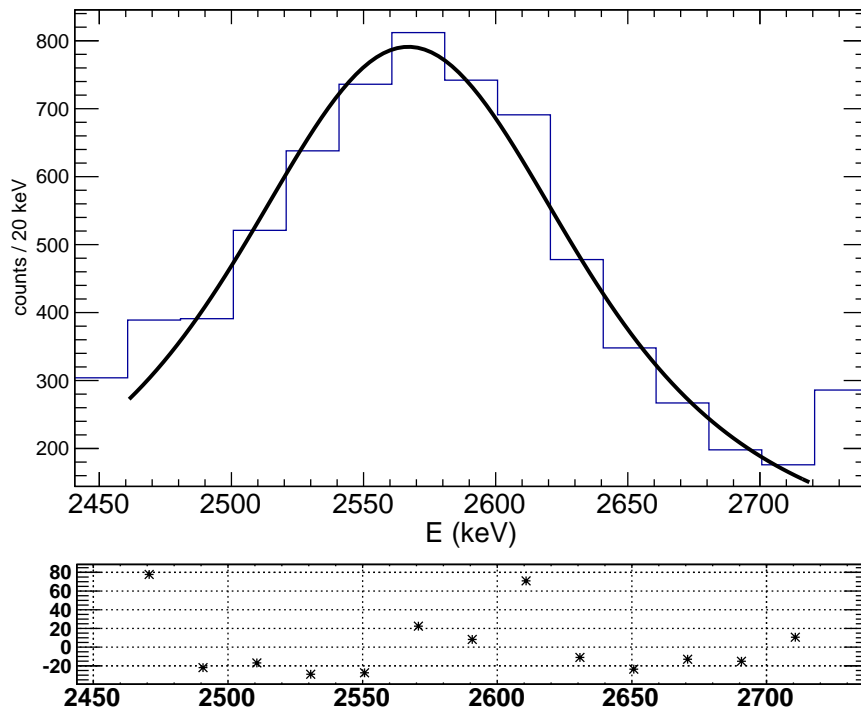


Figure 8.9: Example of a line shape fit of the proton branch p_7 in detector P1 with the line shape function described in Equation (4.7). The fit results in $\chi^2/\text{ndf} = 31.93/10$. The residuals from the fit is shown below with the same energy scale as the data. The uncertainty of the residuals are not shown.

The energy spectra of the different detectors were divided into smaller regions to be able to fit the proton peaks individually. At all times we assumed the background level to be zero. An example of a fit can be seen on Figure 8.9. The high value of χ^2/ndf is mainly due to a simplified response function of the detector which is not sufficiently accurate in especially the tail of the peak.

The proton center-of-mass energies determined from this procedure are presented in Table 8.3. The results from all the detectors are collected and compared here. In the last column the weighted average of the energies have been computed. The uncertainty quoted for the weighted average energy is in several cases an estimate (p_1 , p_4 , p_5 , p_7 , p_8 , p_{IV} , p_{10} , p_{11} , and p_I).

Gamma-ray gated proton spectra: To obtain more precise knowledge about the components contained in the individual proton peaks, we have for several of the

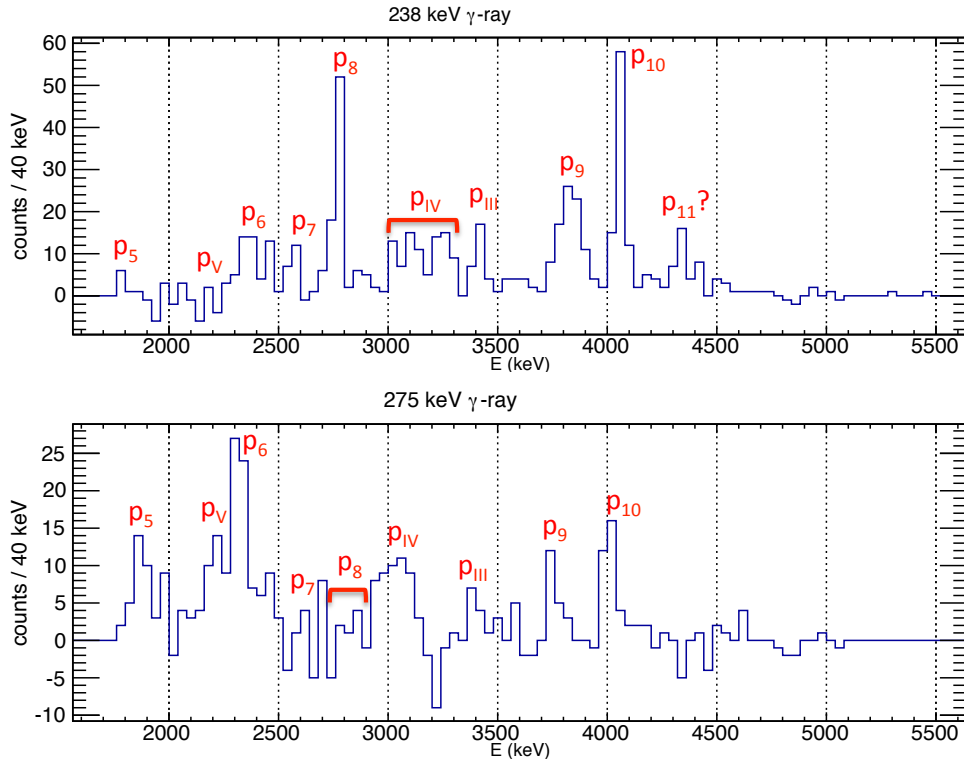


Figure 8.10: Gamma-ray gated proton spectra from P1 with the background from the Compton continuum of the 511 keV gamma-ray subtracted. It is the proton center-of-mass energy. *Top:* Proton spectrum from P1 in coincidence with the 238 keV gamma-ray. It is uncertain whether we observe coincidences with p₁₁. *Bottom:* Proton spectrum from P1 in coincidence with the 275 keV gamma-ray.

silicon detectors made gamma-ray gates in order to know, which proton peaks are in coincidence with the 238 keV and the 275 keV gamma-rays, respectively. When analyzing the proton spectra generated by gating on one of the two gamma-rays, it is important to be aware of the background contribution from the Compton continuum of the 511 keV gamma-ray. This gamma-ray will be emitted in every β^+ -decay when the positron annihilates with an electron in the surroundings. We have therefore subtracted a background spectrum from the 238 keV and 275 keV gamma-ray gated proton spectra. The three energy gates applied to the gamma-ray data all has the same width in terms of energy and the background gate is placed between the two gamma-rays. The energies determined from investigations of such spectra can be found in Table 8.4, however, the energies quoted in the table from the detector U5 is from the non-gated spectra as the energy resolution is very good here ($\sigma(\text{U5}) = 13.9(2)$ keV).

Table 8.4: Gamma-ray coincident proton center-of-mass energies. The upper value of the energies is the 238 keV gamma-ray coincident proton, while the lower one is the 275 keV gamma-ray coincident proton. The energies from U5 is not gamma-ray gated as the energy resolution here is so good that we can distinguish the individual branches contained in the proton peaks. The uncertainty on the weighted average energy for p_4 , p_5 , and p_V are estimated on the basis of the energy spread between the detectors. It is uncertain whether we observe evidence for p_{11} in coincidence with the 238 keV gamma-ray.

| Line | E_{cm} (keV), U1 | E_{cm} (keV), U5 | E_{cm} (keV), P1 | E_{cm} (keV), P3 | $\overline{E_{cm}}$ (keV) |
|-----------|--------------------|--------------------|--------------------|--------------------|---------------------------|
| p_1 | | | | | |
| p_4 | 1580(20) | 1673.6(22) | | | 1672(40) |
| | 1600(40) | 1622(4) | | | 1622(4) |
| p_5 | 1900(20) | 1857(8) | 1780(20) | | 1853(40) |
| | 1940(20) | 1906(5) | 1860(20) | | 1905(5) |
| p_V | 2060(20) | | 2180(20) | | 2120(50) |
| | 2020(20) | | 2220(20) | | 2120(70) |
| p_6 | 2340(20) | | 2360(40) | | 2344(18) |
| | 2340(20) | | 2300(20) | | 2320(14) |
| p_7 | 2540(20) | | 2580(20) | | 2560(14) |
| | 2620(20) | | 2620(20) | | 2620(14) |
| p_8 | 2800(40) | | 2780(20) | 2780(20) | 2782(13) |
| | 2720(40) | | 2820(40) | 2860(20) | 2830(16) |
| p_{IV} | 3060(40) | | 3140(60) | 3100(20) | 3096(17) |
| | 2980(20) | | 3060(20) | 3060(20) | 3033(12) |
| p_{III} | 3200(70) | | 3420(20) | 3200(70) | 3389(19) |
| | 3500(80) | | 3380(20) | 3400(50) | 3389(18) |
| p_9 | 3820(20) | | 3820(20) | 3820(20) | 3820(12) |
| | 3820(60) | | 3740(20) | 3820(20) | 3782(14) |
| p_{10} | 4040(20) | | 4060(20) | 4060(20) | 4053(12) |
| | 4020(20) | | 4020(20) | 4060(20) | 4033(12) |
| p_{11} | | | ? | | |
| p_I | | | | | |
| p_{II} | | | | | |

The two gamma-rays, the 238 keV and the 275 keV, are emitted when ^{19}Ne decays from the first or second excited state to the ground state. If the third and fourth excited state of ^{19}Ne is populated these will decay by gamma-ray emission to the second and the first excited state, respectively. I.e. a gamma-ray of 1232 keV connects the third and second excited state, while a gamma-ray of 1298 keV connects the fourth and first excited state. The third and fourth excited states only have low intensity decay branches directly to the ground state if they have any.

Examples of the background subtracted gamma-ray gated proton spectra from P1 can be seen on Figure 8.10. The spectra exhibits many small bumps, which might be significant proton peaks but more clear proton peaks are also visible. However, the number of counts in the coincidence spectra limits the reliability of the determination of the proton center-of-mass energy. The energies of the peaks and bumps in the spectra have been determined either by fitting with a standard Gaussian distribution or by simply taking the center value of the most intense bin in the local region of the peak. If a single bin contains more events than the others in the peak, the uncertainty have been set equal to 20 keV as the bin width is 40 keV. If two bins contains the same number of counts the uncertainty have been set equal to 40 keV.

Having determined the energy of the individual peaks, they have been sorted, such that for a given silicon detector one proton peak from the 238 keV gamma-ray coincident proton spectrum have been paired with a proton peak from the 275 keV gamma-ray coincident proton spectrum. The condition used for the pairing of the two proton peaks are that the proton energies are sufficiently close in energy to originate from the same resonance in ^{20}Na . The energies determined in this way are presented in Table 8.4.

8.3.2 Classification of proton peaks

As already mentioned several times the proton peaks will contain several decay branches. This is due to the structure of the particle daughter nucleus ^{19}Ne which have the four lowest excited state energies 238.27(11) keV, 275.09(13) keV, 1507.56(30) keV, and 1536.0(4) keV, [Tilley 1995]. As a result pairwise beta-delayed proton branches emitted from the same resonance in ^{20}Na will only be separated by ≈ 30 keV. This is too small an energy difference to be observed as two distinguishable peaks with the energy resolution obtained in the current experiment. Therefore we have constructed gamma-ray spectra with the condition that the events are in coincidence with the individual proton peaks. An example can be seen on Figure 8.11.

We use these proton gated gamma-ray spectra to classify the proton peaks. We determine the number of counts in the gamma-ray peaks using the same line shape as we used in the efficiency calibration of the HPGe-detector array, see Equation (7.6), and we correct the number of counts for the absolute efficiency. The total number of

Table 8.5: The ratio R as measured in the individual detectors. The classification is made according to the description in the text (A: only ground state transition, B: only excited state transition, C: mixture).

| Line | R_{U1} | R_{U3} | R_{U4} | R_{P1} | R_{P3} | Classification |
|-----------|----------|----------|----------|----------|----------|----------------|
| p_1 | | 0.00 | 0.02(2) | | | A |
| p_4 | 0.31(3) | 0.30(7) | 0.34(6) | | | C |
| p_5 | 0.16(8) | 0.00 | | 0.60(17) | | C |
| p_V | 2.0(19) | | | 3.5(29) | | B |
| p_6 | 2.02(28) | | | 2.43(30) | | B |
| p_7 | 0.41(9) | | | 0.38(10) | | C |
| p_8 | 2.5(8) | | | 0.85(11) | | B |
| p_{IV} | 3.5(5) | | | 3.21(43) | 1.42(22) | B |
| p_{III} | 3.86(83) | | | 3.17(68) | 0.89(31) | B |
| p_9 | 3.5(5) | | | 3.70(59) | 1.54(37) | B |
| p_{10} | 1.34(14) | | | 1.07(12) | 0.75(16) | B |
| p_{11} | 0.22(8) | | | 0.28(9) | 0.00 | A |
| p_I | 0.46(31) | | | 0.32(9) | 0.00 | ? |
| p_{II} | 0.29(77) | | | 0.50(19) | 0.00 | ? |

For p_5 we obtain varying results between the detectors. The result from U3 of $R = 0.0$ is not reliable as the front detectors are suffering from large amounts of contamination and the intensity of p_5 is too low to give rise to a clear peak, see Figure 8.5. On the basis of the remaining two detectors and the results of [Piechaczek 1995] we assign p_5 as consisting of both ground state and excited state transitions.

For p_{11} we suspect that the small amount of gamma-rays observed in coincidence with the detectors U1 and P1 mainly comes from the broad proton peak p_I . Therefore we assign p_{11} as being a pure ground state transition.

Finally for p_I and p_{II} the classification does not give any conclusive results. More statistics are needed to give a clear classification of the components contained in the two peaks. However, from the data we observe clear evidence for an interference minimum between the two peaks, which points to the fact that they populate the same final state in ^{19}Ne . They also have to be emitted from states above the IAS in ^{20}Na as p_{11} is the ground state emission from the IAS. Hence, p_I and p_{II} are assigned as ground state transitions from highly excited states in ^{20}Na . Considering the broad nature of both peaks, however, it can not be excluded that more components are present here.

Table 8.6: The ^{20}Na energies are taken from [Piechaczek 1995, Tilley 1998, Wallace 2012a, Wallace 2012b, Glassman 2015]. The 7183(16) keV resonance is either the ≈ 6920 keV or the ≈ 7440 keV resonance which are observed by [Piechaczek 1995]. Two previously unobserved resonances in ^{20}Na have been introduced at 5507(10) keV and at 5836(13) keV. The position of p_2 and p_3 are based on previous experiments as we do not observe any clear evidence for these. It is mainly due to the contamination from the beta-decay of ^{20}Na in the front detectors.

| $E^*(^{20}\text{Na})$ (keV) | $\overline{E}_{\text{meas.}}^*$ (keV) | ^{19}Ne resonances (MeV, I^π) | | | | |
|-----------------------------|---------------------------------------|---|----------------|----------------|----------------|----------------|
| | | 0.0, $1/2^+$ | 0.238, $5/2^+$ | 0.275, $1/2^-$ | 1.508, $5/2^-$ | 1.536, $3/2^+$ |
| 0.0, T= 1 | | | | | | |
| 984.25(10) | | | | | | |
| 2647(3) | | | | | | |
| 2987(2) | 2970(8) | p_1 | | | | |
| 3077(2) | | p_2 | | | | |
| 3871(9) | 3846(10) | p_4 | p_3 | p_3 | | |
| 4123(16) | 4094(2) | p_5 | p_4 | p_4 | | |
| ≈ 4800 | 4760(4) | p_7 | p_6 | p_6 | | |
| | 5507(10) | | p_{IV} | p_{IV} | | |
| ≈ 5600 | 5604(5) | | | | p_5 | p_5 |
| | 5836(13) | | p_{III} | p_{III} | p_V | |
| 6266(30) | 6273(7) | | p_9 | p_9 | p_7 | p_7 |
| 6498.4(5), T= 2 | 6496(3) | p_{11} | p_{10} | p_{10} | p_8 | p_8 |
| ≈ 6770 | 6734(25) | p_I | | | | |
| | 7183(16) | p_{II} | | | | |

8.3.3 Reconstruction of the decay scheme

We will now proceed with the reconstruction of the decay scheme on the basis of the information presented so far. In Sect. 8.4 we will discuss the relative intensity of the individual components, translate them into absolute intensities, and construct the beta-decay strength distribution.

For the construction of the decay scheme we take as a starting point the fair assumption that no new states are to be introduced in the particle daughter ^{19}Ne . Then we use the measured center-of-mass energies and the classification of the proton peaks in order to place them in the decay scheme. When placing beta-delayed proton branches to the excited states, we need to consider if they go to the first and second excited state or to the third and fourth excited state. To distinguish between the two options we look at the energy of the paired proton lines from the gamma-ray gated proton spectra in Table 8.4. We compare these with knowledge of the gamma-ray decay sequence of the third (1232 keV+275 keV gamma-rays) and fourth (1298 keV+238 keV gamma-rays) excited state as presented in Chapter 6. If the proton branch emitted in coincidence with the 238 keV gamma-ray has higher energy than the proton branch

(from the same ^{20}Na resonance) emitted in coincidence with the 275 keV gamma-ray, we can place the two proton branches as transitions to the first and second excited state, respectively. If it is the reverse situation with respect to their energies, we know that the beta-delayed proton branches must populate the third and the fourth excited state due to the known gamma-ray de-excitations.

As discussed in the last section on the classification of the proton peaks, p_I and p_{II} are interpreted as ground state transitions only. The same goes for p_{11} . However, we observe some gamma-rays from the decay of ^{20}Mg in coincidence with this region of the proton spectrum which points to the presence of decay branches to excited states in ^{19}Ne . Unfortunately we do not have enough statistics to clarify this completely so we assume the only strength here are the ground state transitions.

The measured center-of-mass energy of p_{II} and the assignment as a ground state transition leads us to a parent resonance at an excitation energy of 7183(16) keV in ^{20}Na . Comparing with the previous work of [Piechaczek 1995] it becomes clear that this resonance can be assigned as either the 6920(100) keV or the 7440(100) keV resonance. However, the uncertainty on the excitation energy of these two resonances makes it impossible to assign p_{II} with absolute certainty to either of the two resonances. Hence, we include the 7183(16) keV resonance as a new resonance in the decay scheme.

For the region between p_8 and p_9 we clearly observe some kind of broad structure as can be seen on Figure 8.3 and 8.4. Looking at the gamma-ray gated proton spectra on Figure 8.10 it seems like this region potentially could contain several narrow proton branches. This would mean the presence of several so far unobserved resonances in ^{20}Na which is not unlikely. However, as we do not have sufficient statistics to make such a claim, we will keep with the simpler interpretation that the region contains two new broad resonances at 5507(10) keV and 5836(13) keV which are responsible for the proton peaks p_{III} and p_{IV} . The hints of the new proton peak p_V between p_5 and p_6 , as is observed on Figure 8.3 and 8.4, can be explained as a proton emission from the 5836(13) keV resonance to the third excited state in ^{19}Ne . It further supports the introduction of the 5836(13) keV resonance.

The final reconstruction of the decay scheme for ^{20}Mg can be seen in Table 8.6 and on Figure 8.12. The energy levels in ^{19}Ne on the figure are quoted on the basis of the most recent measurement of the proton separation energy of ^{20}Na , $S_p(^{20}\text{Na}) = 2190.1(11)$ keV, [Wrede 2010]. In both the table and the figure we also quote the most recent value for the excitation energy of the IAS in ^{20}Na , $E_{IAS}(^{20}\text{Na}) = 6498.4(5)$ keV, [Glassman 2015]. The figure also quotes the most recent Q -value, $Q_{EC} = 10627.1(23)$ keV, as measured by [Glassman 2015]. The measured weighted average energies of the ^{20}Na resonances, $\overline{E_{\text{meas}}^*}$, have estimated uncertainties quoted, because the spread in energy is too large in some cases, to make a naive uncertainty estimate based on the

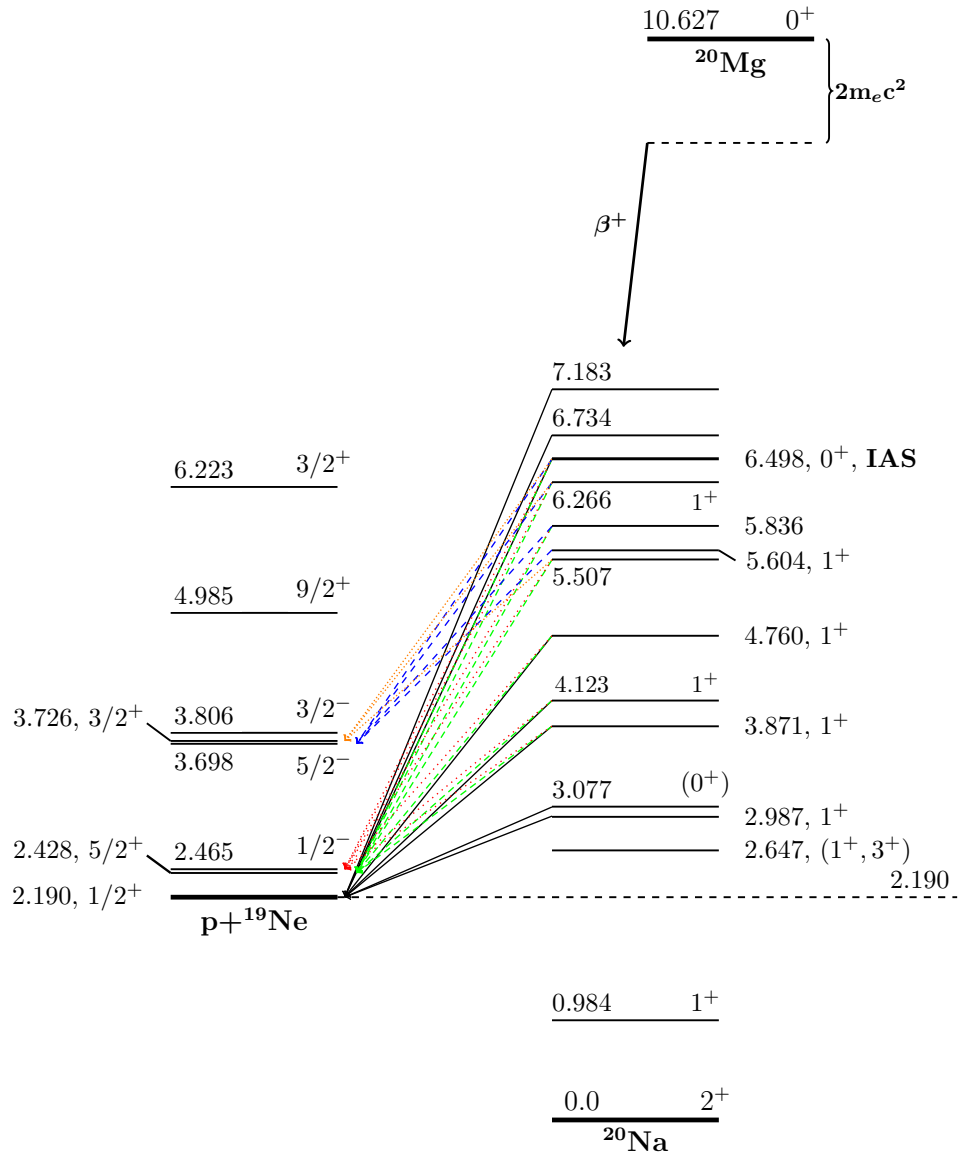


Figure 8.12: Decay scheme for ^{20}Mg including p_2 and p_3 which are not observed here. Also presented in Table 8.6. The different types of lines connecting ^{20}Na and ^{19}Ne indicate proton branches to different final states. The ground state transitions are solid black, the first excited state transitions are dashed green, the second excited state transitions are dotted red, the third excited state transitions are dashed blue, and the fourth excited state transitions are dotted orange.

Table 8.7: Summary of the relative intensity of the proton peaks observed in the different detectors. The columns 2-4 are relative intensities with respect to p_4 . The columns 5-7 are relative intensities with respect to p_{11} .

| Line | $I_{\text{rel},p_4}^{\text{U1}}$ (%) | $I_{\text{rel},p_4}^{\text{U3}}$ (%) | $I_{\text{rel},p_4}^{\text{U4}}$ (%) | $I_{\text{rel},p_{11}}^{\text{U1}}$ (%) | $I_{\text{rel},p_{11}}^{\text{P1}}$ (%) | $I_{\text{rel},p_{11}}^{\text{P3}}$ (%) |
|-----------|--------------------------------------|--------------------------------------|--------------------------------------|---|---|---|
| p_1 | | 129.9(44) | 141.5(47) | | | |
| p_4 | 100.0(11) | 100.0(27) | 100.0(29) | 577(13) | | |
| p_5 | 6.26(29) | 8.5(9) | | 36.1(18) | 35.8(17) | |
| p_V | 0.18(12) | | | 1.04(68) | 2.5(9) | |
| p_6 | 7.62(41) | | | 44(3) | 49.2(27) | |
| p_7 | 20.8(5) | | | 120(4) | 144(4) | |
| p_8 | 4.27(29) | | | 24.6(18) | 99.5(28) | |
| p_{IV} | 4.99(40) | | | 28.8(24) | 36.4(28) | |
| p_{III} | 2.86(44) | | | 16.5(26) | 15.9(24) | |
| p_9 | 3.21(29) | | | 18.5(17) | 17.6(18) | 20.2(23) |
| p_{10} | 15.96(38) | | | 92.1(29) | 91.5(30) | 89.1(31) |
| p_{11} | 17.34(40) | | | 100.0(31) | 100.0(31) | 100.0(33) |
| p_I | 2.15(14) | | | 12.4(9) | 31.3(14) | 33.9(14) |
| p_{II} | 1.03(11) | | | 5.9(7) | 3.95(76) | 6.0(8) |

weighted average formula.

8.4 Beta-decay strength distribution

Now that we have reconstructed the decay scheme of ^{20}Mg and identified all decay branches, we can proceed with the determination of the beta-decay strength distribution in terms of the $\log(ft)$ -values for the individual resonances in ^{20}Na . In order to obtain this knowledge we need to first determine the relative intensities of the decay branches. Second, we must calculate a normalization factor to translate the relative intensities into absolute intensities. Finally, we can calculate the absolute beta-decay branching ratios and the corresponding $\log(ft)$ -values.

8.4.1 Relative intensities

To construct the relative intensities we first extract the number of proton counts in the individual peaks. We determine this as the number of events inside the energy interval which surrounds the proton peak. From this value we subtract an estimate for the background contribution to reach the final number of proton counts in the

individual peaks. Here the background contribution is the tails of the surrounding proton peaks, which are estimated on the basis of the decay scheme. It means that we include interference effects in the background contribution estimates. In Table 8.7 we present the relative intensities constructed on the basis of these numbers. We use both p_4 and p_{11} as reference points in order to compare the values across all detectors.

It is immediately clear that the relative intensities with respect to p_4 are consistent between the different detectors. For the relative intensities with respect to p_{11} we observe diverging numbers for p_8 , which we can explain with a too large background subtraction in U1 due to the poor energy resolution in this detector (see the line shape of p_8 on Figure 8.3 and 8.4). The value for p_1 in the detector U1 also disagrees with the detectors P1 and P3. Otherwise the relative intensities agree fairly well when comparing the values measured in the various detectors.

8.4.2 Absolute normalization with the 984 keV gamma-ray

In order to translate the relative intensities into absolute intensities we will use the 984 keV gamma-ray from ^{20}Na to determine how many ^{20}Mg ions we have implanted in the carbon foil of the detector setup. The 984 keV gamma-ray has a well-known absolute intensity $I_\gamma = 69.7(12)\%$ which has been measured by [Piechaczek 1995].

The first step towards an absolute normalization factor is to determine the absolute efficiency of the combined HPGe-detector array at a gamma-ray energy of 984 keV. This has been done in Sect. 7.3.2 where the results have been summarized in Table 7.6. The final absolute efficiency for the total HPGe-detector array is determined to be 1.72(4)%.

The second step is to determine the number of observed 984 keV gamma-rays. According to gamma-ray background measurements we know that the 984 keV gamma-ray will be contaminated with a 969 keV gamma-ray from ^{228}Ac which belongs to the natural background. To get around this obstacle we produce two different gates which we apply to the total gamma-ray spectrum. The first gate is a demand to have a coincident event in one of the silicon back detectors (i.e. P1, P2, P3, U1, or U5) which should reduce the background contribution considerable. The resulting gamma-ray spectrum can be seen as the top spectrum on Figure 8.13. The second gate is a time gate that demands to only use events from within the first 300 ms after proton impact on the ISOLDE production target. The resulting gamma-ray spectrum can be seen as the bottom spectrum on Figure 8.13. To determine the total number of observed 984 keV gamma-rays correctly, we have to be aware of the fact that the applied gates will have reduced the total number of 984 keV gamma-rays by an unknown fraction. We need to first determine this fraction in order to find the true number of gamma-rays observed.

The gate that demands a coincident observation of a particle in either P1, P2, P3,

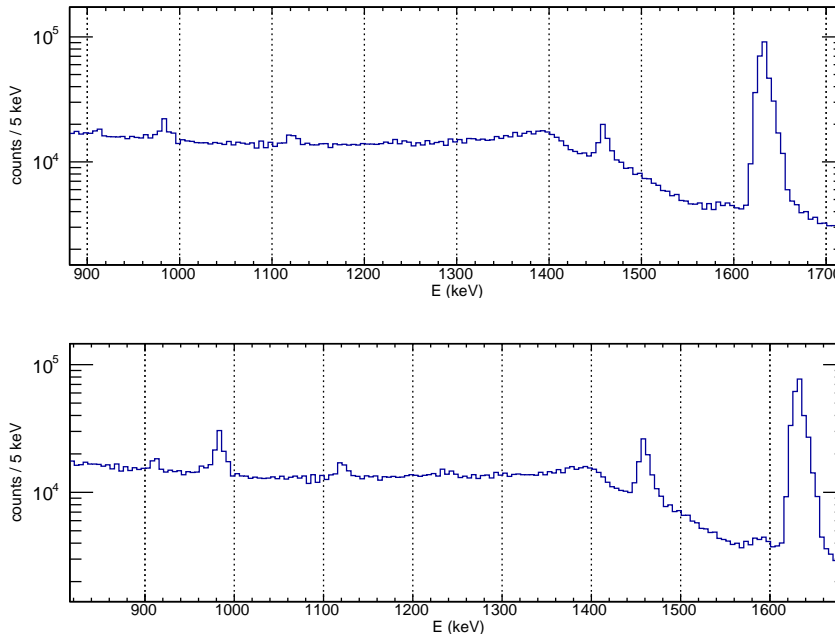


Figure 8.13: *Top:* Total gamma-ray spectrum with the demand that we have at least one coincident event in one of the following silicon detectors: P1, P2, P3, U1, or U5. *Bottom:* Total gamma-ray spectrum with the demand that the gamma-ray event must happen within the first 300 ms after proton impact on the ISOLDE production target.

U1, or U5 is efficiently a demand of observing a beta-particle in coincidence with a gamma-ray. To find the fraction of 984 keV gamma-ray events lost by applying this gate we can use the 1634 keV gamma-ray, which is visible in the top spectrum of Figure 8.13. As both the 984 keV gamma-ray from the beta-decay of ^{20}Mg and the 1634 keV gamma-ray from the beta-decay of ^{20}Na are emitted in coincidence with only one beta-particle, both gamma-rays should be equally affected by the gate. Using the same line shape function as we used in the determination of the absolute efficiency, see Equation (7.6), we find the following ratio between the number of 1634 keV gamma-rays with and without the gate applied:

$$R(E_\gamma = 1634 \text{ keV}) = \frac{2.646(6) \cdot 10^5}{1.0042(11) \cdot 10^6} = 0.26349(66) \quad (8.8)$$

We can now use this ratio as a correction factor to the number of 984 keV gamma-ray events within the gate:

$$\frac{1.196(31) \cdot 10^4}{0.26349(66)} = 4.539(118) \cdot 10^4 \quad (8.9)$$

which is a relative uncertainty of 2.6%. It means that we have observed a total of $4.539(118) \cdot 10^4$ gamma-rays with an energy of 984 keV. This number has not been corrected for the absolute gamma-ray efficiency.

The second gate demands that we only look at events within the first 300 ms after proton impact on the ISOLDE production target. To find the fraction of 984 keV gamma-ray events inside this time window out of the total number of events, we look at the time distribution for the beta-decay of ^{20}Mg . We use the time distribution of the beta-delayed protons measured in P1, to determine the fraction of events which occurs earlier than 300 ms.. We find the following correction factor:

$$R = 0.6962(55) \quad (8.10)$$

We can now use this correction factor to determine the number of 984 keV gamma-ray events observed:

$$\frac{3.5303(387) \cdot 10^4}{0.6962(55)} = 5.071(69) \cdot 10^4 \quad (8.11)$$

which is a relative uncertainty of 1.4%. The two methods for determining the observed number of 984 keV gamma-rays agree with each other within 3 standard deviations.

Finally, we can determine the number of collected ^{20}Mg ions by correcting the number of observed 984 keV gamma-rays for the absolute gamma-ray efficiency (1.72 (4)%) and the gamma-ray intensity (69.7(12)%). Combining the two methods above results in the following weighted average number of ^{20}Mg ions:

$$\langle \#(^{20}\text{Mg}) \rangle = 4.06(9) \cdot 10^6 \quad (8.12)$$

This is the total number of collected ^{20}Mg ions during the 68.0167 hrs the experiment were collecting ^{20}Mg and it has a 2.2% relative uncertainty.

8.4.3 Absolute beta-decay branching ratios

In Sect. 8.4.1 we determined the number of counts in the individual proton peaks as the number of events inside the corresponding energy gate with an estimate of the background contribution subtracted, see Table 8.7. Here the background contribution is the tails of the surrounding proton peaks. Together with the total number of ^{20}Mg ions collected in the detection chamber, see Equation (8.12), and the solid angle of the individual detectors, see Table 7.2, we can determine the absolute intensity of the proton peaks as

$$I_{\text{abs},i}^{\text{det}} = \frac{\#(p)_i}{\Omega_{\text{det}} \cdot \langle \#(^{20}\text{Mg}) \rangle} \cdot 100 \quad (8.13)$$

where $\#(p)_i$ is the number of proton events in the proton peak i and $I_{\text{abs},i}^{\text{det}}$ is the absolute intensity of the proton peak i as measured in detector "det" in percent.

Table 8.8: The absolute intensities of the individual proton lines for the different detectors. The two absolute intensities written in italic numbers are values taken from a different detector and used for normalization. See the text for more detail.

| Line | $I_{\text{abs},i}^{\text{U1}}$ (%) | $I_{\text{abs},i}^{\text{U3}}$ (%) | $I_{\text{abs},i}^{\text{U4}}$ (%) | $I_{\text{abs},i}^{\text{P1}}$ (%) | $I_{\text{abs},i}^{\text{P3}}$ (%) |
|-----------|------------------------------------|------------------------------------|------------------------------------|------------------------------------|------------------------------------|
| p_1 | | 9.7(11) | 10.6(13) | | |
| p_4 | 10.22(32) | 7.5(9) | 7.5(9) | | |
| p_5 | 0.639(35) | <i>0.639(35)</i> | | 0.609(32) | |
| p_V | 0.018(12) | | | 0.043(16) | |
| p_6 | 0.778(48) | | | 0.837(49) | |
| p_7 | 2.125(81) | | | 2.448(90) | |
| p_8 | 0.436(33) | | | 1.692(60) | |
| p_{IV} | 0.509(43) | | | 0.619(50) | |
| p_{III} | 0.293(46) | | | 0.270(41) | |
| p_9 | 0.328(32) | | | 0.300(31) | 0.362(41) |
| p_{10} | 1.630(62) | | | 1.556(62) | 1.599(64) |
| p_{11} | 1.771(67) | | | 1.701(64) | 1.795(70) |
| p_I | 0.220(16) | | | 0.533(26) | 0.608(29) |
| p_{II} | 0.105(12) | | | 0.067(13) | 0.108(15) |

For the calculation to give accurate absolute intensities, it is important that the gates applied to the data when producing the proton spectra does not cut away any real proton events. For the detectors U1, P1, and P3 we only apply a graphical gate to the data, which makes sure we only have events in the spectrum that punch through the front detector. Examples of such graphical gates can be seen on Figure 8.1 and 8.2. The graphical gate fulfills the requirement of not removing any proton events. For the detectors U3 and U4 we have applied a time gate that removes events, which occurred later than 100 ms after proton impact on the ISOLDE production target, in order to get a cleaner proton spectrum as demonstrated on Figure 8.5. Such a time gate will also remove a certain fraction of the proton events. To get the correct absolute intensities in U3, we use $I_{\text{abs},p_5}^{\text{U1}}$ as a normalization constant of the number of proton events observed. We could also have chosen to use $I_{\text{abs},p_5}^{\text{P1}}$, however, the two numbers are consistent with each other so it is not important which one we choose. In U4 we use $I_{\text{abs},p_4}^{\text{U3}}$ as a normalization constant. $I_{\text{abs},p_4}^{\text{U3}}$ and $I_{\text{abs},p_4}^{\text{U1}}$ agrees to 2.2 standard deviations, however, using the $I_{\text{abs},p_4}^{\text{U3}}$ gives more consistent results for the absolute intensity of p_1 .

An overview of the obtained absolute intensities can be seen in Table 8.8. Overall the obtained absolute intensities agree with each other within two standard devia-

tions when comparing between different detectors. The only two exceptions are p_8 and p_I . For p_I the absolute intensities determined on the basis of the data from P1 and P3 agree within 1.5 standard deviations. However, the measured value in U1 disagrees with the other two detectors to ≈ 8 standard deviations. Such a difference is mainly to be attributed to the low intensity and to the very broad nature of the proton line. For the proton line p_8 we observe a ≈ 14 standard deviations difference between U1 and P1, which we can explain with a too large background subtraction in U1 due to the poor energy resolution in this detector. We also mentioned this when discussing the relative intensities. We will adopt the absolute intensity of p_8 as measured in P1 as this is the more reliable value.

The next step is to quantify how much of the intensity in each of the proton peaks that consist of decay branches to excited states in ^{19}Ne . I.e. we want to know the ratio of the efficiency corrected number of proton coincident 238 keV and 275 keV gamma-rays to the measured number of protons in the individual detectors. A summary of these ratios can be found in Table 8.9. The ratios are overall consistent when comparing the different detectors, however, some disagreements are present. In the case of p_8 we observe some differences when comparing detectors. For the 238 keV gamma-ray they disagree with 2.4 standard deviations and for the 275 keV they disagree with 1.6 standard deviations. For the proton line p_{10} the results agree very well when comparing U1 and P1, however, the results from P3 disagrees with the two other detectors.

The final step is to combine the measured values in Table 8.9 with the absolute intensities in Table 8.8 for each detector. The result is shown in Table 8.10 where we present the weighted average of the absolute beta-decay intensities found in the different detectors. From this we find the absolute beta-decay intensity to the individual levels in ^{20}Na under the assumption that no other decay channels such as gamma-ray deexcitations contribute significantly. This assumption appears to be justified on the basis of [Tilley 1998]. It results in the I_β -values presented in Table 8.11. They are compared with the result of [Piechaczek 1995]. The two experiments do in general obtain consistent results. However, for the 5602(4) keV resonance we observe a major difference between the observed lower limit of $\geq 1.5\%$ in [Piechaczek 1995] and the measured value of 0.16(6)% in the present work. The explanation for this discrepancy is most likely the introduction of the new resonance at 5507(10) keV as it is responsible for a total absolute beta-decay intensity of 1.80(17)%. Another minor discrepancy exists for the 6272(4) keV resonance as the two experiments only agree with each other to 2.7 standard deviations.

The absolute beta-decay intensities I_β are translated into $\log(ft)$ -values by use of the parametrization of the phase space factor given in [Wilkinson 1974]. We use the present measurement of $T_{1/2} = 90.9(12)$ ms, see Sect. 8.2, and the measurement of

Table 8.9: The ratio of the efficiency corrected number of gamma-rays in coincidence with the given proton line (γ) to the integrated and background corrected number of protons in the same proton line (p) for the individual detectors. For each proton line we quote two numbers: the top one corresponds to coincidences with the 238 keV gamma-ray and the bottom one corresponds to coincidences with the 275 keV gamma-ray.

| Line | $(\gamma/p)_{U1}$ | $(\gamma/p)_{U3}$ | $(\gamma/p)_{U4}$ | $(\gamma/p)_{P1}$ | $(\gamma/p)_{P3}$ |
|-----------|-------------------|-------------------|-------------------|-------------------|-------------------|
| p_1 | | 0.0 | 0.0 | | |
| | | 0.0 | 0.0 | | |
| p_4 | 0.0 | 0.0 | 0.0 | | |
| | 0.31(3) | 0.25(6) | 0.33(7) | | |
| p_5 | 0.0 | 0.0 | | 0.11(7) | |
| | 0.16(8) | 0.50(25) | | 0.43(15) | |
| p_V | 0.0 | | | 0.0 | |
| | 2.0(19) | | | 3.5(29) | |
| p_6 | 0.40(15) | | | 0.75(19) | |
| | 1.62(23) | | | 1.68(22) | |
| p_7 | 0.21(5) | | | 0.16(5) | |
| | 0.16(5) | | | 0.19(9) | |
| p_8 | 1.34(25) | | | 0.54(8) | |
| | 0.51(20) | | | 0.12(4) | |
| p_{IV} | 2.18(61) | | | 1.65(26) | |
| | 1.32(27) | | | 1.41(26) | |
| p_{III} | 2.84(61) | | | 2.62(58) | |
| | 1.02(42) | | | 0.55(10) | |
| p_9 | 2.60(43) | | | 2.99(49) | 2.04(40) |
| | 0.87(24) | | | 0.71(26) | 2.08(40) |
| p_{10} | 0.83(10) | | | 0.68(9) | 0.0 |
| | 0.51(9) | | | 0.39(8) | 0.0 |
| p_{11} | 0.22(8) | | | 0.28(9) | 0.0 |
| | 0.0 | | | 0.0 | 0.0 |
| p_I | 0.46(31) | | | 0.32(9) | 0.0 |
| | 0.0 | | | 0.0 | 0.0 |
| p_{II} | 0.11(53) | | | 0.50(19) | 0.37(70) |
| | 0.18(56) | | | 0.0 | 0.47(61) |

Table 8.10: Absolute proton intensities for the individual proton emission branches. It is the weighted average of the different detectors. Note that p_2 and p_3 have not been observed here but both are known from previous experiments. Their position in the decay scheme are marked.

| $E^*(^{20}\text{Na})$ (keV) | $\overline{E}_{\text{meas.}}^*$ (keV) | ^{19}Ne resonances (MeV, I^π) | | | | |
|-----------------------------|---------------------------------------|---|-------------------------|-------------------------|-------------------------|-------------------------|
| | | 0.0, 1/2 ⁺ | 0.238, 5/2 ⁺ | 0.275, 1/2 ⁻ | 1.508, 5/2 ⁻ | 1.536, 3/2 ⁺ |
| 0.0, T= 1 | | | | | | |
| 984.25(10) | | | | | | |
| 2647(3) | | | | | | |
| 2987(2) | 2970(8) | 10.1(9) | | | | |
| 3077(2) | | p_2 | | | | |
| 3871(9) | 3846(10) | 6.59(39) | p_3 | p_3 | | |
| 4123(16) | 4094(2) | 0.52(5) | 0.0 | 2.69(24) | | |
| ≈4800 | 4760(4) | 1.41(14) | 0.4(1) | 1.33(14) | | |
| | 5507(10) | | 1.1(1) | 0.76(11) | | |
| ≈5600 | 5604(5) | | | | 0.09(4) | 0.07(5) |
| | 5836(13) | | 0.8(1) | 0.16(3) | 0.05(2) | |
| 6266(30) | 6273(7) | | 0.8(1) | 0.30(6) | 0.37(10) | 0.42(8) |
| 6498.4(5), T= 2 | 6496(3) | 1.75(4) | 0.6(1) | 0.71(10) | 0.20(6) | 0.92(14) |
| ≈6770 | 6734(25) | 0.358(12) | | | | |
| | 7183(16) | 0.093(8) | | | | |

$Q_{\text{EC}} = 10627.1(23)$ keV from [Glassman 2015] in the calculation of the $\log(ft)$ -values. We also use the excitation energies measured in the present experiment. The resulting $\log(ft)$ -values can be found in Table 8.11 together with the values measured in [Piechaczek 1995]. The given uncertainty on the $\log(ft)$ -values only includes the uncertainty from the I_β measurement, which is the dominating uncertainty.

The $\log(ft)$ -values measured in the present experiment are in general consistent with the values measured by [Piechaczek 1995]. However, the upper limit on the $\log(ft)$ -value for the 5604(5) keV resonance from [Piechaczek 1995] disagrees with the value assigned here. This is expected to be due to the introduction of two additional resonances in the present work. Another issue when comparing the two experiments is the 7183(16) keV resonance. The energy of this resonance as measured in the present experiment does not uniquely identify it with either the 6920(100) keV or the 7440(100) keV resonance. The latter two resonances were measured by [Piechaczek 1995].

The total branching ratio for beta-delayed proton emission can now be calculated to be 32.6(11)% on the basis of Table 8.11. This is to be compared with the value 26.9(32)% measured by [Piechaczek 1995]. The two numbers are consistent, however, the value obtained from the data presented here has a factor of three improvement on the uncertainty.

Table 8.11: Absolute beta-decay branching ratios and $\log(ft)$ -values for the individual resonances in ^{20}Na determined as the weighted average of all detectors. The present work is compared with [Piechaczek 1995]. Note that the absolute intensity of p_2 and p_3 are not included here. The resonances marked with a * are not observed here and the energy quoted are from [Piechaczek 1995].

| $\overline{E_{\text{meas.}}^*}(^{20}\text{Na})$ (keV) | I_β (%) | | $\log(ft)$ | |
|---|---------------|-------------|------------|-------------|
| | This work | Ref. | This work | Ref. |
| 2970(8) | 10.11(85) | 11.5(14) | 4.10(8) | 4.08(6) |
| 3846(10) | 6.59(39) | 4.8(6) | 4.11(6) | 4.17(6) |
| 4094(2) | 3.21(25) | 2.7(3) | 4.33(8) | 4.33(6) |
| 4760(4) | 3.16(22) | ≥ 1.9 | 4.08(7) | ≤ 4.23 |
| 5507(10) | 1.80(17) | | 3.99(9) | |
| 5604(5) | 0.16(6) | ≥ 1.5 | 5.00(38) | ≤ 3.97 |
| 5836(13) | 0.97(15) | | 4.09(15) | |
| 6273(7) | 1.93(17) | 1.2(1) | 3.55(9) | 3.72(6) |
| 6496(3), $T=2$ | 4.16(20) | 3.3(4) | 3.09(5) | 3.13(6) |
| 6734(25) | 0.358(12) | ≥ 0.03 | 4.00(3) | ≤ 5.01 |
| 6920(100)* | | ≥ 0.01 | | ≤ 5.39 |
| 7183(16) | 0.093(8) | | 5.14(67) | |
| 7440(100)* | | ≥ 0.01 | | ≤ 4.99 |

A comparison with the mirror beta-decay of ^{20}O can be made for two allowed $0^+ \rightarrow 1^+$ transitions according to [Wallace 2012a]:

- $^{20}\text{O} \rightarrow ^{20}\text{F}(1.057 \text{ MeV})$ and $^{20}\text{Mg} \rightarrow ^{20}\text{Na}(984 \text{ keV})$
- $^{20}\text{O} \rightarrow ^{20}\text{F}(3.488 \text{ MeV})$ and $^{20}\text{Mg} \rightarrow ^{20}\text{Na}(2987 \text{ keV})$

As we have used the beta-decay transition to the bound state in ^{20}Na at 984 keV to determine the number of ^{20}Mg ions collected based on the known branching ratio for this transition, it is not meaningful to calculate the mirror asymmetry parameter $\delta = \frac{\log(ft)^+}{\log(ft)^-} - 1$ for this transition (see Chapter 1). For the second transition, however, we determine the isospin asymmetry parameter to be $\delta = 0.12(3)$, where we have used $\log(ft)^- = 3.65(6)$ taken from [Alburger 1987]. This value is comparable to the value of δ found in [Piechaczek 1995] and points to a pronounced isospin asymmetry.

A calculation of the ^{20}Mg beta-decay is presented in [Piechaczek 1995], which is made in the sd-shell model space. The theoretical half-life is calculated to be 101.8 ms, which is in fair agreement with the value measured in this experiment of 90.9(12) ms. The shell-model calculation also specifies that the total proton emission intensity to

the 238 keV state in ^{19}Ne relative to the total proton emission intensity to the ground state amounts to 0.13 and for the 1536 keV state relative to the ground state it amounts to 0.01. In this experiment we measure the two ratios to be 0.18(1) and 0.07(1), respectively. The agreement between theory and experiment is qualitatively good. It should be noted that in [Piechaczek 1995] they quote experimental values of 0.10 and 0.06, respectively. The first of these is not in agreement with the measurement we have made.

Using Equation (1.10) we determine that $B_F = 5.0^{+0.6}_{-0.5}$. We have used the measured value of $\log(ft) = 3.09(5)$ for the IAS. This is to be compared with the sum-rule given by Equation (1.12), which states that the Fermi strength for the beta-decay of ^{20}Mg to the IAS should be 4 as $Z = 12$ and $N = 8$. The measured Fermi strength is consistent with the sum-rule.

8.5 Summary and conclusions

A summary of the main conclusions drawn from the beta-decay study of ^{20}Mg are presented in the following list:

- Two new resonances have been introduced above the proton separation energy in ^{20}Na : 5507(10) keV and 5836(13) keV.
- The approximate resonance energies from [Piechaczek 1995] of 4800 keV and 5600 keV have been measured more accurately: 4760(4) keV and 5604(5) keV.
- The 7183(16) keV resonance in ^{20}Na is possibly a new resonance.
- We observe 5 new beta-delayed proton peaks and we confirm the 11 beta-delayed proton peaks of [Piechaczek 1995] (with the exception of p_2 and p_3 due to high levels of contamination).
- We measure the half-life of ^{20}Mg to be $T_{1/2} = 90.9(12)$ ms.
- We confirm the value of the isospin asymmetry parameter δ as determined by [Piechaczek 1995] for the $^{20}\text{O} \rightarrow ^{20}\text{F}(3.488 \text{ MeV})$ and $^{20}\text{Mg} \rightarrow ^{20}\text{Na}(2987 \text{ keV})$ mirror transitions to be $\delta = 0.12(3)$.
- The measured Fermi strength to the IAS is consistent with the sum-rule.

It is not possible to improve upon the 0.02% upper limit of the beta-delayed proton decay branch going through the astrophysical relevant resonance at 2645(6) keV with these data. The reason for this is the very large background of ^{16}O nuclear recoils below approximately 500 keV in the front detectors as is evident from the spectrum observed in U4 as shown on Figure 8.5.

Summary and outlook

In this final chapter we will summarize the results obtained by studying the beta-decays of ^{21}Mg and ^{20}Mg . All of the results have been presented and discussed in detail throughout the thesis. After the summary of the results follows a discussion of the outlook for the future based on the results. We will among other things discuss possibilities for analysis of data from the two experiments that have not been presented here and how these can complement the results presented. In Sect. 9.1 we will present the summary and outlook for the study of the beta-decay of ^{21}Mg . In Sect. 9.2 we will present the summary and outlook for the study of the beta-decay of ^{20}Mg .

9.1 Beta-decay study of ^{21}Mg

We will start with a presentation of the results obtained by studying the beta-decay of ^{21}Mg in Sect. 9.1.1. In Sect. 9.1.2 we will discuss what possibilities the results open for in the future.

9.1.1 Summary of results

The study of the beta-decay of ^{21}Mg presented in Chapter 4 and 5 have given several results worth mentioning. A summary of the main results are gathered in the following list:

- Seven new beta-delayed proton branches were observed. A total of 27 beta-delayed proton branches were measured with energies ranging between 0.39 MeV and 7.2 MeV.
- An improved interpretation of the ^{21}Mg beta-decay is proposed, which is based on the extracted spectroscopic information from the delayed protons. The proposed decay scheme is consistent with the results of various reaction studies and with comparisons to the mirror nucleus and mirror decay.
- The line shape of p_{15} is interpreted as being due to interference with the high-intensity proton branch p_{11} . As a consequence we assign $I^\pi = \frac{3}{2}^+$ to the 5020(9) keV

resonance in ^{21}Na in agreement with a study of the mirror nucleus ^{21}Ne in [Hoffmann 1989].

- The 5979(15) keV resonance proposed by [Sextro 1973] is no longer needed, as the proton branch p_{17} now is assigned as having the first excited state in ^{20}Ne as final state. This new assignment is supported by the study of the mirror nucleus ^{21}Ne presented in [Hoffmann 1989].
- For the first time has the total width Γ_{tot} of the 5020(9) keV, 5380(9) keV, 5884(20) keV, 6165(30) keV, 6341(20) keV, 8135(15) keV, and the 8303(13) keV resonances been measured. The values can be found by looking in Table 4.3 and 4.6.
- We constrain the total width Γ_{tot} of the 6468(20) keV resonance to be close to the upper uncertainty limit of the literature value $\Gamma_{\text{tot}} = 145(15)$ keV.
- We constrain the total width Γ_{tot} of the 8397(15) keV resonance to be close to the lower uncertainty limit of the literature value $\Gamma_{\text{tot}} = 30(13)$ keV.
- The half-life of ^{21}Mg is determined to be $T_{1/2} = 118.6(5)$ ms, which is a factor of four improvement on the uncertainty.
- First observation of beta-delayed alpha-particle emission from ^{21}Mg - four different $\beta\alpha$ decay branches are observed with center-of-mass energies between 2.2 and 3.1 MeV.
- First observation of the rare $\beta p\alpha$ decay mode from ^{21}Mg with the ground state of ^{16}O as the final state - this is the third identified case of $\beta p\alpha$ emission.
- Based on the systematics of beta-delayed particle emission we observe certain patterns, which to a large extent can be explained by odd-even effects. The observed decay modes $\beta\alpha$ and $\beta p\alpha$ from ^{21}Mg fits naturally into this pattern.

9.1.2 Outlook

The modified interpretation of the decay scheme resulting from the study of the beta-decay of ^{21}Mg , calls for a dedicated measurement of the beta-decay with both charged particle and gamma-ray detectors to verify the results. In particular coincidences between beta-delayed charged particles and gamma-rays could prove valuable in the reconstruction of the decay scheme. An experimental setup designed with this in mind, would ideally consist of a highly segmented and compact silicon detector setup with the detectors pairwise placed in the ΔE - E telescope configuration. It would be good to have at least one telescope with a thin front detector as the beta-particle response is confined at lower energy the thinner the detector is. To surround the silicon

detector array a highly efficient gamma-ray detector array is needed in order to observe the emitted gamma-rays. These are to be used for the construction coincidences between charged particles and gamma-rays.

The experiment that we performed in April 2015 at the ISOLDE Decay Station (IDS), which were presented in Chapter 7, does in many ways fulfill the desired features for a new study of the beta-decay of ^{21}Mg that we have just described. We have presented the results of the beta-decay study of ^{20}Mg performed with this setup, however, besides the approximately 68 hours of ^{20}Mg beam, we also measured the beta-decay of ^{21}Mg for approximately 9.5 hours as a check of the experimental setup and for calibration purposes. These data are ideal for the desired cross-check of the conclusions drawn from the study of the beta-decay of ^{21}Mg performed with the 2011 data. We will present a few very preliminary results from these data here.

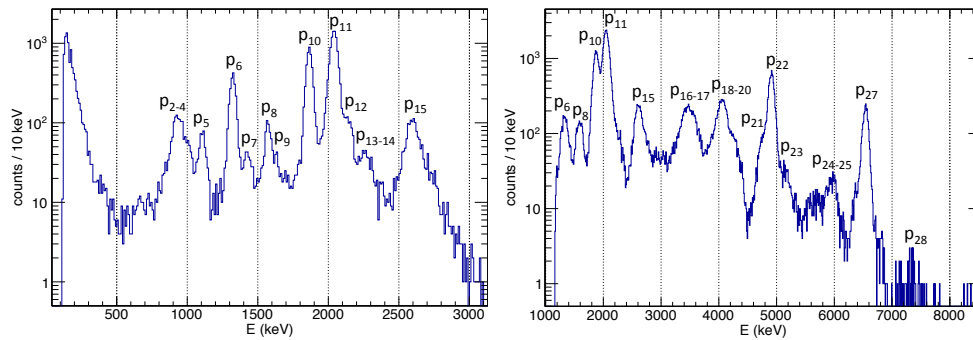


Figure 9.1: Beta-delayed proton spectrum observed with the IDS experimental setup showing the center-of-mass proton energy. *Left:* Spectrum from the detector U3 with the demands of no particle events in the opposing detector (U4), no punch through events, and to only look at events within 100 ms from the last proton pulse on the ISOLDE production target. *Right:* Spectrum from the detector U1 with the demands that only one particle event are observed in both U1 and U2 and a demand to only look at events that punch through the front detector (U2).

The first natural thing to present is the complete beta-delayed proton spectrum as observed in the 2015 experiment. On Figure 9.1 we present the low-energy part of the proton spectrum as observed by the $60\ \mu\text{m}$ thin DSSSD called U3 (left part of the figure, front detector), and we present the high-energy part of the proton spectrum as observed by the $500\ \mu\text{m}$ thick DSSSD called U1 (right part of the figure, backing detector for the $20\ \mu\text{m}$ SSD called U2). To produce the low-energy proton spectrum we have applied the conditions that no particle event is observed in the opposing front detector (U4), no punch through events of U3 are allowed, and the events have to occur within the first 100 ms after proton impact on the ISOLDE production target.

To produce the high-energy spectrum we have applied the conditions that only one particle event is to be observed in U1 and U2 at the same time, and we apply a gate to the ΔE - E spectrum to only look at events that punch through the front detector U2.

It immediately becomes clear that the new beta-delayed proton spectrum confirm the observation of several of the seven new βp branches that we reported with the 2011 data. Looking in the low-energy part of the proton spectrum, which have a good energy resolution ($\sigma_{U3} = 19.2(2)$ keV), we do not observe clear signs of the low-energy proton branch p_1 . However, it might be signs of this proton branch that are observed as a small bump in the beta-particle distribution at roughly 400 keV. More analysis is needed to settle the nature of this bump. At higher energies we clearly observe structure in the proton peak p_{2-4} as we have proposed on the basis of the 2011 data. At this early point of the analysis, however, we do not observe the $\beta p \alpha$ decay branch that is present in this proton peak. We do also confirm the observation of the low-intensity proton branches p_7 and p_9 . Unfortunately, we cannot confirm that the peak p_{13-14} with the preliminary data presented here in fact is a double peak structure.

Looking at the high-energy part of the beta-delayed proton spectrum, which have a poor energy resolution ($\sigma_{U1} = 47.0(5)$ keV) unfortunately, we can confirm the observation of p_{23} and p_{28} . As was the case with the 2011 data, we also observe signs of an interesting structure between p_{23} and p_{24} , which potentially can be a new proton branch. We discussed two different explanations for this structure in connection with the old data as either a proton branch between the 9725(25) keV resonance and the first excited state in ^{20}Ne or as a ground state transition from the 8135(15) keV resonance.

For the high-energy beta-delayed protons it is particularly important to obtain more precise and accurate beta-decay intensities and resonance energies in ^{21}Na , in order to get a better understanding of the beta-decay strength distribution. As the phase space factor f has a strong energy dependence as we showed in Chapter 1, it is essential to obtain precise and accurate information about the beta-decay branching ratios and the resonance energies. From the high-energy part of the proton spectrum we observe signs of a possible new proton branch between p_{27} and p_{28} , which is important in the regards to the beta-decay strength distribution.

Another important cross-check to make is the assignment of beta-delayed proton branches to excited states in ^{20}Ne . On Figure 9.2 we show the total observed gamma-ray spectrum in coincidence with the protons observed in U1 (the spectrum on the left). We clearly observe the 1634 keV gamma-ray in coincidence with the protons as expected. On the spectrum to the right we show the proton spectrum in U1 for events that are in coincidence with the 1634 keV gamma-ray. This spectrum should include proton branches that have the first excited state in ^{20}Ne as their final state,

Table 9.1: The energy and intensity of the observed gamma-ray decays of the three lowest excited states in ^{20}Ne according to [Tilley 1998]. It is evident that both the second and third excited state mainly deexcites to the first excited state.

| $E(^{20}\text{Ne})$ (keV) | E_γ (keV) | I_γ (%) |
|---------------------------|------------------|----------------|
| 1633.674 | 1633.602 | 100 |
| 4247.7 | 2613.8 | 100 |
| 4966.51 | 3332.54 | 99.4 |
| | 4965.85 | 0.6 |

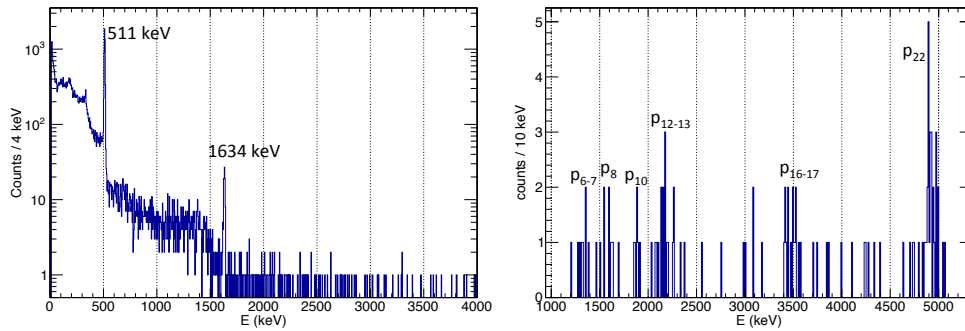


Figure 9.2: *Left:* Gamma-ray spectrum from all HPGe-clover detectors gated on the U1 proton spectrum (see Figure 9.1). We clearly observe the expected 1634 keV gamma-ray, which is the deexcitation of the first excited state in the proton daughter ^{20}Ne . *Right:* Proton spectrum in U1 if we also demand that $1600 \text{ keV} < E_\gamma < 1650 \text{ keV}$. The spectrum is to be compared with the spectrum on the right on Figure 9.1.

which means that we would expect to observe p_1 , p_6 , p_{12} , p_{13} , p_{17} , p_{19} , p_{20} , p_{21} , and p_{22} here. As is shown on the figure, part of these proton branches are observed to be in coincidence with the 1634 keV gamma-ray, but we also observe proton branches that were not believed to be going to the first excited state. However, as is evident from the data presented in Table 9.1 the second and third excited state in ^{20}Ne will decay to the first excited state by emission of a gamma-ray. Hence, the beta-delayed proton branches going to either of these excited states will be in coincidence with the 1634 keV gamma-ray and no immediate conclusions can be drawn here. A more careful analysis is needed.

Having investigated the beta-delayed proton spectrum from ^{21}Mg , it is time to look at the beta-delayed alpha-particle spectrum. The spectrum in the left part of Figure 9.3 shows coincidence events between the two opposing front detectors U3

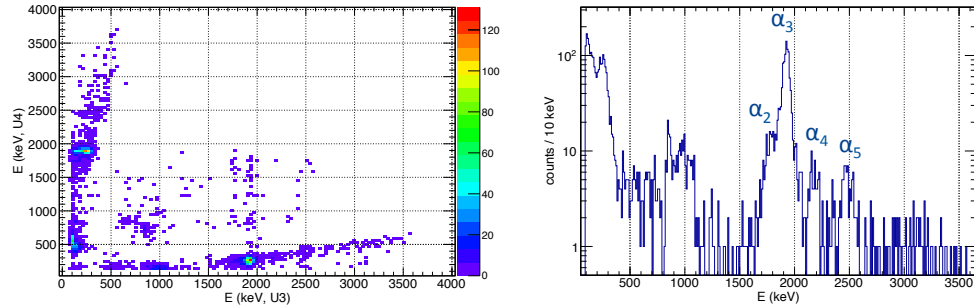


Figure 9.3: *Left:* The U3 laboratory energy (x-axis) against the U4 laboratory energy (y-axis) with a demand of particle multiplicity one in both detectors and no events in their respective back detectors (P1 and P3). The two detectors are facing each other with the decay point located in between them. *Right:* Projection of all events shown in the spectrum on the left side onto the x-axis, i.e. the laboratory energy in U3 for events that are coincident in U3 and U4.

and U4 under the conditions to only have a particle multiplicity of one in both detectors and that no events are observed in their respective backing detectors. Projecting all of these events on the U3 energy axis produces the spectrum shown in the right part of the figure, which exhibits a clean high-energy alpha-particle spectrum. As we discussed in Sect. 8.1.2 the events showing up under these conditions are the delayed particle and the nuclear recoil if both of them have sufficient energy to make it into the detector and through the front-back matching criteria. As a consequence of these considerations it becomes clear that the events below roughly 1.5 MeV in the coincidence spectrum from U3 mainly consists of nuclear recoils. On the other hand does the events above this energy appear to be quite clean of contaminants. We clearly observe all four beta-delayed alpha-particle branches plus something that appears to be a fifth alpha-particle at roughly 3.2 MeV.

More careful considerations of the energetics of the beta-delayed proton and alpha-particle emissions from ^{21}Mg should reveal if part of the events below 1.5 MeV are alpha-particle events, proton events, or nuclear recoil events. Determining the expected energies of the nuclear recoils and their energy deposition in the detection setup proved helpful in Sect. 8.1.2.

Lets now turn to the model that we developed on the basis of the interpretation of the patterns observed in beta-delayed particle emission as being caused by odd-even effects. It can be used to predict other cases with rare exotic decay modes like $\beta p \alpha$. This decay mode may not happen in heavier $T_3 = -3/2$ nuclei than ^{21}Mg due to the evolution of the separation energies and the Q_{EC} -values, however, it may be found in the $T_3 = -5/2$ nuclei ^{23}Si , ^{27}S , ^{31}Ar , etc.

9.2 Beta-decay study of ^{20}Mg

In this section we will first summarize the results obtained from the study of the beta-decay of ^{20}Mg . Then we will discuss the outlook and future possibilities on the basis of the obtained results.

9.2.1 Summary of results

A summary of the main conclusions drawn from the beta-decay study of ^{20}Mg are presented in the following list:

- Two new resonances have been introduced above the proton separation energy in ^{20}Na : 5507(10) keV and 5836(13) keV.
- The approximate resonance energies from [Piechaczek 1995] of 4800 keV and 5600 keV have been measured more accurately: 4760(4) keV and 5604(5) keV.
- The 7183(16) keV resonance in ^{20}Na is possibly a new resonance.
- We observe 5 new beta-delayed proton peaks and we confirm the 11 beta-delayed proton peaks of [Piechaczek 1995] (with the exception of p_2 and p_3 due to high levels of contamination).
- We measure the half-life of ^{20}Mg to be $T_{1/2} = 90.9(12)$ ms.
- We confirm the value of the isospin asymmetry parameter δ as determined by [Piechaczek 1995] for the $^{20}\text{O} \rightarrow ^{20}\text{F}$ (3.488 MeV) and $^{20}\text{Mg} \rightarrow ^{20}\text{Na}$ (2987 keV) mirror transitions to be $\delta = 0.12(3)$.
- The measured Fermi strength to the IAS is consistent with the sum-rule.

A final remark is that it is not possible to improve upon the 0.02% upper limit of the beta-delayed proton decay branch going through the astrophysical relevant resonance at 2645(6) keV with these data. The reason for this is the very large background of ^{16}O nuclear recoils below approximately 500 keV in the front detectors as is evident from the spectrum observed in U4 as shown on Figure 8.5.

9.2.2 Outlook

As have been pointed out several times is the produced beam of ^{20}Mg highly contaminated with ^{20}Na . In fact we observe a factor of 10 more sodium than magnesium on average even though we use a magnetic separator (the HRS) and a slit system to cut part of the beam on the low-mass side. It would be a big step forward if it is possible to suppress the produced sodium by a few orders of magnitude more than it is

possible now at the ISOLDE facility. This could be obtained with a magnet separator with a higher mass resolution.

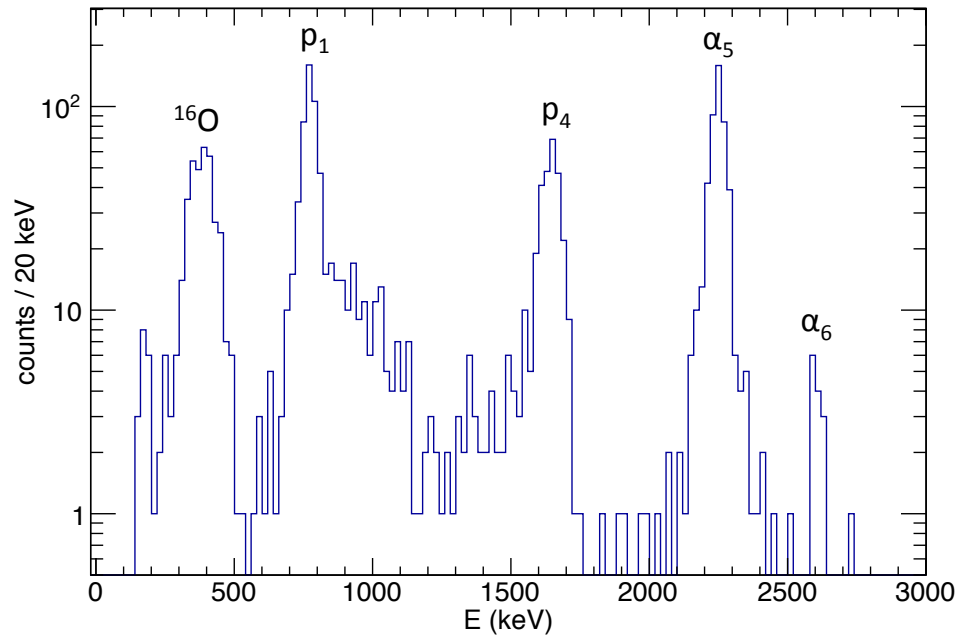


Figure 9.4: Center-of-mass proton energy spectrum from U4. The spectrum is made with the same gates as the green spectrum on Figure 8.5 plus the additional demand to only look at events in the central 4×4 pixels of U4. Comparison with Figure 8.5 makes it clear that we do not significantly reduce the low-energy contamination of ^{16}O recoils.

The two experimental setups that we used in the 2011 and the 2015 experiments focus on slightly different objectives. The detection setup that we used in the 2011 experiment was mainly designed to study the low-energy region of the beta-delayed proton spectrum by employing a gas telescope to separate protons from beta-particles, alpha-particles, and recoils down to a few hundred keV. The detection setup that we used in the 2015 experiment was designed with a more general purpose in mind but including the possibility to search for low-intensity and low-energy decay branches by using particle-recoil coincidences to clean the spectrum. As we have shown on Figure 8.5 we are, however, not able to reduce the amount of ^{16}O recoils below 500 keV efficiently enough to be able to improve upon the existing upper limit of the feeding of the 2645(6) keV resonance. One of the main problems is that the efficiency for observing particle-recoil coincidences with two opposing detectors like U3 and U4 in the current configuration is too small (roughly 70-75% below 1.0 MeV). It is possible to improve the coincidence efficiency by increasing the solid angle of the recoil de-

detector with respect to the particle detector. The recoil detector is the detector used for the recoil-veto, i.e. it is the detector where we demand that no particle event must be observed in coincidence with a particle event in the particle detector. The particle detector is where we produce the clean low-energy spectrum. One can obtain this improved efficiency in two ways: by only looking for particles in the central part of the particle detector or by moving the recoil detector closer to the decay point in order to increase the solid angle coverage. The disadvantage of restricting the particle data to only be from the central part of the particle detector is that you lose statistics due to the lower solid angle. This would not be a problem if you put the recoil detector very close to the decay point. On Figure 9.4 we demonstrate that a restriction of the U4 detector to the central 4×4 pixels in addition to the gates applied to produce the cleanest proton spectrum shown on Figure 8.5 (the green spectrum) is not sufficient to remove the low-energy ^{16}O recoils. The particle-recoil coincidence efficiency when only looking at the central 4×4 pixels of U4 is roughly 75-80%.

From an analysis of the ^{20}Mg data taken during the 2011 experiment, we can only put an upper limit on the 2645(6) keV resonance proton branching ratio of the order 0.1% by using the gas telescope. This upper limit is to be compared with the value of 0.02% measured by [Wallace 2012b]. The main reason that we are not able to set a better limit is the contamination of ^{20}Na in the beam. If we were able to suppress the factor of 40 more sodium than magnesium in the detection chamber by an order of magnitude we would have been able to put a competing upper limit. So again we end up at the conclusion that we need to do improvements on the production and beam purity when measuring the decay of ^{20}Mg at the ISOLDE facility.

An ideal experiment to measure the low-energy beta-delayed proton branch would be to have an accelerated beam of high intensity ^{20}Mg ions implanted in a highly segmented silicon detector and surrounded by beta-particle veto detectors and a highly efficient gamma-ray detection setup. By implanting the beam in the silicon detector we would observe the alpha-particle and the ^{16}O recoil as a single event. We would therefore not be contaminated by low-energy ^{16}O recoils. However, the production rate of ^{20}Mg at the ISOLDE facility is not large enough to re-accelerate the beam with sufficient yields so other facilities seems at the moment to be better suited for the task.

In Chapter 6 we discussed the possibility of measuring the $^{20}\text{Mg}(\beta p \alpha)^{15}\text{O}$ decay mode, which will go through the 4033 keV excited state in ^{19}Ne . However, we have not observed any signs of beta-delayed protons feeding states above the 1536 keV state in ^{19}Ne . A different approach to the search of this expected low-intensity decay mode is by investigating the gamma-ray spectrum for the 4033 keV gamma-ray de-excitation of the proton fed resonance. The search for such a high-energy gamma-ray would need a proper treatment of add-back, which we do not have at the present moment.

Bibliography

- [Ajzenberg-Selove 1991] F. Ajzenberg-Selove. *Energy levels of light nuclei $A = 13 - 15$* . Nucl. Phys. A, vol. 523, page 1, 1991. 72
- [Alburger 1987] D.E. Alburger, G. Wang and E.K. Warburton. *Beta decay of ^{20}O* . Phys. Rev. C, vol. 35, no. 1479, 1987. 141
- [Audi 2012] G. Audi, F.G. Kondev, M. Wang, B. Pfeiffer, X. Sun, J. Blachot and M. MacCormick. *The Nubase2012 evaluation of nuclear properties*. Chin. Phys. C, vol. 36, no. 12, 2012. 12, 18, 39, 69, 73, 81, 113, 120
- [Barlow 2000] R.J. Barlow. *SLUO Lectures on Statistics and Numerical Methods in HEP. Lecture 7: Fitting Methods*, 2000. 27
- [Barton 1963] R. Barton, R. McPherson, R.E. Bell, W.R. Frisken, W.T. Link and R.B. Moore. *Observation of Delayed Proton Radioactivity*. Can. J. Phys., vol. 41, page 2007, 1963. 15
- [Beane 2012] S.R. Beane, E. Chang, W. Detmold, H.W. Lin, T.C. Luu, K. Orginos, A. Parreño, M.J. Savage, A. Torok and A. Walker-Loud (NPLQCD Collaboration). *Deuteron and exotic two-body bound states from lattice QCD*. Phys. Rev. D, vol. 85, no. 054511, 2012. 1
- [Bergmann 2002] U.C. Bergmann and K. Riisager. *New statistical methods for exotic nuclei*. Nucl. Phys. A, vol. 701, 2002. 39
- [Bhattacharya 2002] M. Bhattacharya and E.G. Adelberger. *Reanalysis of $\alpha + \alpha$ scattering and the β -delayed α spectra from ^8Li and ^8B decays*. Phys. Rev. C, vol. 65, no. 055502, 2002. 44, 45
- [Bhattacharya 2006] M. Bhattacharya, E.G. Adelberger and H.E. Swanson. *Precise study of the final-state continua in ^8Li and ^8B decays*. Phys. Rev. C, vol. 73, 2006. 45
- [Blank 2008] B. Blank and M.J.G. Borge. *Nuclear structure at the proton drip line: Advances with nuclear decay studies*. Prog. Part. Nucl. Phys., vol. 60, 2008. 4, 5, 9, 18, 70, 72, 73
- [Bloch 1969] R. Bloch, T. Knellwolf and R.E. Pixley. *Several narrow resonances in the proton bombardment of ^{20}Ne* . Nucl. Phys. A, vol. 123, pages 129–146, 1969. 56, 61

- [Borge 2010] M.J.G. Borge, J. Cederkäll, L.M. Fraile, H.O.U. Fynbo, T. Giles, K.L. Laursen, J.S. Johansen, B. Jonson, G.T. Koldste, E. Nacher, T. Nilsson, A. Perea, K. Riisager, T. Storra and O. Tengblad. *Study of the β -decay of ^{20}Mg* . Proposal to the INTC, 2010. 12, 13
- [Butler 1968] G.W. Butler, J. Cerny, S.W. Cosper and R.L. McGrath. *Mass and Spectroscopic Measurements in the Completed Mass-21 and -37 Isospin Quartets*. Phys. Rev., vol. 166, page 1096, 1968. 57
- [Caurier 1995] E. Caurier, A. Poves and A.P. Zuker. *Missing and quenched Gamow-Teller strength*. Phys. Rev. Lett., vol. 74, page 1517, 1995. 7
- [Choulakian 1994] V. Choulakian, R.A. Lockhart and M.A. Stephens. *Cramér-von Mises statistics for discrete distributions*. Can. J. Stat., vol. 22, pages 125–137, 1994. 40
- [Chow 2002] J.C. Chow, J.D. King, N.P.T. Bateman, R.N. Boyd, L. Buchmann, J.M. D’Auria, T. Davinson, M. Dombisky, E. Gete, U. Giesen, C. Iliadis, K.P. Jackson, A.C. Morton, J. Powell and A. Shotter. *β -delayed particle decay of ^{17}Ne into $p + \alpha + ^{12}\text{C}$ through the isobaric analog state in ^{17}F* . Phys. Rev. C, vol. 66, 2002. 72
- [Davids 2011] B. Davids, R.H. Cyburt, J. José and S. Mythili. *The Influence of Uncertainties in the $^{15}\text{O}(\alpha, \gamma)^{19}\text{Ne}$ Reaction Rate on Models of Type I X-Ray*. Astrophys. J., vol. 735, no. 40, 2011. 84
- [Debertin 1988] K. Debertin and R.G. Helmer. *Gamma- and x-ray spectrometry with semiconductor detectors*. North-Holland, 1988. 103, 104, 105, 171
- [der Leun 1964] C. Van der Leun and W.L. Mouton. *The reaction $^{20}\text{Ne}(p, \gamma)^{21}\text{Na}$* . Physica, vol. 30, pages 330–340, 1964. 56
- [Dürr 2008] S. Dürr, Z. Fodor, J. Frison, C. Hoelbling, R. Hoffmann, S.D. Katz, S. Krieg, T. Kurth, L. Lellouch, T. Lippert, K.K Szabo and G. Vulvert. *Ab initio determination of light hadron masses*. Science, vol. 322, no. 5905, page 1224, 2008. 1
- [Erler 2012] J. Erler, N. Birge, M. Kortelainen, W. Nazarewicz, E. Olsen, A.M. Perhac and M. Stoitsov. *The limits of the nuclear landscape*. Nature, vol. 486, page 509, 2012. 2
- [Eu1 2015] *WWW Table of Radioactive Isotopes*, August 2015. 100, 102, 171
- [Fedoseyev 2000] V.N. Fedoseyev, G. Huber, U. Köster, J. Lettry, V.I. Mishin, H. Ravn, V. Sebastian and the ISOLDE Collaboration. *The ISOLDE laser ion source for exotic nuclei*. Hyperfine Interactions, vol. 127, pages 409–416, 2000. 11

- [Fernández 1981] M. Fernández, G. Murillo, J. Ramirez, O. Avila, S.E. Darden, M.C. Rozak, J.L. Foster, B.P. Hichwa and P.L. Jolivet. $^{20}\text{Ne}(p,p_0)^{20}\text{Ne}$ and states of ^{21}Na . Nucl. Phys. A, vol. 369, pages 425–452, 1981. 52, 56, 57, 60
- [Firestone 2004] R.B. Firestone. *Nuclear Data Sheets for A = 21*. Nucl. Data Sheets, vol. 103, pages 269–324, 2004. 56
- [Fortune 2000] H.T. Fortune, R. Sherr and B.A. Brown. $\omega\gamma$ for $^{19}\text{Ne}(p,\gamma)^{20}\text{Na}(2.64\text{ MeV})$. Phys. Rev. C, vol. 61, no. 057303, 2000. 84
- [Fynbo 1999] Hans O.U. Fynbo. *Beta-delayed particle emission from the dripline nuclei ^{11}Li , ^{31}Ar and ^9C* . PhD thesis, Institute of Physics and Astronomy, University of Aarhus, 1999. 6, 161
- [Gete 2000] E. Gete, L. Buchmann, R.E. Azuma, D. Anthony, N. Bateman, J.C. Chow, J.M. D’Auria, M. Dombisky, U. Giesen, C. Iliadis, K.P. Jackson, J.D. King, D.F. Measday and A.C. Morton. β -delayed particle decay of ^9C and the $A = 9, T = 1/2$ nuclear system: Experiment, data, and phenomenological analysis. Phys. Rev. C, vol. 61, no. 064310, 2000. 72
- [Glassman 2015] B.E. Glassman, D. Pérez-Loureiro, C. Wrede, J. Allen, D.W. Bardayan, M.B. Bennett, B.A. Brown, K.A. Chipps, M. Febraro, C. Fry, M.R. Hall, O. Hall, S.N. Liddick, P. O’Malley, W. Ong, S.D. Pain, S.B. Schwartz, P. Shidling, H. Sims, P. Thompson and H. Zhang. *Revalidation of the isobaric multiplet mass equation for the A = 20 quintet*. Phys. Rev. C, vol. 92, 2015. 80, 130, 131, 140, 172
- [Görres 1992] J. Görres, M. Wiescher, K. Scheller, D.J. Morrissey, B.M. Sherrill, D. Bazin and J.A. Winger. β -delayed proton decay of ^{20}Mg and its astrophysical implications. Phys. Rev. C, vol. 46, no. 3, 1992. 78
- [Gruhle 1977] W. Gruhle and B. Kober. *The reactions $^{16}\text{O}(p,\alpha)$, $^{20}\text{Ne}(p,\alpha)$ and $^{24}\text{Mg}(p,\alpha)$* . Nucl. Phys. A, vol. 286, pages 523–530, 1977. 69
- [Hardy 1965] J.C. Hardy and R.E. Bell. *New information on the emission of delayed protons following the decay of ^{17}Ne , ^{21}Mg , and ^{25}Si* . Can. J. Phys., vol. 43, page 1671, 1965. 16
- [Hoffmann 1989] A. Hoffmann, P. Betz, H. Röpke and B.H. Wildenthal. *Structure of the Mirror Nuclei ^{21}Ne and ^{21}Na* . Z. Phys. A, vol. 332, 1989. 52, 54, 55, 63, 65, 144
- [Iliadis 2007] C. Iliadis. *Nuclear physics of stars*. Wiley-VCH, 2007. 82
- [Jackson 1998] J.D. Jackson. *Classical electrodynamics*. John Wiley & Sons, 1998. 9

- [James 2004] Fred James and Matthias Winkler. *Minuit User's Guide*. CERN, Geneva, June 2004. 39, 119
- [Jensen 1987] A.S. Jensen and P.J. Siemens. *Elements of nuclei*. Addison Wesley, 1987. 4, 9
- [Jeppesen 2002] H. Jeppesen, U.C. Bergmann, M.J.G. Borge, J. Cederkäll, V.N. Fedoseyev, H.O.U. Fynbo, V.Y. Hansper, B. Jonson, K. Markenroth, V.I. Mishin, T. Nilsson, G. Nyman, K. Riisager, O. Tengblad and K. Wilhelmsen Rolander. *Search for beta-delayed charged particles from the halo nucleus ^{14}Be* . Nucl. Phys. A, vol. 709, pages 119–130, 2002. 13, 21
- [Kanungo 2006] R. Kanungo, T.K. Alexander, A.N. Andreyev, G.C. Ball, R.S. Chakrawarthy, M. Chicoine, R. Churchman, B. Davids, J.S. Forster, S. Gujrathi, G. Hackman, D. Howell, J.R. Leslie, A.C. Morton, S. Mythili, C.J. Pearson, J.J. Ressler, C. Ruiz, H. Savajols, M.A. Schumaker, I. Tanihata, P. Walden and S. Yen. *Lifetime of $^{19}\text{Ne}^*(4.03\text{ MeV})$* . Phys. Rev. C, vol. 74, no. 045803, 2006. 84
- [Knudsen 2005] H.H. Knudsen, H.O.U. Fynbo, M.J.G. Borge, R. Boutami, P. Dendooven, C.Aa. Diget, T. Eronen, S. Fox, L.M. Fraile, B. Fulton, J. Huikary, H.B. Jeppesen, A.S. Jokinen, B. Jonson, A. Kankainen, I. Moore, A. Nieminen, G. Nyman, H. Penttilä, K. Riisager, S. Rinta-Antila, O. Tengblad, Y. Wang, K. Wilhelmsen and J. Äystö. *β -decay of ^{13}O* . Phys. Rev. C, vol. 72, no. 044312, 2005. 72
- [Koldste 2014] G.T. Koldste, B. Blank, M.J.G. Borge, J.A. Briz, M. Carmona-Gallardo, L.M. Fraile, H.O.U. Fynbo, J. Giovinazzo, J.G. Johansen, A. Jokinen, B. Jonson, T. Kurturkian-Nieto, T. Nilsson, A. Perea, V. Pesudo, E. Picado, K. Riisager, A. Saastamoinen, O. Tengblad, J.-C. Thomas and J. Van de Walle. *Sizeable beta-strength in $^{31}\text{Ar}(\text{beta } 3p)$ decay*. Phys. Lett. B, vol. 737, 2014. 73
- [Kubo 1989] T. Kubo, M. Ishihara, N. Inabe, T. Nakamura, H. Okuno, K. Yoshida, S. Shimoura, K. Asahi, H. Kumagai and I. Tanihata. *Radioactive nuclear beams*. World Scientific, Singapore, 1989. 78
- [Kubono 1992] S. Kubono, N. Ikeda, Y. Funatsu, M.H. Tanaka, T. Nomura, H. Orihara, S. Kato, M. Ohura, T. Kubo, N. Inabe, A. Yoshida, T. Ichihara, M. Ishihara, I. Tanihata, H. Okuno, T. Nakamura, S. Shimoura, H. Toyokawa, C.C. Yun, H. Ohnuma, K. Asahi, A. Chakrabarti, T. Mukhopadhyay and T. Kajino. *Decay property of ^{20}Na for the onset mechanism of the rapid-proton process*. Phys. Rev. C, vol. 46, no. 1, 1992. 78
- [Kugler 2000] E. Kugler. *The ISOLDE facility*. Hyperfine Interact., vol. 129, 2000. 11

- [Lane 1958] A.M. Lane and R.G. Thomas. *R-Matrix Theory of Nuclear Reactions*. Rev. Mod. Phys., vol. 30, no. 2, 1958. 44
- [Lanford 1973] W.A. Lanford and B.H. Wildenthal. *Calculations of Allowed Beta Decay in the (0d, 1s) Shell*. Phys. Rev. C, vol. 7, no. 2, 1973. 77
- [Laursen 2013] K.L. Laursen, O.S. Kirsebom, H.O.U. Fynbo, A. Jokinen, M. Madurga, K. Riisager, A. Saastamoinen, O. Tengblad and J. Äystö. *High-statistics measurement of the β -delayed α spectrum of ^{20}Na* . Eur. Phys. J. A, vol. 49, no. 79, 2013. 13, 69, 91, 108, 115, 118, 171
- [Lennard 1986] W.N. Lennard, H. Geissel, K.B. Winterbon, D. Phillips, T.K. Alexander and J.S. Forster. *Nonlinear response of Si detectors for low-Z ions*. Nucl. Instrum. Methods Phys. Res. A, vol. 248, 1986. 33
- [Lund 2015a] M.V. Lund, M.J.G. Borge, J.A. Briz, J. Cederkäll, H.O.U. Fynbo, J.H. Jensen, B. Jonson, K.L. Laursen, T. Nilsson, A. Perea, V. Pesudo, K. Riisager and O. Tengblad. *Beta-delayed proton emission from ^{21}Mg* . Eur. Phys. J. A, vol. 51, 2015. vii, 22, 35, 37, 38, 40, 42, 47, 48, 59, 161, 163, 164
- [Lund 2015b] M.V. Lund, M.J.G. Borge, J.A. Briz, J. Cederkäll, H.O.U. Fynbo, J.H. Jensen, B. Jonson, K.L. Laursen, T. Nilsson, A. Perea, V. Pesudo, K. Riisager and O. Tengblad. *Systematic trends in beta-delayed particle emitting nuclei: The case of $\beta p \alpha$ emission from ^{21}Mg* . Phys. Lett. B, vol. 750, 2015. vii, 36, 67, 68, 71, 73, 75, 76, 162, 164, 165
- [Mathar 2015] R.J. Mathar. *Solid Angle of a Rectangular Plate*, May 2015. 88, 170
- [McPherson 1965] R. McPherson and J.C. Hardy. *Delayed protons following ^{21}Mg and ^{25}Si decay*. Can. J. Phys., vol. 43, page 1, 1965. 16
- [Michel 2007] N. Michel. *Precise Coulomb wave functions for a wide range of complex l , η and z* . Comput. Phys. Commun., vol. 176, pages 232–249, 2007. 49
- [Moltz 1979] D.M. Moltz, J. Äystö, M.D. Cable, R.D. von Dincklage, R.F. Parry, J.M. Wouters and J. Cerny. *Completion of the Mass-20 Isospin Quintet by Employing a Helium-Jet-Fed On-Line Mass Separator*. Phys. Rev. Lett., vol. 42, no. 1, 1979. 77
- [Navrátil 2009] P. Navrátil, S. Quaglioni, I. Stetcu and B.R. Barrett. *Recent developments in no-core shell-model calculations*. J. Phys. G: Nucl. Part. Phys., vol. 36, 2009. 2
- [Pfützner 2012] M. Pfützner, L.V. Grigorenko, M. Karny and K. Riisager. *Radioactive decays at limit of nuclear stability*. Rev. Mod. Phys., vol. 84, 2012. 7, 9, 72

- [Piechaczek 1995] A. Piechaczek, M.F. Mothar, R. Anne, V. Borrel, B.A. Brown, J.M. Corre, D. Guillemaud-Mueller, R. Hue, H. Keller, S. Kubono, V. Kunze, M. Lewitowicz, P. Magnus, A.C. Mueller, T. Nakamura, M. Pfützner, E. Roeckl, K. Rykaczewski, M.G. Saint-Laurent, W.-D. Schmidt-Ott and O. Sorlin. *Beta-decay of ^{20}Mg* . Nuclear Physics A, vol. 584, 1995. 78, 80, 81, 84, 108, 109, 111, 117, 118, 129, 130, 131, 134, 138, 140, 141, 142, 149, 171, 172, 173
- [Rutherford 1911] E. Rutherford. *The Scattering of α and β Particles by Matter and the Structure of the Atom*. Philosophical Magazine, vol. 21, May 1911. 1
- [Schardt 1993] D. Schardt and K. Riisager. *Beta-neutrino recoil broadening in β -delayed proton emission of ^{32}Ar and ^{33}Ar* . Z. Phys. A, vol. 345, pages 265–271, 1993. 21, 23
- [Sextro 1973] R.G. Sextro, R.A. Gough and J. Cerny. *β^+ -delayed proton decay of ^{21}Mg* . Phys. Rev. C, vol. 8, 1973. 16, 17, 18, 19, 28, 37, 44, 49, 50, 51, 52, 53, 54, 55, 57, 61, 62, 64, 65, 92, 144, 161, 169, 170
- [Smith 2001] M.S. Smith and K.E. Rehm. *Nuclear astrophysics measurements with radioactive beams*. Annual Review of Nuclear and Particle Science, vol. 51, 2001. 83, 165
- [Stephens 1986] M.A. Stephens. *Goodness-of-fit techniques*. Marcel Dekker, 1986. 40
- [Tan 2005] W.P. Tan, J. Görres, J. Daly, M. Couder, A. Couture, H.Y. Lee, E. Stech, E. Strandberg, C. Ugalde and M. Wiescher. *Lifetime of the astrophysically important 4.03-MeV state in ^{19}Ne* . Phys. Rev. C, vol. 72, no. 041302(R), 2005. 84
- [Thomas 2003] J.-C. Thomas. *Spectroscopie des noyaux légers déficients en neutrons*. PhD thesis, University of Bordeaux, 2003. 18, 37, 50, 51, 52, 54, 55, 57, 60, 61, 62, 63, 64, 169, 170
- [Tilley 1995] D.R. Tilley, H.R. Weller, C.M. Cheves and R.M. Chasteler. *Energy levels of light nuclei, $A = 18 - 19$* . Nucl. Phys. A, vol. 595, page 1, 1995. 81, 121, 127, 170
- [Tilley 1998] D.R. Tilley, C.M. Cheves, J.H. Kelley, S. Raman and H.R. Weller. *Energy levels of light nuclei, $A = 20^*$* . Nuclear Physics A, vol. 636, 1998. 115, 119, 130, 138, 147, 172, 173
- [Towner 2010] I.S. Towner and J.C. Hardy. *The evaluation of V_{ud} and its impact on the unitarity of the Cabibbo-Kobayashi-Maskawa quark-mixing matrix*. Rep. Prog. Phys., vol. 73, no. 046301, 2010. 5

- [Tribble 1989] R.E. Tribble, R.H. Burch and C.A. Gagliardi. *MARS: A momentum achromat recoil spectrometer*. Nucl. Instrum. Methods Phys. Res. A, vol. 285, page 441, 1989. 80
- [TUN 2014] *TUNL Nuclear Data Evaluation Project*, June 2014. 77, 79, 165
- [Wallace 2012a] J.P. Wallace and P.J. Woods. *Level structure above the proton threshold of ^{20}Na* . Phys. Rev. C, vol. 86, 2012. 130, 141, 172
- [Wallace 2012b] J.P. Wallace, P.J. Woods, G. Lotay and A. Alharbi, A. Banu, H.M. David, T. Davinson, M. McCleskey, B.T. Roeder, E. Simmons, A. Spiridon, L. Trache and R.E. Tribble. *β -Delayed proton-decay study of ^{20}Mg and its implications for the $^{19}\text{Ne}(p,\gamma)^{20}\text{Na}$ breakout reaction in X-ray bursts*. Phys. Lett. B, vol. 712, 2012. 80, 84, 130, 151, 172
- [Wang 2012] M. Wang, G. Audi, A.H. Wapstra, F.G. Kondev, M. MacCormick, X. Xu and B. Pfeiffer. *The Ame2012 atomic mass evaluation*. Chin. Phys. C, vol. 36, no. 12, 2012. 19, 58, 68, 170
- [Wilkerson 1992] J.F. Wilkerson, T.M. Mooney, R.E. Fauber, T.B. Clegg, H.J. Karwowski, E.J. Ludwig and W.J. Thompson. *Isospin-nonconserving particle decays in light nuclei*. Nucl. Phys. A, vol. 549, pages 223–253, 1992. 52, 56
- [Wilkinson 1974] D.H. Wilkinson and B.E.F. Macefield. *A parametrization of the phase space factor for allowed β -decay*. Nucl. Phys. A, vol. 232, 1974. 5, 61, 138
- [Wrede 2010] C. Wrede, J.A. Clark, C.M. Deibel, T. Faestermann, R. Hertenberger, A. Parikh, H.-F. Wirth, S. Bishop, A.A. Chen, K. Eppinger, A. García, R. Krücken, O. Lepyoshkina, G. Rugel and K. Setoodehnia. *Toward precise Q_{EC} values for the superallowed $0^+ \rightarrow 0^+ \beta$ decays of $T = 2$ nuclides: The masses of ^{20}Na , ^{24}Al , ^{28}P , and ^{32}Cl* . Phys. Rev. C, vol. 81, no. 055503, 2010. 80, 81, 121, 131
- [Wrede 2014] C. Wrede. *β delayed γ decay measurements to probe thermonuclear astrophysical explosions*. In Proceedings of XIII Nuclei in the Cosmos, 2014. 76, 84
- [Ziegler 2008] J.F. Ziegler, J.P. Biersack and M.D. Ziegler. *Srim - the stopping and range of ions in matter*. SRIM Co., 2008. 24, 29, 35, 36, 38, 67, 85, 89, 90, 99, 121, 162, 170

List of Figures

| | | |
|-----|---|----|
| 1.1 | A schematic overview of the beta-decay strength distribution, S_{β} , for a neutron rich nucleus. As discussed in the text B_F will mainly be collected in the IAS, while B_{GT} has a broader distribution over the final states in the beta-decay daughter nucleus. However, the B_{GT} strength is collected in the Gamow-Teller Giant Resonance (GTGR). For proton rich nuclei the IAS and the GTGR will be situated inside the available beta-decay energy window. Figure taken from [Fynbo 1999]. | 6 |
| 1.2 | Sketch of the ISOLDE facility at CERN showing the target area behind the concrete blocks (grey colors), the High Resolution Separator (HRS), and the LA1 beam line in the experimental hall among other things. . . | 11 |
| 2.1 | Decay scheme for the beta-decay of ^{21}Mg based on the measured proton decay branches and the resonance energies in [Sextro 1973]. We also show the energetically allowed resonances of the $\alpha+^{17}\text{F}$ system even though the decay mode have not been observed. The lines that highlight the proton branches are color coded according to the final state (black: ground state, blue: first excited state, magenta: second excited state, cyan: third excited state). | 17 |
| 3.1 | Sketch of the experimental setup for the beta-decay study of ^{21}Mg . The beam is transported from the right, passing through the collimator (no. 7) and is implanted in the polypropylene window (no. 4). The window contains the CF_4 gas in the gas detector (no. 3) which is backed by two non-segmented silicon detectors (no. 1-2). Directly opposite is a thin DSSSD detector (no. 5), backed by a thick silicon pad detector (no. 6). From [Lund 2015a]. | 22 |
| 3.2 | A schematic drawing of the DSSSD detector type. The detector has 16 vertical strips on the frontside, each of them separated by a so-called interstrip region. On the backside the detector has 16 horizontal strips also separated by interstrip regions. If a particle deposits energy in the interstrip region, it will not be detected by the detector. A strip is rectangular in shape and characterized by the fact that if a particle deposits energy in it, only this specific strip observes the signal. This is due to the fact that an electrical conductor is running along the strip. The combination of vertical and horizontal strips gives a position sensitive detector with 256 pixels in the case of a 16 x 16 strip detector. | 23 |

- 3.3 Illustration of the energy loss calculation. The ion enters the material at point A with energy E_i . The material has the thickness d (blue rectangle) and the ion will leave the material at point B with energy E_f after having lost the energy $E_i - E_f$. The grey rectangle is a hypothetical extension of the physical material (blue rectangle). The equations shown in the right part of the figure specifies the energy E and the range R of the ion at the three different points (A, B, C). 25
- 3.4 Hit pattern of DSSSD from ^{21}Mg data. Back strip 2, 4, and 16 did not work properly as is clearly seen (horizontal lines). The color gives the number of counts in each pixel. 27
- 3.5 Result of the fitting procedure. Red dots are the values of the fitting polynomial, black dots are the pixels. The x-axis shows the distance from the center of each pixel to (x_0, y_0) in millimeters. 27
- 3.6 Example of a fit with a Gaussian response function and a linear background. Strip number 2 on the backside is shown with channel number on the axis. The data are from the beta-decay of ^{21}Mg 29
- 3.7 The DSSSD energy calibration applied to the ^{21}Mg data. The figure shows the energy difference between front- and backside strips for the individual events measured. 29
- 3.8 Gaussian function fitted to the four individual alpha peaks from the quadruple alpha-source (^{148}Gd , ^{239}Pu , ^{241}Am , ^{244}Cm) as seen in the thick pad detector behind the DSSSD. 32
- 3.9 Residuals from a linear energy calibration using the quadruple alpha-source (^{148}Gd , ^{239}Pu , ^{241}Am , ^{244}Cm) for the pad detector behind the DSSSD. The assumption of linearity appears to be good. 32
- 4.1 ΔE - E figure from the gas telescope with the gas channel number on the y-axis and the deposited energy in the first silicon detector on the x-axis. Scaled stopping power curves from SRIM [Ziegler 2008] for alpha-particles and protons in silicon is drawn on top of the data in solid and dashed red respectively. The graphical cuts to produce the alpha-particle spectrum and the proton spectrum are also drawn as long-dashed black and solid black respectively. The events located at 3.18 MeV in the silicon detector and above channel number 2300 in the gas detector is a contamination source of ^{148}Gd located inside of the silicon detector. Figure from [Lund 2015b]. 36

- 4.2 Proton singles spectrum from the gas telescope with the center-of-mass energy shown. New proton branches are marked with a ★. A ★★ indicates two new proton branches in the same peak. *Left*: events from the first silicon detector of the gas telescope. *Right*: events from the second silicon detector of the gas telescope. Figure from [Lund 2015a]. 37
- 4.3 Proton singles spectrum in the DSSSD telescope with the center-of-mass energy shown. New proton branches are marked with a ★. A ★★ indicates two new proton branches in the same peak. Note that proton branch p_{15} punch-through the central part of the DSSSD but is stopped in the outer parts of the detector. The proton branch p_{28} is placed tentatively at the expected energy. The small peak just below p_{24} is not identified as a proton branch and a further discussion can be found in Sect. 4.5 as part of the discussion on the 8135(15) keV resonance. *Left*: events from the DSSSD. *Right*: events from the pad detector. Figure from [Lund 2015a]. 38
- 4.4 Half-life fit for the ^{21}Mg decay. The time distribution is from the two most intense proton branches, p_{10} and p_{11} , measured in the DSSSD. Figure from [Lund 2015a]. 40
- 4.5 Result of the Anderson-Darling goodness-of-fit test, A^2 , of the β -particle region in the ΔE - E plot with the $^{21}\text{Mg}(\beta p)$ time distribution as the reference distribution. The vertical axis shows the channel number of the gas detector and the horizontal axis shows the energy of the first silicon detector in the gas telescope. The proton branch p_1 is marked with a black rectangle. Figure from [Lund 2015a]. 42
- 4.6 The result of a simultaneous fit of p_{10} , p_{11} , p_{12} , p_{13} , and p_{14} as measured in the DSSSD. The solid black line is combined line shape of all five proton branches. The line shape of the individual proton branches is shown with dashed blue. The residuals from the fit are drawn without indicating the uncertainty. Note that only the combined line shape is limited to the fitting interval. Figure from [Lund 2015a]. 47

- 4.7 Two different line shape fits are shown here. The energy region contains two peaks that overlap and the two line shape fits are based on different assumptions about the proton branches contributing to the low energy peak. The thick full drawn line shape (black) assumes a broad proton branch with an energy dependent width Γ as described in the text ($L = 0$ and $r_0 = 1.4$ fm). This line shape also includes p_5 and the low intensity branch p_3 . The second interpretation of the low energy peak is shown by the thick dashed line shape (black) which assumes two proton branches, both with a constant width Γ , instead of the broad proton branch. The low intensity branch p_3 and the proton branch p_5 is also included. The thin blue curves in solid and dashed shows the individual components of the two line shape fits. Figure from [Lund 2015a]. 48
- 4.8 The decay scheme for the beta-decay of ^{21}Mg showing only resonances populated in the beta-decay. Resonances in ^{21}Na with $I^\pi = (\frac{3}{2}, \frac{5}{2}, \frac{7}{2})^+$ have not been assigned any I^π value on the figure. The dashed, dotted, and solid lines in various colors are used to distinguish the many different decay branches, however, all branches to one particular final state has the same line type. Figure from [Lund 2015a]. 59
- 5.1 Alpha-particle spectrum as measured in the first silicon detector of the gas telescope. The inset in the top right corner shows the DSSSD proton spectrum in coincidence with the alpha-particle branch α_1 . Figure from [Lund 2015b]. 68
- 5.2 Decay scheme for ^{21}Mg focusing on the alpha-particle emission. Dashed blue lines indicate alpha-particle branches, solid red lines indicate the $\beta p \alpha$ decay mode. Figure from [Lund 2015b]. 71
- 5.3 The $Z > N$ nuclei from N to Si with the experimentally observed dominant beta-delayed particle decay modes marked. Note that the $\beta \alpha$ and βp decay modes are not shown if the $\beta p \alpha$ or $\beta 2p$ decay modes also occur. The $^{21}\text{Mg}(\beta p \alpha)$ and $^{13}\text{O}(\beta p \alpha)$, see Sect. 5.2.1, decays are marked in blue. Figure from [Lund 2015b]. 73
- 5.4 Q_{EC} -values for nuclei up to Ge. Filled symbols marks nuclei with even Z and open symbols odd Z nuclei. The squares marks nuclei with even N and the circles marks odd N nuclei. The isospin values shown are for the even-even nuclei. The green symbols correspond to $T = 1$ ($T_3 = 1$) and the red symbols correspond to $T = 4$. The dashed and dotted lines are a liquid drop estimate of Q_{EC} for nuclei with $T_3 = -1/2$ and $T_3 = -3/2$ respectively. The full lines marks a quartet of Al-Si nuclei. Figure from [Lund 2015b]. 75

| | | |
|------|--|----|
| 5.5 | <i>Left:</i> The quartet of nuclei with similar Q_{EC} -value. <i>Right:</i> The favored beta-delayed particle decay modes. Figures from [Lund 2015b]. | 76 |
| 6.1 | Decay scheme for allowed beta-decay of ^{20}Mg populating 1^+ states in ^{20}Na . Figure from the TUNL evaluation in [TUN 2014]. | 79 |
| 6.2 | The stellar nucleosynthesis path under various different conditions. The HCNO cycle and the breakout from the HCNO cycle is running close to or at the proton drip-line in explosive environments. Figure from [Smith 2001] | 83 |
| 7.1 | HPGe clover detector setup at the IDS. Collection chamber is at the central position where the four detectors meet. | 86 |
| 7.2 | Silicon detector array surrounding the carbon collection foil in the center. In the top left corner the final collimator before the beam enters the chamber is visible. | 87 |
| 7.3 | Schematic drawing of the silicon array with naming conventions and detector thicknesses. | 87 |
| 7.4 | The χ^2 estimator for the carbon foil thickness. We have four data points and one parameter so the number of degrees of freedom is 3. | 89 |
| 7.5 | Hit patterns in the 6 strip detectors from ^{21}Mg data except in the case of U2 and U4 where ^{20}Na data is used. The $20\ \mu\text{m}$ detector U2 is a single-sided strip detector with only the 16 vertical strips. | 92 |
| 7.6 | Example of a fit for the geometry from ^{21}Mg data measured with the detector U6. The black points are data points and the red points are the value of the polynomial used to describe the data. | 93 |
| 7.7 | Example of a fit with a Gaussian response function to the individual calibration peaks. Strip number 2 on the frontside of detector U3 is shown. It is uncalibrated ^{21}Mg data. | 94 |
| 7.8 | The U3 DSSSD energy calibration applied to the ^{21}Mg data. It shows the energy difference between the front- and backside strips for the individual events observed. | 94 |
| 7.9 | The two spectra shown here are the total data sample collected on the mass of ^{20}Mg in two different strips of the $20\ \mu\text{m}$ thin detector U2. The spectrum is dominated by the alpha-particles from ^{20}Na . The top figure is the spectrum as observed in strip 1. The bottom figure is the spectrum observed in strip 16. No cuts have been applied to the data. . | 96 |
| 7.10 | Total energy calibrated spectrum in U2 from a 3 hour background measurement with the ISOLDE beam gate closed such that no beam was allowed into the detection chamber. What is observed is electronic noise. | 97 |

- 7.11 *Left:* The proton spectrum from ^{21}Mg as observed in P1. *Right:* The measured energy loss in the front detector (U4) for the three proton branches p_{18} (blue), p_{22} (red), and p_{27} (green). 98
- 7.12 Example of a ^{152}Eu gamma-ray spectrum from crystal 1 in clover 1. The spectrum is not energy calibrated but all six calibration peaks are visible and the Gaussian fits to the peaks are also present. 101
- 7.13 Example of residuals from the gamma-ray energy calibration of crystal 1 in clover 1. The calibration is made with a ^{152}Eu source. 101
- 7.14 ^{152}Eu gamma-ray spectrum from the measurement for the absolute efficiency calibration. Several fits to the relevant peaks is shown. 103
- 7.15 The measured absolute efficiencies at the energies summarized in Table 7.5. The best fit to the data points is shown with the analytic form presented in Equation (7.9). 103
- 8.1 The ΔE - E spectrum from the U4-P1 telescope with no conditions applied to the data. The energies quoted are the measured proton energy in the detector. The closed blue line marks the applied graphical gate to produce a clean proton spectrum in pad 1. The closed green line marks the applied graphical gate to produce a clean proton spectrum in the U4 with no contribution from the particles that are not stopped here. 109
- 8.2 The ΔE - E spectrum from the U1-U2 telescope with the condition that the energy in U2 must be greater than 200 keV. The energies quoted are the measured proton energy in the detector. The closed blue line shows the applied graphical gate to produce a clean proton spectrum in U1. The alpha-particles that punch through U2 is visible below 3 MeV in U1 and above 2.8 MeV in U2. The data shown here have not been subjected to the matching routine of the U1 and U2 events as described in Sect. 7.2.3. 110
- 8.3 Proton spectrum measured in U1. The graphical gate shown in Figure 8.2 is applied to the data along with the condition of particle multiplicity one in U1. The signals in the U1 have been matched with the signal in U2, as to avoid the noise signals from U2. It is the measured sum energy of U1 and U2 that is shown, i.e. no corrections for dead layers have been made. 111
- 8.4 Proton spectrum measured in P1. The graphical gate shown on Figure 8.1 has been applied to the data in order to produce this spectrum. It shows the proton center-of-mass energy. 112

- 8.5 Three different proton spectra with the proton center-of-mass energy as measured in U4. *Blue*: Data from the U4-P1 telescope submitted to the graphical gate that cuts away events that punch through U4 (see green curve in Figure 8.1). *Red*: On top of the punch through gate for the blue spectrum we have also applied a time cut ($t < 100$ ms). *Green*: On top of the punch through gate and the time gate we have also applied the condition that the opposing front detector (U3) measures no particle events. 114
- 8.6 *Left*: Beta-decayed alpha-particle spectrum from the decay of ^{20}Na as measured in U4 with the deposited proton energy on the axis. It is produced by applying the gate shown on the figure to the right and by demanding particle multiplicity one in both detectors and demanding that no events is observed in the two backing detectors. *Right*: Coincidence spectrum between U4 and U3 with a demand of a particle multiplicity of one in both detectors and demanding that no events are observed in the two backing detectors. The closed blue line shows the graphical gate applied to remove the main part of the nuclear recoils. 118
- 8.7 *Left*: Total gamma-ray spectrum from all crystals under the condition $t < 300$ ms. *Right*: Total data set from all crystals in coincidence with the protons measured in U1 as shown in Figure 8.3. 119
- 8.8 Half-life fit for the ^{20}Mg decay. The time distribution is from the U1 detector which is placed behind a $20\ \mu\text{m}$ thick silicon detector. 120
- 8.9 Example of a line shape fit of the proton branch p_7 in detector P1 with the line shape function described in Equation (4.7). The fit results in $\chi^2/\text{ndf} = 31.93/10$. The residuals from the fit is shown below with the same energy scale as the data. The uncertainty of the residuals are not shown. 124
- 8.10 Gamma-ray gated proton spectra from P1 with the background from the Compton continuum of the 511 keV gamma-ray subtracted. It is the proton center-of-mass energy. *Top*: Proton spectrum from P1 in coincidence with the 238 keV gamma-ray. It is uncertain whether we observe coincidences with p_{11} . *Bottom*: Proton spectrum from P1 in coincidence with the 275 keV gamma-ray. 125
- 8.11 *Left*: The measured proton spectrum in P1. The two vertical lines (green) mark the energy region that we gate on (p_8). *Right*: Total gamma-ray spectrum with the proton gate shown in the left figure applied. The central gamma-ray is the 511 keV from e^+e^- annihilation. The remaining three gamma-rays are from the decay of ^{20}Mg : 238 keV (I), 275 keV (II), and 1298 keV (III). 128

- 8.12 Decay scheme for ^{20}Mg including p_2 and p_3 which are not observed here. Also presented in Table 8.6. The different types of lines connecting ^{20}Na and ^{19}Ne indicate proton branches to different final states. The ground state transitions are solid black, the first excited state transitions are dashed green, the second excited state transitions are dotted red, the third excited state transitions are dashed blue, and the fourth excited state transitions are dotted orange. 132
- 8.13 *Top*: Total gamma-ray spectrum with the demand that we have at least one coincident event in one of the following silicon detectors: P1, P2, P3, U1, or U5. *Bottom*: Total gamma-ray spectrum with the demand that the gamma-ray event must happen within the first 300 ms after proton impact on the ISOLDE production target. 135
- 9.1 Beta-delayed proton spectrum observed with the IDS experimental setup showing the center-of-mass proton energy. *Left*: Spectrum from the detector U3 with the demands of no particle events in the opposing detector (U4), no punch through events, and to only look at events within 100 ms from the last proton pulse on the ISOLDE production target. *Right*: Spectrum from the detector U1 with the demands that only one particle event are observed in both U1 and U2 and a demand to only look at events that punch through the front detector (U2). 145
- 9.2 *Left*: Gamma-ray spectrum from all HPGe-clover detectors gated on the U1 proton spectrum (see Figure 9.1). We clearly observe the expected 1634 keV gamma-ray, which is the deexcitation of the first excited state in the proton daughter ^{20}Ne . *Right*: Proton spectrum in U1 if we also demand that $1600 \text{ keV} < E_\gamma < 1650 \text{ keV}$. The spectrum is to be compared with the spectrum on the right on Figure 9.1. 147
- 9.3 *Left*: The U3 laboratory energy (x-axis) against the U4 laboratory energy (y-axis) with a demand of particle multiplicity one in both detectors and no events in their respective back detectors (P1 and P3). The two detectors are facing each other with the decay point located in between them. *Right*: Projection of all events shown in the spectrum on the left side onto the x-axis, i.e. the laboratory energy in U3 for events that are coincident in U3 and U4. 148
- 9.4 Center-of-mass proton energy spectrum from U4. The spectrum is made with the same gates as the green spectrum on Figure 8.5 plus the additional demand to only look at events in the central 4×4 pixels of U4. Comparison with Figure 8.5 makes it clear that we do not significantly reduce the low-energy contamination of ^{16}O recoils. . . . 150

List of Tables

| | | |
|-----|---|----|
| 3.1 | Dead layer and detector thicknesses with the detector names referring to Figure 3.1. | 24 |
| 4.1 | Established confidence levels for the three different EDF statistics based on Monte Carlo simulations. The confidence levels are calculated for the hypotheses that the time distribution in question belong to the decay of ^{21}Mg . Hence a good fit will have a confidence level less than 95%. | 41 |
| 4.2 | Results of the three different goodness-of-fit tests of the time distribution to settle if the events in question do belong to the ^{21}Mg decay. The values are to be compared with the confidence levels in Table 4.1. . . . | 41 |
| 4.3 | Comparison of the fitted Breit-Wigner widths Γ with the known literature values (Γ_{tot}). For references to the literature values see Table 4.5. An upper limit on Γ is set when the obtained value from the line shape fit is less than the Gaussian detector resolution. Such cases are assigned an upper limit $\Gamma \leq \sigma_{\text{det}}$ | 46 |
| 4.4 | E_{cm} in keV and relative proton intensities with respect to p ₁₁ compared to earlier results [Sextro 1973, Thomas 2003]. #: p ₁₃ -p ₁₄ and p ₂ -p ₄ were observed as a single proton line in [Sextro 1973, Thomas 2003]. | 51 |
| 4.5 | A comparison of the measured weighted averages of the ^{21}Na resonances ($\bar{E}_{\text{meas.}}^*$) with the literature energies (E^*) is shown in the first two columns. The column marked I^π is the spin and parity according to the literature, Γ_{tot} is the total width of the resonance according to the literature, and $\Gamma_{\text{p,el}}$ is the elastic proton scattering width of the resonance according to the literature. In the following column is the reference for this information given. Note that if $I^\pi = \left(\frac{3}{2}, \frac{5}{2}, \frac{7}{2}\right)^+$ it is marked by a #. The quoted uncertainties on $\bar{E}_{\text{meas.}}^*$ do not take the systematic uncertainty of around 10 keV (see Sect. 3.3) into account - only the statistical uncertainty from the line shape fit is included. | 56 |

| | | |
|-----|--|----|
| 4.6 | The first two columns show the measured weighted averages of the ^{21}Na resonances ($\bar{E}_{\text{meas.}}^*$) and the literature energies (E^*). The right part of the table shows the new interpretation of the decay scheme. If the proton line is in italic, p_i , the assignment is not conclusive. An x marks an unobserved but energetically allowed proton emission. The particle emission thresholds are $S_p(^{21}\text{Na})= 2431.68(28)\text{ keV}$ and $S_\alpha(^{21}\text{Na})= 6561.3(4)\text{ keV}$, [Wang 2012]. The quoted uncertainties on $\bar{E}_{\text{meas.}}^*$ do not take the systematic uncertainty of around 10 keV (see Sect. 3.3) into account - only the statistical uncertainty from the line shape fit is included. | 58 |
| 4.7 | Absolute β branching ratios compared to earlier results by [Sextro 1973, Thomas 2003]. | 62 |
| 4.8 | log(ft)-values compared to earlier results by [Sextro 1973, Thomas 2003]. | 64 |
| 5.1 | EDF goodness-of-fit test results of the time distribution of the individual observed alpha-particle peaks and of the proton branch p_3 . The first column specifies which test is used, the second column gives the 95% confidence level (obtained through Monte Carlo simulations) for having the ^{21}Mg time distribution. For other confidence levels see Table 4.1. | 70 |
| 5.2 | E_{cm} in keV, relative intensities with respect to the proton branch p_{11} , and absolute intensities. | 72 |
| 6.1 | The energy and intensity of the observed gamma-ray decays of the four lowest excited states in ^{19}Ne according to [Tilley 1995]. | 81 |
| 7.1 | Punch through laboratory energies for protons and alpha-particles in the front detectors of the four charged particle telescopes. It is calculated for the thickness specified in the second column of the table with the SRIM stopping power tables [Ziegler 2008]. | 85 |
| 7.2 | Dead layer and detector thicknesses with the detector names referring to Figure 7.3. The solid angle of each detector is calculated with equation (A4) in [Mathar 2015] and the uncertainty is coming from a ± 1 mm change in the distance between the carbon foil and the detector center. The determination of the detector energy resolution σ_{det} is described in more detail in Sect. 7.2.2 and in Sect. 8.3.1. | 88 |
| 7.3 | Summary of the geometry fits for (x_0, y_0) . All but U4 is based on ^{21}Mg data while U4 is based on ^{20}Na data. The distance z_0 from the carbon foil to the detector center is based on measurements of the support structure used for the detectors which is 3D-printed to high precision. | 91 |

- 7.4 The parameters used in the front-back matching routine for constructing the particle energies in the DSSSD detectors. 94
- 7.5 ^{152}Eu gamma-ray energies and intensities according to [Eu1 2015] used for the efficiency calibration of the HPGe-detectors. Due to the poor energy resolution of the HPGe-detectors we use the summed intensities of the 1085.869 keV and the 1089.737 keV gamma-rays, $I_\gamma = 11.934(22)\%$, and for the 1109.174 keV and the 1112.074 keV gamma-rays, $I_\gamma = 13.830(22)\%$. 102
- 7.6 Calculation of the total absolute gamma-ray efficiency for the HPGe-detector array. R_{E_γ} is the scaling factor for the efficiencies. For the 238.27 keV and 275.09 keV gamma-rays we scale from the 244.6975 keV gamma-ray. For the 983.70 keV gamma-ray we scale from the 964.079 keV gamma-ray. For the 1232.47 keV gamma-ray we scale from the 1112.074 keV gamma-ray. For the 1297.73 keV gamma-ray we scale from the 1408.006 keV gamma-ray. The table includes two columns with $\varepsilon_{\text{corr.}}(E_\gamma)$ which is the corrected absolute efficiency. However, only the last column of $\varepsilon_{\text{corr.}}(E_\gamma)$ has the uncertainty corrected for the change in the deviation of the absolute efficiency as determined in Figure 4.9 in [Debertin 1988]. 105
- 8.1 The laboratory alpha-particle energies, E_α , are taken from [Laursen 2013]. The ^{16}O laboratory energy, $E_{^{16}\text{O}}$, is calculated with Equation (8.3). Range of ^{16}O recoil in silicon after passing through 0.0545 μm of carbon, i.e. the implantation depth of the Mg ion beam in the carbon foil, is calculated as described in Sect. 3.2. The last column, E_{det} , shows the remaining energy of the recoil after having passed the carbon and 0.1 μm of silicon which is equivalent to the dead layer thickness on the DSSSD's. 115
- 8.2 The center-of-mass proton energies, E_{cm} , are adopted from [Piechaczek 1995]. The laboratory energy of the ^{19}Ne nuclear recoils are calculated according to Equation (8.4). Range of ^{19}Ne recoil in silicon after passing through 0.0545 μm of carbon, i.e. the implantation depth of the Mg ion beam in the carbon foil, is determined as described in Sect. 3.2. The last column, E_{det} , shows the remaining energy of the recoil after having passed the carbon and 0.1 μm of silicon equivalent to the dead layer thickness on the DSSSD's. E_{det} is only assigned a value if the recoil actually have enough energy to pass through the carbon foil and the thin silicon layer. 117
- 8.3 Center-of-mass proton energies as measured in the various silicon detectors. The energy quoted is the centroid energy of the line shape function presented in Equation (4.7). 122

- 8.4 Gamma-ray coincident proton center-of-mass energies. The upper value of the energies is the 238 keV gamma-ray coincident proton, while the lower one is the 275 keV gamma-ray coincident proton. The energies from U5 is not gamma-ray gated as the energy resolution here is so good that we can distinguish the individual branches contained in the proton peaks. The uncertainty on the weighted average energy for p_4 , p_5 , and p_V are estimated on the basis of the energy spread between the detectors. It is uncertain whether we observe evidence for p_{11} in coincidence with the 238 keV gamma-ray. 126
- 8.5 The ratio R as measured in the individual detectors. The classification is made according to the description in the text (A: only ground state transition, B: only excited state transition, C: mixture). 129
- 8.6 The ^{20}Na energies are taken from [Piechaczek 1995, Tilley 1998, Wallace 2012a, Wallace 2012b, Glassman 2015]. The 7183(16) keV resonance is either the ≈ 6920 keV or the ≈ 7440 keV resonance which are observed by [Piechaczek 1995]. Two previously unobserved resonances in ^{20}Na have been introduced at 5507(10) keV and at 5836(13) keV. The position of p_2 and p_3 are based on previous experiments as we do not observe any clear evidence for these. It is mainly due to the contamination from the beta-decay of ^{20}Na in the front detectors. 130
- 8.7 Summary of the relative intensity of the proton peaks observed in the different detectors. The columns 2-4 are relative intensities with respect to p_4 . The columns 5-7 are relative intensities with respect to p_{11} . 133
- 8.8 The absolute intensities of the individual proton lines for the different detectors. The two absolute intensities written in italic numbers are values taken from a different detector and used for normalization. See the text for more detail. 137
- 8.9 The ratio of the efficiency corrected number of gamma-rays in coincidence with the given proton line (γ) to the integrated and background corrected number of protons in the same proton line (p) for the individual detectors. For each proton line we quote two numbers: the top one corresponds to coincidences with the 238 keV gamma-ray and the bottom one corresponds to coincidences with the 275 keV gamma-ray. 139
- 8.10 Absolute proton intensities for the individual proton emission branches. It is the weighted average of the different detectors. Note that p_2 and p_3 have not been observed here but both are known from previous experiments. Their position in the decay scheme are marked. 140

-
- 8.11 Absolute beta-decay branching ratios and $\log(ft)$ -values for the individual resonances in ^{20}Na determined as the weighted average of all detectors. The present work is compared with [Piechaczek 1995]. Note that the absolute intensity of p_2 and p_3 are not included here. The resonances marked with a * are not observed here and the energy quoted are from [Piechaczek 1995]. 141
- 9.1 The energy and intensity of the observed gamma-ray decays of the three lowest excited states in ^{20}Ne according to [Tilley 1998]. It is evident that both the second and third excited state mainly deexcites to the first excited state. 147